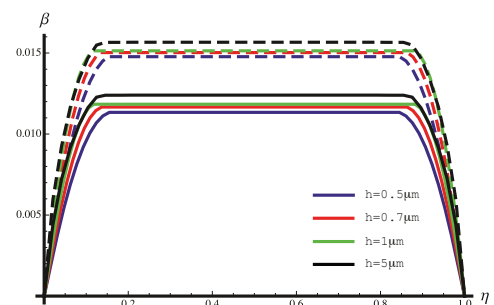
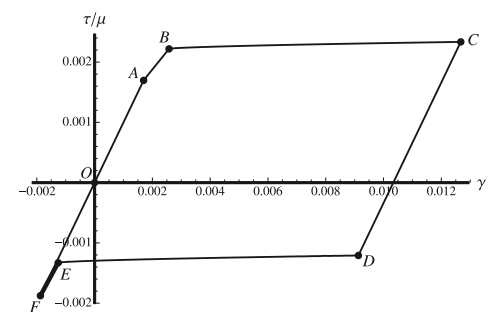
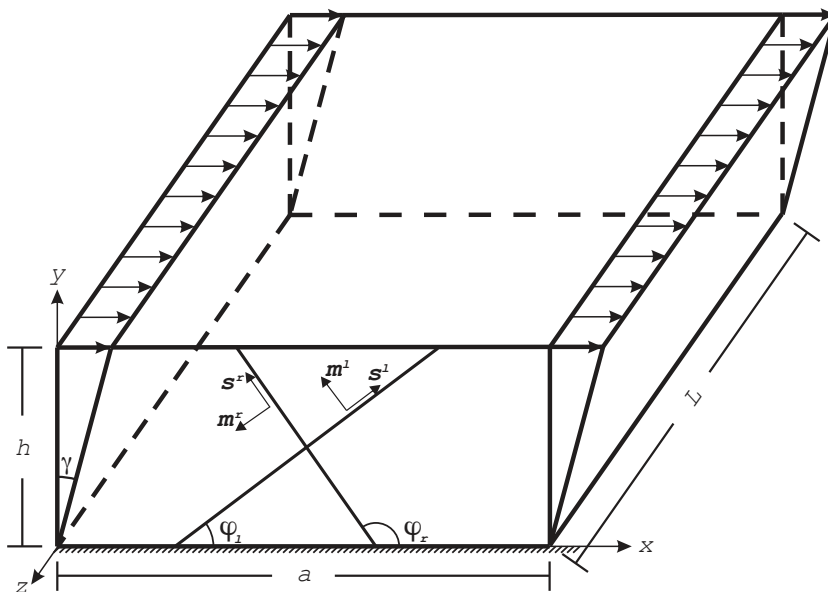


# Analytical and Numerical Solutions to Plane Strain Problems in Continuum Dislocation Theory

Pramio G. Sembiring



Dissertation

**Analytical and numerical solutions to plane strain  
problems in continuum dislocation theory**

Zur Erlangung des akademischen Grades

Dr.-Ing.

vorgelegt der

Fakultät für Bau- und Umweltingenieurwissenschaften

an der Ruhr-Universität Bochum

von

Pramio Garson Sembiring  
aus Medan, Indonesien

Bochum 2014



*For my parents:  
T. Sembiring and R. Simanjuntak*

Mündliche Prüfung: 25.06.2014

Erster Referent: Prof. Dr. rer. nat. Khanh Chau Le

Zweiter Referent: Prof. Dr. rer. nat. Klaus Hackl

Dritter Referent: Prof. Dr. rer. nat. Alexander Hartmaier

Fachfremder Referent: Prof. Dr. rer. nat. Harro Stolpe

Vorsitzender : Prof. Dr.-Ing. Markus Thewes

## **Abstract**

This dissertation studies the plane strain problems of single crystal strip deforming in one and two active slip systems within continuum dislocation theory. To include the dislocation characteristics in the constitutive equations as an integral part, the free energy is modified to account the energy of lattice defects.

A closed-form analytical solutions are found for dislocations pile-up at the boundaries of single crystal strip with single and symmetric double slip systems subject to plane constrained shear, uniaxial extension and mixed deformation of shear and extension. For non-symmetric double slip system for all three loading cases, the solutions are sought numerically.

The solutions exhibit the energetic and dissipative thresholds for dislocation nucleation, the Bauschinger translational work hardening, and the size effects. The comparison of plane constrained shear problem results with discrete dislocation simulations shows good agreement between continuum and discrete approaches.

## **Kurzfassung**

In der hier vorliegenden Arbeit wird die Kontinuumsversetzungstheorie auf einen Einkristall angewendet und verschiedene Beispiele mit ebenen Dehnungszustand sowie ein und zwei Gleitsystemen werden gezeigt. Um die Eigenschaften der Versetzungen in die Konstitutivgleichungen einzubringen wird die freie Energie modifiziert indem die Energie aus Gitterdefekten hinzugefügt wird.

Für die Beispiele ebene Scherung, einaxialer Zug und ebene Scherung mit einaxialen Zug werden für ein Gleitsystem und für zwei symmetrische Gleitsysteme analytische Lösungen hergeleitet. Für zwei nicht symmetrische Gleitsysteme werden numerische Lösungen für diese drei Lastfälle gefunden.

Die Ergebnisse zeigen energetische und dissipative Grenze für die Versetzungsbildung sowie den Bauschinger Effekt und den Skaleneffekt. Die Ergebnisse aus ebener Scherung weisen eine gute Übereinstimmung mit der Simulation disketer Versetzungen auf.

## Acknowledgements

I would never have been able to finish this dissertation without the help from many persons. Therefore I would like to express my gratitude to all of those who have supported me.

Foremost, I would like to express my sincere gratitude to my advisor Prof. Khanh Chau Le for the continuous support, for always believing in me, for his patience, motivation, enthusiasm and immense knowledge. His guidance helped me in all the time of research and writing of this thesis. I could not have imagined having a better advisor and mentor for my doctoral study.

Equally important, I am also grateful to Prof. Klaus Hackl for giving me a chance to work at the chair of Mechanik-Material Theorie for all of the years during my doctoral study and also for acting as the second dissertation of this thesis.

My sincere thanks also goes to the rest of my dissertation committee: Prof. Alexander Hartmaier, Prof. Harro Stolpe and Prof. Markus Thewes.

Next, I would like to thank all co-workers at the chair of Mechanik-Material Theorie that created a pleasant atmosphere to work with: Ulrich Hoppe, Barbara Fromme, Dennis Kochmann, Christina Günther, Sandra Klinge, Phillip Junker, Mehdi Goodarzi, Christoph Moos, Trinh Bach Tuyet, Bojan Dimitrijevic, Nicola Wessels and Khayal Musayef. In particular, I am grateful to Ulrich Hoppe for helping me with many difficulties either related or not to my research. I would like also to thank Jörg Sahlmen for giving me a chance to work at Computational Engineering.

I would like to express my deepest gratitude to my closest families in Medan and Palembang, especially my father, T. Sembiring, my brother, Coku Sembiring, and my sister, Klaudia Sembiring, for always giving me support.

Last but not least, I would like to express my deepest appreciation to my wife, Ros Marya Yasintha, for always supporting me, for trusting me and for bearing with me during my time writing this dissertation.

# Contents

<b>1</b>	<b>Introduction</b>	<b>1</b>
1.1	Motivation . . . . .	1
1.2	Scope of this thesis . . . . .	2
<b>2</b>	<b>Physical background</b>	<b>5</b>
2.1	Stress-Strain diagram . . . . .	5
2.2	Microscopic phenomena throughout plastic deformation . . . . .	7
2.2.1	Crystalline structures of metals . . . . .	7
2.2.2	Crystal plasticity . . . . .	8
2.2.3	Critical Resolved Shear Stress . . . . .	9
2.2.4	Theoretical shear strength of single crystal . . . . .	10
2.3	Dislocation . . . . .	12
2.3.1	Types of dislocation . . . . .	12
2.3.2	Dislocation motion . . . . .	13
2.3.3	Properties of dislocations . . . . .	16
2.3.3.1	Stress field around a dislocation . . . . .	16
2.3.3.2	Self energy of a dislocation line . . . . .	18
2.3.3.3	Forces on a dislocation . . . . .	19
2.3.3.4	Interaction of dislocations . . . . .	20
2.3.3.5	Dislocation nucleation, multiplication and pile-ups . . . . .	23
2.4	Continuum theory of dislocation . . . . .	25
2.4.1	Elastic and plastic distortions . . . . .	26
2.4.2	Dislocation density . . . . .	30
2.4.3	Energy of dislocation network . . . . .	31
2.4.4	System of equations . . . . .	33
2.4.5	Energy minimization . . . . .	36
<b>3</b>	<b>Dislocation nucleation in anti-plane constrained shear of single crystals</b>	<b>39</b>
3.1	Anti-plane constrained shear energy . . . . .	39
3.2	Total energy of the crystal in anti-plane constrained shear . . . . .	40
3.3	Anti-plane constrained shear at zero dissipation . . . . .	41
3.3.1	Dislocation nucleation at zero dissipation . . . . .	41
3.3.2	Dislocation density, energetic threshold value, stress strain curve and size effect . . . . .	44
3.4	Anti-plane constrained shear at non-zero dissipation . . . . .	48
<b>4</b>	<b>Plane-constrained shear of single crystals with one active slip system</b>	<b>55</b>
4.1	Boundary value problem . . . . .	55
4.2	Single slip plane-constrained shear at zero resistance . . . . .	59
4.2.1	Energetic threshold for dislocation nucleation . . . . .	60
4.2.2	Dislocation pile-up at zero resistance . . . . .	62
4.3	Single slip plane-constrained shear with energy dissipation . . . . .	69
4.4	Comparison with discrete dislocation simulations . . . . .	79

<b>5</b>	<b>Uniaxial extension and combined loading of single slip system</b>	<b>83</b>
5.1	Energy of the crystal . . . . .	83
5.2	Dislocation nucleation and evolution at zero resistance . . . . .	85
5.2.1	Plane-constrained uniaxial extension . . . . .	85
5.2.2	Plane-constrained combined loading . . . . .	91
5.3	Dislocation nucleation and evolution with energy dissipation . . . . .	95
5.3.1	Plane-constrained uniaxial extension . . . . .	95
5.3.2	Plane-constrained combined loading . . . . .	103
<b>6</b>	<b>Single crystals plane-constrained shear problem with double slip systems</b>	<b>107</b>
6.1	Energy of the crystal . . . . .	107
6.2	Double slip plane-constrained shear at zero resistance . . . . .	110
6.2.1	Energetic threshold values . . . . .	110
6.2.2	Symmetric double slip systems at zero dissipation . . . . .	117
6.2.3	General double slip systems case at zero dissipation . . . . .	124
6.3	Double slip plane-constrained shear at non-zero dissipation . . . . .	134
6.3.1	Energetic threshold values . . . . .	135
6.3.2	Symmetric double slip systems at non-zero dissipation . . . . .	137
6.3.3	General double slip systems case with energy dissipation . . . . .	144
6.4	Comparison with discrete dislocation simulations . . . . .	155
<b>7</b>	<b>Uniaxial extension and combined loading of two active slip systems</b>	<b>159</b>
7.1	Energy of the crystal . . . . .	159
7.2	Plane-constrained uniaxial extension . . . . .	162
7.2.1	Energetic threshold values . . . . .	162
7.2.2	Symmetric double slip systems . . . . .	167
7.2.3	General double slip systems case . . . . .	177
7.3	Plane-constrained combined loading of shear and uniaxial extension . . . . .	190
7.3.1	Dislocations nucleation at zero dissipation . . . . .	190
7.3.2	Dislocations nucleation at non-zero dissipation . . . . .	195
<b>8</b>	<b>Conclusion</b>	<b>201</b>

# 1 Introduction

## 1.1 Motivation

From the experimental observation, it is known that at room temperature the motions of dislocations through the crystal lattice play an important role in plastic deformation. These dislocation motions take place on certain crystal planes in certain crystallographic directions.

The evolution of the dislocation network has a strong influence on the plastic deformation of crystalline solids. Unfortunately, since a direct treatment of dislocations in the deformed crystal is not considered in classical plasticity theory, the influence of dislocations cannot be explicitly be accounted for in the constitutive equations. When crystalline solids begin to deform plastically, the nucleation of geometrically necessary dislocations takes place in order to reduce crystal's energy. The pile-ups of these newly generated geometrically necessary dislocations near the obstacles impede the further movement of dislocations resulting in the work hardening of the crystal. Motion of dislocations generates the dissipation of energy which, in turn, results in a resistance to dislocation motion. The nucleation and subsequent pile-up of dislocations on the crystal boundaries are in some sense responsible for causing the size-dependent plastic yielding (size effect). Consequently, the nucleation and motion of dislocations become an important mechanism for size effect, work hardening and hysteresis in crystal plasticity theory.

Due to the complex behavior of the dislocation network and due to the high dislocation densities accompanying plastic deformation (which is typically in the range of  $10^8 - 10^{15} \text{ m}^{-2}$ ), continuum dislocation theory was established as a mathematical tool to describe the evolution of dislocation network. The framework of continuum dislocation theory has been laid down by Kondo [1952], Nye [1953], Bilby et al. [1955], Kröner [1958], Berdichevsky and Sedov [1967], Le and Stumpf [1996a,b], and Gurtin [2004]. Nevertheless, owing to the progress in statistical mechanics and thermodynamics of dislocation network reported in [Berdichevsky, 2005, 2006a], the applicability of the theory became feasible only in recent years [Berdichevsky, 2006a, Groma et al., 2003, Ortiz and Repetto, 1999, Ortiz et al., 2000].

By all of various alternative strain-gradient plasticity theories, we only mention here the theories that closely relevant to the continuum dislocation theory, namely, Shu and Fleck [1999], Gao et al. [1999], Acharya and Bassani [2000], Huang et al. [2000, 2004], Fleck and Hutchinson [2001], and Han et al. [2005a,b]. Contrary to the continuum dislocation theory, all of these strain gradient plasticity theories incorporate the plastic strain gradient into the energy which make it depending on the history of plastic deformation. The incorporation of the energy of microstructure using second powers of plastic strain gradients was proposed in the works of Gurtin and coworkers [Gurtin, 2003, 2004, Gurtin and Anand, 2005].

By reason of these variety of strain-gradient plasticity theories, it is important to have the exact solutions of test problems so that different models can be tested and compared. One of such test problem is the plane constrained shear of a single crystal strip deforming in single or double slip. Needleman and Van der Giessen [2001] solved this problem numerically by the discrete dislocation simulations for single and double symmetric slip. Shu et al. [2001] compared these results with the numerical solutions obtained by the nonlocal plasticity theories of Shu and Fleck [1999] and Acharya and Bassani [2000] (see also Anand et al. [2005]).

In pursuance of formulating the contribution of the microstructural dislocation network to the free energy in a physically-reasoned way rather than for reasons of mathematical regularization we make use of the free energy formulation proposed by Berdichevsky [2006a,b] which has a logarithmic dependency on the scalar dislocation density. Since the dislocation density depends only on the current of dislocations' characteristics (i.e. Burgers vector and positions of dislocation lines), this kind of energy has no dependency on the history of plastic deformation. Additionally, this approach is also physically-reasoned due to the linear increase of the energy of microstructure at small dislocation densities (where the interaction energy is ignored, see e.g., Le and Berdichevsky [2001] ) and the increase of the energy of microstructure toward infinity as the dislocation density reaches some saturation density [Berdichevsky, 2006b], preventing over-saturation.

Berdichevsky and Le [2007] were the firsts to have found the analytical solution of the anti-plane constrained shear problem within the framework of continuum dislocation theory. The interesting features of this solution are the energetic and dissipative yielding thresholds, the Bauschinger translational work hardening, and the size effect. The dislocation nucleation admits a clear characterization by the variational principle for the final plastic states [Berdichevsky, 2006a]. Le and Sembiring [2008a,b, 2009] generalized the previous study, which will be explained in detail in this thesis, to single- and double-slip in thin, infinitely extended single crystal strips being subjected to several types of deformation. The comparison of the results in Le and Sembiring [2008a,b] with the results of discrete dislocation simulations reported by Needleman and Van der Giessen [2001] and Shu et al. [2001] shows good agreement between the continuum and discrete approaches. Kochmann and Le [2008, 2009b] investigated the dislocation pile-up near the phase boundaries of a bicrystal under plane constrained shear, extension, and mixed deformation of extension and shear, whose solution exhibit similar characteristics as for the single crystal. Various examples of the application of continuum theory of dislocation that adopt the free energy form proposed by Berdichevsky [2006a,b] can be found in Le and Nguyen [2009, 2010], Kochmann and Le [2009a], Le and Nguyen [2012, 2013] and Kaluza and Le [2011]. The most recent approach of non-linear continuum dislocation theory is presented in Le and Günther [2014].

## 1.2 Scope of this thesis

This thesis discusses the application of continuum theory of dislocation to a strip made up of a single crystal deforming in single and double slip undergoing several types of deformation. The slip systems are oriented differently with respect to the boundary. The objective of this thesis is twofold. For the first objective, the closed analytical solutions to the equations of continuum dislocation theory for crystals deforming in single and symmetric double slip

are sought. Then the second objective, the numerical procedures for crystals deforming in non-symmetric double slip are developed. The agreement between the numerical and the analytical solutions for symmetric double slip will justify the correctness of the developed numerical procedures. To simplify the analysis, we assume the isotropic elastic properties of the crystal. Besides, the dislocations are not allowed to penetrate the upper and lower boundaries of the strip which model the grain boundaries. The problem is to determine the displacements and the plastic distortion as functions of the given overall shear strain or tensile strain or the mixed of the both strains.

Following this introduction chapter, the essential physical backgrounds of this thesis are explained in **Chapter 2** containing a short explanation of stress-strain diagram, plastic deformation from microscopic point of view, a short introduction of dislocation theory and finally an introduction to a continuum dislocation theory. Afterwards, in order to get a better understanding to the following chapters, a detail re-derivation of the simplest example of this theory, namely, the nucleation of dislocation in anti-plane constrained shear of single crystals [Berdichevsky and Le, 2007], is presented in **Chapter 3**. **Chapter 4** investigates the plane-strain constrained shear and **Chapter 5** the plane-strain uniaxial extension and then combined loading of a strip made up of a single crystal deforming in single slip system. Then we extend the examples presented previously by applying the plane-strain constrained shear load in **Chapter 6** to the same strip made up of a single crystal but now with two active slip systems. For completeness, the application of the plane-strain uniaxial extension load and then the mixed load of extension and shear to the identical single crystal strip as in previous cases with double slip systems is studied in **Chapter 7**. Finally, **Chapter 8** concludes this thesis.



## 2 Physical background

### 2.1 Stress-Strain diagram

When external forces are applied to any material body, it undergoes the deformation. The resulting deformation of the body includes an elastic part which is reversible deformation along with permanent or irreversible plastic deformation. These properties are ascertained

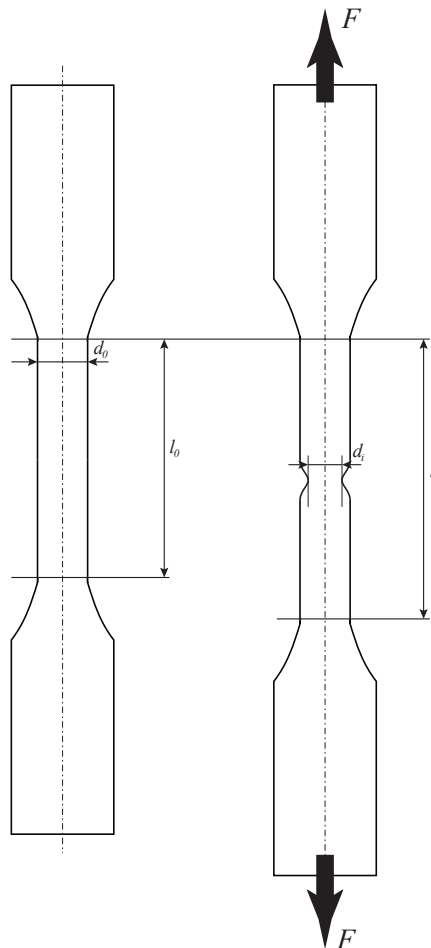


Figure 2.1: Tensile test.

by performing some mechanical test for instance uniaxial extension test resulting load or force versus elongation (schematically shown in Fig. 2.1). By measuring the load  $F$  and the related elongation  $\Delta l$  of the specimen, we can plot the nominal stress by dividing the axial load,  $F$ , by the original cross-sectional area,  $A_0 = \pi d_0^2/4$ , namely

$$\sigma = \frac{F}{A_0}, \quad (2.1)$$

versus the nominal strain

$$\varepsilon = \frac{l_i - l_0}{l_0} = \frac{\Delta l}{l_0}, \quad (2.2)$$

which is shown in Fig. 2.1, where  $l_0$  and  $d_0$  being the original length and diameter, respectively, before any load is applied and  $l_i$  being the instantaneous length.

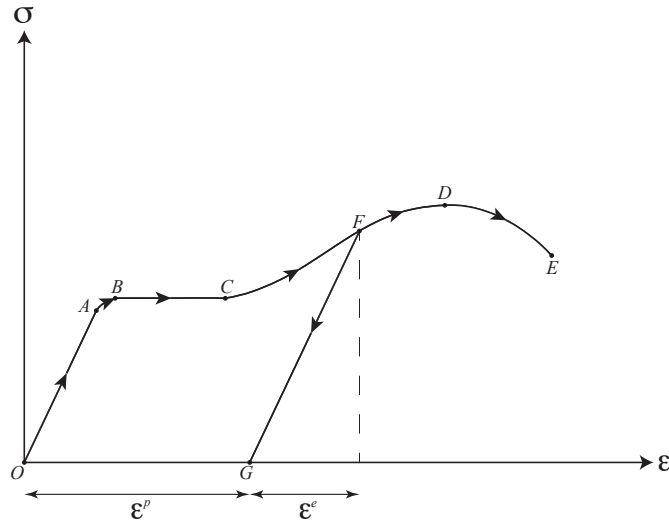


Figure 2.2: Stress-strain diagram for a typical structural steel undergoing uniaxial extension test (not in scale).

Fig. 2.2 illustrates the typical  $\sigma - \varepsilon$  curve for mild steel or low-carbon steel as a result of uniaxial extension test of a slender bar shown in Fig. 2.1). Due to the appearance of a very large strains in the plastic region, we prefer to plot the stress strain curve (Fig. 2.2) not to scale. For the correct relationships of stress-strain diagram for mild steel, the initial part of the diagrams (line OAB) appears to be a vertical lines because the strains from zero to point B are so small in comparison to the strains from point B to point E.

The straight line from the origin O to point A from Fig. 2.2 shows the linear and proportional relationship between stress and strain. The stress at point A is called the proportional limit because the proportionality between stress and strain beyond this point is no longer true. The slope of the straight line OA is called the proportionality constant known as modulus of elasticity. For the region AB, this linear relationship breaks down and the slope of stress strain curve becomes smaller and smaller since the strain increases more rapidly for each increment in stress. The section OAB is then described as a *purely elastic loading* of a material where the loading is completely reversible and the initial state is recovered as all external loads are removed. Start from point B up to point C, the test specimen is considerably elongated with no significant increase in the tensile stress. As a consequence the curve becomes horizontal for region BC where material becomes *perfectly plastic*, i.e. there is no increasing in applied load during the deformation. Point B is called the yield point with the corresponding stress known as the *yield stress*,  $\sigma_y$ . In region BC, the material undergoes perfectly plastic deformation where it deforms without an increase in the applied load. After point C, the steel begins to strain harden. During this strain hardening process, the crystalline structure of the steel is changed resulting in increased resistance of the material to further deformation. As a consequence, the stress-strain diagram has a positive slope

from C to D. The section CD is known as *work hardening* or *material hardening*. The corresponding stress at point D is called the *ultimate stress* where the maximum value of the load is reached. When the load is applied further beyond point D, the deformation is accompanied by the reduction in the load. The fracture finally occurs at point E. The material is *plastically deforming* in the entire section BCDE.

If the material is unloaded at point F, the path FG which is parallel to the initial elastic loading path OA will be followed. Accordingly only *elastic strain*,  $\epsilon^e$ , is recovered, while the other part of the strain will remain as the permanent strain or *plastic strain*,  $\epsilon^p$ . It can be observed from the Fig. 2.2 that the *total strain* in the plastic region can be written as

$$\epsilon = \epsilon^e + \epsilon^p. \quad (2.3)$$

## 2.2 Microscopic phenomena throughout plastic deformation

In order to understand the mechanism of plastic deformation and their manifestation in macroscopic levels as seen experimentally, we need to investigate the mechanism of plastic deformation on the microscopic level.

### 2.2.1 Crystalline structures of metals

As reported in Ewing and Rosenhain [1900], metals and alloys are crystalline solids (i.e. consist of atoms arranged in pattern that repeats itself periodically in three dimensions) and composed of aggregates of *single crystals* or grains. This arranged patterns of atoms are called a *crystal lattice*.

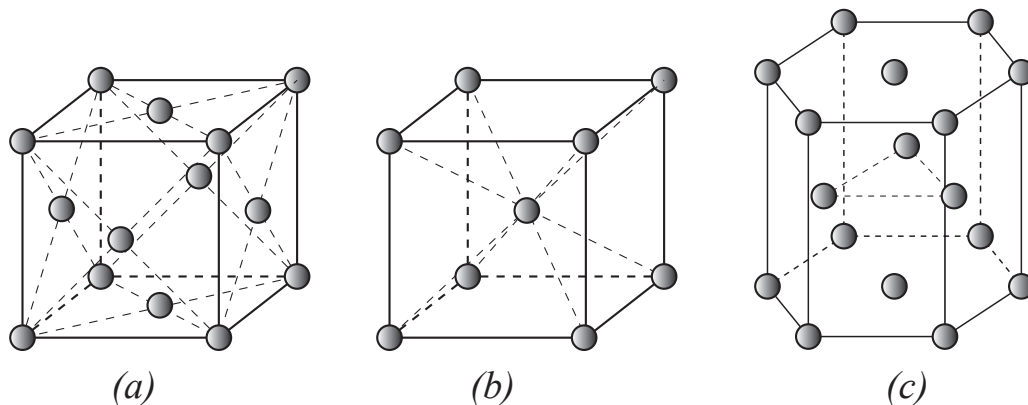


Figure 2.3: The crystal structures of common metals: (a) face-centered cubic, (b) body-centered cubic, (c) hexagonal close-packed.

Due to periodic nature of the crystal lattice, for describing the the crystal structures, it is convenient to subdivide the structures into small repeat entities called *unit cells*. Unit cells for most crystal structures take the prisms or parallelepipeds form with three sets of parallel faces. The common metals have one of the three relatively simple crystal structures, namely:

- Face-centered cubic (FCC) crystal structure. As depicted in Fig. 2.3(a), the unit cell has equal length for every edge. Each of the eight corners of the cubic cell contains one atom and one atom in the middle position on each of the six faces of the unit cell.
- Body-centered cubic (BCC) crystal structure. The unit cell of this crystal structure is shown in Fig. 2.3(b). Similar to FCC crystal, the lengths of the edges of the unit cell are equal and each of eight corners of the faces contains one atom. In addition, there exists one extra atom at the centroid of the cell.
- Hexagonal close-packed (HCP) crystal structure. Fig. 2.3(c) illustrates the unit cell for this crystal structure. The upper and lower basal planes are regular hexagon.

As we deal with crystalline materials, it is necessary to specify a line between two atoms (*crystallographic direction*) or the orientation of planes of crystal structure (*crystallographic planes*). For the purpose of indicating them, we shall use the Miller indices. The detail explanation about Miller indices can be found in Callister [2007].

### 2.2.2 Crystal plasticity

One of the important properties of these crystals, due to the crystallinity, is their ability to glide easily on certain crystallographic planes and certain crystallographic directions. In their study of crystalline plasticity [Ewing and Rosenhain, 1899, 1900], plastic deformation takes place due to the glide of certain families of crystal planes over each other in certain crystallographic directions. So in other words, without glide there is no plasticity.

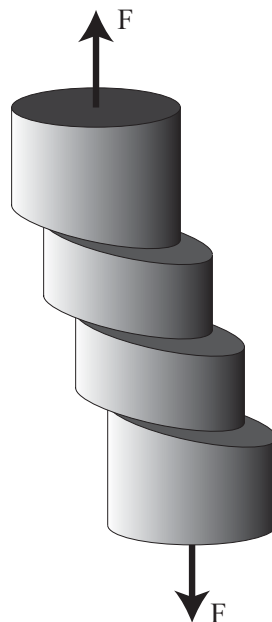


Figure 2.4: Macroscopic slip in a single crystal.

Since it is possible nowadays to grow specimens of crystalline solids in the form of single crystals large enough for mechanical testing, we can apply again the same uniaxial extension test as in Fig. 2.1 to the single crystal in order to obtain the stress-strain relation. Again we

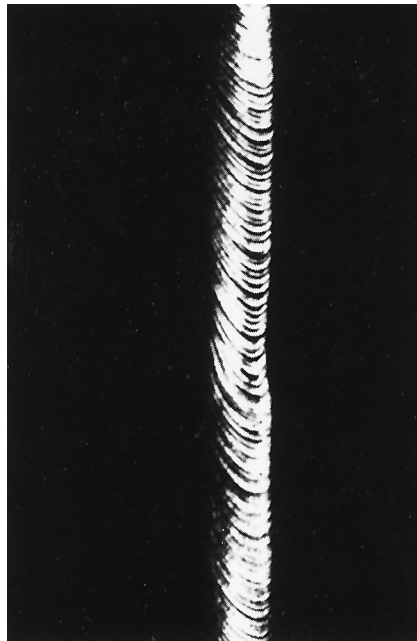


Figure 2.5: Slip in a zinc single crystal [Elam, 1935] (from Callister [2007]).

will have the elastic deformation for small stresses ( $\sigma < \sigma_y$ ). If we load the specimen further, starting from the yield stress ( $\sigma_y$ ) the single crystal undergoes plastic deformation. For a single-crystal specimen that is stressed in tension, deformation will be schematically shown in Fig. 2.4. If the surface of the plastically deformed single crystal is examined, there exist small steps on the surface of the crystal that are parallel to one another. These steps appear as witnesses of the plastic slips that occur along a number of equivalent and most favorably oriented planes (*slip planes*) and directions (*slip directions*) at various positions along the specimen length. The combination of any one of slip planes and any one of the slip directions on that plane is called a *slip system*. Fig. 2.5 illustrates the experimental example of plastically deformed single crystal zinc which shows clearly the steps due to the plastic slip.

From the experiment, it is observed that in most metals plastic slips occur on the planes with the closest atomic packing along the directions with the shortest interatomic distances. The precise description of the plastic slip can be given in terms of Miller indices. For Example, the slip occurs on  $\{111\}$  planes in  $\langle 111 \rangle$  directions for FCC metals, while for BCC metals, the slip plane maybe occurs on one of the following slip planes, i.e.  $\{110\}$ ,  $\{112\}$  and  $\{123\}$  with the slip directions on  $\langle 111 \rangle$ .

### 2.2.3 Critical Resolved Shear Stress

As mentioned previously, plastic slips occur in response to shear stresses applied along a slip plane and in a slip direction. Even for pure tensile or compressive applied stress, shear components exist at all but parallel or perpendicular alignments to the direction of stress. These shear components are defined as *resolved shear stresses* with the magnitudes depend on the applied stress together with the orientation of the slip plane and slip direction within that plane. Fig. 2.6 illustrates the geometrical relationships between the tensile axis, slip plane, and slip direction where  $\phi$  being the angle between the normal to the slip plane and

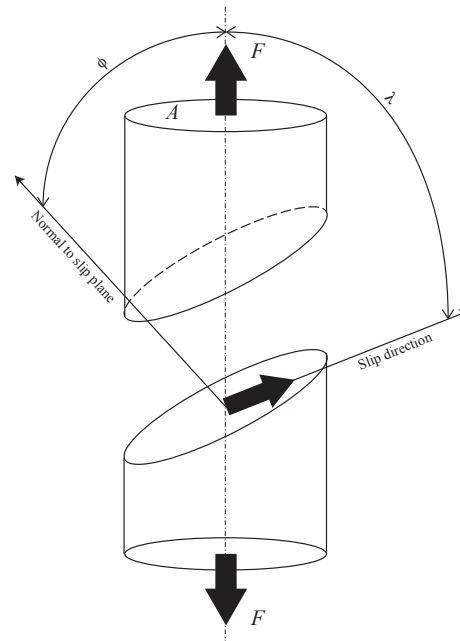


Figure 2.6: Geometry of slip in crystalline material.

stress direction, and  $\lambda$  the angle between the slip and stress directions. If the cross-sectional area of specimen depicted in Fig. 2.6 is  $A$ , then the tensile stress parallel to tensile axis is  $\sigma = F/A$ . In the slip direction, the force has the component  $F \cos \lambda$  and acts over the slip surface with an area  $A/\cos \phi$ . Then the relation between applied stress,  $\sigma$ , and the resolved shear stress on the slip plane in the slip direction,  $\tau$ , takes the form

$$\tau = \sigma \cos \phi \cos \lambda. \quad (2.4)$$

As reported in Schmid [1924], the plastic slip in a single crystal starts to appear when resolved shear stress reaches a critical value,  $\tau_{cr}$ , called the *critical resolved shear stress*. This critical resolved shear stress is a constant for a given material at a given temperature. This result is known as *Schmid's law*.

### 2.2.4 Theoretical shear strength of single crystal

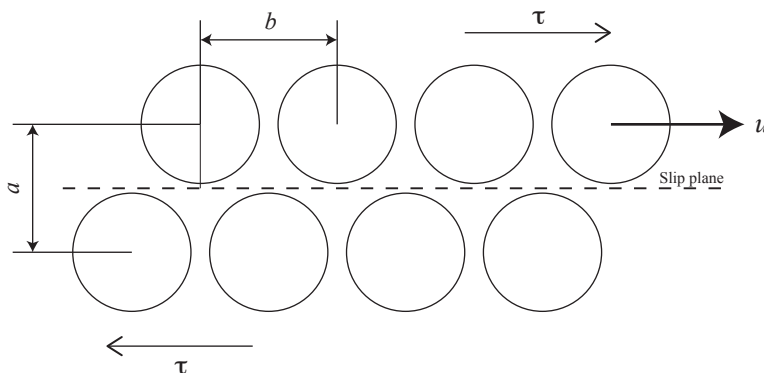


Figure 2.7: Slip between two rows of atoms.

The theoretical estimation of the critical shear strength of a perfect crystal at which the plastic slip occurs was first given by Frenkel [1926]. It can be calculated by assuming that slip appears by the uniform displacement of adjacent atomic planes. Therefore a simple model of shearing two rows of atoms with the spacing between the rows,  $a$ , and the interatomic distance in the slip direction,  $b$ , is considered as shown in Fig. 2.7. From Fig. 2.7, it can be observed that initially the two rows is in a stable equilibrium configuration under zero shear stress,  $\tau$ . For non-zero applied shear stress,  $\tau$ , the slip of upper row over the lower row is denoted as  $u$ . The applied shear stress can be calculated by

$$\tau = \frac{dE}{du}, \quad (2.5)$$

where  $E$  is the total energy of crystal in terms of  $u$ .

It is assumed that there is a periodic shearing force required to move the top row of atoms across the bottom row. Therefore the energy,  $E$ , is proposed in sinusoidal form with the period  $b$ . This assumed energy has the minimum at  $u = 0$  and the maximum at  $u = b/2$ . Therefore the simplest energy formula,  $E$ , that satisfies these requirements can be presented in the form

$$E(u) = \frac{kb}{2\pi} \left( 1 - \cos \frac{2\pi u}{b} \right). \quad (2.6)$$

Substituting (2.6) into (2.5) we obtain the shear stress as follows

$$\tau = k \sin \frac{2\pi u}{b}. \quad (2.7)$$

For small displacement,  $u \ll b$ , Eq. (2.7) can be approximated into

$$\tau = k \frac{2\pi u}{b}. \quad (2.8)$$

Comparing (2.8) with Hooke's law

$$\tau = \mu \frac{u}{a}, \quad (2.9)$$

with  $\mu$  being the shear modulus, we determine the value of  $k$ , i.e.

$$k = \frac{\mu b}{2\pi a}. \quad (2.10)$$

Applying (2.10) to (2.7) we obtain

$$\tau = \frac{\mu b}{2\pi a} \sin \frac{2\pi u}{b}. \quad (2.11)$$

It can be seen from (2.11) that the maximum (critical) theoretical shear strength can be obtained if  $\sin(2\pi u/b) = 1$ , so that

$$\tau_c = k = \frac{\mu b}{2\pi a}. \quad (2.12)$$

From (2.12), it is observed that the minimum value of  $\tau_c$  (the minimum shear stress required to initiate slip) is achieved when the atomic spacing,  $a$ , is maximum and the interatomic distance,  $b$ , is minimum. It then explains that the closely packed plane in a closely packed

direction is the weakest plane and direction under shear where the plastic slip happens as described already in section 2.2.2. For most metal crystals,  $b \approx a$ , so that the theoretical critical shear strength is estimated to be

$$\tau = \frac{\mu}{2\pi}. \quad (2.13)$$

It has been found, from many experiments conducted to measure the yield strength, that this theoretically estimated critical shear strength is three or four order of magnitude larger than the observed shear strength. Due to this large discrepancy between theoretical and experiment, it can be concluded that the plastic slip in crystals must take place by some mechanism other than the movement of whole planes of atoms past one another. This mechanism is associated with lattice defects that reduce the strength of the crystal. The concept of defect called a *dislocation* that causes the disparity we noted above has been introduced independently by Taylor [1934], Polanyi [1934] and Orowan [1934].

## 2.3 Dislocation

Dislocations are the most important line defects in crystals since they are responsible for the low strength of real crystals. As a consequence, plastic deformation takes place due to the motion of large numbers of dislocations. This concept of dislocation was first introduced by Volterra [1905]. But the foundation for the modern concept of dislocation based plasticity are introduced by Taylor [1934], Polanyi [1934] and Orowan [1934].

### 2.3.1 Types of dislocation

A dislocation is a linear or one-dimensional defect in the periodic crystal lattice where some of the atoms are misaligned. There are two fundamental dislocation types, namely, *edge dislocation* and *screw dislocation*.

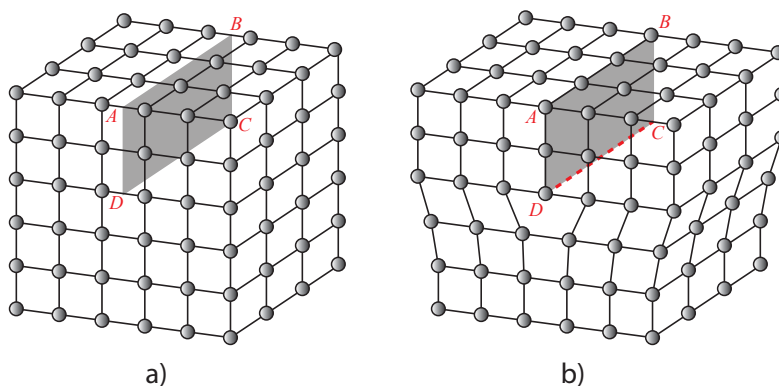


Figure 2.8: (a) Simple lattice cubic structure; (b) Positive edge dislocation DC formed by inserting an extra half-plane of atoms ABCD.

When explaining the big discrepancy of the critical shear strength of the crystals between experimental result and theoretical estimation, Taylor [1934], Polanyi [1934] and Orowan

[1934] introduced for the first time edge dislocation shown in Fig. 2.8. It can be observed from Fig. 2.8 that an extra portion of a plane of atoms, or half-plane, ABCD with the edge that terminates within the crystal. This dislocation is called edge dislocation due to the fact that this type of linear defect centers around the line DC, known as *dislocation line*, which is the edge of extra half plane ABCD. The dislocation line DC in Fig. 2.8 is called a positive edge dislocation and is presented with symbol  $\perp$ . For the case where half-plane ABCD is inserted from below, then we have a negative edge dislocation and is represented by  $\top$ .

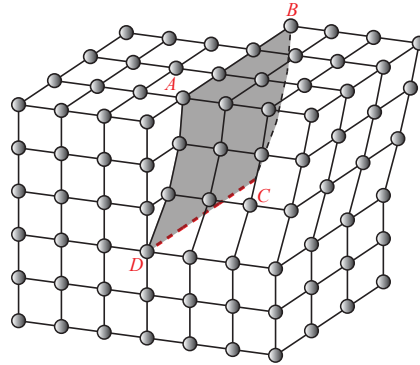


Figure 2.9: Left handed screw dislocation.

The second basic type of dislocation is screw dislocation which was introduced by Burgers [1939]. A screw dislocation may be thought of as being formed by a shear stress that is applied to displace the crystal on one side of ABCD relative to the other side in the direction AB as in Fig. 2.9. A linear defect around DC in Fig. 2.9 is a screw dislocation. It is called screw dislocation due to the spherical or helical path that is traced around the dislocation line DC. As we look down the dislocation line, it is called a left-handed screw dislocation, with the symbol  $\ominus$ , if the helix comes forward one atomic distance in a counterclockwise direction (see Fig. 2.9). For the reverse case, it is called right-handed screw dislocation, with the symbol  $\oplus$ .

### 2.3.2 Dislocation motion

As noted in section 2.2.4, the permanent or plastic deformation of most crystalline material is caused by the motion of large number dislocations under the action of stresses. The process where the plastic deformation being the product of the most important movement of dislocations is denoted as *slip* or *glide*. This slip or glide is confined on the slip planes of the crystal. The slip system (slip plane and slip direction combination) for this process has been explained in section 2.2.2. A dislocation which able to move in this way is known as *glissile* and the one which is not able is called *sessile*. It can also be mentioned here that the critical resolved shear stress ( $\tau_{cr}$ ), introduced in section 2.2.2, is the material's resistance to the dislocation motion. The other type of dislocation movement is climb, which will not be discussed here (for detail see Hirth and Lothe [1982], Hull [2001], Weertman and Weertman [1966]), where the dislocation moves out of the glide surface by interaction with vacancy.

As can be seen in Fig. 2.7, a shear stress acting across a slip plane moves the atom above the slip plane past those below it. For the case where a dislocation line lies on the slip plane, the movement of the dislocation along the slip plane can make the atoms on either side of slip plane to move past each other. The mechanism of dislocation motion of an edge dislocation

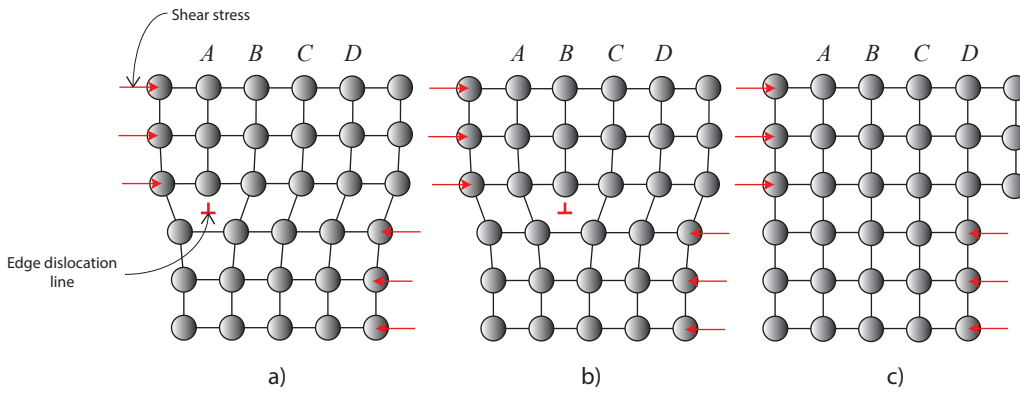


Figure 2.10: Dislocation motion mechanism of an edge dislocation in response to an applied shear stress.

is described in Fig. 2.10. As can be seen in Fig. 2.10 (a) the initial half-plane is plane A. When the shear stress of sufficient magnitude is applied as shown in Fig. 2.10(a), plane A is forced to the right and the interatomic bonds of plane B are ruptured throughout the shear plane. As a consequence, the upper half of plane B turns into the extra half-plane as plane A ties up with the bottom half of plane B (see Fig. 2.10(b)). For subsequently repeated processes for the other planes, the extra half-plane moves from the left to the right. Finally, this extra half-plane emerges from the right surface of the crystal forming an edge with one atomic distance wide (see Fig. 2.10(c)).

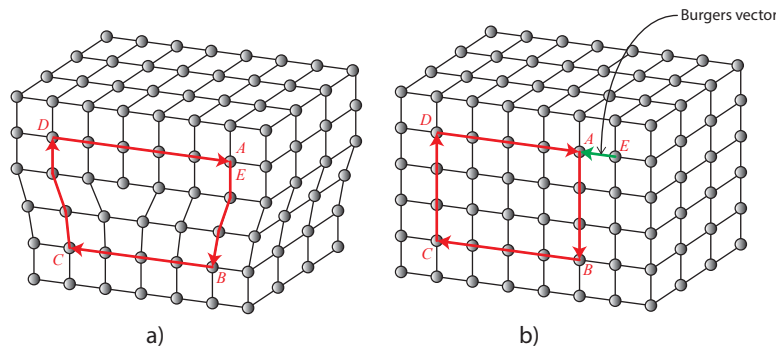


Figure 2.11: (a) Burgers circuit around edge dislocation with positive sign of dislocation line into the paper; (b) the same circuit in a perfect crystal.

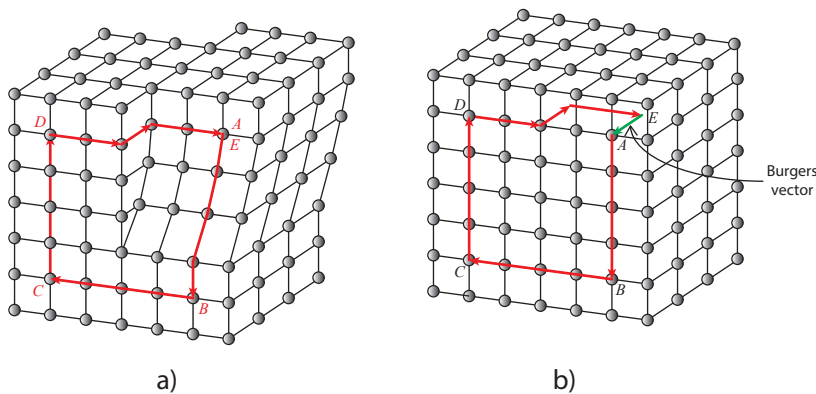


Figure 2.12: (a) Burgers circuit around screw dislocation; (b) the same circuit in a perfect crystal.

*Burgers circuit* is an important element of theory that has been developed to explain plastic deformation due to the dislocation motion. An atom to atom path ABCDE that forms a closed loop in a crystal containing dislocations, as observed in Fig. 2.11(a), is called Burgers circuit. If we apply the same atom to atom sequence ABCDE to a dislocation free crystal, the circuit does not close (see Fig. 2.11(b)). The vector required to complete the circuit (or the closure failure EA) is denoted as *Burgers vector*,  $\mathbf{b}$ . For metals, the magnitude of the Burgers vector is equal to the interatomic spacing. The Burgers vector in Fig. 2.11(b) is at right angles to the dislocation lines. Fig. 2.12(a) illustrates the Burgers circuit around a screw dislocation. If the same Burgers circuit is drawn in a perfect crystal as shown in Fig. 2.12(b), the closure failure EA is parallel to the dislocation line. Therefore, it can be concluded that:

- The Burgers vector of an edge dislocation is perpendicular to the dislocation line.
- The Burgers vector of a screw dislocation is parallel to the dislocation line.

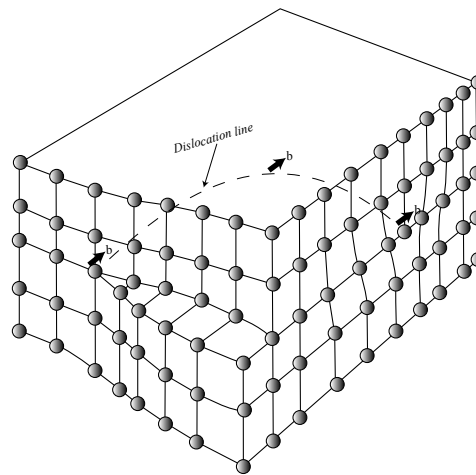


Figure 2.13: Mixed type of dislocation.

It has been found, that the most general type of dislocations found in crystalline materials are *mixed dislocations* (have edge and screw dislocation properties) with the dislocation lines lie at an arbitrary angle to the Burgers vector (see Fig. 2.13). However, the length and direction of a single dislocation is fixed and it is independent of the position and orientation of the dislocation line. Meaning that, the Burgers vector will be always the same at all points along its line even though the dislocation line's orientation is changed from edge to mixed to screw.

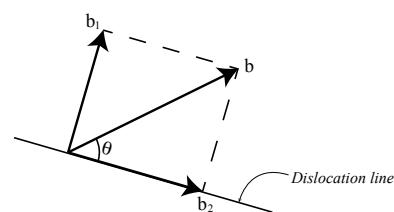


Figure 2.14: Decomposition of Burgers vector of mixed dislocation.

This dislocation of the mixed type can be decomposed into two components, namely, the edge and screw dislocations, by resolving its Burgers vector,  $\mathbf{b}$ , into two mutually orthogonal

components (see Fig. 2.14). With  $\mathbf{b}_1$  and  $\mathbf{b}_2$  are perpendicular and parallel to the dislocation line, respectively, we can write

$$\mathbf{b} = \mathbf{b}_1 + \mathbf{b}_2, \quad (2.14)$$

where

$$|\mathbf{b}_1| = |\mathbf{b}| \sin \theta, \quad |\mathbf{b}_2| = |\mathbf{b}| \cos \theta,$$

and  $\theta$  being the angle between the dislocation line and its Burgers vector.

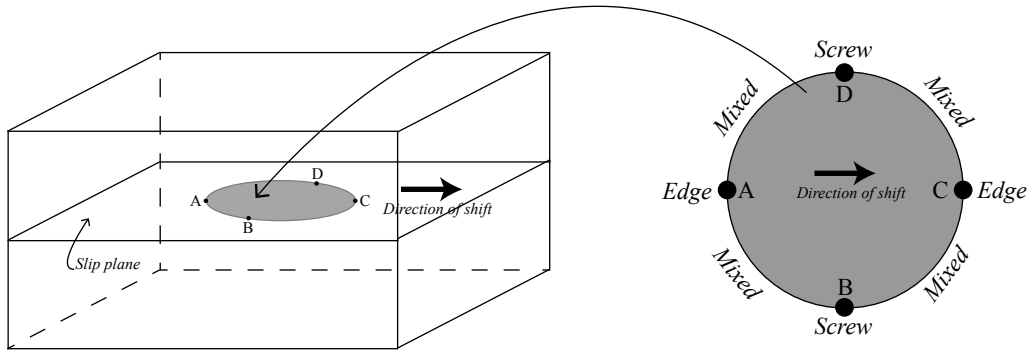


Figure 2.15: Dislocation loop.

In fact, as found in the real imperfect crystal, dislocations exist not only in straight configuration such as edge or screw dislocations, but the dislocation line can be made in the form of a ring or a closed loop instead of terminates at the crystal surface (dislocation line cannot terminate in the interior of the crystal). This dislocation loop can be made in any arbitrary shape. As can be observed in Fig. 2.15, the dislocation line called *dislocation loop* separates two regions: the one inside the loop ABCD where the atoms above the slip plane have displaced one atomic spacing relative to the atoms below the plane, and the one outside the loop where no slip has taken place between the atoms. It should be noted that, for a circular dislocation loop ABCD shown in Fig. 2.15, the character of each dislocation segment of the loop varies continuously from pure edge to mixed to screw dislocation.

### 2.3.3 Properties of dislocations

In the followings, the basic properties of dislocations will be explained briefly. It is meaningful to treat dislocations within linear elasticity because stresses and elastic strains in crystals induced by them change slowly except at the vicinity of the dislocation core. The more detail information about this topic can be found in [Friedel, 1964, Hirth and Lothe, 1982, Hull, 2001, Weertman and Weertman, 1966].

#### 2.3.3.1 Stress field around a dislocation

A dislocation is a linear type of defect that causes the disturbance of the regular atomic order. Due to this disturbance, there exists the elastic distortion around a dislocation line that can be explained by linear dislocation theory. We will consider here only the stationary dislocation which means that the displacement field cannot be a function of time.

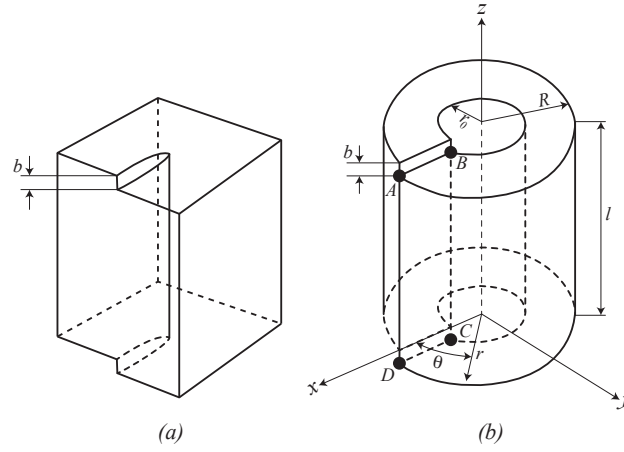


Figure 2.16: Screw dislocation: (a) in a crystal; (b) in an elasticity model.

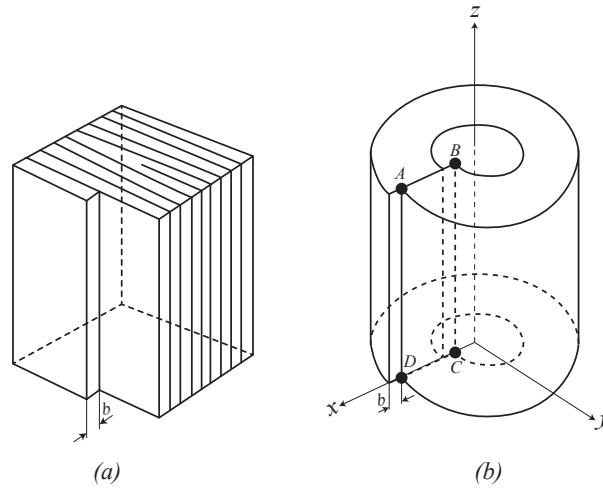


Figure 2.17: Edge dislocation: (a) in a crystal; (b) in an elasticity model.

Since we are dealing here with the elastic deformation, the elastic distortion around an infinitely-long, straight dislocation can be characterized in terms of a cylinder of an elastic material. For a screw dislocation, the deformation of the elastic cylinder in Fig. 2.16(b) produces a similar distortion as in a crystal in Fig. 2.16(a). The similar condition is also true for an edge dislocation as depicted in Fig. 2.17. The results will be given here in cylindrical coordinates system  $(r, \theta, z)$  without presenting any details of derivation.

For a screw dislocation case, the stress field can be expressed as

$$\sigma_{\theta z} = \frac{\mu b}{2\pi r}, \quad \sigma_{rr} = \sigma_{\theta\theta} = \sigma_{zz} = \sigma_{r\theta} = \sigma_{rz} = 0. \quad (2.15)$$

On the other hand, the non zero components of the stress field around an edge dislocation are

$$\begin{aligned} \sigma_{rr} = \sigma_{\theta\theta} &= -\frac{\mu b}{2\pi(1-\nu)} \frac{\sin \theta}{r}, \\ \sigma_{zz} &= -\frac{\mu\nu b}{\pi(1-\nu)} \frac{\sin \theta}{r}, \\ \sigma_{r\theta} &= \frac{\mu b}{2\pi(1-\nu)} \frac{\cos \theta}{r}. \end{aligned} \quad (2.16)$$

These stress fields above are valid only at location where  $r > r_0 \approx 5b$ . Weertman and Weertman [1966] argued that the core radius of the dislocation is  $5b$ , where  $b$  is the magnitude of Burgers vector. Due to the stress concentration, the situation becomes more complex for  $r \leq 5b$  so that the linear elasticity theory cannot be applied anymore. From the results, it can be seen that the stress fields are long-range but decay rapidly with increasing distance  $r$  from the dislocation core.

It should be noted also that the stress field around the dislocation will interact with other stress fields by other dislocations. Therefore, this stress field around the dislocation will produce the resistance to the movement of the dislocation line.

### 2.3.3.2 Self energy of a dislocation line

It is known that energy is stored in any stressed elastic medium. As we know from before that a dislocation distorts the crystal lattice which, in turn, produces elastic pre-strains and pre-stresses in the crystal. Therefore, due to the stress field around a dislocation explained in the previous section, there exists the elastic energy that stored in that region. This energy is known as the *self energy* or *stored energy* of the dislocation. The total stored energy of dislocation of a crystal in the region  $V_0$  takes the form

$$E_{\text{disl}} = \int_{V_0} \boldsymbol{\sigma} : \boldsymbol{\varepsilon} \, dV. \quad (2.17)$$

It is more convenient to consider that  $E_{\text{disl}}$  represents the work done in order to displace the faces of the cut ABCD by  $b$  against the resisting internal stresses (see Fig. 2.16 and Fig. 2.17). This self energy can be easily calculated from the known stress field explained in the previous section.

Assuming that the value of the core radius of the dislocation,  $r_0$ , equals  $5b$  [Weertman and Weertman, 1966], the self-energy per unit length of dislocation line for a screw dislocation takes the form

$$\xi_{\text{screw}} = \frac{\mu b^2}{4\pi} \ln \frac{R}{5b}, \quad (2.18)$$

and for edge dislocation

$$\xi_{\text{edge}} = \frac{\mu b^2}{4\pi(1-\nu)} \ln \frac{R}{5b}, \quad (2.19)$$

where  $R$  is the outer dimension of the crystal (see Fig. 2.16(b) and Fig. 2.17(b)). Note that the value  $R$  is chosen so that the disturbance caused by the dislocation can be ignored for  $r > R$ . From Eq. 2.18 and Eq. 2.19, it can be observed that the self-energy of an edge dislocation is larger than that of a screw dislocation, namely (for  $\nu = 0.3$ )

$$\xi_{\text{edge}} \approx 1.43 \xi_{\text{screw}}. \quad (2.20)$$

The energy of a mixed dislocation line, whose Burgers vector is inclined at an angle  $\theta$  from the dislocation line, is the sum of the energy of the screw components (with Burgers vector of length  $b \cos \theta$ ) and the energy of the edge components (with Burgers vector of length

$b \sin \theta$ ). Therefore, the total energy per unit length for this mixed type of dislocation is given in the form

$$\xi_{\text{mixed}} = \frac{\mu b^2}{4\pi} \left[ \cos^2 \theta + \frac{\sin^2 \theta}{1 - \nu} \right] \ln \frac{R}{5b}. \quad (2.21)$$

The comparably high energy of dislocations shown above implies that dislocations are non-equilibrium defects which means that an externally applied force is needed to create a dislocation.

### 2.3.3.3 Forces on a dislocation

As we know that for the application of sufficiently high stress to a crystal, the plastic deformation takes place in the crystal due to the dislocation motion. As a consequence, the result of applying a stress to a crystal equals to applying the force on a dislocation line.

Mott and Nabarro [1948] studied first this problem and proposed that the *force per unit length* acting on the dislocation line equals to the product of the shear stress acting on the plane,  $\tau$ , and the magnitude of the Burgers vector,  $b$ , i.e.

$$F = \tau b. \quad (2.22)$$

Dislocation glide is the product of this force. Accordingly, this force acts in the slip plane and is normal to the dislocation line.

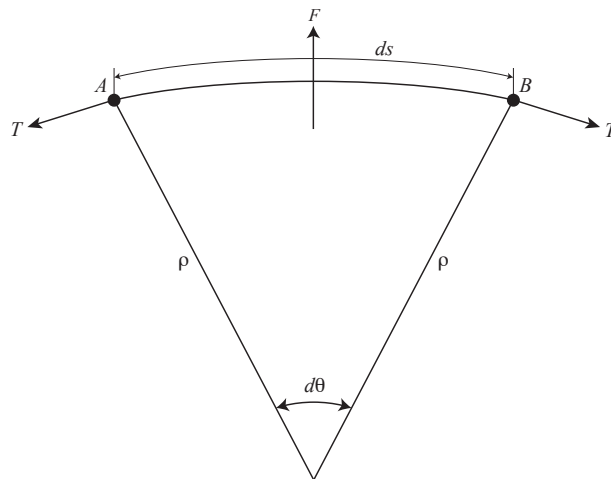


Figure 2.18: Line tension of a dislocation.

In fact, generally, dislocation lines observed in crystals are rarely straight. Fig. 2.18 illustrates the example of this case, where a segment of a dislocation line is pinned at point  $A$  and point  $B$  by impurities in the crystal. The applied force per unit length,  $F$ , tends to bend this line segment as shown in Fig. 2.18.

In place of obtaining a minimum of energy that proportional to its length, the *line tension*,  $T$ , will try to straighten the dislocation line to reduce its length. An equilibrium for the

line tension,  $T$ , and the driving force,  $F$ , is reached at a particular configuration where the segment  $ds$  will have a radius of  $\rho$  (see Fig. 2.18).

From Fig. 2.18, it is clear to be seen that the equilibrium of the force in the normal direction of  $ds$  takes the form

$$\tau_0 b ds = 2T \sin \frac{d\theta}{2}, \quad (2.23)$$

where  $\tau_0$  is the shear stress needed to maintain the configuration. With  $ds = \rho d\theta$  and very small  $d\theta$  (so that  $\sin(d\theta/2) \approx d\theta/2$ ), we obtain

$$\tau_0 = \frac{T}{b\rho}. \quad (2.24)$$

With the approximation (see Hull [2001])

$$T = \alpha\mu b^2, \quad (2.25)$$

where  $\alpha$  being a proportional factor ( $\alpha \approx 0.5 - 1.0$ ), we can write

$$\tau_0 = \frac{\alpha\mu b}{\rho}, \quad (2.26)$$

which explains the required stress to bend a dislocation to a radius of curvature  $R$ . The rigidity of a dislocation line can also be expressed by showing that the radius  $\rho$  increases with  $\mu b$  and decreases with  $\tau_0$ , i.e.

$$\rho = \frac{\alpha\mu b}{\tau_0}. \quad (2.27)$$

### 2.3.3.4 Interaction of dislocations

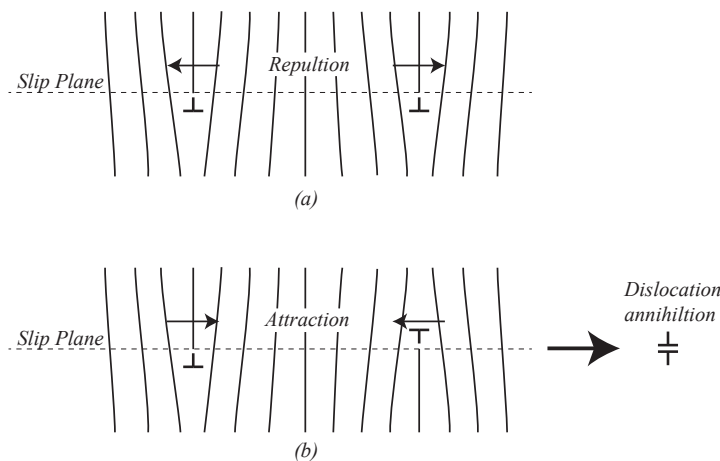


Figure 2.19: Interaction of two edge dislocations lying on the same slip plane: (a) of the same sign; (b) of the opposite sign.

As explained before that, due to the presence of distortion around dislocation, the energy state of a crystal containing a dislocation is not at its lowest. Therefore, in order to obtain a

configuration of reduced total stored energy, the dislocations in a crystal will interact with each other by reason of the existence of the stress field around dislocation line.

Consider the situation where two parallel edge dislocations with the same sign lying in the same slip plane as depicted in Fig. 2.19(a). The strain field interaction between these two dislocations is a mutual repulsive force that tends to move them apart. This phenomena can be explained as follows (see Hull [2001]): If the two dislocations are considered separate by a large distance, the total stored energy (Eq. 2.19 ) is given by

$$\xi_{\text{edge}} = \frac{2\mu b^2}{4\pi(1-\nu)} \ln \frac{R}{5b}. \quad (2.28)$$

On the other hand, when these two dislocations are very close to each other, it can be considered approximately as a single dislocation with Burgers vector  $2b$  with the total stored energy in the form

$$\xi_{\text{edge}} = \frac{\mu(2b)^2}{4\pi(1-\nu)} \ln \frac{R}{5b}. \quad (2.29)$$

As a consequence, these two dislocations will repel each other to reduce its energy.

For the case in Fig. 2.19(b) where two edge dislocations on the same slip plane but with opposite sign, the total stored energy will be given in the similar form as in (2.28) if they are separated by a large distance. If they are close to each other, since their Burgers vectors have the opposite sign, the total stored energy equals zero. Thus, in order to reduce their total stored energy, the dislocations of opposite sign will attract each other.

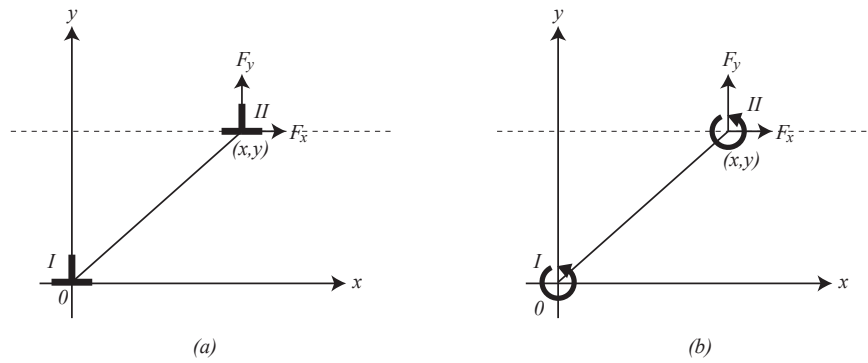


Figure 2.20: Interaction of two parallel: (a) edge dislocations; (b) screw dislocations.

The interaction between dislocations that lie not in the same slip plane can be described by the forces between them. For this case, we consider two edge dislocations (Fig. 2.20(a)) and two screw dislocations (Fig. 2.20(b)) that lie parallel in  $z$ -axis. For two parallel edge dislocations from Fig. 2.20(a), the interaction forces on  $II$  due to the presence of  $I$  at origin takes the form

$$F_x = \frac{\mu b^2}{2\pi(1-\nu)} \frac{x(x^2 - y^2)}{(x^2 + y^2)^2} \quad \text{and} \quad F_y = -\frac{\mu b^2}{2\pi(1-\nu)} \frac{y(3x^2 - y^2)}{(x^2 + y^2)^2}, \quad (2.30)$$

where  $F_x$  is the force in the glide direction and  $F_y$  the force perpendicular to the glide plane. By first assuming that the Burgers vectors of the two screw dislocations shown in

Fig. 2.20(b) are in the same direction, the forces acting on  $II$  due to the stress field of  $I$  yields

$$F_x = \frac{\mu b^2}{2\pi} \frac{x}{(x^2 + y^2)} \quad \text{and} \quad F_y = \frac{\mu b^2}{2\pi} \frac{y}{(x^2 + y^2)}. \quad (2.31)$$

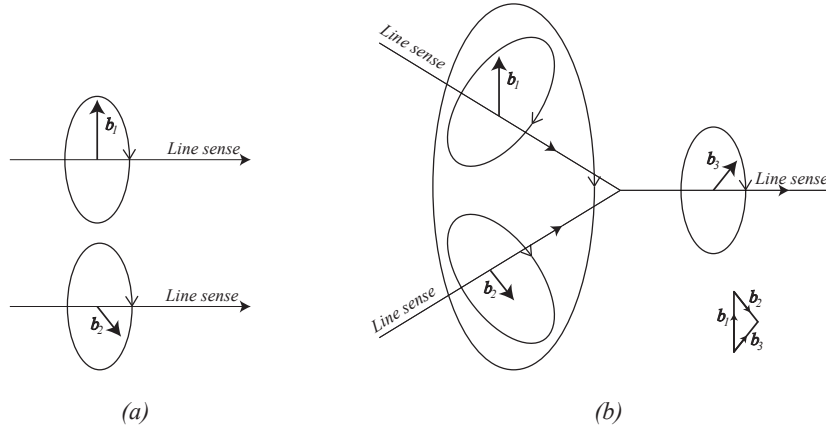


Figure 2.21: Reaction of two dislocations to form a third.

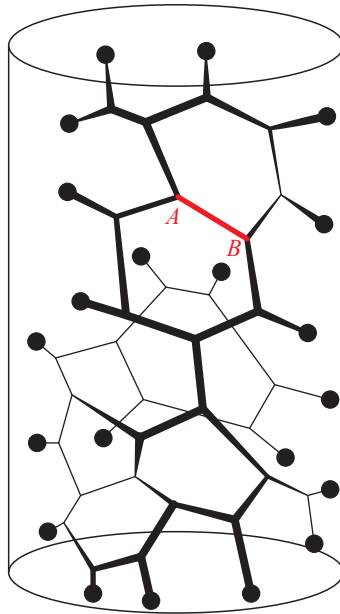


Figure 2.22: Schematic representation of dislocation network in a well annealed crystal (From [Cottrell, 1957]).

If two dislocations attract each other due to the stress field around them, they will meet to form a node. As an example we consider the initially separated two dislocations in Fig. 2.21(a) with Burgers vectors  $b_1$  and  $b_2$ . Due to the attraction between this two dislocations, they will meet and form a node resulting in a third dislocation with Burgers vectors  $b_3$  as depicted in Fig. 2.21(b). The resultant Burgers vector or the vectorial sum of the Burgers vectors for all dislocations that meet at a node must be zero, namely

$$\mathbf{b}_1 + \mathbf{b}_2 - \mathbf{b}_3 = 0, \quad (2.32)$$

where the negative sign of  $b_3$  due to its line sense is pointed out of the node. The feasibility for two dislocations to react and combine to form another is explained by a very simple rule, i.e. *Frank's rule* (see Hull [2001] for detail).

Dislocation networks are the product of the interaction of dislocations mentioned above. [Frank, 1950] introduced for the first time a three-dimensional network of the equilibrium distribution of dislocations in crystal as seen in Fig. 2.22.

### 2.3.3.5 Dislocation nucleation, multiplication and pile-ups

It has been found experimentally that the dislocation density in an annealed metal is insufficient to produce the observed slip steps due to the dislocation motion on the slip plane on the deformed body. In fact, during the deformation process, there exists a rapid multiplication of dislocations inside annealed crystals that causes an increase in dislocation density. This multiplication process requires preexisting dislocations in order to become operative. These preexisting dislocations are introduced into a crystal during solidification process, plastic deformation and as a consequence of thermal stresses throughout rapid cooling.

The presence of large thermal stresses may lead to the introduction of dislocations in form of dipole pairs (*dislocation dipoles*) into a crystal. A dislocation dipole has two dislocations of opposite sign which glide past each other on parallel slip planes separated by an atomic scale distance. When large enough shear stress is applied to a crystal, the equal number of positive and negative dislocations are moved in the opposite directions (dislocation dipoles dissociation) resulting in *dislocation nucleation*. These newly nucleated dislocations in place of accommodating a change of crystal lattice are called *geometrically necessary dislocations*. On the other hand, the dislocations that appear at arbitrary positions in a crystal during deformation are known as *statistically stored dislocations*. The analog differentiation to the two types dislocations mentioned before is made into mobile (glissile) and immobile (sessile) dislocations, respectively.

One of the common sources that able to generate a large number of dislocation loops under very small shear stress,  $\tau$ , is called *Frank-Read source* proposed by [Frank and Read, 1950]. To explain the Frank-Read source we take one segment of the dislocation network which is locked at both ends by immovable dislocation knots such as AB in Fig. 2.22. When a shear stress,  $\tau$ , is applied to the slip plane containing the segment AB with a length  $L$  as illustrated in Fig. 2.23(a), a force  $F = \tau b$  (see (2.22)) will be applied to the dislocation line AB. Since knots A and B are locked, the application of the force,  $F$ , will cause the dislocation line to bend into curves. The dislocation line will form a half-circle (Fig. 2.23(b)) if  $\tau$  reaches the value

$$\tau = \frac{2T}{bL} = \frac{2\alpha\mu b}{L}, \quad (2.33)$$

where  $T$  from (2.25). Applying (2.33) to (2.27) we obtain the radius for the case in Fig. 2.23(b), namely

$$\rho = \frac{L}{2}. \quad (2.34)$$

This equilibrium condition is not stable, so that the dislocation will move further and rotate around the locked knots A and B due to any small increase of the shear stress,  $\tau$

(Fig. 2.23(c)). When  $\tau$  is increased further, the curve dislocation line will meet resulting in a new dislocation loop called *Frank-Read loop* (Fig. 2.23(d)-(f)). The new dislocation line AB is formed inside this dislocation loop. By applying again  $\tau$  to this new dislocation line AB, the procedure to produce more new dislocation loops can be repeated.

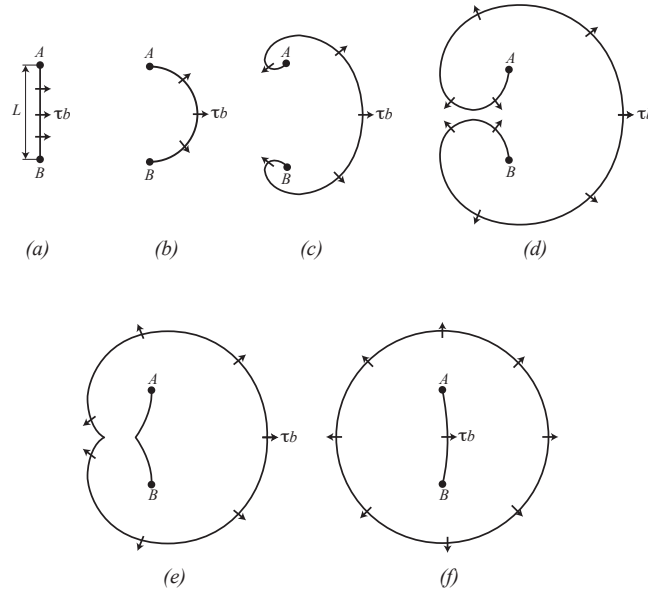


Figure 2.23: Schematic representation of Frank-Read loop formation.

When dislocations generated by a source i.e. Frank-Read source meet an obstacle such as grain boundary, they will pile-up against this obstacle as illustrated in Fig. 2.24. Since all the moving dislocations toward the grain boundary will displace at the same amount  $\delta x$ , the work done throughout this displacement takes the form

$$W = n\tau b\delta x, \quad (2.35)$$

where  $n$  is the total number of dislocations that piled-up near the grain boundary. The dislocations that pile-up near the grain boundary will exert a force on the grain boundary and vice versa. The reaction force per unit length of the grain boundary to these dislocations is  $\tau_l b$ , where  $\tau_l$  is called internal stress. Therefore, the work done to overcome  $\tau_l$  by the first dislocation that moves forward by  $\delta x$  is

$$W = \tau_l b\delta x. \quad (2.36)$$

From (2.35) and (2.36) we obtain

$$\tau_l = n\tau. \quad (2.37)$$

Eq. 2.37 explains that, in an equilibrium process, the internal stress,  $\tau_l$ , due to the dislocation pile-up equals to  $n$  times the applied stress,  $\tau$ . The internal stress is responsible for the hardening process in crystal by exerting a force known as *back stress* on the dislocation source. As a consequence, dislocation pile-ups are the reason for the strain hardening and the Bauschinger effect observed in experiment.

[Hall, 1951] and [Petch, 1953] showed independently from the experimental measurement of the yield stress of polycrystalline materials that the relation between yield stress and grain

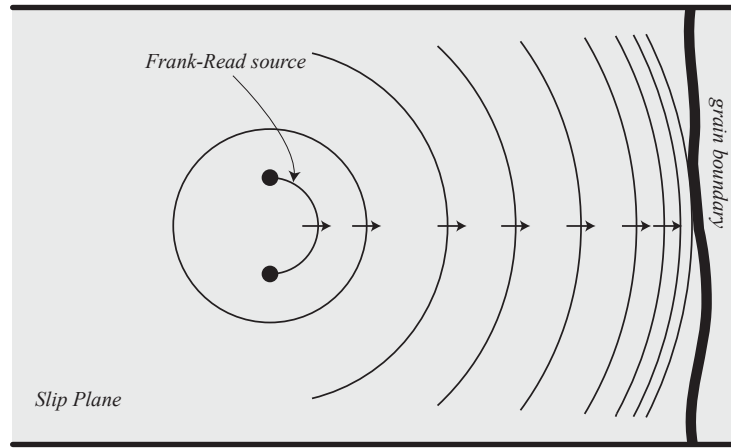


Figure 2.24: Dislocation pile-up against a grain boundary.

size is described mathematically as

$$\sigma_y = \sigma_0 + \frac{k_y}{d^n}, \quad (2.38)$$

known as *Hall-Petch relationship* where exponent  $n$  is approximately 0.5,  $\sigma_y$  the yield stress,  $\sigma_0$  a material constant for the resistance of the lattice to dislocation motion,  $k_y$  a material constant and  $d$  the average grain diameter. Since the yield stress is inversely proportional to the square root of the diameter of the grains in (2.38), this Hall-Petch relationship explains that a sufficiently small diameter of grain is needed in order to have a sufficiently large stresses (due to the dislocation pile-up by a grain boundary) to propagate dislocations through the crystal. As a consequence, due to the dislocation pile-up near the grain boundary, the crystal with smaller diameter is harder and tougher than the larger one. This phenomenon is known as *size effect*. Mention that Hall-Petch relationship is no longer valid for both very large grain and extremely fine grain polycrystalline materials.

## 2.4 Continuum theory of dislocation

The aim of the continuum theory of dislocations is to describe the behavior of the ensemble of huge numbers of dislocations by means of continuum mechanics. Due to the complexity of the system, the phenomenological approach is used as the major tool of the theory. The guiding principles to choose the appropriate phenomenological models are the laws of thermodynamics which govern the general structure of the basic equations. Following the standard thermodynamic approach, the kinematic parameters of the dislocation network will be chosen first then afterwards the dependence of energy and dissipation on these kinematic parameters will be specified.

In this thesis, for simplicity, we limit our work only to geometrically linear continuum theory of dislocation. By geometrically linear continuum dislocation theory, we mean that the approximation of small kinematic quantities (i.e. they all can be neglected in comparison with unity). The non-linear theory of continuum theory of dislocation can be found in [Berdichevsky, 2006a, Le and Günther, 2014]

The first problem that arises here is to find the stress field for a given set of dislocations.

Kröner [1958] presented the general solution of this problem. Kondo [1952] and Bilby et al. [1955] proposed the general kinematic framework of continuum dislocation theory. They considered in their work that the natural state of a crystal as a manifold equipped with an affine connection. The dislocation field is characterized by the metric tensor of the manifold, the curvature tensor and the torsion tensor. Bilby et al. [1955] argued that the curvature tensor obtained from this connection must vanish for crystal lattices. As a result, the remaining kinematic characteristics are the metric tensor (the plastic strain) and the torsion tensor (the dislocation density tensor). This set of kinematic characteristics is equivalent to *plastic distortions*. In the linear case, the plastic strains and the dislocation density tensor can be found if the plastic distortion is known. The inverse statement is also true, namely, the plastic distortion can be found if the plastic strains and the dislocation density tensor are known [Le and Stumpf, 1996c].

We assume here the zero curvature for the natural state of a crystal. Accordingly, the kinematics is characterized by the plastic distortion only and the dislocation density tensor is determined by the plastic distortion.

### 2.4.1 Elastic and plastic distortions

Let us assume that the initial state of an infinitesimal cubic primitive lattice structure will be defined to be stress-free state of the medium. The lattice plane of the undeformed volume of

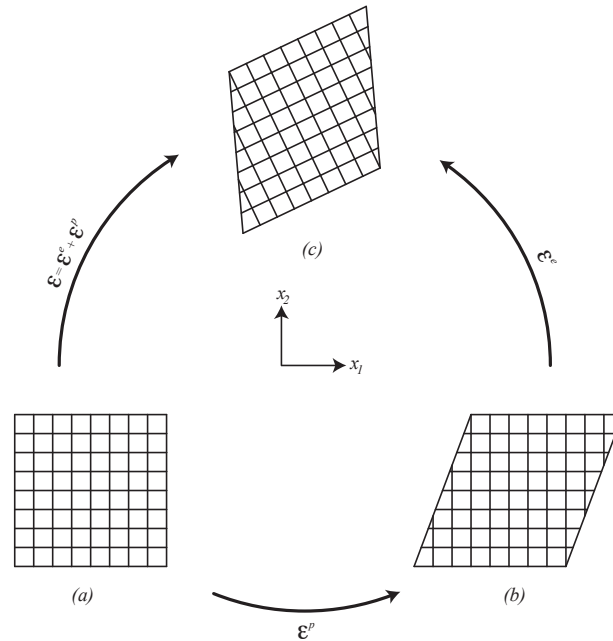


Figure 2.25: Additive decomposition of the total strain.

this cubic primitive crystal with vanishing lattice constants is shown in Fig. 2.25(a) where the positive  $x_3$  direction pointed out of the paper. Similar to section 2.1, for an infinitesimal element of crystal, there are two types of strains, namely elastic and plastic strain, which can be added up into the total strain as shown in Fig. 2.25, i.e.

$$\epsilon_{ij} = \epsilon_{ij}^e + \epsilon_{ij}^p. \quad (2.39)$$

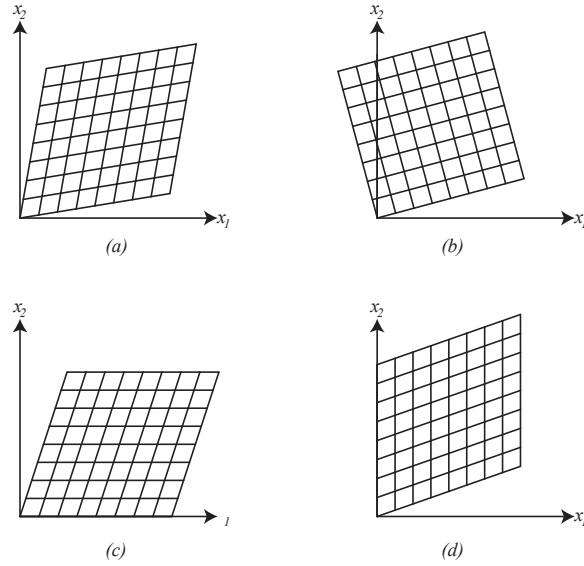


Figure 2.26: Examples of homogeneously elastic distorted states of Fig. 2.25(a): (a)  $\varepsilon_{12}^e = \varepsilon_{21}^e$ ; (b)  $\omega_{12}^e = -\omega_{21}^e$ ; (c)  $\beta_{21}^e$ , (d)  $\beta_{12}^e$ .

Throughout the elastic deformation, the lattice structure is deformed into new atomic configuration in accordance with the Hooke's law as illustrated in Fig. 2.26 where a few homogeneously distorted states of Fig. 2.25(a) are presented. This elastic deformation has an important feature, namely neighboring atoms remain as neighboring atoms during elastic deformation as can be seen in Fig. 2.26. The asymmetric elastic distortion tensor,  $\beta^e$ , is introduced to describe the geometric situation of the elastically deformed volume element. In the linear theory,  $\beta^e$  can be decomposed into the symmetric elastic strain tensor,  $\varepsilon^e$ , and the antisymmetric elastic rotation tensor,  $\omega^e$ , i.e.

$$\beta_{ij}^e = \varepsilon_{ij}^e + \omega_{ij}^e. \quad (2.40)$$

The change of shape of the element and the corresponding strain of the lattice structure is explained by the elastic strain tensor,  $\varepsilon^e$ . In addition, the elastic rotation tensor,  $\omega^e$ , describes a rigid rotation of the element.

For plastic deformation, a few corresponding homogeneous plastic distortions are shown in Fig. 2.27. Even though the elastic and plastic distortions cause the same change of shape of the small volume of Fig. 2.25(a), the change in lattice orientation are not the same for both distortions. For elastic case, the distortion of the shape and the lattice are always the same (see Fig. 2.26). This means that the internal state of the volume is changed during an elastic deformation which results in an elastic strain. On the other hand, the change of shape due to the plastic deformation is not considered to change the internal state of the volume (the lattice orientation remains the same).

The impact of dislocation on the crystal lattice is characterized by the tensor of plastic distortion,  $\beta = \beta_{ij}$ . The first index of  $\beta_{ij}$  describes the glide plane and the second one, the glide direction. The plastic distortion  $\beta_{21}$  of Fig. 2.27(c) ( $\beta_{12}$  of Fig. 2.27(d)) is produced by the gliding of some edge dislocations in  $x_1$ -direction ( $x_2$ -direction) with the Burgers vector directed along  $x_1$ -axis ( $x_2$ -axis) and the dislocation lines parallel to the  $x_3$ -direction ( $x_3$ -direction). The plastic strain in Fig. 2.27(a),  $\varepsilon_{21}^p = \varepsilon_{12}^p = (\varepsilon_{12}^p + \varepsilon_{21}^p)/2$ , and the plastic rotation in Fig. 2.27(b),  $\omega_{21}^p = -\omega_{12}^p = (\omega_{12}^p - \omega_{21}^p)/2$ , imply glide along two sets of plane. The decomposition of the plastic distortion into strain and rotation tensor is analogous to

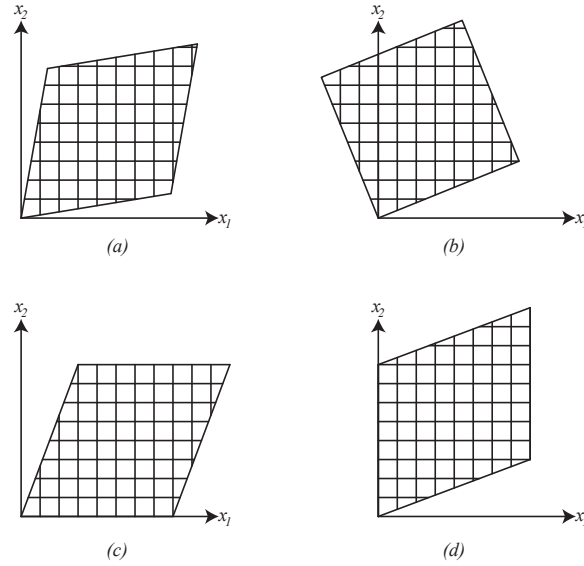


Figure 2.27: Examples of homogeneously plastic distorted states of Fig. 2.25(a): (a)  $\varepsilon_{12}^p = \varepsilon_{21}^p$ ; (b)  $\omega_{12}^p = -\omega_{21}^p$ ; (c)  $\beta_{21}$ , (d)  $\beta_{12}$ .

(2.40), i.e.

$$\beta_{ij} = \varepsilon_{ij}^p + \omega_{ij}^p. \quad (2.41)$$

Plastic strains,  $\varepsilon_{ij}^p$ , and plastic rotations,  $\omega_{ij}^p$ , represents the symmetric and antisymmetric parts of the plastic distortion, namely

$$\varepsilon_{ij}^p = \frac{1}{2}(\beta_{ij} + \beta_{ji}) \equiv \beta_{(ij)}, \quad \omega_{ij}^p = \frac{1}{2}(\beta_{ij} - \beta_{ji}) \equiv \beta_{[ij]}, \quad (2.42)$$

where round and square brackets in indices denoting symmetrization and skew-symmetrization, respectively.

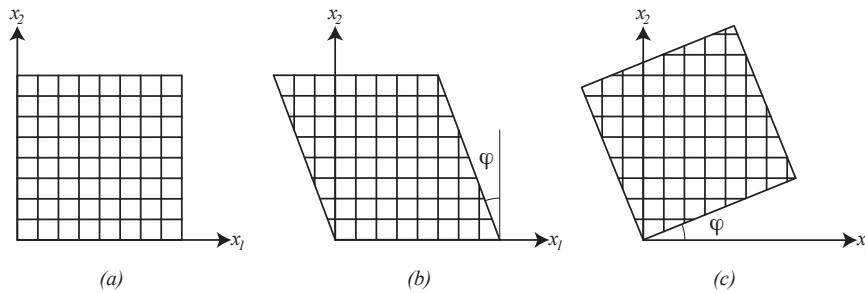


Figure 2.28: Dislocation flow leads to plastic rotation.

Including plastic rotations in the set of the dislocation network kinematical parameters in addition to the plastic strains adds a natural complication to the classical plasticity theory. Such phenomena can be observed from the following *Gedankenexperiment* presented in Fig. 2.28. First we consider a piece of a perfect two-dimensional lattice structure as seen in Fig. 2.28(a). Then this lattice structure is subjected to a homogeneous plastic deformation caused by the motion of some edge dislocations, with the Burgers vector directed along  $x_1$ -axis, throughout the crystal lattice in  $x_1$ -direction (see Fig. 2.28(b)). Then the crystal is plastically deformed further, as shown in Fig. 2.28(c), due to the movement of an additional similar set of edge dislocations that go through the crystal in  $x_2$ -direction (Burgers vector

directed along  $x_2$ -axis). With the assumption of the crystal with isotropic body and the shear angle,  $\psi$ , is small, the crystals in Fig. 2.28(a) and Fig. 2.28(c) differ by just a rigid rotation with no plastic deformation. If we only account the plastic deformations, as in the classical plasticity theory, such rigid plastic rotation is unnoticeable. Therefore, they would not affect any relation of the classical plasticity theory. As a matter of fact, the temperature of the crystal in the final state is higher than in the initial state due to the passing dislocations (Berdichevsky [2006a]). Therefore, in order to obtain the energy balance, the plastic rotation must be taken into account.

From the Gedankenexperiment shown in Fig. 2.28, it can be observed that the passing dislocations do not alter the orientation of the crystal lattice in space. On the other hand, as a consequence, material coordinate system rotates. Accordingly, the tensors determining the crystal anisotropy rotate with respect to the material frame due to the plastic flow. For that reason, the free energy density is reduced to an explicit function of the plastic distortion.

Considering a crystal deforming in single slip, a spatial average description of plastic distortion caused by this slip system is proposed in the form

$$\beta_{ij} = \beta(\mathbf{x})s_i m_j, \quad (2.43)$$

where  $\mathbf{s}$  the unit vector pointing in the slip direction and  $\mathbf{m}$  the normal vector to the slip plane. The function  $\beta(\mathbf{x})$  is assumed to be continuously differentiable. It can be easily seen that, in general,  $\beta_{ii} = 0$ , so that continuous plastic distortions do not cause any volumetric change. For the case of crystal with  $n$ -number of slip systems, the plastic distortion has the form

$$\beta_{ij} = \sum_{\vartheta=1}^n \beta(\mathbf{x})s_i^{\vartheta} m_j^{\vartheta}, \quad (2.44)$$

with index  $\vartheta$  indicating the slip systems.

For the case with a large volume of the cubic lattice crystal, the distortions ( $\beta_{ij}^T$ ,  $\beta_{ij}^e$  and  $\beta_{ij}$ ) are not constant and can be explained in terms of global instead of local displacement field. In order not to exclude this situations, it is convenient to introduce the relative displacement vector fields of two neighboring points separated by  $dx_i$ , namely

$$\begin{aligned} du_j^T &= \beta_{ij}^T dx_i & (d\mathbf{u}^T = d\mathbf{x} \cdot \boldsymbol{\beta}^T), \\ du_j^e &= \beta_{ij}^e dx_i & (d\mathbf{u}^e = d\mathbf{x} \cdot \boldsymbol{\beta}^e), \\ du_j^p &= \beta_{ij} dx_i & (d\mathbf{u}^p = d\mathbf{x} \cdot \boldsymbol{\beta}), \end{aligned} \quad (2.45)$$

with  $u_j^e$ ,  $u_j^p$  and  $u_j^T$  being the elastic, plastic and total displacement vector fields, respectively. Considering, up to now, we have only studied the very small cubic lattice crystal, it can be assumed that the distortions are constant and the relative displacement fields ( $du_j^e$ ,  $du_j^p$  and  $du_j^T$ ) are perfect differential. As a consequence we can determine the distortions as the gradients of the corresponding displacement fields, i.e.

$$\beta_{ij}^e = \partial_i u_j^e, \quad \beta_{ij} = \partial_i u_j^p. \quad (2.46)$$

Both distortion tensors mentioned before add up to the total distortion tensor

$$\beta_{ij}^T = \beta_{ij}^e + \beta_{ij}. \quad (2.47)$$

Both elastic and plastic distortions are incompatible so that the sum of them becomes compatible and derivable from a displacement field.

### 2.4.2 Dislocation density

We assume in this theory that the final state of the elements of the body undergoing plastic deformation are perfectly connected so that the total distortion,  $\beta_{ij}^T$ , is compatible and the total relative displacement,  $du_j^T$  is a perfect differential. Therefore, for any circuit  $c$  within the body, we have the relation

$$\oint_c du_j^T = \oint_c du_j^e + \oint_c du_j^p = 0. \quad (2.48)$$

From (2.45), Eq. (2.48) can also be written in the form

$$\oint_c d\mathbf{x} \cdot \boldsymbol{\beta}^T = \oint_c d\mathbf{x} \cdot \boldsymbol{\beta}^e + \oint_c d\mathbf{x} \cdot \boldsymbol{\beta} = 0. \quad (2.49)$$

Seeing that Eq. (2.49) is valid for any circuit  $c$ , with the help of Stokes' theorem for an arbitrary infinitesimal surface  $dA$  with the unit normal  $\mathbf{n}$ , we arrive at

$$\text{curl} \boldsymbol{\beta}^T = 0, \quad (2.50)$$

and

$$\text{curl} \boldsymbol{\beta}^e = -\text{curl} \boldsymbol{\beta}. \quad (2.51)$$

Eq. (2.50) is the compatibility equation for the total distortion which means that  $\beta_{ij}^T$  can be written as  $\partial_i u_j^T$ . On the other hand Eq. (2.51) explains the incompatibility equation for the elastic distortion.

According to Burgers [1939], for densely distributed dislocation, the Burgers vector takes the form

$$\mathbf{b} = - \oint_c d\mathbf{u}^e, \quad (2.52)$$

so that, based on relation in (2.48) and (2.49),

$$\mathbf{b} = \oint_c d\mathbf{u}^p = \oint_c d\mathbf{x} \cdot \boldsymbol{\beta}. \quad (2.53)$$

Once again we can apply the Stokes' theorem to (2.53) to obtain

$$b_j = \iint_a (\text{curl} \boldsymbol{\beta})_{ij} n_i dA. \quad (2.54)$$

Nye [1953] introduced the *dislocation density tensor*,  $\alpha_{ij}$ , which takes all geometrically necessary dislocations into account, where the index  $i$  indicates the dislocation line direction and  $j$  the direction of Burgers vector. The resultant Burgers vector of all geometrically necessary dislocations, whose dislocation lines cut the area  $A$  takes the form

$$b_j = \iint_a \alpha_{ij} n_i dA. \quad (2.55)$$

Since (2.54) and (2.55) are true for any circuit, we can write the dislocation density tensor in terms of  $\boldsymbol{\beta}$ , namely

$$\alpha_{ij} = \epsilon_{jkl} \beta_{il,k} \quad (\boldsymbol{\alpha} = \text{curl} \boldsymbol{\beta}), \quad (2.56)$$

where  $\epsilon_{jkl}$  being the Levi-Civita symbol and the coma in indices denoting the partial derivative with respect to the corresponding coordinates.

It is convenient to introduce the *scalar dislocation density*,  $\rho$ , which describing the amount of dislocations stored in a crystal by a scalar quantity. For a crystal with one active slip system, the scalar dislocation density can be written in the form

$$\rho = \frac{1}{b} |\epsilon_{jkl} \beta_{,k} m_l n_j|, \quad (2.57)$$

with  $b$  the magnitude of Burgers vector.

### 2.4.3 Energy of dislocation network

Kröner [1992] explained that the elastic strain,  $\epsilon^e$ , and the dislocation density tensor,  $\alpha$ , which characterize the current state of crystal, are the state variables of the continuum dislocation theory. A variable that characterizes the body in question is called a state variable if it can be uniquely measured or computed without having to know the history of the body. On the other hand the plastic strain,  $\epsilon^p$ , is not a state variable due to its dependency on the cut surfaces and accordingly on the whole history of creating dislocations (for example, the dislocations glide or climb are created quite differently). In a different manner, the dislocation density tensor,  $\alpha$ , is a proper state variable because it does not depend on how the dislocations are created but only on the current state of dislocations' characteristics (Burgers vector and positions of dislocation lines).

In addition to these state variables, the density of statistically stored dislocations has to be included also into the list of state variables. Nevertheless, these statistically stored dislocations exist only in the form of dislocation dipoles at low temperature to obtain the lowest energy state of the crystal. The density of dislocation dipoles depends only on temperature. Therefore, if the isothermal processes of deformation is considered, the contribution of the dislocation dipoles' density to the energy is a constant that can be omitted.

The free energy per unit volume of crystal can be written as

$$\Phi(\epsilon^e, \alpha) = \Phi_0(\epsilon^e) + \Phi_m(\alpha), \quad (2.58)$$

where  $\Phi_0$  is the elastic energy density and  $\Phi_m$  the microstructure energy density (the energy density of the dislocation network). The latter accounts also the plastic rotations. The elastic strain tensor,  $\epsilon^e$ , is given by

$$\epsilon_{ij}^e = \epsilon_{ij} - \epsilon_{ij}^p, \quad (2.59)$$

where

$$\epsilon_{ij} = \frac{1}{2} (u_{i,j} + u_{j,i}) \equiv u_{(i,j)}, \quad (2.60)$$

and  $\epsilon_{ij}^p = \beta_{(ij)}$  (see (2.42)) with round bracket in indices denoting symmetrization. Therefore Eq. (2.59) can also be written as

$$\epsilon_{ij}^e = u_{(i,j)} - \beta_{(ij)}. \quad (2.61)$$

For the reason that it does not follow from any physical law, it is necessary to choose correctly the type of  $\Phi_m$  that agrees, as close as possible, to the experimental observations and to the thermodynamic principles. Up to the end of twentieth century, it is believed that the energy of microstructure has a quadratic dependency on the dislocation density as can be seen in Gurtin [1973], namely

$$\Phi_m(\boldsymbol{\alpha}) = \frac{1}{2} \boldsymbol{\alpha} : \mathbf{E} : \boldsymbol{\alpha}, \quad (2.62)$$

with  $E_{ijkl}$  being the material constant. The relevance of this model of energy to describing the behavior of the dislocation networks was in question for a long time. The major concern was the smallness of the second term in (2.58), i.e.  $\Phi_m$ . To estimate its order, the dimension of the material constant  $E_{ijkl}$  must be the shear modulus,  $\mu$ , times characteristic material length squared. Berdichevsky [2006a] mentioned that, for a macroscopic size body, the second term in (2.58) is negligible in comparison with the first one if the corresponding characteristic material length is of the same order as one of the followings, namely, interatomic distance ( $b$ ), the average distance between dislocations, the average dislocation size and the average grain size. The mesoscopic and microscopic size of bodies problems were not seen at that time and the theory was not pursued further. Mention that, up to now, the physical meaning of the characteristic material length is still not yet clear.

The new understanding of the of the microstructure energy was gained owing to the progress in statistical mechanics and thermodynamics of the dislocation network [Berdichevsky, 2005, Groma et al., 2003, 2007, Le, 2010, Le and Berdichevsky, 2001]. The preposition about the microstructure energy reported in Berdichevsky [2006b], is able to overcome, at least partially, the difficulty mentioned previously. The energy of microstructure or the energy of all dislocations in a crystal includes the interaction energy between dislocations and the self-energy of dislocations. As explained in Berdichevsky [2006b], the energy density of the dislocation network,  $\Phi_m$ , is a function of local characteristics of dislocations only, despite the long-range character of the dislocation interactions. The simplest local characteristic of the dislocation network is the scalar dislocation density,  $\rho$ , introduced in (2.57), with the advantage that the state without dislocation corresponds to the zero value of  $\rho$ . Therefore, it is assumed that the energy of the dislocation network in a material body  $V_0$  is a function of  $\rho$ , i.e.

$$\Psi_m = \int_{V_0} \Phi_m(\rho) dx, \quad (2.63)$$

with  $dx = dx_1 dx_2 dx_3$  being the volume element.

It is assumed that the scalar dislocation density must be smaller than some saturated value,  $\rho_s$ , that corresponds to the material completely filled with dislocations. This saturated dislocation density,  $\rho_s$ , characterizes the closest packing of dislocations admissible in the discrete crystal lattice in a bounded domain. If  $\rho \sim \rho_s$  the energy grows into very large. On the contrary, the energy is linear in  $\rho$  (the sum of energies of non-interacting dislocations) for small dislocation density. Berdichevsky [2006b] suggested that the energy of microstructure satisfying Voce's law of phenomenological plasticity for a single crystal deforming in single slip is in the form

$$\Phi_m = \mu k \left( \ln \frac{1}{1 - \sqrt{\rho/\rho_s}} - \sqrt{\frac{\rho}{\rho_s}} \right), \quad (2.64)$$

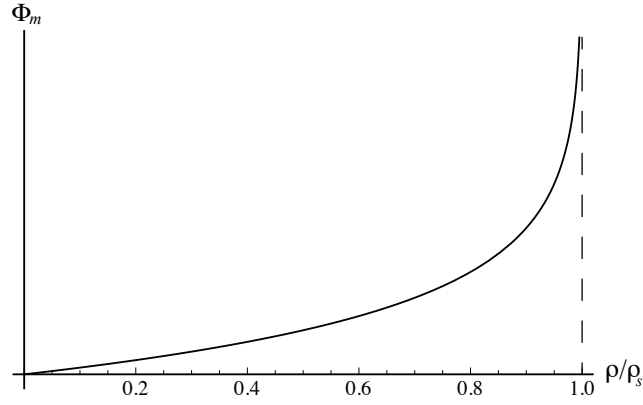


Figure 2.29: Energy density of dislocation network.

where  $k$  is the material constant. As a good approximation we will use the less complex form that also fit to the features of  $\rho$  mentioned above, namely

$$\Phi_m = \mu k \ln \frac{1}{1 - \rho/\rho_s}. \quad (2.65)$$

The logarithmic term in (2.65) guarantees that the energy for small dislocation density increases linearly and the energy moves toward infinity as  $\rho \sim \rho_s$  as can be observed in Fig. 2.29. Therefore, the energetic barrier against over-saturation is also provided by this form of energy.

#### 2.4.4 System of equations

Let  $V_0$  be a subregion of the crystal in its initial state. For the following discussion, we assume that the free energy of the crystal in the region  $V_0$  is a function of only local characteristics, namely, elastic strains ( $\varepsilon_{ij}^e$ ), plastic distortions ( $\beta_{ij}$ ), dislocation density tensor ( $\alpha_{ij}$ ) and entropy per unit mass ( $S$ ):

$$\Psi = \int_{V_0} \Phi (\varepsilon_{ij}^e, \beta_{ij}, \alpha_{ij}, S) dx. \quad (2.66)$$

For simplicity, we assume that the crystal is adiabatically isolated so that the heat conductivity can be neglected. Then, from the first law of thermodynamics, the energy rate equivalent to the power of the external forces, i.e.

$$\dot{\Psi} = \frac{d}{dt} \int_{V_0} \Phi (\varepsilon_{ij}^e, \beta_{ij}, \alpha_{ij}, S) dx = P, \quad (2.67)$$

where dot denotes the time derivative. The structure of the power,  $P$ , is controlled by the form of energy (see Sedov's variational formulation reported in Sedov [1968]) so that, due to the assumed form of the internal energy in our case, the power is presented in the form

$$P = \int_{\partial V_0} \left( \sigma_{ij} n_j \dot{u}_i + \sigma_{ijk} n_k \dot{\beta}_{ij} \right) dA, \quad (2.68)$$

with  $\partial V_0$  being the boundary of  $V_0$  and  $\mathbf{n}$  being the components of unit normal vector at  $\partial V_0$ . Note that, since the energy density depends on the gradient of plastic distortion, some stresses of higher order,  $\sigma_{ijk}$ , comes into the theory.

By means of divergence theorem, the surface integral in (2.68) can be transformed into the volume integral

$$P = \int_{V_0} \left( \sigma_{ij} \dot{u}_{i,j} + \sigma_{ij,j} \dot{u}_i + \sigma_{ijk} \dot{\beta}_{ij,k} + \sigma_{ijk,k} \dot{\beta}_{ij} \right) dx. \quad (2.69)$$

Then, by considering the relation in (2.61), we obtain from (2.67) and (2.69) the equation

$$\int_{V_0} \left[ \frac{\partial \Phi}{\partial S} \dot{S} + \frac{\partial \Phi}{\partial \varepsilon_{ij}^e} (\dot{u}_{(i,j)} - \dot{\beta}_{(ij)}) + \frac{\partial \Phi}{\partial \beta_{ij}} \dot{\beta}_{ij} + \frac{\partial \Phi}{\partial \alpha_{ij}} \epsilon_{jkl} \partial_k \dot{\beta}_{il} - \sigma_{ij} \dot{u}_{i,j} - \sigma_{ij,j} \dot{u}_i - \sigma_{ijk} \dot{\beta}_{ij,k} - \sigma_{ijk,k} \dot{\beta}_{ij} \right] dV = 0. \quad (2.70)$$

Due to the fact that region  $V_0$  is arbitrary, Eq. 2.70 is satisfied if the integrand equals zero. Since the derivatives,  $\partial \Phi / \partial \varepsilon_{ij}^e$ , is symmetry, we have

$$\frac{\partial \Phi}{\partial \varepsilon_{ij}^e} \dot{u}_{(i,j)} = \frac{\partial \Phi}{\partial \varepsilon_{ij}^e} \dot{u}_{i,j}, \quad \frac{\partial \Phi}{\partial \varepsilon_{ij}^e} \dot{\beta}_{(ij)} = \frac{\partial \Phi}{\partial \varepsilon_{ij}^e} \dot{\beta}_{ij}. \quad (2.71)$$

Therefore, considering (2.71) and denoting the absolute temperature (assumed to be constant),

$$T = \frac{\partial \Phi}{\partial S}, \quad (2.72)$$

we arrive at

$$\begin{aligned} T \dot{S} + \left( \frac{\partial \Phi}{\partial \varepsilon_{ij}^e} - \sigma_{ij} \right) \dot{u}_{i,j} + \left( \frac{\partial \Phi}{\partial \beta_{ij}} - \frac{\partial \Phi}{\partial \varepsilon_{ij}^e} - \sigma_{ijk,k} \right) \dot{\beta}_{ij} \\ + \left( \frac{\partial \Phi}{\partial \alpha_{im}} \epsilon_{mkj} - \sigma_{ijk} \right) \dot{\beta}_{ij,k} - \sigma_{ij,j} \dot{u}_i = 0. \end{aligned} \quad (2.73)$$

For rigid translation, entropy,  $S$ , and stress,  $\sigma_{ij}$ , remain constant while  $\dot{u}_{i,j}$ ,  $\dot{\beta}_{ij}$  and  $\dot{\beta}_{ij,k}$  equal zero. Consequently, in place of satisfying the first law of thermodynamics, the stresses have to fulfill the equilibrium equation (in the absence of body forces)

$$\sigma_{ij,j} = 0. \quad (2.74)$$

Likewise, the first law of thermodynamics can be fulfilled for the case of rigid rotations if and only if the stress tensor is symmetric

$$\sigma_{ij} = \sigma_{ji}. \quad (2.75)$$

Let us now introduce the following notations:

$$\tau_{ij} = \sigma_{ij} - \frac{\partial \Phi}{\partial \varepsilon_{ij}^e}, \quad (2.76)$$

$$\tau_{ijk} = \sigma_{ijk} - \frac{\partial \Phi}{\partial \alpha_{im}} \epsilon_{mkj}, \quad (2.77)$$

$$\varkappa_{ij} = \frac{\partial \Phi}{\partial \varepsilon_{ij}^e} - \frac{\partial \Phi}{\partial \beta_{ij}} + \sigma_{ijk,k}. \quad (2.78)$$

Accordingly, the first law of thermodynamics (Eq. 2.73) can now be written in the form

$$T\dot{S} = \tau_{ij}\dot{u}_{i,j} + \varkappa_{ij}\dot{\beta}_{ij} + \tau_{ijk}\dot{\beta}_{ij,k} \quad (2.79)$$

The tensors  $\tau_{ij}$  in Eq.2.76 and  $\tau_{ijk}$  in Eq.2.77 are the parts of the stresses,  $\sigma_{ij}$ , and the higher order stresses,  $\sigma_{ijk}$ , respectively, which cause heating of the crystal. Tensor  $\tau_{ij}$  explains heating in a non-uniform flow, so it has the meaning of viscous stresses. On the other hand, tensors  $\varkappa_{ij}$  and  $\tau_{ijk}$  describe heating caused by homogeneous and inhomogeneous plastic deformation, respectively.

The widely used closure of non-equilibrium thermodynamics assumes that the right hand side of Eq. 2.79 is equivalent to the *dissipation*,  $\mathcal{D}$ , which is strictly non-negative and a given function of  $\dot{u}_{i,j}$ ,  $\dot{\beta}_{ij}$  and  $\dot{\beta}_{ij,k}$ , namely

$$T\dot{S} = \mathcal{D} \left( \dot{u}_{i,j}, \dot{\beta}_{ij}, \dot{\beta}_{ij,k} \right) \geq 0. \quad (2.80)$$

It is supposed that there exists *dissipation potential*,  $D$ , which is related to the dissipation,  $\mathcal{D}$ , with the condition that  $D$  is a homogeneous function, namely

$$D \left( \lambda \dot{u}_{i,j}, \lambda \dot{\beta}_{ij}, \lambda \dot{\beta}_{ij,k} \right) = \lambda^m D \left( \dot{u}_{i,j}, \dot{\beta}_{ij}, \dot{\beta}_{ij,k} \right), \quad (2.81)$$

for any  $\lambda$  and some number  $m$ . By differentiation of (2.81) with respect to  $\lambda$  and setting  $\lambda = 1$ , we obtain the Euler's identity for homogeneous functions

$$\frac{\partial D}{\partial \dot{u}_{i,j}} \dot{u}_{i,j} + \frac{\partial D}{\partial \dot{\beta}_{ij}} \dot{\beta}_{ij} + \frac{\partial D}{\partial \dot{\beta}_{ij,k}} \dot{\beta}_{ij,k} = mD \left( \dot{u}_{i,j}, \dot{\beta}_{ij}, \dot{\beta}_{ij,k} \right). \quad (2.82)$$

Hence the dissipation potential differs from the dissipation by the factor  $m$ , i.e.

$$\mathcal{D} = mD. \quad (2.83)$$

In the matter of rate-independent processes the dissipation function is homogeneous first order function of the internal variable rates ( $m = 1$ ). Therefore dissipation equals to dissipation potential ( $\mathcal{D} = D$ )

The tensors  $\tau_{ij}$ ,  $\varkappa_{ij}$  and  $\tau_{ijk}$ , which control the irreversible processes in the crystal, are linked to  $\dot{u}_{i,j}$ ,  $\dot{\beta}_{ij}$  and  $\dot{\beta}_{ij,k}$  by the relations

$$\begin{aligned} \tau_{ij} &= \frac{\partial D}{\partial \dot{u}_{i,j}} \\ \varkappa_{ij} &= \frac{\partial D}{\partial \dot{\beta}_{ij}} \\ \tau_{ijk} &= \frac{\partial D}{\partial \dot{\beta}_{ij,k}}, \end{aligned} \quad (2.84)$$

The set of equations (2.74), (2.75), (2.76), (2.77), (2.78) and (2.84) is closed with respect to the unknown functions  $u_i$  and  $\beta_{ij}$ . The temperature can be obtained by means of Eq. 2.79.

### 2.4.5 Energy minimization

Every continuum model of dislocations is fixed by two functions, namely, the free energy density,  $\Phi$ , and the dissipation potential,  $D$ .

With elastic energy density presented in the form

$$\Phi_0 = \frac{1}{2} C_{ijkl} \varepsilon_{ij}^e \varepsilon_{kl}^e, \quad (2.85)$$

with  $C_{ijkl}$  being a fourth-order elasticity tensor, the free energy density for isothermal process (2.58) can now be written in the form

$$\Phi(\varepsilon^e, \alpha) = \frac{1}{2} C_{ijkl} \varepsilon_{ij}^e \varepsilon_{kl}^e + \Phi_m(\alpha), \quad (2.86)$$

with  $\Phi_m$  from (2.65) for single crystal deforming in single slip system. With the assumption of the isotropic elastic property of the crystal, for simplicity, the free energy density per unit volume of the crystal with continuously distributed dislocations is presented in the form [Berdichevsky, 2006a,b]

$$\Phi(\varepsilon_{ij}^e, \rho) = \frac{1}{2} \lambda (\varepsilon_{ii}^e)^2 + \mu \varepsilon_{ij}^e \varepsilon_{ij}^e + \Phi_m(\rho), \quad (2.87)$$

with  $\mu$  and  $\lambda$  being Lamé constants.

In the future, the viscous effect will be neglected, so that dissipation does not depend on the velocity gradients and viscous stresses vanish, i.e.

$$\tau_{ij} = 0. \quad (2.88)$$

Applying (2.88) to (2.76), we obtain the equation to determine stresses, namely

$$\sigma_{ij} = \frac{\partial \Phi}{\partial \varepsilon_{ij}^e}, \quad (2.89)$$

with  $\Phi$  from (2.87).

Let us consider the undeformed single crystal that occupies region  $V_0$  of the three dimensional euclidean space. The displacements at the boundary  $\partial V_0$  are prescribed, i.e.

$$u_i = u_i^{(b)} \quad \text{at} \quad \partial V_0, \quad (2.90)$$

with  $u_i^{(b)}$  being the boundary displacements. It is assumed that functions  $u_i^{(b)}$  are continuous so that no dislocations enter into the crystal in the course of deformation. In consequence, the plastic slip,  $\beta$ , at the boundary equals zero, namely

$$\beta(x) = 0 \quad \text{at} \quad \partial V_0. \quad (2.91)$$

The energy functional of this crystal is defined as

$$\Psi[u_i, \beta] = \int_{V_0} \Omega(u_{(i,j)}, \beta, \beta_{,i}) \, dx, \quad (2.92)$$

where

$$\Omega(u_{(i,j)}, \beta, \beta_{,i}) = \Phi(\varepsilon_{ij}^e, \alpha_{ij}), \quad (2.93)$$

and  $dx = dx_1 dx_2 dx_3$  denotes the volume element.

Regarding the dissipation potential, several model can be considered. The simplest model assumes that the dissipation is zero meaning that the resistance to the dislocation motion can be neglected. In this case all tensors  $\tau_{ij}$ ,  $\tau_{ijk}$  and  $\varkappa_{ij}$  from (2.76)-(2.78) vanish, so that the displacement vector,  $u_i$ , and the plastic slip,  $\beta(x)$ , minimize the energy functional (2.92) under constraints (2.90) and (2.91).

For the next model of the dissipation potential, we neglect the viscous effect in addition to the dissipation caused by  $\dot{\beta}_{i,j,k}$ . It is assumed in this model that the dissipation potential,  $D$ , depends only on  $\dot{\beta}_{ij}$  so that  $\tau_{ij} = 0$  and  $\tau_{ijk} = 0$ . Consequently we have the relation

$$\sigma_{ij} = \frac{\partial \Phi}{\partial \varepsilon_{ij}^e}, \quad \sigma_{ijk} = \frac{\partial \Phi}{\partial \alpha_{im}} \epsilon_{mkj}. \quad (2.94)$$

If  $D$  is a homogeneous function of first order with respect to  $\dot{\beta}_{ij}$ , then  $\mathcal{D} = D$  and from Eq. 2.84<sub>2</sub> we have

$$\varkappa_{ij} = \frac{\partial D}{\partial \dot{\beta}_{ij}}.$$

Accordingly, with this case with dissipation, the energy minimization should be replaced by the following variational equation [Sedov, 1968]

$$\delta \Psi + \int_{V_0} \frac{\partial D}{\partial \dot{\beta}} \delta \beta \, dx = 0. \quad (2.95)$$

The last term in (2.95) explains the energy dissipation due to the dislocation motion. Since the dissipation potential  $D(\dot{\beta})$  is assumed to depend only on the rate of the plastic distortion, we consider for this thesis the simplest rate independent theory for which

$$D(\dot{\beta}) = K |\dot{\beta}|, \quad (2.96)$$

where  $K$  being the critical resolved shear stress.

If we assume that the sign of  $\dot{\beta}$  remains constant throughout the evolution of  $\beta$ , the variational equation (2.95) reduces to minimizing the following "effective energy" functional

$$\hat{\Psi} = \int_{V_0} \left[ \Omega(u_{(i,j)}, \beta, \beta_{,i}) + K (\text{sign} \dot{\beta}) \beta \right] dx. \quad (2.97)$$

For that reason, the displacements,  $u_i$ , and the plastic slip,  $\beta$ , in the final equilibrium state of deformation minimize the effective energy functional among all admissible functions.

Finally, for the case of  $\dot{\beta} = 0$ , then the plastic slip,  $\beta$ , is frozen. Therefore, the displacements should be found by minimizing (2.92) for this frozen  $\beta$ .



### 3 Dislocation nucleation in anti-plane constrained shear of single crystals

Before dealing with the plane constrained problem of single crystals in the following chapters, we would like to present the detail derivation of the simplest example of this theory, i.e. anti-plane constrained shear of single crystals reported in Berdichevsky and Le [2007].

#### 3.1 Anti-plane constrained shear energy

Consider the beam made of a single crystal undergoing an anti-plane shear deformation as shown in Fig. 3.1. The displacement field of the beam is called anti-plane if

$$u = v = 0, \quad w = w(x, y). \quad (3.1)$$

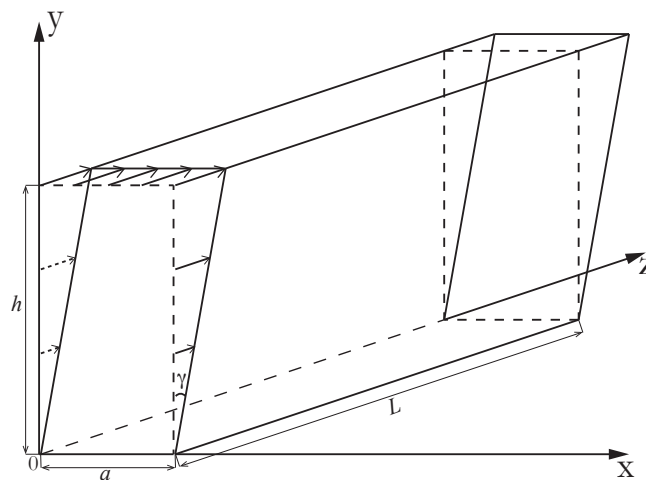


Figure 3.1: Anti-plane constrained shear

Let  $C$  be the cross section of the beam by planes  $z = \text{constant}$ . The cross section  $C$  is considered to be rectangle with width  $a$  and height  $h$  where  $0 < x \leq a$  and  $0 < y \leq h$ . We assume that the height,  $h$ , and the length of the beam,  $L$ , are much larger than the width,  $a$ , ( $a \ll h$  and  $a \ll L$ ) to disregard the end effects and to have the stresses and strains depending only on one variable  $x$  in the central part of the beam. To model the grain boundary, the beam has the prescribed displacement at the boundary  $\partial C \times [0, L]$

$$w = \gamma y, \quad (3.2)$$

with  $\gamma$  being the overall shear strain. The crystal is deformed elastically and  $w = \gamma y$  everywhere in the specimen for sufficiently small shear strain.

In case  $\gamma$  goes beyond some critical value, the screw dislocations may appear. Therefore it is assumed that the slip planes parallel to the plane  $y = 0$  and the dislocation line parallels to the  $z$ -axis.

### 3.2 Total energy of the crystal in anti-plane constrained shear

For anti-plane shear deformation there are only two independent non-zero components of the strain tensor, namely

$$\varepsilon_{xz} = \frac{1}{2}w_{,x}, \quad \varepsilon_{yz} = \frac{1}{2}w_{,y}, \quad (3.3)$$

where the comma in indices denotes the partial derivative with respect to the corresponding coordinates. With (3.2) and (3.3), we have the total shear strain tensor

$$\varepsilon_{ij} = \begin{pmatrix} 0 & 0 & 0 \\ 0 & 0 & \frac{1}{2}\gamma \\ 0 & \frac{1}{2}\gamma & 0 \end{pmatrix}. \quad (3.4)$$

For the screw dislocations with the slip planes parallel to the plane  $y = 0$ , the tensor of plastic distortion,  $\beta_{ij}$ , has only one non-zero component, i.e.

$$\beta_{zy} = \beta. \quad (3.5)$$

We assume that  $\beta$  depends only on  $x$ -coordinates:  $\beta = \beta(x)$ . Seeing that the displacements are prescribed at the boundaries  $x = 0$  and  $x = a$ , dislocations are not able to penetrate these boundaries, ergo

$$\beta(0) = \beta(a) = 0. \quad (3.6)$$

The plastic strain tensor can be presented in the form

$$\varepsilon_{ij}^p = \frac{1}{2}(\beta_{ij} + \beta_{ji}) = \frac{1}{2} \begin{pmatrix} 0 & 0 & 0 \\ 0 & 0 & \beta \\ 0 & \beta & 0 \end{pmatrix}. \quad (3.7)$$

With Fig. 3.4 and Fig. 3.7, we can write the elastic strain tensor in the form

$$\varepsilon_{ij}^e = \varepsilon_{ij} - \varepsilon_{ij}^p = \begin{pmatrix} 0 & 0 & 0 \\ 0 & 0 & \frac{1}{2}(\gamma - \beta) \\ 0 & \frac{1}{2}(\gamma - \beta) & 0 \end{pmatrix}. \quad (3.8)$$

The only non-zero component of the tensor of dislocation density tensor  $\alpha_{ij} = \epsilon_{jkl}\beta_{il,k}$  [Bilby, 1955, Kröner, 1955, Nye, 1953], with  $\epsilon_{jkl}$  being the permutation symbol is

$$\alpha_{zz} = \beta_{,x}. \quad (3.9)$$

The number of dislocation per unit area (scalar dislocation density) equals

$$\rho = \frac{1}{b} \sqrt{\alpha_{zz}^2} = \frac{1}{b} |\beta_{,x}|, \quad (3.10)$$

with  $b$  being the magnitude of Burgers' vector.

Assuming for simplicity the isotropic elastic property of the crystal, as stated in Berdichevsky [2006a,b], the free energy per unit volume of the crystal with dislocations is in the form

$$\Phi(\varepsilon_{ij}^e, \alpha_{ij}) = \frac{1}{2}\lambda (\varepsilon_{ii}^e)^2 + \mu\varepsilon_{ij}^e\varepsilon_{ij}^e + \Phi_m(\rho), \quad (3.11)$$

where  $\mu$  and  $\lambda$  are Lamé constants. The first and second term of (3.11) describe the energy due to the elastic strain, the last term is the energy of the dislocation network. The energy density of the dislocation network for anti-plane constrained shear case takes the form

$$\Phi_m(\rho) = \mu k \ln \frac{1}{1 - \frac{\rho}{\rho_s}}, \quad (3.12)$$

with  $\rho$  from (3.10),  $\rho_s$  the saturated dislocation density and  $k$  a material constant.

Applying (3.12) to (3.11) then integrating over the volume, the total energy is presented by

$$\Psi = hL \int_0^a \left[ \frac{1}{2}\lambda (\varepsilon_{ii}^e)^2 + \mu\varepsilon_{ij}^e\varepsilon_{ij}^e + \mu k \ln \frac{1}{1 - \frac{|\beta,x|}{b\rho_s}} \right] dx. \quad (3.13)$$

By substituting (3.8) into (3.13), we write the total energy, which is a functional of  $\beta(x)$ , in the form

$$\Psi(\beta(x)) = hL \int_0^a \left[ \frac{1}{2}\mu(\gamma - \beta)^2 + \mu k \ln \frac{1}{1 - \frac{|\beta,x|}{b\rho_s}} \right] dx. \quad (3.14)$$

### 3.3 Anti-plane constrained shear at zero dissipation

#### 3.3.1 Dislocation nucleation at zero dissipation

The dissipation of energy equals zero on condition that the resistance to the dislocation motion is negligible. For this zero resistance case, the true plastic distortion minimizes the total energy (3.14). Accordingly the determination of  $\beta(x)$  reduces to the minimization of total energy (3.14). The unique solution can be obtained from the variational problem because of the convexity of the energy density,  $\Phi$ , with respect to  $\beta$  and  $\beta_{,x}$ .

It is advantageous for us to introduce (3.14) in term of dimensionless quantities. For that purpose, we multiply left and right hand side of (3.14) with  $1/\mu a L h$

$$\frac{\Psi(\beta)}{\mu a L h} = \int_0^{a/a} \left[ \frac{1}{2}(\gamma - \beta)^2 + k \ln \frac{1}{1 - \frac{|\beta,x|}{b\rho_s}} \right] \frac{dx}{a}. \quad (3.15)$$

In consequence, we can now introduce the dimensionless quantities

$$E = \frac{\Psi}{\mu a L h}, \quad \eta = \frac{x}{a}, \quad \bar{\beta}(\eta) = \beta(x), \quad c = ab\rho_s, \quad (3.16)$$

so that  $d\eta = dx/a$  and  $\beta_{,x}(x) = \bar{\beta}'(\eta)/a$ , where the dimensionless variable  $\eta$  changes on the interval  $(0, 1)$  and the prime denotes differentiation with respect to  $\eta$ . Substituting (3.16) into (3.15) gives us the dimensionless form of the total energy, i.e.

$$E(\bar{\beta}(\eta)) = \int_0^1 \left[ \frac{1}{2}(\gamma - \bar{\beta})^2 + k \ln \frac{1}{1 - \frac{|\bar{\beta}'|}{c}} \right] d\eta. \quad (3.17)$$

Since we shall deal further only with the dimensionless form of the total energy, it is convenient, for short, to drop the bar over  $\beta$ .

The logarithmic term in the energy functional (3.17) for small up to moderate dislocation densities is replaced by an asymptotic formula

$$\ln \frac{1}{1 - \frac{|\beta'|}{c}} \cong \frac{|\beta'|}{c} + \frac{1}{2} \frac{(\beta')^2}{c^2}. \quad (3.18)$$

Correspondingly the dimensionless total energy functional (3.17) becomes

$$E(\beta(\eta)) = \int_0^1 \left[ \frac{1}{2}(\gamma - \beta)^2 + \frac{k|\beta'|}{c} + \frac{k}{2} \frac{(\beta')^2}{c^2} \right] d\eta. \quad (3.19)$$

Due to the boundary conditions (3.6),  $\beta'(\eta)$  should change its sign on the interval  $\eta \in (0, 1)$ . The one-dimensional theory of dislocation pile-ups reported in Leibfried [1951] suggests to seek the minimizer in the form

$$\beta(\eta) = \begin{cases} \beta_1(\eta), & \text{for } \eta \in (0, l), \\ \beta_m, & \text{for } \eta \in (l, 1-l), \\ \beta_1(1-\eta), & \text{for } \eta \in (1-l, 1), \end{cases} \quad (3.20)$$

where  $\beta_m$  is a constant,  $l$  an unknown length,  $0 \leq l \leq 1/2$ , and  $\beta_1(l) = \beta_m$ . Function  $\beta_1$  must obey the following boundary conditions

$$\beta_1(0) = 0, \quad \beta_1(l) = \beta_m. \quad (3.21)$$

Our aim is to obtain  $\beta_1(\eta)$  and the constants,  $\beta_m$  and  $l$ .

Applying  $\beta_1' > 0$  for  $\eta \in (0, l)$  and (3.20) to (3.19), the total energy functional reduces to

$$E = 2 \int_0^l \left[ \frac{1}{2}(\gamma - \beta_1)^2 + \frac{k|\beta_1'|}{c} + \frac{k}{2} \frac{(\beta_1')^2}{c^2} \right] d\eta + \frac{1}{2}(\gamma - \beta_m)^2(1 - 2l). \quad (3.22)$$

We calculate the variation of (3.22) with respect to  $\beta_1$ ,  $\beta_m$  and  $l$  then apply the partial integration and (3.21) to have

$$\begin{aligned} \delta E = & \int_0^l \left[ 2(\beta_1 - \gamma) - \frac{2k\beta_1''}{c^2} \right] \delta\beta_1 d\eta + \left( \frac{2k\beta_1'(l)}{c} + \frac{k(\beta_1'(l))^2}{c^2} \right) \delta l \\ & + \left( \frac{2k}{c} + \frac{2k\beta_1'(l)}{c^2} - (1 - 2l)(\gamma - \beta_m) \right) \delta\beta_m. \end{aligned} \quad (3.23)$$

To find the minimum of the energy functional, we have to set  $\delta E = 0$  for arbitrary  $\delta\beta_1$ ,  $\delta\beta_m$  and  $\delta l$ . Choosing first the orientations such that  $\delta l$  and  $\beta_m$ , so that for the case  $\delta E = 0$  for arbitrary  $\delta\beta_1$  we have

$$2(\beta_1 - \gamma) - \frac{2k\beta_1''}{c^2} = 0. \quad (3.24)$$

Then for  $\delta\beta_m = 0$  but arbitrary  $\delta l$  we obtain

$$\frac{2k\beta_1'(l)}{c} + \frac{k(\beta_1'(l))^2}{c^2} = 0, \quad (3.25)$$

which yields an additional boundary condition at  $\eta = l$ , namely

$$\beta_1'(l) = 0, \quad (3.26)$$

which means that the dislocation density must be continuous at  $\eta = l$ . Yet, solving  $\delta E = 0$  for only arbitrary  $\delta\beta_m$  gives

$$\frac{2k}{c} - (1 - 2l)(\gamma - \beta_m) = 0. \quad (3.27)$$

A general solution of the differential equation (3.24) is the sum of a particular solution ( $\beta_{1p}$ ) and a general solution of the homogeneous equation ( $\beta_{1h}$ ), i.e.

$$\beta_1 = \beta_{1p} + \beta_{1h}. \quad (3.28)$$

It is easy to see from

$$2(\beta_{1p} - \gamma) - \frac{2k\beta_{1p}''}{c^2} = 0. \quad (3.29)$$

that

$$\beta_{1p} = \gamma. \quad (3.30)$$

To find the general solution of the homogeneous equation, we need to solve

$$\beta_{1h} - \frac{k\beta_{1h}''}{c^2} = 0. \quad (3.31)$$

We seek the solution in the form

$$\beta_{1h} = e^{\zeta\eta}, \quad \beta'_{1h} = \zeta e^{\zeta\eta}, \quad \beta''_{1h} = \zeta^2 e^{\zeta\eta}. \quad (3.32)$$

Substituting (3.32) into (3.31) we obtain

$$\zeta = \frac{c}{\sqrt{k}}. \quad (3.33)$$

The general solution of the homogeneous equation is the linear combination of (3.32)

$$\beta_{1h} = C_1 \cosh \zeta\eta + C_2 \sinh \zeta\eta, \quad (3.34)$$

where  $C_1$  and  $C_2$  are constants. Thus by applying (3.30) and (3.34) to (3.28), the solution of (3.24) reads

$$\beta_1 = \gamma + C_1 \cosh \zeta \eta + C_2 \sinh \zeta \eta. \quad (3.35)$$

From applying boundary condition (3.21)<sub>1</sub> to (3.35) we have

$$C_1 = -\gamma. \quad (3.36)$$

Applying boundary condition (3.26) to (3.35) with (3.36), we obtain

$$C_2 = \gamma \tanh \zeta l. \quad (3.37)$$

Finally, substituting (3.33), (3.36) and (3.37) into (3.35), we obtain the general solution of the differential equation (3.24) for  $\eta \in (0, l)$ , namely

$$\beta_1 = \gamma \left( 1 - \cosh \frac{c\eta}{\sqrt{k}} + \tanh \frac{cl}{\sqrt{k}} \sinh \frac{c\eta}{\sqrt{k}} \right). \quad (3.38)$$

Applying (3.21)<sub>2</sub> to (3.38), the general solution of the differential equation (3.24) for  $\eta \in (l, 1-l)$  is given by

$$\beta_m = \gamma \left( 1 - \frac{1}{\cosh \frac{cl}{\sqrt{k}}} \right). \quad (3.39)$$

It is easy to find the solution for  $\eta \in (1-l, 1)$ , namely

$$\beta_1 = \gamma \left( 1 - \cosh \frac{c(1-\eta)}{\sqrt{k}} + \tanh \frac{cl}{\sqrt{k}} \sinh \frac{c(1-\eta)}{\sqrt{k}} \right). \quad (3.40)$$

We substitute (3.39) into (3.27) to obtain

$$\gamma(l) = \frac{2k \cosh \zeta l}{c(1-2l)}. \quad (3.41)$$

### 3.3.2 Dislocation density, energetic threshold value, stress strain curve and size effect

To compute the normalized dislocation density, we apply the solutions (3.38)-(3.40) to

$$\alpha(\eta) = \beta'(\eta). \quad (3.42)$$

to obtain

$$\alpha = \begin{cases} \gamma(-\zeta \sinh \zeta \eta + \zeta \tanh \zeta l \cosh \zeta \eta), & \text{for } \eta \in (0, l), \\ 0, & \text{for } \eta \in (l, 1-l), \\ \gamma(-\zeta \sinh \zeta(1-\eta) + \zeta \tanh \zeta l \cosh \zeta(1-\eta)), & \text{for } \eta \in (1-l, 1), \end{cases} \quad (3.43)$$

where  $\zeta$  from (3.33).

As explained in Berdichevsky and Le [2007], as long as  $\gamma$  smaller than some energetic threshold value,  $\gamma_{en}$ , the plastic distortion,  $\beta$ , equals zero and the nucleation of dislocations

are not yet started. The global minimum of the energy of the crystal is achieved without geometrically necessary dislocations for  $\gamma < \gamma_{en}$  and by means of newly nucleated dislocations for  $\gamma \geq \gamma_{en}$ . By reason of the width of the boundary layer,  $l$ , tends to zero as  $\gamma$  approaches  $\gamma_{en}$ , we can compute the energetic threshold value by assigning  $l = 0$  to (3.41) and yields

$$\gamma_{en} = \gamma(0) = \frac{2k}{c}, \quad (3.44)$$

with  $c = ab\rho_s$ . Since  $\gamma_{en}$  is inversely proportional to the width of specimen,  $a$ , then (3.44) explains clearly the size effect.

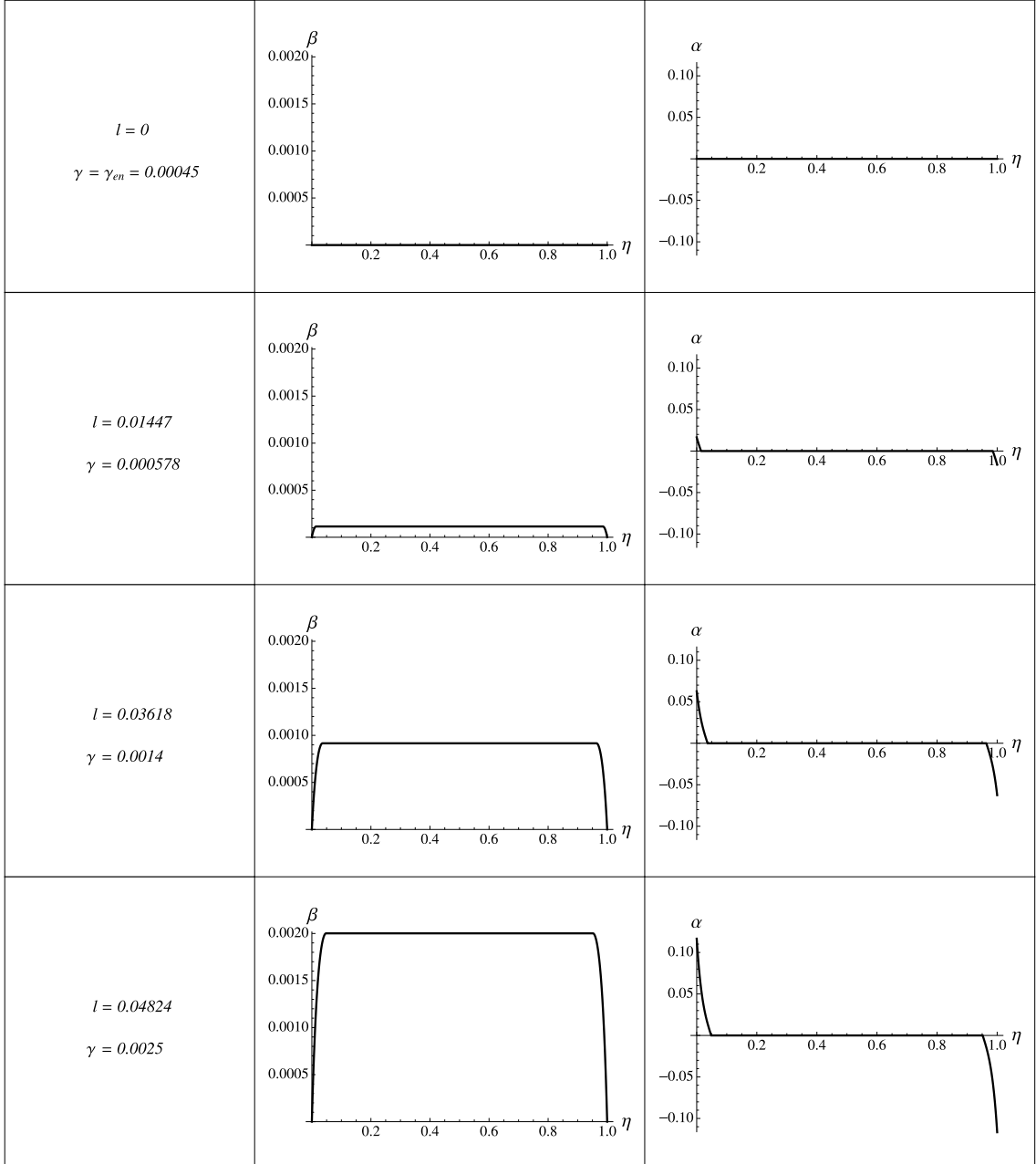


Figure 3.2: Evolution of  $\beta$  and  $\alpha$  for zero dissipation anti-plane constrained shear of single crystal with  $a = 1\mu\text{m}$  where  $\eta = x/a$  for increasing  $\gamma$

It is interesting to calculate the shear stress  $\tau$  which is a measurable quantity. We assume

Material	$\mu$ (GPa)	$\nu$	$b$ (Å)	$\rho_s$ (m <sup>-2</sup> )	$k$
Aluminum	26.3	0.33	2.5	$2.04 \times 10^{15}$	0.000115

Table 3.1: Material characteristics

that the stress distribution is uniformly distributed or averaged over the crystal width. The average shear stress takes the form

$$\tau = \frac{1}{a} \int_0^a \sigma_{yz} dx. \quad (3.45)$$

Applying

$$\sigma_{yz} = 2\mu\varepsilon_{yz}^e, \quad (3.46)$$

to (3.45) with  $\varepsilon_{yz}^e$  from (3.8) we obtain

$$\frac{\tau}{\mu} = \frac{1}{a} \int_0^a [\gamma - \beta] dx. \quad (3.47)$$

As before it is also convenient to work with dimensionless form of the average shear stress by applying (3.16) to (3.47).

$$\frac{\tau}{\mu} = \int_0^1 [\gamma - \beta] d\eta. \quad (3.48)$$

Then assigning (3.20) to (3.48) we obtain the normalized average shear stress equation in the form

$$\frac{\tau}{\mu} = \int_0^l 2[\gamma - \beta_1] d\eta + (\gamma - \beta_m)(1 - 2l), \quad (3.49)$$

with  $\beta_1$  from (3.38) and  $\beta_m$  from (3.39).

For the numerical simulation we took the material parameters from Table 3.1. In this approach, we use all material parameters well known to aluminum except the additional parameters  $k$  and  $\rho_s$ . We choose these additional parameters to have good agreement of discrete dislocation simulations and the continuum dislocation theory with respect to the yield stress and the hardening rate for both single and double slip (see section 4.4 and section 6.4, respectively).

The evolution of plastic distortion  $\beta(\eta)$  and normalized dislocation density  $\alpha(\eta)$  for increasing  $\gamma$  (by increasing  $l$ ) at  $a = 1 \mu\text{m}$  can be observed in Fig. 3.2 which illustrates the dislocation pile-up near the boundary and dislocation free zone in the middle of the crystal.

Curve OAB in Fig. 3.3 shows the normalized average shear stress versus shear strain. There is a "work hardening" section AB for  $\gamma > \gamma_{en}$  caused by the dislocation pile-up near the crystal boundaries. When we unload the crystal by decreasing  $\gamma$ , the stress strain curve follows the same path BAO. This phenomenon can be explained by the fact that there is no residual strain when we decrease  $\gamma$ . In the course of unloading, since the plastic deformation is completely reversible and no energy dissipation occurs, the newly nucleated dislocations annihilate and disappear completely at point A.

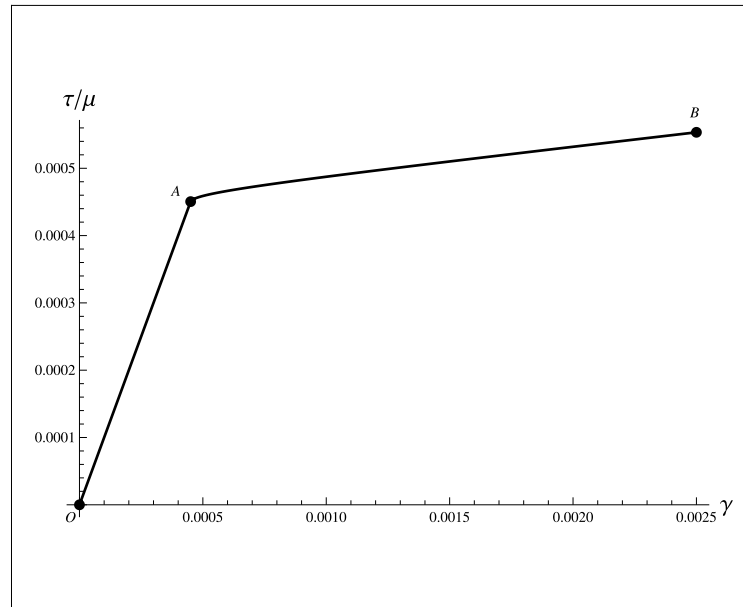


Figure 3.3: Normalized average shear stress versus shear strain curve for anti-plane constrained shear of single crystal at zero dissipation at  $a = 1 \mu\text{m}$

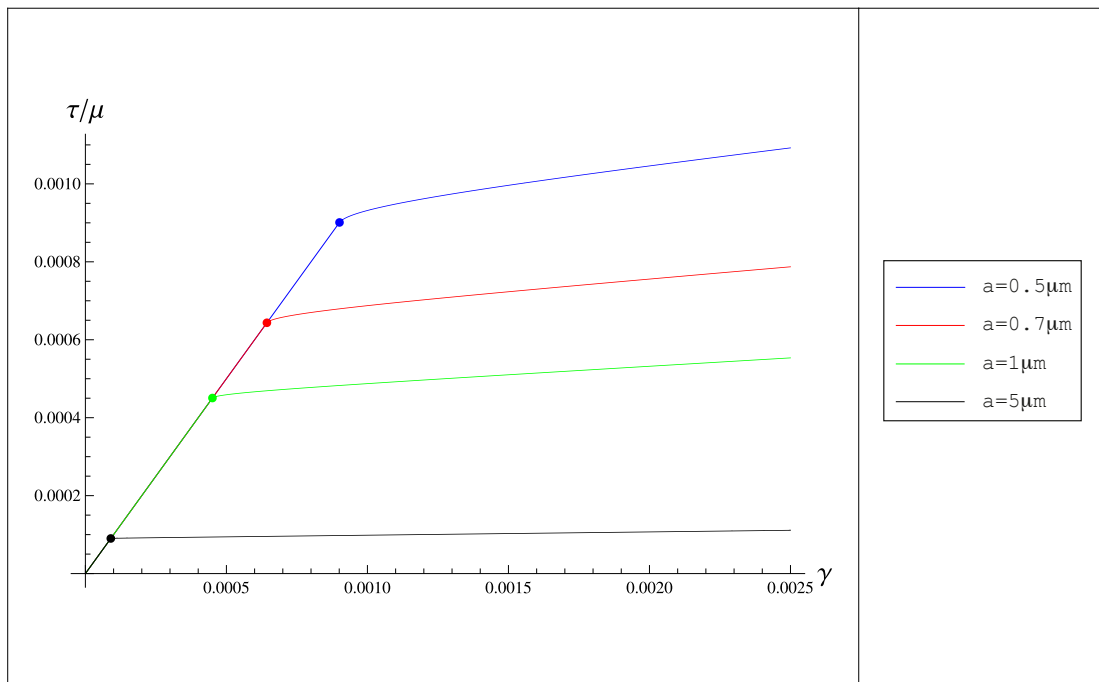


Figure 3.4: Normalized shear stress versus shear strain curves for zero dissipation anti-plane constrained shear of single crystal with different crystal widths  $a$

To visualize the size effect, we plot the normalized average shear stress versus strain curves for different crystal widths,  $a$ , as shown in Fig. 3.4, where the dot explain the energetic threshold value for each curve. We observe that the energetic threshold value and the the work hardening is higher for the smaller material. This can be explained from Fig. 3.5 which shows the evolution of plastic distortion,  $\beta(\eta)$  and normalized dislocation density  $\alpha(\eta)$  for different  $a$ . Our form of energy with its saturated dislocation density,  $\rho_s$ , bounds the local concentration of dislocation. Therefore, as  $a$  decreased, the dislocation pile-ups are forced to distribute more into the middle of the crystal which causes the increasing inner back

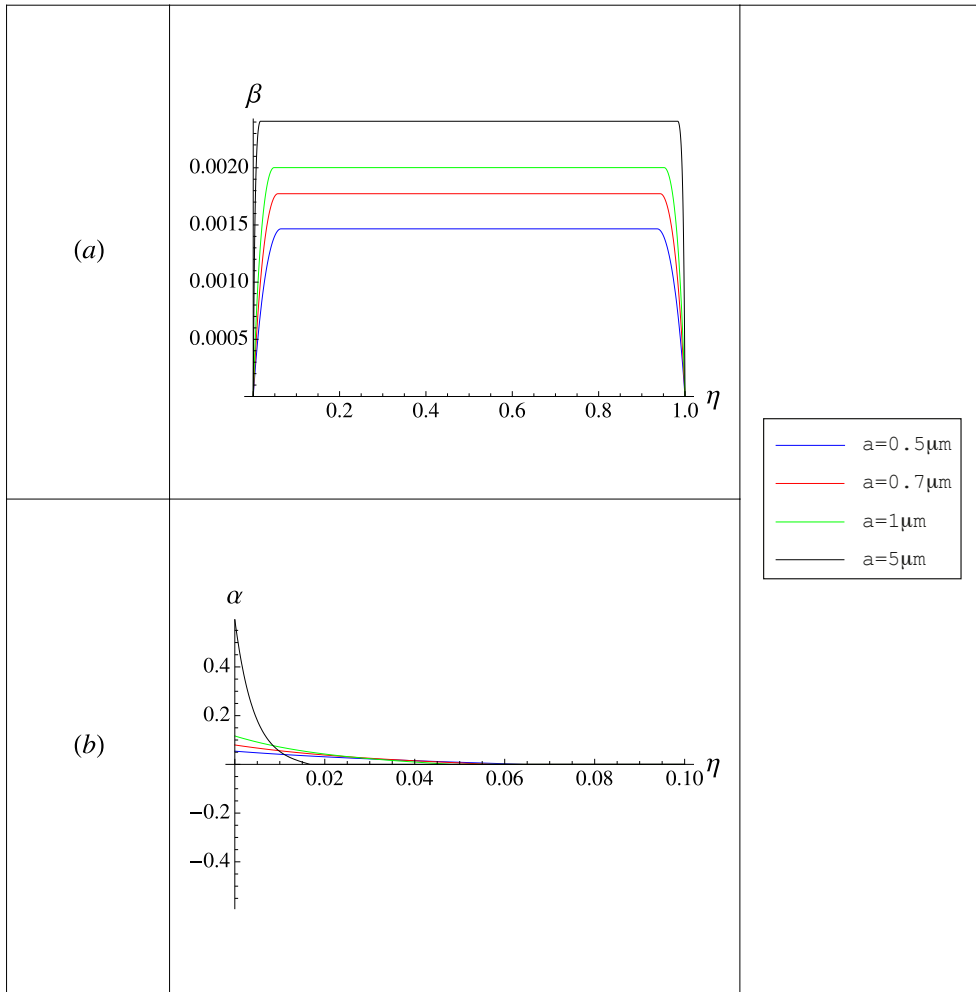


Figure 3.5: Plot of (a):  $\beta$  within the interval  $(0, 1)$  and (b):  $\alpha$  within the interval  $(0, 0.1)$  for zero dissipation anti-plane constrained shear of single crystal at  $\gamma = 0.0025$  with different crystal widths  $a$

stress of dislocation. As a consequence, we can say that the smaller crystal is harder than the bigger one.

### 3.4 Anti-plane constrained shear at non-zero dissipation

The resistance to the dislocation motion is responsible for energy dissipation during the motion of dislocations. If the resistance cannot be ignored, then the energy minimization must be replaced by the variational equation, introduced by Sedov [1968], i.e.

$$\delta\Psi + hL \int_0^a \frac{\partial D}{\partial \dot{\beta}} \delta\beta \, dx = 0, \quad (3.50)$$

where  $\Psi$  being the total energy functional from (3.14) and  $D$  being the dissipation potential. The simplest form of this dissipation potential can be taken as

$$D = K|\dot{\beta}|, \quad (3.51)$$

with  $K$  being positive constants called critical resolved shear stress of the corresponding slip system, and the dot above a function denoting its time derivative.

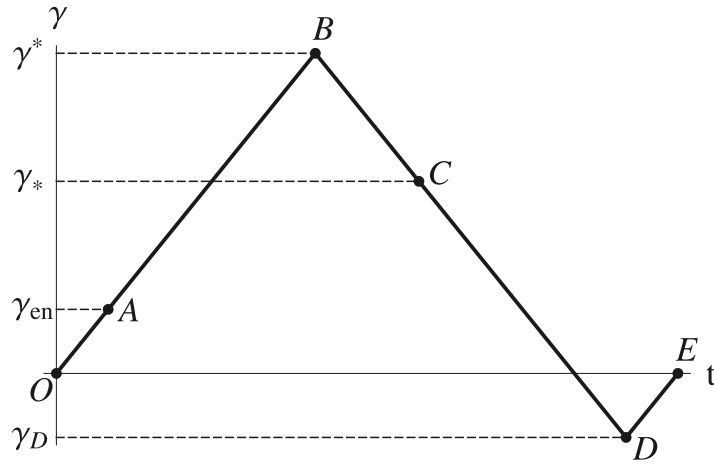


Figure 3.6: A closed loading path for anti-plane constrained shear with non-zero dissipation problem

The second term of (3.50) is the virtual work done by the resistance force acting on dislocation. Since  $\beta$  is always positive for anti-plane constrained case,  $\text{sign}\dot{\beta}$  is always constant during the loading process. Consequently we could find the solution of (3.50) by finding the global minimum of the "effective energy"

$$\delta\hat{\Psi} = 0, \quad (3.52)$$

where  $\hat{\Psi}$  takes the form

$$\hat{\Psi} = \Psi + hL \int_0^a K (\text{sign}\dot{\beta}) \beta dx. \quad (3.53)$$

In the case of  $\dot{\beta} = 0$ , the equation (3.52) does not have to be solved. It is replaced by equation  $\dot{\beta} = 0$ .

For this case, we follow the closed loading path depicted in Fig. 3.6. We want to find the evolution  $\beta(t, \eta)$  by regarding  $\gamma$  as the driving variable. The rate of change of  $\gamma(t)$  will not influence the results due to the rate independence of dissipation assumption. Applying (3.14) and (3.51) to (3.53), the effective energy takes the form

$$\hat{\Psi}(\beta) = hL \int_0^a \left[ \frac{1}{2} \mu (\gamma - \beta)^2 + \mu k \ln \frac{1}{1 - \frac{|\beta_x|}{b\rho_s}} + K\beta \right] dx. \quad (3.54)$$

For convenient, we introduce also here the dimensionless quantities

$$\hat{E} = \frac{\hat{\Psi}}{\mu a L h}, \quad \eta = \frac{x}{a}, \quad \bar{\beta}(\eta) = \beta(x), \quad c = hb\rho_s, \quad \gamma_{cr} = \frac{K}{\mu}, \quad (3.55)$$

so that  $d\eta = dx/a$  and  $\beta_{,x}(x) = \bar{\beta}'(\eta)/a$  with changes on interval  $\eta \in (0, 1)$  and the prime implies differentiation with respect to  $\eta$ .

There is no plastic distortion,  $\beta = 0$ , at point O for closed loading path shown in Fig. 3.6. As we increase  $\gamma$  further from O to A, the plastic distortion is frozen,  $\dot{\beta} = 0$ , so that  $\beta$  remains zero and the crystal undergoes elastic deformation.

For loading case AB (increasing  $\gamma$  from  $\gamma_{en}$  to  $\gamma^*$ ), we have the constantly increasing  $\beta$ . Therefore  $\text{sign}\dot{\beta} = 1$  all through the loading path AB. Assigning (3.55) (ignoring the bar over  $\beta$  for short) and (3.18) to (3.54), the effective energy for loading case is presented by

$$\hat{E}(\beta) = \int_0^1 \left[ \frac{1}{2}(\gamma - \beta)^2 + \frac{k|\beta'|}{c} + \frac{k(\beta')^2}{2c^2} + \gamma_{cr}\beta \right] d\eta. \quad (3.56)$$

With slight modification, Eq. (3.56) can be written in the form

$$\hat{E}(\beta) = \int_0^1 \left[ \frac{1}{2}(\gamma_l - \beta)^2 + \frac{1}{2}(\gamma^2 - \gamma_l^2) + \frac{k|\beta'|}{c} + \frac{k(\beta')^2}{2c^2} \right] d\eta, \quad (3.57)$$

with

$$\gamma_l = \gamma - \gamma_{cr}. \quad (3.58)$$

Since  $\frac{1}{2}(\gamma^2 - \gamma_l^2)$  will not give any contribution to the effective energy minimization, this term can be ignored so that (3.57) reduces to

$$\hat{E}(\beta) = \int_0^1 \left[ \frac{1}{2}(\gamma_l - \beta)^2 + \frac{k|\beta'|}{c} + \frac{k(\beta')^2}{2c^2} \right] d\eta. \quad (3.59)$$

Notice that the effective energy functional (3.59) has the comparable form as the energy functional (3.19). As a consequence we obtain the similar solutions of  $\beta$  and  $\alpha$  as in zero dissipation case, but now with  $\gamma_l$  instead of  $\gamma$ . The equation of  $\gamma$  as a function of  $l$  takes the form

$$\gamma(l) = \gamma_{cr} + \frac{2k \cosh \zeta l}{c(1 - 2l)}. \quad (3.60)$$

To find the energetic threshold value (point A), we need to apply  $l = 0$  to (3.60) and obtain

$$\gamma_{en} = \gamma(0) = \gamma_{cr} + \frac{2k}{c}. \quad (3.61)$$

For numerical computation we assign  $\gamma_{cr} = 0.0008$  in addition to the same material properties as in non-zero dissipation case. The evolution of plastic distortion,  $\beta$ , and plastic distortion,  $\alpha$ , for increasing  $\gamma$  at  $a = 1 \mu\text{m}$  all along loading path AB is illustrated in Fig. 3.7.

By decreasing  $\gamma$ , we load the crystal in the opposite direction after arriving at point B ( $\gamma = \gamma^*$ ). The plastic distortion,  $\beta = \beta = \beta^*(\eta)$ , is frozen all along loading path BC. Function  $\beta^*(\eta)$  is the solution of  $\beta(\eta)$  at  $\gamma = \gamma^*$ . In order to assure the continuity of  $\beta$  at point C,  $\gamma_l$  at point B must be equal to  $\gamma_u$  at point C which gives

$$\gamma_* = \gamma^* - \gamma_{cr}. \quad (3.62)$$

Starting from point C ( $\gamma = \gamma_*$ ),  $\beta$  decreases further up to zero at point D ( $\gamma = \gamma_D$ ). Therefore we have the case of constantly decreasing  $\beta$  throughout this inverse loading path CD so

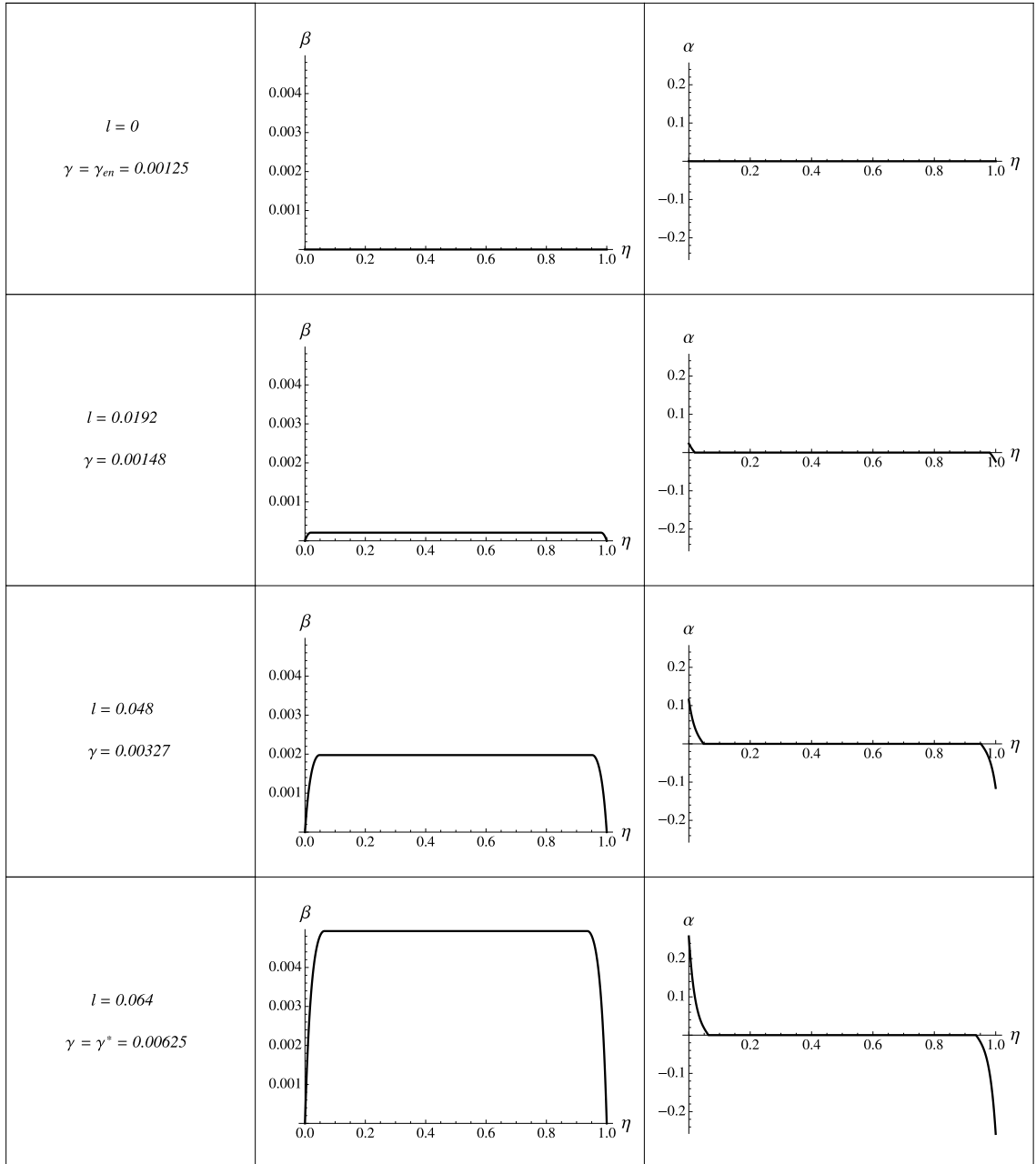


Figure 3.7: Evolution of  $\beta$  and  $\alpha$  during loading process AB for anti-plane constrained shear of single crystal with dissipation where  $a = 1\mu\text{m}$

that  $\text{sign}\dot{\beta} = -1$ . The effective energy functional for inverse loading case CD is presented by

$$\hat{E}(\beta) = \int_0^1 \left[ \frac{1}{2}(\gamma_u - \beta)^2 + \frac{k|\beta'|}{c} + \frac{k(\beta')^2}{2c^2} \right] d\eta, \quad (3.63)$$

where

$$\gamma_u = \gamma + \gamma_{cr}. \quad (3.64)$$

The solutions of  $\beta$  and  $\alpha$  for inverse loading path CD have the similar form as in loading path AB but now with  $\gamma_u$  replacing  $\gamma_u$ . The equation of  $\gamma$  as a function of  $l$  for loading path

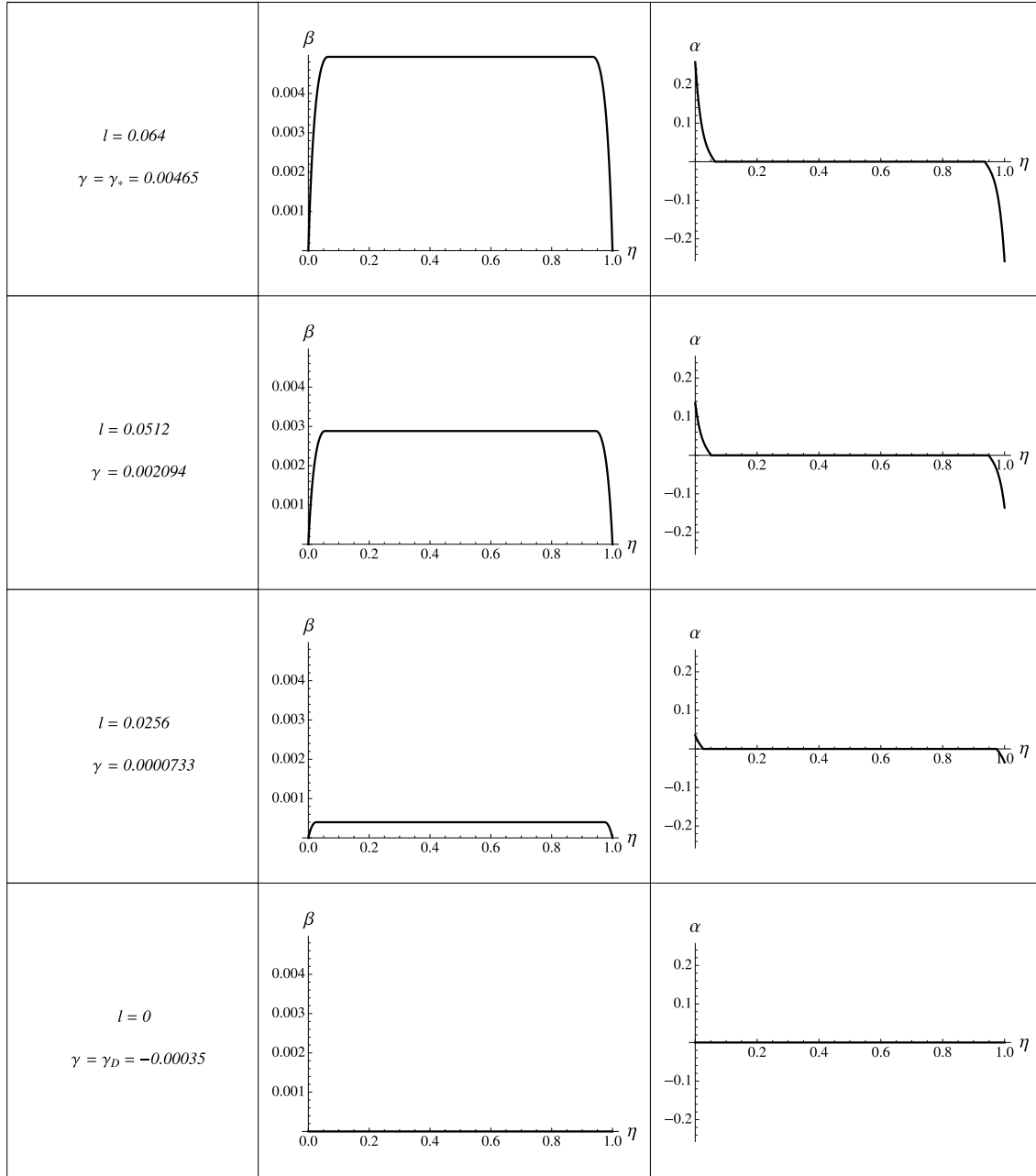


Figure 3.8: Evolution of  $\beta$  and  $\alpha$  during inverse loading DE for anti-plane constrained shear of single crystal with dissipation where  $a = 1\mu\text{m}$

CD takes the form

$$\gamma(l) = -\gamma_{cr} + \frac{2k \cosh \zeta l}{c(1 - 2l)}. \quad (3.65)$$

To obtain point D,  $l = 0$  is assigned to (3.65) to give

$$\gamma_D = \gamma(0) = -\gamma_{cr} + \frac{2k}{c}. \quad (3.66)$$

Fig. 3.8 illustrate the evolution of plastic distortion,  $\beta$ , and plastic distortion,  $\alpha$ , at  $a = 1$  for decreasing  $\gamma$  throughout inverse loading path DE.

Finally, the crystal is loaded by increasing  $\gamma$  from  $\gamma_D$  to zero all along loading path DE. During loading path DE,  $\beta$  remains zero and the crystal deforms elastically.

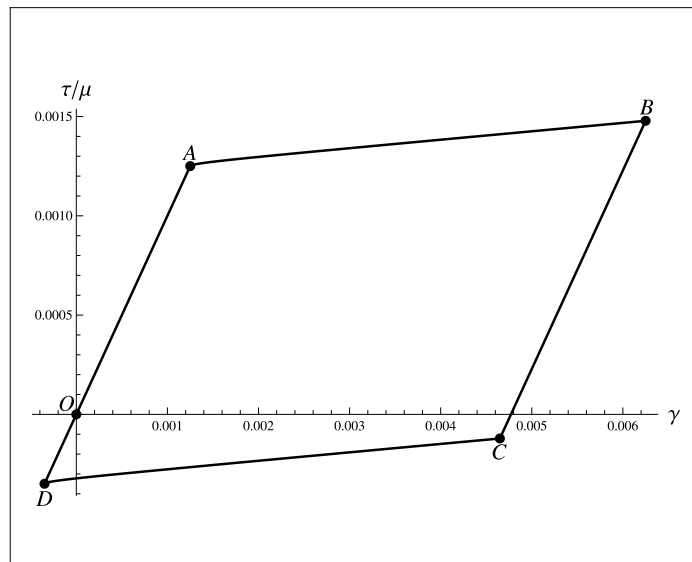


Figure 3.9: Normalized shear stress versus shear strain curve of anti-plane constrained shear at non-zero dissipation of single crystal for  $a = 1 \mu\text{m}$

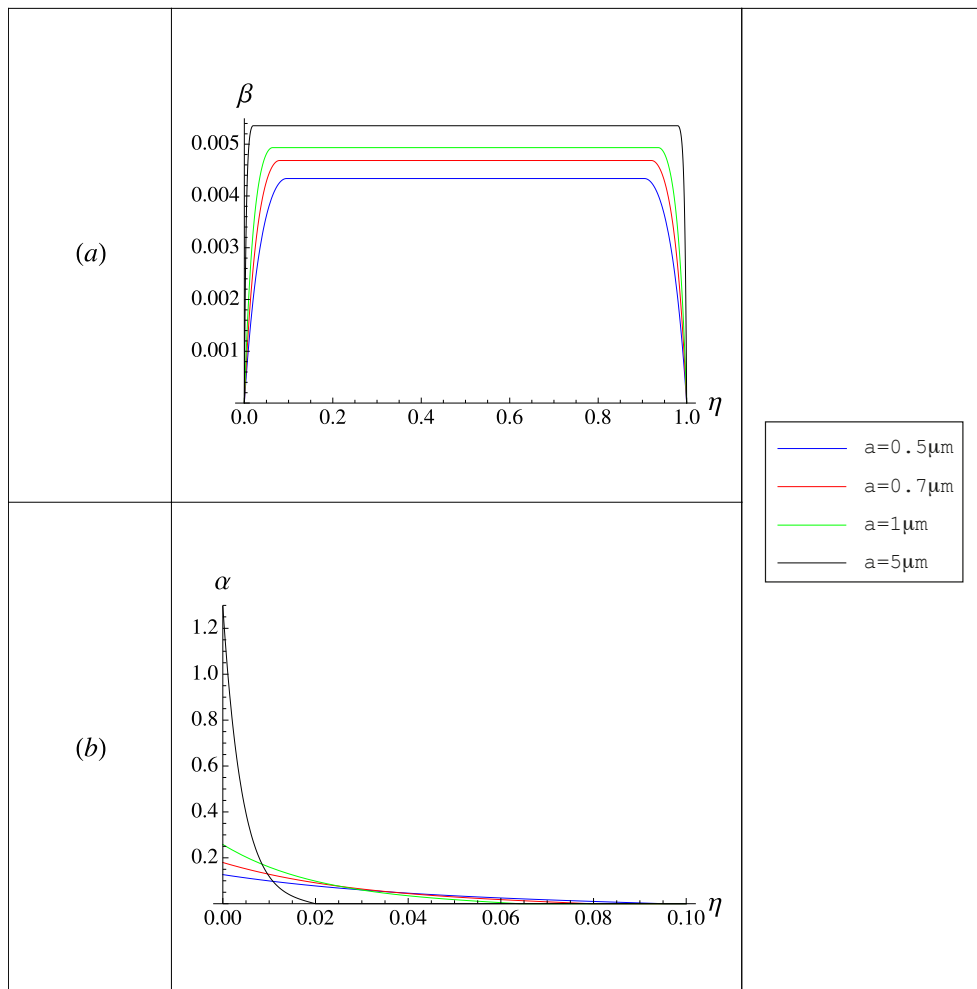


Figure 3.10: Plot of (a):  $\beta$  and (b):  $\alpha$  within the interval  $(0, 1)$  for non-zero dissipation anti-plane constrained shear of single crystal at  $\gamma = 0.00625$  with different crystal widths  $a$

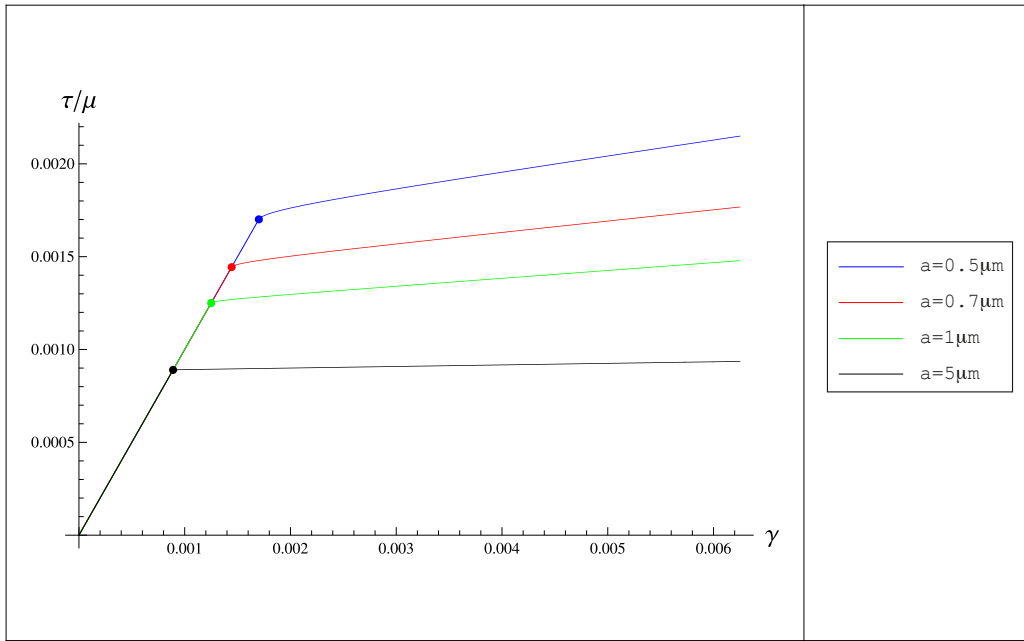


Figure 3.11: Normalized shear stress versus shear strain curves for non-zero dissipation anti-plane constrained shear of single crystal with different crystal widths,  $a$ , throughout the loading process OAB

As soon as the plastic deformation develops, the shear stress  $\tau$  becomes inhomogeneous. It is interesting also here to calculate the average shear stress which is a measurable quantity. The plot of the normalized average shear stress, which has the same form as in (3.49), following the loading path depicted in Fig. 3.6 is illustrated in Fig. 3.9.

The straight line OA corresponds to the purely elastic loading and line AB corresponds to the plastic deformation where the yield begins at point A with  $\gamma = \gamma_{en}$ . The work hardening due to the dislocation pile-ups can be observed at line AB. During the inverse loading as  $\gamma$  decreases from  $\gamma^*$  to  $\gamma_*$  (line BC) the plastic distortion,  $\beta = \beta^*$  is frozen. The plastic distortion starts to decrease at point C and decreases further as we decrease  $\gamma$  from point C to point D. The nucleated dislocations are completely disappear at point D so that  $\beta = 0$ . Finally, as  $\gamma$  increases from  $\gamma_D$  to zero, the crystal behaves elastically with  $\beta = 0$ .

In this close cycle OABCDO, dissipation takes place only on lines AB and CD. It is interesting that lines DA and BC are parallel and have the same length. In phenomenological plasticity theory this property is modeled as the translational shift of the yield surface in the stress space, the so-called Bauschinger effect.

The plots of plastic distortions and dislocation densities (Fig. 3.10) and normalized average shear stress versus shear strain (Fig. 3.11) explains the size effect in this case with the same reason as in section 3.3.2.

## 4 Plane-constrained shear of single crystals with one active slip system

The aim of this chapter is to solve the boundary value problem for single crystals with one active slip system subjected to plane-strain shear deformation. For this particular case of plane-constrained shear we can derive neat analytical solutions, following Le and Sembring [2008a].

### 4.1 Boundary value problem

We consider the strip made up of a single crystal having a rectangular cross-section of width  $a$  and height  $h$ ,  $0 \leq x \leq a$ ,  $0 \leq y \leq h$  and undergoing a plane-constrained shear deformation (see Fig. (4.1)). The single crystal is placed in a hard device, which models the grain boundary, with prescribed displacements at its upper and lower sides as

$$u(0) = 0, \quad v(0) = 0, \quad u(h) = \gamma h, \quad v(h) = 0, \quad (4.1)$$

where  $u(y)$  and  $v(y)$  are the longitudinal and transverse displacements, respectively, with  $\gamma$  being the overall shear strain. We assume that the length of the strip  $L$  is very large, and the width  $a$  is much greater than the height  $h$  ( $L \gg a \gg h$ ) to neglect the end effects and to have the stresses and strains depending only on one variable  $y$  in the central part of the strip.

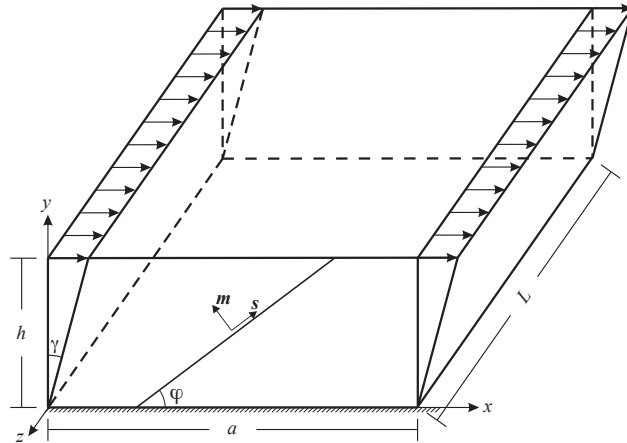


Figure 4.1: Plane-strain constrained shear of single crystal deforming in single-slip

For the plane strain state, the normal strain  $\varepsilon_{zz}$  and the shear strain  $\varepsilon_{xz}$  and  $\varepsilon_{yz}$  are constrained by nearby material and are small compared to the cross-sectional strains. The in-plane components of the strain tensor,  $\varepsilon_{ij} = \frac{1}{2}(u_{i,j} + u_{j,i})$ , are given by

$$\varepsilon_{xx} = 0, \quad \varepsilon_{xy} = \varepsilon_{yx} = \frac{1}{2}u_{,y}, \quad \varepsilon_{yy} = v_{,y}, \quad (4.2)$$

where the comma in indices denotes the derivative with respect to the corresponding coordinate system. If the overall shear strain  $\gamma$  is sufficiently small, then the crystal deforms elastically and  $u = \gamma y$  everywhere in the strip. If  $\gamma$  exceeds some critical threshold the edge dislocations may appear. We admit the slip direction (or the direction of the Burgers vectors) perpendicular to the  $z$ -axis and inclined at an angle  $\varphi$  ( $0 \leq \varphi \leq \pi/2$ ) with the  $x$ -axis and the dislocation lines parallel to the  $z$ -axis. Our goal is to determine the distribution of dislocations as function of  $\gamma$  within the framework of continuum theory of dislocations.

Since only one slip system is active, the plastic distortion is given by  $\beta_{ij} = \beta s_i m_j$ , where  $s_i = (\cos \varphi, \sin \varphi, 0)^T$  being the slip direction, and  $m_j = (-\sin \varphi, \cos \varphi, 0)^T$  being the normal vector to the slip plane. Therefore the plastic distortion is

$$\beta_{ij} = \begin{pmatrix} -\beta \sin \varphi \cos \varphi & \beta \cos^2 \varphi & 0 \\ -\beta \sin^2 \varphi & \beta \sin \varphi \cos \varphi & 0 \\ 0 & 0 & 1 \end{pmatrix}. \quad (4.3)$$

We assume that  $\beta$  depends on  $y$  only:  $\beta = \beta(y)$  (a translational invariance). Because of the prescribed boundary conditions (4.1), dislocations cannot penetrate the boundaries  $y = 0$  and  $y = h$ , hence

$$\beta(0) = \beta(h) = 0. \quad (4.4)$$

Thus, in this model the boundaries  $y = 0$  and  $y = h$  serve as the obstacles to dislocation motion. Note that the grain boundary remains an obstacle to dislocation motion only up to certain level. Moreover, this assumption is a simplification of the physical reality as effects such as dislocation emission in grain boundaries, grain boundary sliding or grain boundary diffusion are not taken into account.

It follows from (4.3) that the non-zero components of the plastic strain tensor  $\varepsilon_{ij}^p = \frac{1}{2}(\beta_{ij} + \beta_{ji})$  are

$$\varepsilon_{xx}^p = -\frac{1}{2}\beta \sin 2\varphi, \quad \varepsilon_{xy}^p = \varepsilon_{yx}^p = \frac{1}{2}\beta \cos 2\varphi, \quad \varepsilon_{yy}^p = \frac{1}{2}\beta \sin 2\varphi. \quad (4.5)$$

With (4.2) and (4.5), the non-zero components of the elastic strain tensor,  $\varepsilon_{ij}^e = \varepsilon_{ij} - \varepsilon_{ij}^p$ , read

$$\varepsilon_{xx}^e = \frac{1}{2}\beta \sin 2\varphi, \quad \varepsilon_{xy}^e = \varepsilon_{yx}^e = \frac{1}{2}(u_{,y} - \beta \cos 2\varphi), \quad \varepsilon_{yy}^e = v_{,y} - \frac{1}{2}\beta \sin 2\varphi. \quad (4.6)$$

With (4.3) and due to the fact that  $\beta$  depends only on  $y$ , there are two non-zero components of dislocation density tensor [Bilby, 1955, Kröner, 1955, Nye, 1953]

$$\alpha_{xz} = \beta_{,y} \sin \varphi \cos \varphi, \quad \alpha_{yz} = \beta_{,y} \sin^2 \varphi.$$

These are the components of the resultant Burgers' vector of all edge dislocations whose dislocation lines cut the area perpendicular to the  $z$ -axis. Thus, the scalar dislocation density (or the number of dislocations per unit area) equals

$$\rho = \frac{1}{b} \sqrt{\alpha_{ij} \alpha_{ij}} = \frac{1}{b} |\beta_{,y}| |\sin \varphi|, \quad (4.7)$$

where  $b$  is the magnitude of the Burgers' vector.

By applying (4.7) to (3.12), the energy density of the dislocation network for single crystals with one active slip system becomes

$$\Phi_m = \mu k \ln \frac{1}{1 - \frac{|\beta_{,y}| |\sin \varphi|}{b\rho_s}}, \quad (4.8)$$

with  $\rho_s$  being the saturated dislocation density, then substituting to the energy density per unit volume (3.11), the total energy yields

$$\begin{aligned} \Psi &= aL \int_0^h \Phi(\varepsilon_{ij}^e, \alpha_{ij}) dy \\ &= aL \int_0^h \left[ \frac{1}{2} \lambda (\varepsilon_{ii}^e)^2 + \mu \varepsilon_{ij}^e \varepsilon_{ij}^e + \mu k \ln \frac{1}{1 - \frac{|\beta_{,y}| |\sin \varphi|}{b\rho_s}} \right] dy. \end{aligned} \quad (4.9)$$

With (4.6) and (4.9), the total energy functional become a functional depending on  $u$ ,  $v$  and  $\beta$ , namely

$$\begin{aligned} \Psi(u, v, \beta) &= aL \int_0^h \left[ \frac{1}{2} \lambda v_{,y}^2 + \frac{1}{2} \mu (u_{,y} - \beta \cos 2\varphi)^2 + \frac{1}{4} \mu \beta^2 \sin^2 2\varphi \right. \\ &\quad \left. + \mu (v_{,y} - \frac{1}{2} \beta \sin 2\varphi)^2 + \mu k \ln \frac{1}{1 - \frac{|\beta_{,y}| |\sin \varphi|}{b\rho_s}} \right] dy. \end{aligned} \quad (4.10)$$

The energy functional (4.10) can be reduced to a functional depending on  $\beta(y)$  only, by first fixing  $\beta(y)$  and then taking the variation of (4.10) with respect to  $u$  and  $v$ . The first variation can be written in the form

$$\delta\Psi = aL \int_0^h \mu \left[ \left( \frac{1}{\kappa} v_{,y} - \beta \sin 2\varphi \right) \delta v_{,y} + (u_{,y} - \beta \cos 2\varphi) \delta u_{,y} \right] dy, \quad (4.11)$$

where

$$\kappa = \frac{\mu}{\lambda + 2\mu}. \quad (4.12)$$

Integrating (4.11) by part and applying boundary conditions (4.1) and (4.4), equation (4.11) can be reduced further to obtain

$$\delta\Psi = -aL \int_0^h \mu \left[ \left( \frac{1}{\kappa} v_{,yy} - \beta_{,y} \sin 2\varphi \right) \delta v + (u_{,yy} - \beta_{,y} \cos 2\varphi) \delta u \right] dy. \quad (4.13)$$

In order to minimize the energy functional, we have to set  $\delta\Psi = 0$ . Because  $\delta u$  and  $\delta v$  are arbitrary, from (4.13) we derive the equilibrium equations

$$\begin{aligned} \mu (u_{,yy} - \beta_{,y} \cos 2\varphi) &= 0, \\ \mu \left( \frac{1}{\kappa} v_{,yy} - \beta_{,y} \sin 2\varphi \right) &= 0. \end{aligned} \quad (4.14)$$

We first integrate (4.14)<sub>1</sub> to obtain

$$u_{,y} - \beta \cos 2\varphi = C_1. \quad (4.15)$$

Then by integrating (4.15) further and using boundary conditions (4.1) we get

$$C_1 = \gamma - \frac{1}{h} \int_0^h [\beta \cos 2\varphi] dy. \quad (4.16)$$

It is convenient to introduce the average of  $\beta$  according to

$$\langle \beta \rangle = \frac{1}{h} \int_0^h \beta dy. \quad (4.17)$$

Thus, with (4.15), (4.16) and (4.17) we obtain

$$u_{,y} = \gamma + (\beta - \langle \beta \rangle) \cos 2\varphi. \quad (4.18)$$

Applying the similar procedure as (4.15) - (4.17) to (4.14)<sub>2</sub> we derive

$$v_{,y} = \kappa(\beta - \langle \beta \rangle) \sin 2\varphi. \quad (4.19)$$

Substituting (4.12), (4.18) and (4.19) into (4.10) and collecting the common terms, the energy functional in terms of  $\beta$  takes the form

$$\begin{aligned} \Psi(\beta) = aL \int_0^h \mu \left[ \frac{1}{2} \kappa \langle \beta \rangle^2 \sin^2 2\varphi + \frac{1}{2} (\langle \beta \rangle \cos 2\varphi - \gamma)^2 + \frac{1}{2} (1 - \kappa) \beta^2 \sin^2 2\varphi \right. \\ \left. + k \ln \frac{1}{1 - \frac{|\beta_{,y}| |\sin \varphi|}{b\rho_s}} \right] dy. \end{aligned} \quad (4.20)$$

For small up to moderate dislocation densities the logarithmic terms in (4.20) may be approximated by retaining only the first two terms of a Taylor expansion, namely

$$\ln \frac{1}{1 - \frac{|\beta_{,y}| |\sin \varphi|}{b\rho_s}} \cong \frac{|\beta_{,y}| |\sin \varphi|}{b\rho_s} + \frac{1}{2} \frac{\beta_{,y}^2 \sin^2 \varphi}{(b\rho_s)^2}. \quad (4.21)$$

Consequently the energy functional (4.20) is transformed into

$$\begin{aligned} \Psi(\beta) = aL \int_0^h \mu \left[ \frac{1}{2} \kappa \langle \beta \rangle^2 \sin^2 2\varphi + \frac{1}{2} (\langle \beta \rangle \cos 2\varphi - \gamma)^2 + \frac{1}{2} (1 - \kappa) \beta^2 \sin^2 2\varphi \right. \\ \left. + k \left( \frac{|\beta_{,y}| |\sin \varphi|}{b\rho_s} + \frac{1}{2} \frac{\beta_{,y}^2 \sin^2 \varphi}{(b\rho_s)^2} \right) \right] dy. \end{aligned} \quad (4.22)$$

We shall deal further with this functional only.

If the dissipation of energy is negligible, the plastic distortion  $\beta$  minimizes (4.22) under constraints (4.4). The overall shear strain  $\gamma$  is regarded as given function of time (control parameter), so the evolution of dislocations network which accompanies the change of  $\gamma$  can be studied.

If the resistance to the dislocations motion and consequently the dissipation cannot be omitted, the energy minimization must be replaced by the variational equation, reported in Sedov [1968], i.e.

$$\delta\Psi + aL \int_0^h \frac{\partial D}{\partial \dot{\beta}} \delta\beta dy = 0, \quad (4.23)$$

with  $\Psi$  being the total energy functional from (4.22) and  $D$  being the dissipation potential in the form

$$D = K|\dot{\beta}|, \quad (4.24)$$

where  $K$  being positive constants and the dot above a function expressing the derivation with respect to time.

The resistance force acting on dislocation causes the virtual work as shown in second term of (4.23). Assuming that the  $\text{sign}\dot{\beta}$  does not change during the loading, the global minimum of the "effective energy" is applied to obtain the solution of (4.23), namely

$$\delta\hat{\Psi} = 0, \quad (4.25)$$

where  $\hat{\Psi}$  takes the form

$$\hat{\Psi} = \Psi + aL \int_0^h K (\text{sign}\dot{\beta}) \beta \, dy. \quad (4.26)$$

For  $\dot{\beta} = 0$ , the equation (4.25) needs not to be satisfied. They are simply replaced by the equation  $\dot{\beta} = 0$ .

## 4.2 Single slip plane-constrained shear at zero resistance

We start by analyzing the situation when the resistance to dislocation motion can be neglected (and hence the energy dissipation is zero). In this case, the determination of  $\beta(y)$  reduces to the minimization of the total energy (4.22) among functions satisfying the boundary conditions (4.4). The variational problem has a unique solution due to the convexity of the free energy per unit volume ( $\Phi$ ) with respect to  $\beta$  and  $\beta_{,y}$ .

For conciseness it is convenient to introduce (4.22) in terms of dimensionless quantities by first multiplying both sides of (4.22) by  $1/\mu aLh$  which gives

$$\begin{aligned} \frac{\Psi(\beta)}{aL\mu h} = & \int_0^{h/h} \left[ \frac{1}{2} \kappa \langle \beta \rangle^2 \sin^2 2\varphi + \frac{1}{2} (\langle \beta \rangle \cos 2\varphi - \gamma)^2 + \frac{1}{2} (1 - \kappa) \beta^2 \sin^2 2\varphi \right. \\ & \left. + k \left( \frac{|\beta_{,y}| |\sin \varphi|}{b\rho_s} + \frac{1}{2} \frac{\beta_{,y}^2 \sin^2 \varphi}{(b\rho_s)^2} \right) \right] \frac{dy}{h}. \end{aligned}$$

Accordingly we can now propose the dimensionless quantities

$$E = \frac{\Psi}{\mu aLh}, \quad \eta = \frac{y}{h}, \quad \bar{\beta}(\eta) = \beta(y), \quad c = hb\rho_s, \quad (4.27)$$

so that  $d\eta = dy/h$  and  $\beta_{,y}(y) = \bar{\beta}'(\eta)/h$ , where the dimensionless variable  $\eta$  changes on the interval  $(0, 1)$ . Applying (4.27) to (4.22), the energy functional now can be written as

$$\begin{aligned} E(\bar{\beta}) = & \int_0^1 \left[ \frac{1}{2} \kappa \langle \bar{\beta} \rangle^2 \sin^2 2\varphi + \frac{1}{2} (\langle \bar{\beta} \rangle \cos 2\varphi - \gamma)^2 + \frac{1}{2} (1 - \kappa) \bar{\beta}^2 \sin^2 2\varphi \right. \\ & \left. + \frac{k}{c} |\bar{\beta}'| |\sin \varphi| + \frac{k}{2c^2} (\bar{\beta}')^2 \sin^2 \varphi \right] d\eta, \quad (4.28) \end{aligned}$$

with the prime denotes differentiation with respect to  $\eta$  and the averaging as follows

$$\langle \bullet \rangle = \int_0^1 \bar{\bullet} d\eta.$$

Since we shall deal further only with  $\bar{\beta}$ , we drop the bar over  $\bar{\beta}(\eta)$  for brevity.

#### 4.2.1 Energetic threshold for dislocation nucleation

As can be seen in Berdichevsky and Le [2007], for the variational problem of this type, there exists a threshold value  $\gamma_{en}$  such that when  $\gamma < \gamma_{en}$  no dislocations are nucleated and  $\beta = 0$ . Below the threshold value, the crystal reaches the global energy minimum elastically without geometrically necessary dislocations. Above the energetic threshold, the energy minimum of the deformed crystal is accommodated by means of newly nucleated dislocations. In addition, we know that as  $\gamma \rightarrow \gamma_{en}$ , the width of the boundary layer tends to zero. This gives us the idea of finding the threshold value by employing the minimizing sequence of the form

$$\beta = \begin{cases} \frac{\beta_m}{\xi} \eta, & \text{for } \eta \in (0, \xi), \\ \beta_m, & \text{for } \eta \in (\xi, 1 - \xi), \\ \frac{\beta_m}{\xi} (1 - \eta), & \text{for } \eta \in (1 - \xi, 1), \end{cases} \quad (4.29)$$

where  $\beta_m$  is an unknown constant, and  $\xi$  is a small unknown length which tends to zero as  $\gamma \rightarrow \gamma_{en}$ . Fig. 4.2 shows the visualization of the form of minimizing sequence (4.29) with exaggerated scale.

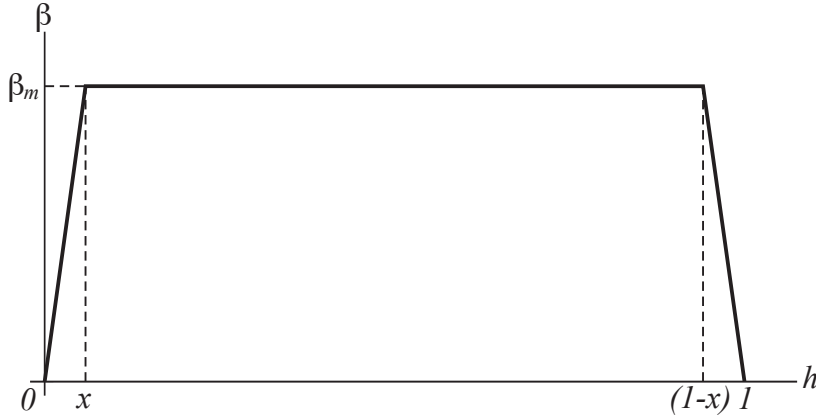


Figure 4.2: The form of minimizing sequence for finding the threshold value

Substituting the minimizing sequence (4.29) into the energy functional (4.28) (with the last term being removed) yields

$$E(\beta_m) = \int_0^\xi \left[ (1 - \kappa) \frac{\beta_m}{\xi} \eta \sin^2 2\varphi + \frac{2k |\beta_m| |\sin \varphi|}{c \xi} \right] d\eta \\ + \frac{1 - \kappa}{2} (1 - 2\xi) \beta_m^2 \sin^2 2\varphi + \frac{\kappa}{2} \langle \beta \rangle^2 \sin^2 2\varphi + \frac{1}{2} (\langle \beta \rangle \cos 2\varphi - \gamma)^2 \quad (4.30)$$

with the average of  $\beta$

$$\langle \beta \rangle = 2 \int_0^\xi \frac{\beta_m}{\xi} \eta \, d\eta + (1 - 2\xi)\beta_m. \quad (4.31)$$

Afterwards, by integrating (4.30) and (4.31) then neglecting all small terms of order  $\xi$  and higher, we obtain  $\langle \beta \rangle = \beta_m$  and

$$E(\beta_m) = \frac{1}{2}(\gamma - \beta_m \cos 2\varphi)^2 + \beta_m^2 \sin^2 2\varphi + \frac{2k}{c} |\beta_m \sin \varphi|. \quad (4.32)$$

For finding the minimum, the partial derivatives of (4.32) with respect to  $\beta_m$  must equal to zero, therefore we obtain

$$\beta_m - \gamma \cos 2\varphi + \frac{2k}{c} |\sin \varphi| \text{sign} \beta_m = 0. \quad (4.33)$$

With (4.33) and assuming that  $\text{sign} \beta_m = 1$ , we have

$$\beta_m = \gamma \cos 2\varphi - \frac{2k}{c} |\sin \varphi| > 0,$$

then

$$\cos 2\varphi < \frac{2k}{c\gamma} |\sin \varphi|. \quad (4.34)$$

Seeing that  $k$ ,  $\gamma$  and  $c$  are positive values, (4.34) is true if and only if  $0^\circ < \varphi < 45^\circ$ . Thus we obtain the energetic threshold value for this case in terms of the original length  $h$

$$\gamma_{en} = \frac{2k}{hb\rho_s} \frac{|\sin \varphi|}{\cos 2\varphi}. \quad (4.35)$$

On the other hand, assuming that  $\text{sign} \beta_m = -1$  and following the same procedure as before, we obtain the threshold value for  $45^\circ < \varphi < 90^\circ$  in original length  $h$

$$\gamma_{en} = -\frac{2k}{hb\rho_s} \frac{|\sin \varphi|}{\cos 2\varphi}. \quad (4.36)$$

It is easy to see that for  $\varphi = 0$ , we have  $\text{sign} \beta_m = 0$ . The previous analysis shows that the minimum of (4.32) is achieved at  $\beta_m \neq 0$  if and only if

$$\gamma > \gamma_{en} = \frac{2k}{hb\rho_s} \frac{|\sin \varphi|}{|\cos 2\varphi|}. \quad (4.37)$$

Note that the threshold value (4.37) is inversely proportional to the product of the size  $h$  of crystal times the saturated dislocation density (showing clearly the size effect). The deviation of equation (4.37) from the well-known Hall-Petch relation is due to the fact that the dislocation pile-up is in fact one-dimensional. The case considering 2-D problem of polycrystal undergoing plane constrained shear found in Kochmann [2009] shows that the energetic threshold value is inversely proportional to the grain size power to  $n$  where  $n = 0.639$  which is relative close to the Hall-Petch relation, i.e.  $n = 0.5$  (see Eq. 2.38).

### 4.2.2 Dislocation pile-up at zero resistance

Due to the boundary conditions (4.4),  $\beta'(\eta)$  should change its sign on the interval  $(0, 1)$ . Therefore, analogous to the anti-plane constrained case, we seek the minimizer in the form

$$\beta(\eta) = \begin{cases} \beta_1(\eta), & \text{for } \eta \in (0, l), \\ \beta_m, & \text{for } \eta \in (l, 1-l), \\ \beta_1[1-\eta], & \text{for } \eta \in (1-l, 1), \end{cases} \quad (4.38)$$

where  $\beta_m$  is a constant,  $l$  an unknown length,  $0 \leq l \leq 1/2$ , and  $\beta_1(l) = \beta_m$ . It is obvious that  $\text{sign}\beta'_1$  on the interval  $(0, l)$  also depends on the angle between slip line and  $x$ -axis,  $\varphi$ , in form

$$\text{sign}\beta'_1 = \begin{cases} 0, & \text{for } \varphi = 0^\circ, \\ +1, & \text{for } 0^\circ < \varphi < 45^\circ, \\ -1, & \text{for } 45^\circ < \varphi < 90^\circ, \end{cases} \quad (4.39)$$

and changes its sign to the opposite sign on the interval  $(1-l, 1)$ . We have to find  $\beta_1(\eta)$  and the constants,  $\beta_m$  and  $l$ .

Function  $\beta_1$  is subjected to boundary conditions

$$\beta_1(0) = 0, \quad \beta_1(l) = \beta_m. \quad (4.40)$$

With  $\beta$  from (4.38) the total energy functional (4.28) can be written as

$$E = \int_0^l \left[ (1-\kappa)\beta_1^2 \sin^2 2\varphi + \frac{2k}{c} |\beta'_1 \sin \varphi| + \frac{k}{c^2} \beta_1'^2 \sin^2 \varphi \right] d\eta \\ + \frac{1}{2} \left( \kappa \langle \beta \rangle^2 \sin^2 2\varphi + (\gamma - \langle \beta \rangle \cos 2\varphi)^2 \right) + \frac{1-\kappa}{2} \beta_m^2 \sin^2 2\varphi (1-2l), \quad (4.41)$$

where the average of the plastic distortion takes the form

$$\langle \beta \rangle = 2 \int_0^l \beta_1 d\eta + (1-2l)\beta_m. \quad (4.42)$$

We calculate now the variation of energy functional (4.41) with respect to  $\beta_1$ ,  $\beta_m$  and  $l$

$$\delta E = 2 \int_0^l \left[ (1-\kappa) \sin^2 2\varphi \beta_1 \delta \beta_1 + \left( \frac{k |\sin \varphi| \text{sign} \beta'_1}{c} + \frac{k \sin^2 \varphi \beta'_1}{c^2} \right) \delta \beta'_1 \right] d\eta \\ + \left( (1-\kappa) \sin^2 2\varphi (\beta_1(l))^2 + \frac{2k |\beta'_1(l) \sin \varphi|}{c} + \frac{k (\beta'_1(l))^2 \sin^2 \varphi}{c^2} \right) \delta l \\ + \left( \kappa \sin^2 2\varphi \langle \beta \rangle - \cos 2\varphi (\gamma - \cos 2\varphi \langle \beta \rangle) \right) \langle \delta \beta \rangle - (1-\kappa) \sin^2 2\varphi \beta_m^2 \delta l \\ + (1-2l)(1-\kappa) \sin^2 2\varphi \beta_m \delta \beta_m, \quad (4.43)$$

where the variation of (4.42) with boundary condition (4.40)<sub>2</sub> takes the form

$$\langle \delta \beta \rangle = 2 \int_0^l \delta \beta_1 d\eta + (1-2l) \delta \beta_m. \quad (4.44)$$

By first substituting (4.44) into (4.43) then integrating partially with (4.40), we can further transform (4.43) into

$$\begin{aligned} \delta E = & 2 \int_0^l \left[ -\frac{k \sin^2 \varphi \beta_1''}{c^2} + (1 - \kappa) \sin^2 2\varphi \beta_1 + (\cos^2 2\varphi + \kappa \sin^2 2\varphi) \langle \beta \rangle \right. \\ & \left. - \gamma \cos^2 2\varphi \right] \delta \beta_1 \, d\eta + \left( \frac{2k |\beta_1'(l) \sin \varphi|}{c} + \frac{k (\beta_1'(l))^2 \sin^2 \varphi}{c^2} \right) \delta l \\ & + \left( (1 - 2l) \left( (\cos^2 2\varphi + \kappa \sin^2 2\varphi) \langle \beta \rangle - \gamma \cos 2\varphi + (1 - \kappa) \sin^2 2\varphi \beta_m \right) \right. \\ & \left. + \frac{2k |\sin \varphi| \text{sign} \beta_1'}{c} + \frac{2k \sin^2 \varphi \beta_1'(l)}{c^2} \right) \delta \beta_m \end{aligned} \quad (4.45)$$

The minimum of the energy functional (4.41) is achieved if  $\delta E = 0$  for arbitrary  $\delta \beta_1$ ,  $\delta \beta_m$  and  $\delta l$ . We first choose the orientations such that  $\delta l$  and  $\delta \beta_m$  are zero, but  $\delta \beta_1$  is arbitrary inside the interval  $\eta \in (0, l)$ . In this case  $\delta E = 0$  implies

$$-\frac{k \sin^2 \varphi \beta_1''}{c^2} + (1 - \kappa) \sin^2 2\varphi \beta_1 + (\cos^2 2\varphi + \kappa \sin^2 2\varphi) \langle \beta \rangle - \gamma \cos^2 2\varphi = 0. \quad (4.46)$$

Then by choosing  $\delta \beta_m = 0$  but  $\delta l$  arbitrary we get

$$\frac{2k |\beta_1'(l) \sin \varphi|}{c} + \frac{k (\beta_1'(l))^2 \sin^2 \varphi}{c^2} = 0,$$

which gives an additional boundary condition at  $\eta = l$

$$\beta_1'(l) = 0. \quad (4.47)$$

Finally,  $\delta E$  reduces just to the term containing only  $\delta \beta_m$ . Equating it to zero for arbitrary  $\delta \beta_m$  we obtain

$$\begin{aligned} (1 - 2l) \left( -\gamma \cos 2\varphi + (\cos^2 2\varphi + \kappa \sin^2 2\varphi) \langle \beta \rangle + (1 - \kappa) \sin^2 2\varphi \beta_m \right) \\ + \frac{2k |\sin \varphi| |\text{sign} \beta_1'|}{c} = 0. \end{aligned} \quad (4.48)$$

The general solution of a differential equation (4.46) on the interval  $(0, l)$  can be written as

$$\beta_1 = \beta_{1p} + \beta_{1h} \quad (4.49)$$

where  $\beta_{1p}$  is the particular solution and  $\beta_{1h}$  is the general solution of the homogeneous equation.

The particular solution of (4.46) can be obtained by computing

$$-\frac{k \sin^2 \varphi \beta_{1p}''}{c^2} + (1 - \kappa) \sin^2 2\varphi \beta_{1p} = \gamma \cos^2 2\varphi - (\cos^2 2\varphi + \kappa \sin^2 2\varphi) \langle \beta \rangle, \quad (4.50)$$

with the solution in the form

$$\beta_{1p} = a, \quad \beta_{1p}' = 0, \quad \beta_{1p}'' = 0, \quad (4.51)$$

where  $a$  is an arbitrary constant. Substituting (4.51) into (4.50) we obtain the particular solution

$$\beta_{1p} = \frac{\gamma \cos 2\varphi - (\cos^2 2\varphi + \kappa \sin^2 2\varphi) \langle \beta \rangle}{(1 - \kappa) \sin^2 2\varphi}. \quad (4.52)$$

For finding the general solution of the homogeneous equation, we need to compute

$$-\frac{k \sin^2 \varphi}{c^2} \beta_{1h}'' + (1 - \kappa) \sin^2 2\varphi \beta_{1h} = 0. \quad (4.53)$$

The standard Ansatz

$$\beta_{1h} = e^{\zeta \eta}, \quad \beta_{1h}' = \zeta e^{\zeta \eta}, \quad \beta_{1h}'' = \zeta^2 e^{\zeta \eta}, \quad (4.54)$$

yields

$$\zeta = 2h \sqrt{\frac{1 - \kappa}{k}} |\cos \varphi|. \quad (4.55)$$

The general solution of the homogeneous equation (4.53) reads

$$\beta_{1h} = C_1 \cosh \zeta \eta + C_2 \sinh \zeta \eta, \quad (4.56)$$

where  $C_1$  and  $C_2$  are constants.

We substitute (4.52) and (4.56) into (4.49) to acquire

$$\beta_1 = \beta_{1p} + C_1 \cosh \zeta \eta + C_2 \sinh \zeta \eta. \quad (4.57)$$

With (4.57) and boundary condition (4.40)<sub>2</sub>, we obtain the constant

$$C_1 = -\beta_{1p}. \quad (4.58)$$

Substituting (4.58) into (4.57) and applying the boundary condition (4.47), we have

$$C_2 = \beta_{1p} \tanh \zeta l. \quad (4.59)$$

Then we substitute (4.58) and (4.59) into (4.57) to obtain the general solution to the differential equation (4.46)

$$\beta_1 = \beta_{1p} (1 - \cosh \zeta \eta + \tanh \zeta l \sinh \zeta \eta), \quad 0 \leq \eta \leq l, \quad (4.60)$$

where  $\beta_{1p}$  from (4.52) and  $\zeta$  from (4.55). The solution for interval  $(l, 1 - l)$  is derived by substituting boundary condition (4.40)<sub>2</sub> into (4.60), namely

$$\beta_m = \beta_{1p} \left( 1 - \frac{1}{\cosh \zeta l} \right). \quad (4.61)$$

With (4.42), (4.40)<sub>2</sub>, (4.52), and (4.60) we obtain the average of  $\beta$

$$\langle \beta \rangle = B(l) \gamma \cos 2\varphi \quad (4.62)$$

where

$$B(l) = \frac{g(l)}{(1 - \kappa) \sin^2 2\varphi + g(l) \times (\cos^2 2\varphi + \kappa \sin^2 2\varphi)}, \quad (4.63)$$

with

$$g(l) = 2 \left( l - \frac{\tanh \zeta l}{\zeta} \right) + \left( 1 - \frac{1}{\cosh \zeta l} \right) (1 - 2l).$$

Substituting (4.60) and (4.61) into the minimizer (4.38), we acquire the solutions for finding the plastic distortion  $\beta$  namely

$$\beta = \begin{cases} \beta_{1p}(1 - \cosh \zeta \eta + \tanh \zeta l \sinh \zeta \eta), & \text{for } \eta \in (0, l), \\ \beta_{1p} \left( 1 - \frac{1}{\cosh \zeta l} \right), & \text{for } \eta \in (l, 1 - l), \\ \beta_{1p}(1 - \cosh \zeta(1 - \eta) + \tanh \zeta l \sinh \zeta(1 - \eta)), & \text{for } \eta \in (1 - l, 1). \end{cases} \quad (4.64)$$

Finally, by substituting (4.61) into (4.48) then applying (4.62) gives

$$\gamma(l) = \frac{2k |\sin \varphi| \text{sign} \beta'_1 \cosh \zeta l}{c(1 - 2l) \cos 2\varphi (1 - (\cos^2 2\varphi + \kappa \sin^2 2\varphi) B(l))}, \quad (4.65)$$

with  $\text{sign} \beta'_1$  from (4.39) and  $B(l)$  from (4.63). We can observe the evolution of plastic distortion,  $\beta$ , and dislocation density,  $\alpha$  by increasing  $\gamma$ . Since  $\gamma$  increases as  $l$  grows, we can also use  $l$  as the control parameter to observe the evolution of  $\beta$  and  $\alpha$ . From (4.65) we found out that  $\gamma = \gamma_{en}$  at  $l = 0$ .

In order to investigate the dislocation pile-ups, we need to calculate the normalized dislocation density which is given by

$$\alpha(\eta) = \beta'(\eta) \sin \varphi. \quad (4.66)$$

By applying the solutions (4.64) to (4.66), we get the normalized dislocation density in the form

$$\alpha = \begin{cases} \beta_{1p} \sin \varphi (-\zeta \sinh \zeta \eta + \zeta \tanh \zeta l \cosh \zeta \eta), & \text{for } \eta \in (0, l), \\ 0, & \text{for } \eta \in (l, 1 - l), \\ \beta_{1p} \sin \varphi (-\zeta \sinh \zeta(1 - \eta) + \zeta \tanh \zeta l \cosh \zeta(1 - \eta)), & \text{for } \eta \in (1 - l, 1), \end{cases} \quad (4.67)$$

where  $\zeta$  from (4.55) and  $\beta_{1p}$  from (4.52).

For computing the results numerically, we make use the material parameters presented in Table 3.1. By increasing  $l$  (hence  $\gamma$  increases), Fig. 4.3 and Fig. 4.4 illustrate the evolution of plastic distortion  $\beta(\eta)$  and normalized dislocation density  $\alpha(\eta)$  distributions along the crystal height for  $\varphi = 30^\circ$  and  $\varphi = 60^\circ$ , respectively, where  $\eta = y/h$ . It is obvious that we can observe the dislocation-free zone at the central part of single crystal and there exists dislocation pile-ups at the crystal boundary. The graphs of  $\alpha$  from both figures have different signs that represent the different orientations of dislocations.

To calculate the shear stress,  $\tau$ , we assume the average distribution of stress throughout the crystal height. Therefore the average shear stress can be found in the form

$$\tau = \frac{1}{h} \int_0^h \sigma_{xy} dy. \quad (4.68)$$

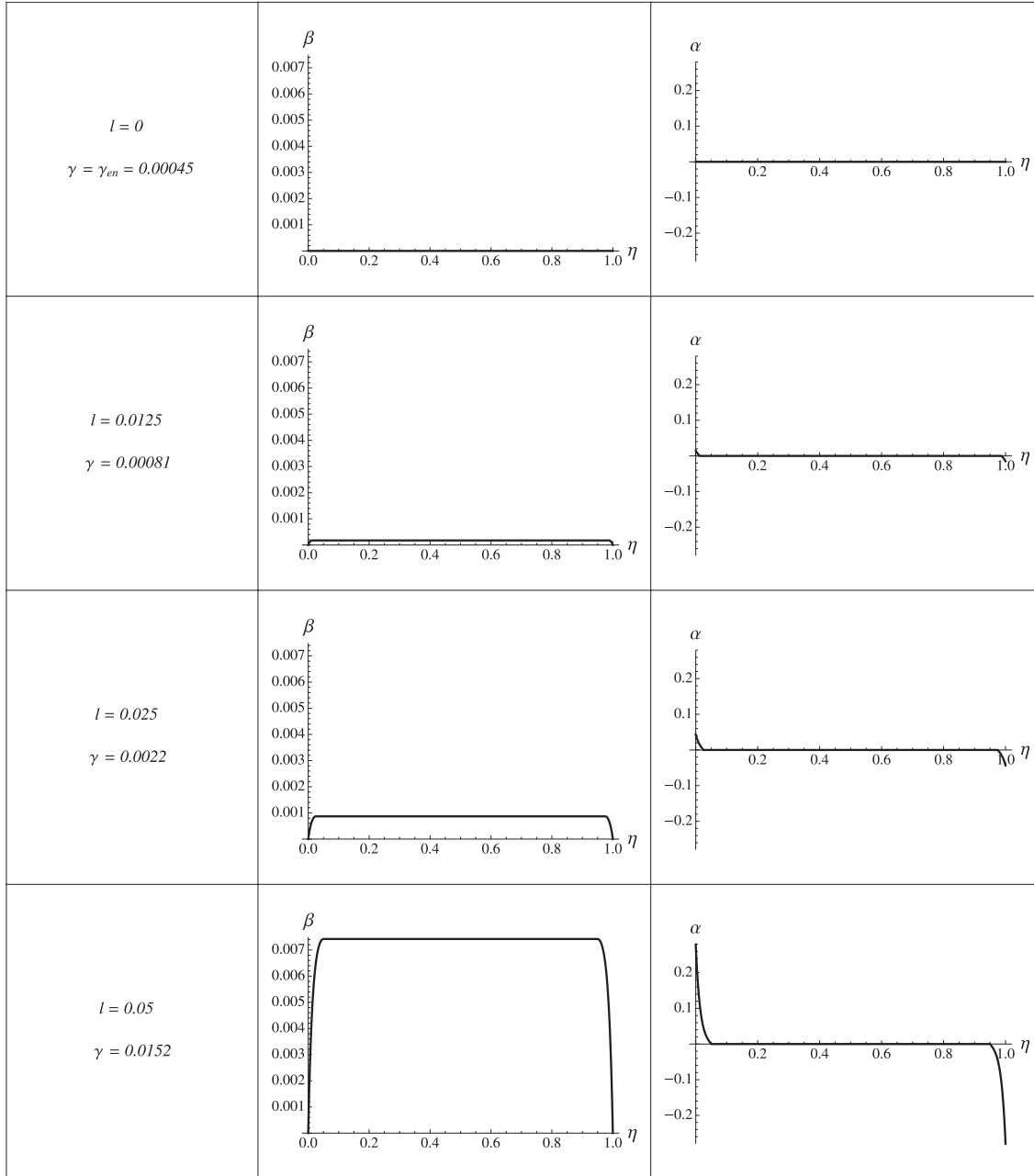


Figure 4.3: Evolution of  $\beta$  and  $\alpha$  for zero dissipation single-slip constrained shear of single crystal with  $h = 1\mu\text{m}$  and  $\varphi = 30^\circ$  where  $\eta = y/h$  for increasing  $\gamma$

As in anti-plane constrained shear case, it is also convenient to work with dimensionless form of average dislocation density by applying (4.27) to (4.68), namely

$$\tau = \int_0^1 \sigma_{xy} d\eta. \quad (4.69)$$

Assigning

$$\sigma_{xy} = 2\mu\varepsilon_{xy}^e, \quad (4.70)$$

with  $\varepsilon_{xy}^e$  from (4.6) together with the minimizer (4.38), (3.11) and (4.18) to (4.69) we obtain the normalized average shear stress as a function of the shear strain

$$\frac{\tau}{\mu} = \gamma - \langle \beta \rangle \cos 2\varphi, \quad (4.71)$$

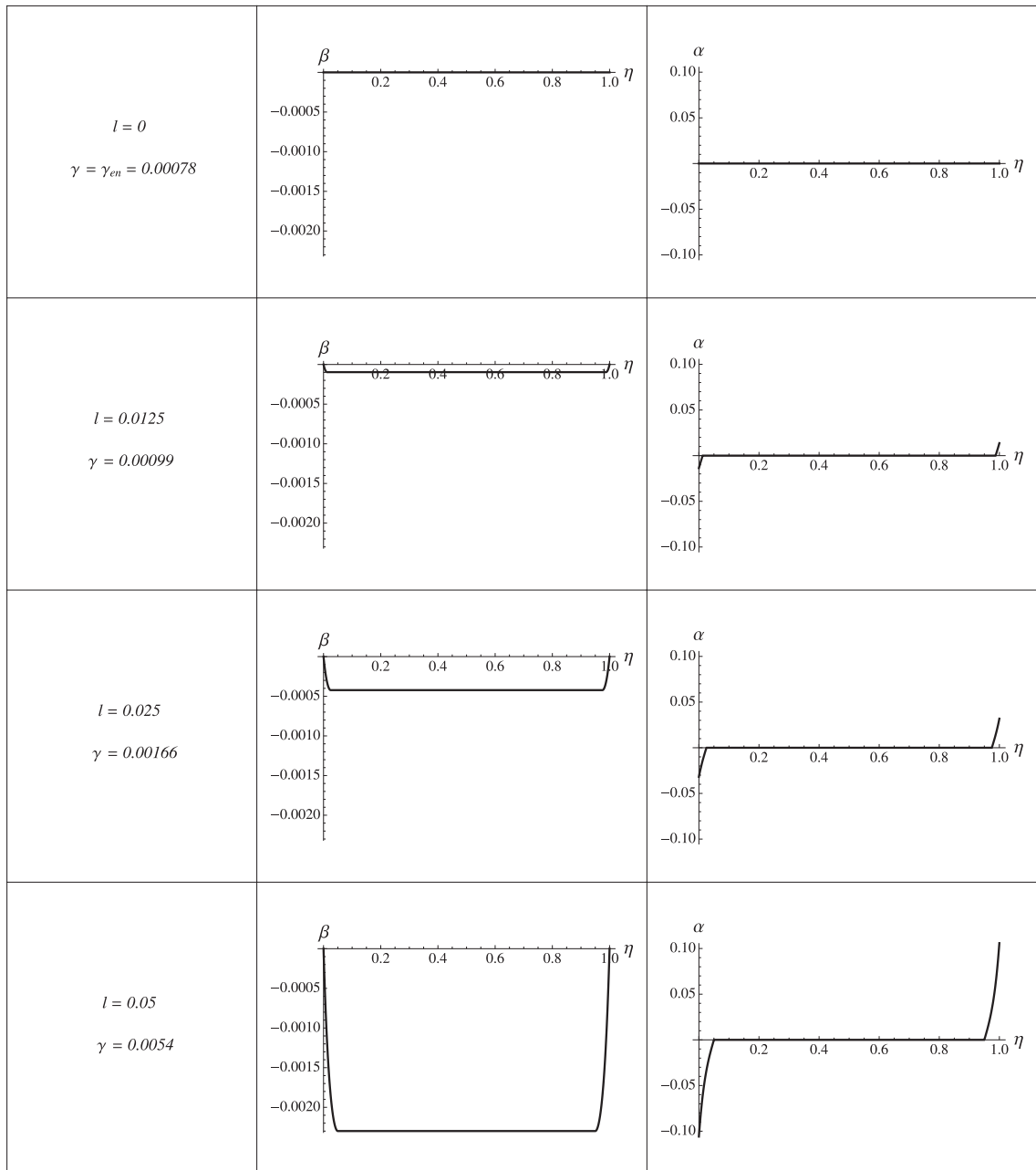


Figure 4.4: Evolution of  $\beta$  and  $\alpha$  for zero dissipation single-slip constrained shear of single crystal with  $h = 1\mu\text{m}$  and  $\varphi = 60^\circ$  where  $\eta = y/h$  for increasing  $\gamma$

with  $\langle\beta\rangle$  from (4.62).

The second term of (4.71) explains the dependency of the hardening rate to the crystal height  $h$ . When  $\gamma < \gamma_{en}$ , no dislocations are nucleated and  $\beta = 0$ . Thus the shear stress is given in the form  $\tau = \mu\gamma$ . For  $\gamma > \gamma_{en}$ , we take  $\langle\beta\rangle$  from (4.62) to compute the shear stress equation (4.71). As a consequence it is interesting to plot the normalized stress strain equation (4.71).

Fig.4.5 shows the normalized shear stress versus shear strain curve OAB for  $\varphi = 30^\circ$  and  $\varphi = 60^\circ$ . For  $\gamma > \gamma_{en}$  the lines AB show the "work hardening" sections caused by the dislocation pile-ups. Mention, however, for the reason that there is no residual strain as we unload the crystal by decreasing  $\gamma$ , the stress-strain curve follows the same paths BAO. Therefore the plastic deformation is completely reversible, and no energy dissipation occurs.

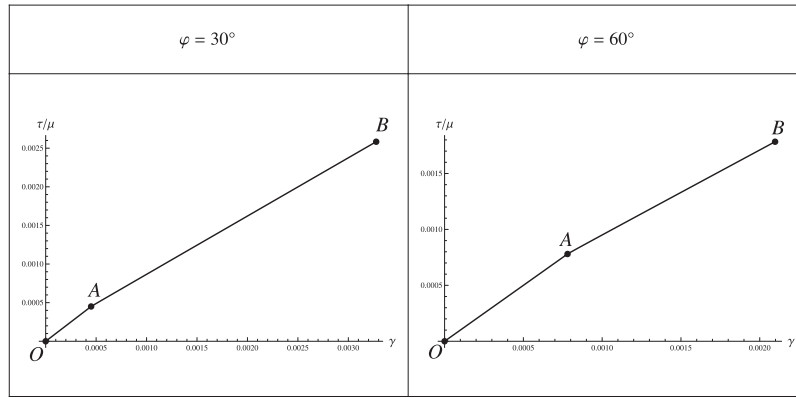


Figure 4.5: Normalized average shear stress versus shear strain curves for single-slip constrained shear of single crystal at zero dissipation with  $h = 1\mu\text{m}$

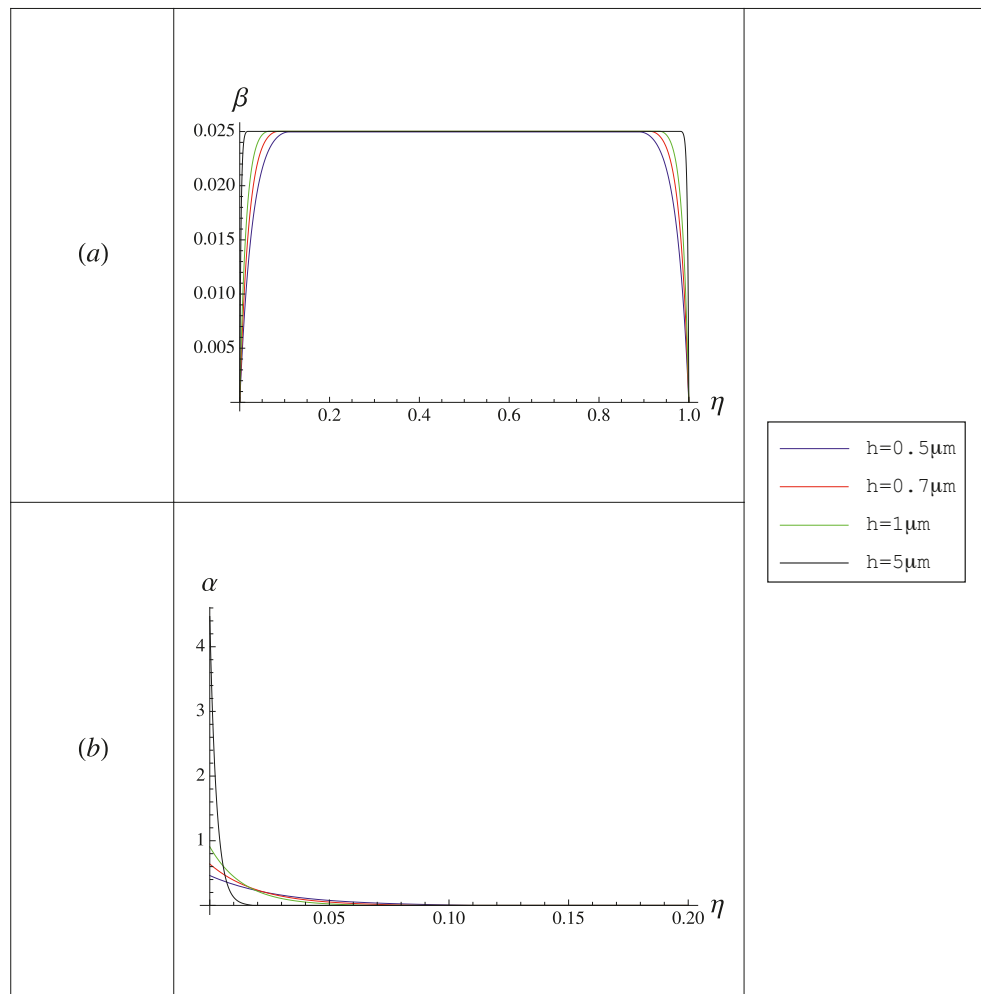


Figure 4.6: Plot of (a):  $\beta$  within the interval  $(0, 1)$  and (b):  $\alpha$  within the interval  $(0, 0.2)$  for zero dissipation single-slip constrained shear of single crystal at  $\varphi = 30^\circ$  and  $\gamma = 0.002$  with different crystal heights  $h$

In the course of unloading the nucleated dislocations start to annihilate at point B, and as we approach the point A they all disappear.

The evolution of plastic distortion  $\beta$  and normalized dislocation density  $\alpha$  at  $\varphi = 30^\circ$  with

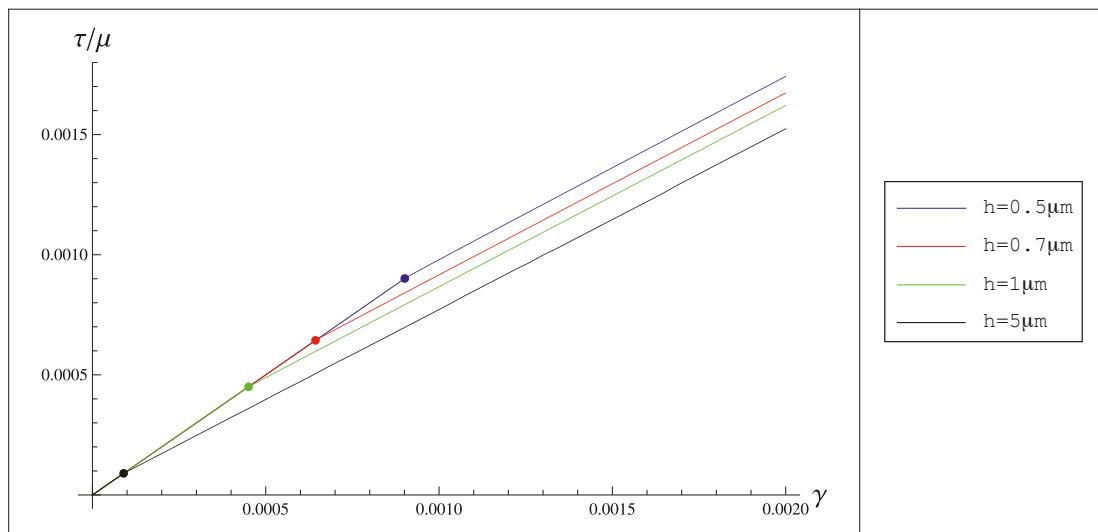


Figure 4.7: Normalized shear stress versus shear strain curves for zero dissipation single-slip constrained shear of single crystal at  $\varphi = 30^\circ$  with different crystal heights  $h$

different height  $h$  are demonstrated in Fig. 4.6. When the height of crystal becomes smaller the mean free length for dislocation pile-ups also decreases. Therefore the dislocation density should be higher at the boundaries for smaller crystal height. But, as we observe from Fig. 4.6-(b), the dislocation density near boundary is smaller for smaller crystal height. It can be explained because the local dislocation concentration is bounded for our form of energy with its saturated dislocation density, the dislocation pile-ups are forced to distribute more into the middle of the crystal for decreasing crystal height as can be observed in Fig. 4.6. As a consequence the inner back stresses of dislocation will increase with decreasing crystal height. In other words, the crystal becomes stronger as its height decreases.

Fig. 4.7 exhibits the stress strain curve for  $\varphi = 30^\circ$  and  $\gamma = 0.05$  with different height  $h$  of the crystal where the dots explain the energetic threshold value. The yield stress and the hardening rate increase as the crystal size decreases. Therefore the size effect mentioned in (4.37) and (4.71) can be understood more clearly from Fig. 4.6 and Fig. 4.7.

### 4.3 Single slip plane-constrained shear with energy dissipation

If the resistance to dislocation motion (and hence the dissipation) cannot be ignored, then the plastic distortion may evolve only in accordance with the variational equation (4.23) under the constraints (4.4).

We consider the following loading path as shown in Fig. 4.8 where the loading path OB and DE being the loading processes and BD being the inverse loading process. We regard  $\gamma$  as a given function of time (the driving variable) and try to determine  $\beta(t, \eta)$ . With the assumption of rate independence of dissipation, the results are not influenced by the rate of change of  $\gamma(t)$ . The problem is to determine the evolution of  $\beta$  as function of  $t$  and  $\eta$ , provided  $\beta(0, \eta) = 0$ . Thus, if the sign of  $\dot{\beta}$  does not change, then the variation of the

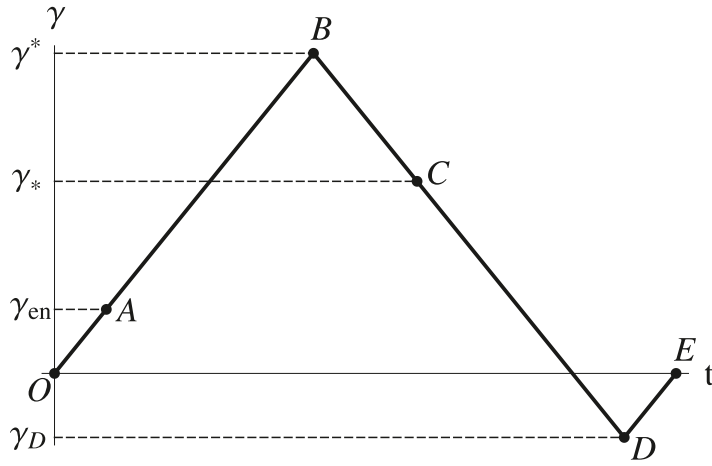


Figure 4.8: A closed loading path for single slip plane-constrained shear problem

effective energy (4.26) should vanish, i.e.

$$\delta \hat{\Psi} = \delta \left( \Psi + aL \int_0^h K(\text{sign} \dot{\beta}) \beta \, dy \right) = 0. \quad (4.72)$$

Substituting from (4.22) to the effective energy (4.26) gives

$$\begin{aligned} \hat{\Psi}(\beta) = & aL \int_0^h \mu \left[ \frac{1}{2} \kappa \langle \beta \rangle^2 \sin^2 2\varphi + \frac{1}{2} (\langle \beta \rangle \cos 2\varphi - \gamma)^2 + \frac{1}{2} (1 - \kappa) \beta^2 \sin^2 2\varphi \right. \\ & \left. + k \left( \frac{|\beta_{,y}| |\sin \varphi|}{b\rho_s} + \frac{1}{2} \frac{\beta_{,y}^2 \sin^2 \varphi}{(b\rho_s)^2} \right) \right] dy + aL \int_0^h K(\text{sign} \dot{\beta}) \beta \, dy, \end{aligned} \quad (4.73)$$

where the average plastic distortion  $\langle \beta \rangle$  from (4.17) and the dissipation potential  $D$  from (4.24).

It is again useful, as in the case with zero dissipation, to introduce the dimensionless quantities

$$\hat{E} = \frac{\hat{\Psi}}{\mu a L h}, \quad \eta = \frac{y}{h}, \quad \bar{\beta}(\eta) = \beta(y), \quad c = h b \rho_s, \quad \gamma_{cr} = \frac{K}{\mu}, \quad (4.74)$$

so that

$$d\eta = \frac{dy}{h}, \quad \beta_{,y}(y) = \frac{\bar{\beta}'(\eta)}{h}, \quad \beta_{,yy}(y) = \frac{\bar{\beta}''(\eta)}{h^2}, \quad (4.75)$$

with  $\eta$  changes on interval  $(0, 1)$  and the prime denotes differentiation with respect to  $\eta$ .

By applying (4.74), the effective energy functional (4.73) reduces to

$$\begin{aligned} \hat{E}(\bar{\beta}) = & \int_0^1 \left[ \frac{1}{2} \kappa \langle \bar{\beta} \rangle^2 \sin^2 2\varphi + \frac{1}{2} (\langle \bar{\beta} \rangle \cos 2\varphi - \gamma)^2 + \frac{1}{2} (1 - \kappa) \bar{\beta}^2 \sin^2 2\varphi \right. \\ & \left. + k \left( \frac{|\bar{\beta}'| |\sin \varphi|}{c} + \frac{1}{2} \frac{(\bar{\beta}')^2 \sin^2 \varphi}{c^2} \right) + \gamma_{cr} (\text{sign} \dot{\bar{\beta}}) \bar{\beta} \right] d\eta, \end{aligned} \quad (4.76)$$

with

$$\langle \bar{\beta} \rangle = \int_0^1 \bar{\beta} \, d\eta, \quad (4.77)$$

where the prime denotes the differentiation with respect to  $\eta$ , and, for brief, the bars over  $\bar{\beta}$  and  $\langle\bar{\beta}\rangle$  will be dropped in the future computation. Ignoring the constant terms which does not influence the effective energy minimization, we can write again (4.76) in the form

$$\hat{E}(\beta) = \int_0^1 \left[ \frac{1}{2} \kappa \langle\beta\rangle^2 \sin^2 2\varphi + \frac{1}{2} (\langle\beta\rangle \cos 2\varphi - \gamma_r)^2 + \frac{1}{2} (1 - \kappa) \beta^2 \sin^2 2\varphi + k \left( \frac{|\beta'| |\sin \varphi|}{c} + \frac{1}{2} \frac{(\beta')^2 \sin^2 \varphi}{c^2} \right) \right] d\eta, \quad (4.78)$$

where

$$\gamma_l = \gamma - \frac{\gamma_{cr} \text{sign} \dot{\beta}}{\cos 2\varphi}. \quad (4.79)$$

Mention that the energy functional (4.78) has now the same form as in (4.28) with  $\gamma_l$  replacing  $\gamma$ . As a consequence, we obtain here the same form of solutions as in section 4.2.2 by substituting  $\gamma$  with  $\gamma_l$ .

Following the same procedure as stated in (4.32 - 4.37), the energetic threshold value in term of original length is given in the form

$$\gamma_{en} = \frac{\gamma_{cr}}{\cos 2\varphi} + \frac{2k}{hb\rho_s} \frac{|\sin \varphi|}{\cos 2\varphi}, \quad (4.80)$$

for  $0^\circ < \varphi < 45^\circ$ , and

$$\gamma_{en} = - \left( \frac{\gamma_{cr}}{\cos 2\varphi} + \frac{2k}{hb\rho_s} \frac{|\sin \varphi|}{\cos 2\varphi} \right), \quad (4.81)$$

for  $45^\circ < \varphi < 90^\circ$ . As a consequence, the plastic distortion will start to appear when the condition

$$\gamma \geq \gamma_{en} = \frac{\gamma_{cr}}{|\cos 2\varphi|} + \frac{2k}{hb\rho_s} \frac{|\sin \varphi|}{|\cos 2\varphi|}, \quad (4.82)$$

is achieved. The second term in (4.82) is inversely proportional to the height  $h$ , thus equation (4.82) shows clearly the size effect. From the energetic threshold value derivation, we found out also that

$$\text{sign} \beta = \begin{cases} 0, & \text{for } \varphi = 0^\circ, \\ +1, & \text{for } 0^\circ < \varphi < 45^\circ, \\ -1, & \text{for } 45^\circ < \varphi < 90^\circ. \end{cases} \quad (4.83)$$

Therefore we have the relation

$$\text{sign} \beta' = \text{sign} \beta, \quad (4.84)$$

for  $\eta \in (0, l)$  and changes its sign for for  $\eta \in (1 - l, 1)$ .

Now we explain the loading path depicted in Fig. 4.8 in more detail. Let  $\beta$  be zero at the beginning of the deformation process. For the loading path OA (see Fig. 4.8),  $\gamma$  is first increased from zero to the energetic threshold value  $\gamma_{en}$ , where  $\gamma_{en}$  from (4.82). As long as  $\gamma < \gamma_{en}$ ,  $\beta$  is "frozen" or  $\dot{\beta} = 0$ , the dislocation density remains constant and the crystal

deforms elastically. As a consequence, for this loading path,  $\beta = 0$  as long as  $\gamma < \gamma_{en}$ . The normalized stress strain equation following the loading path OA takes the form

$$\frac{\tau}{\mu} = \gamma. \quad (4.85)$$

For loading path AB, we increase  $\gamma$  from  $\gamma_{en}$  to  $\gamma^*$  (loading process). Since  $\gamma \geq \gamma_{en}$ , the geometrically necessary dislocations are nucleated to minimize the effective energy. Accordingly the plastic distortion  $\beta$  starts to appear. In the course of this loading path, we found out that

$$\text{sign}\dot{\beta} = \text{sign}\beta, \quad (4.86)$$

with  $\text{sign}\beta$  from (4.83). Eq.(4.86) explains the case with constantly increasing  $\beta$  for  $0^\circ < \varphi < 45^\circ$  and constantly decreasing  $\beta$  for  $45^\circ < \varphi < 90^\circ$  ( $\beta$  increases in the opposite direction) as we increases  $\gamma$  during the loading process AB. With (4.86) and fulfilling the same step as in the dislocation pile-up at zero resistance case (see section 4.2.2) we obtain, for loading path AB, the solutions similar to (4.60)-(4.64) but now with  $\gamma_l$  instead of  $\gamma$  where

$$\gamma_l = \gamma - \frac{\gamma_{cr}\text{sign}\beta}{\cos 2\varphi}. \quad (4.87)$$

The equation of  $\gamma$  as a function of  $l$  is given in the form

$$\gamma(l) = \frac{\text{sign}\beta}{\cos 2\varphi} \left( \gamma_{cr} + \frac{2k |\sin \varphi| \cosh \zeta l}{c(1-2l) (1 - (\cos^2 2\varphi + \kappa \sin^2 2\varphi) B(l))} \right), \quad (4.88)$$

with  $\text{sign}\beta$  from (4.83) and  $B(l)$  from (4.63). We found out also that  $\gamma = \gamma_{en}$  at  $l = 0$  and  $\gamma$  is increased as we increase  $l$ . Ergo we can use  $l$  as the control parameter for loading path AB.

The normalized dislocation density,  $\alpha$ , takes the same form as in (4.67). The normalized stress strain equation for loading path AB is

$$\frac{\tau}{\mu} = \gamma - \left( \gamma - \frac{\gamma_{cr}\text{sign}\beta}{\cos 2\varphi} \right) B(l) \cos^2 2\varphi. \quad (4.89)$$

For plotting the results, in addition to  $\gamma_{cr} = 0.000513$  we take again the same material parameters presented in Table 3.1. For loading path AB, the distributions of plastic distortion  $\beta$  and the normalized dislocation density  $\alpha$  along the crystal height for increasing  $l$ , hence  $\gamma$  grows, at  $\varphi = 30^\circ$  ( $\beta$  increases to the positive direction) and  $\varphi = 60^\circ$  ( $\beta$  increases to the negative direction), with  $h = 1\mu\text{m}$ , are illustrated in Fig. 4.9 and Fig. 4.10, respectively. It can be seen from both figures that there is no dislocation in the middle of the crystal and there exists the dislocations pile-ups near the grain boundary.

After reaching  $\gamma = \gamma^*$  (point B), we load the crystal in the opposite direction (inverse loading) by decreasing  $\gamma$ . For loading path BC, the crystal deforms elastically and  $\beta = \beta^*(\eta)$  remains constant up to the point where the plastic deformation starts to appear (point

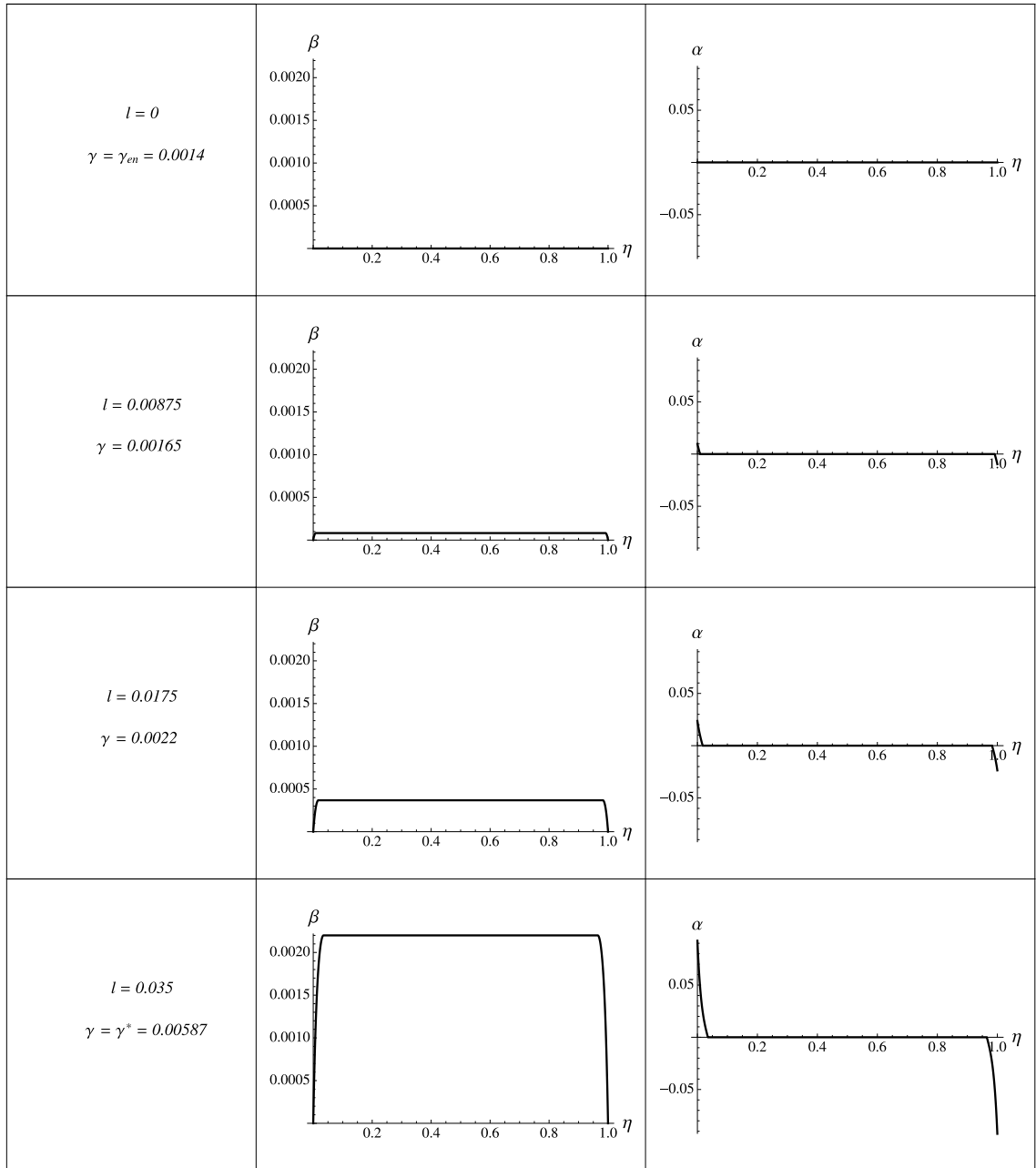


Figure 4.9: Evolution of  $\beta$  and  $\alpha$  during loading process AB for single-slip constrained shear of single crystal with dissipation where  $h = 1\mu\text{m}$  and  $\varphi = 30^\circ$

C). Function  $\beta^*(\eta)$  is the solution of  $\beta(\eta)$  at  $\gamma = \gamma^*$ . The normalized stress strain equation for loading path BC is expressed by

$$\frac{\tau}{\mu} = \gamma + \left( \frac{\tau}{\mu} \right)_B - \gamma^*, \quad (4.90)$$

where  $(\tau/\mu)_B$  be the solution of Eq. (4.89) at  $\gamma^*$  (point B).

As for loading path CD, starting from point C,  $\beta$  begins to decrease (or increase) until  $\beta = 0$  at point D. During this inverse loading process CD,  $\beta$  is constantly decreasing towards zero for  $0^\circ < \varphi < 45^\circ$  (increasing towards zero for  $45^\circ < \varphi < 90^\circ$ ). Therefore now we have the relation

$$\text{sign}\dot{\beta} = -\text{sign}\beta, \quad (4.91)$$

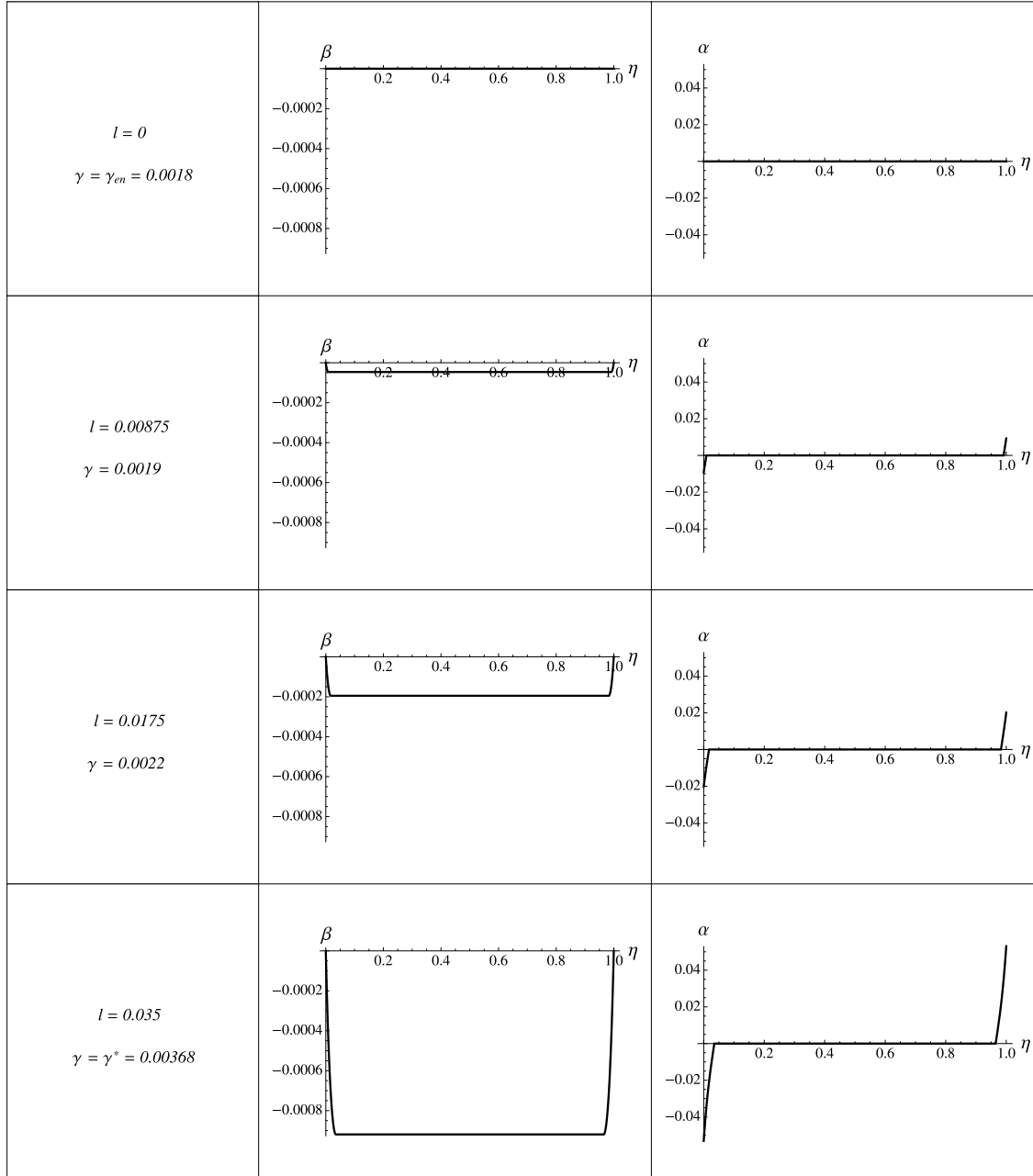


Figure 4.10: Evolution of  $\beta$  and  $\alpha$  during loading process AB for single-slip constrained shear of single crystal with dissipation where  $h = 1\mu\text{m}$  and  $\varphi = 60^\circ$

where  $\text{sign}\beta$  from (4.83). Considering the relation (4.91) for the inverse loading process, the general solutions for inverse loading path CD can now be computed exactly the same manner to give the same form of solutions as in the previous loading path AB but now with

$$\gamma_u = \gamma + \frac{\gamma_{cr} \text{sign}\beta}{\cos 2\varphi}. \quad (4.92)$$

We can also have  $l$  as the control parameter here since  $\gamma$  decreases as  $l$  increases, with the relation

$$\gamma(l) = \frac{\text{sign}\beta}{\cos 2\varphi} \left( -\gamma_{cr} + \frac{2k |\sin \varphi| \cosh \zeta l}{c(1-2l) (1 - (\cos^2 2\varphi + \kappa \sin^2 2\varphi) B(l))} \right), \quad (4.93)$$

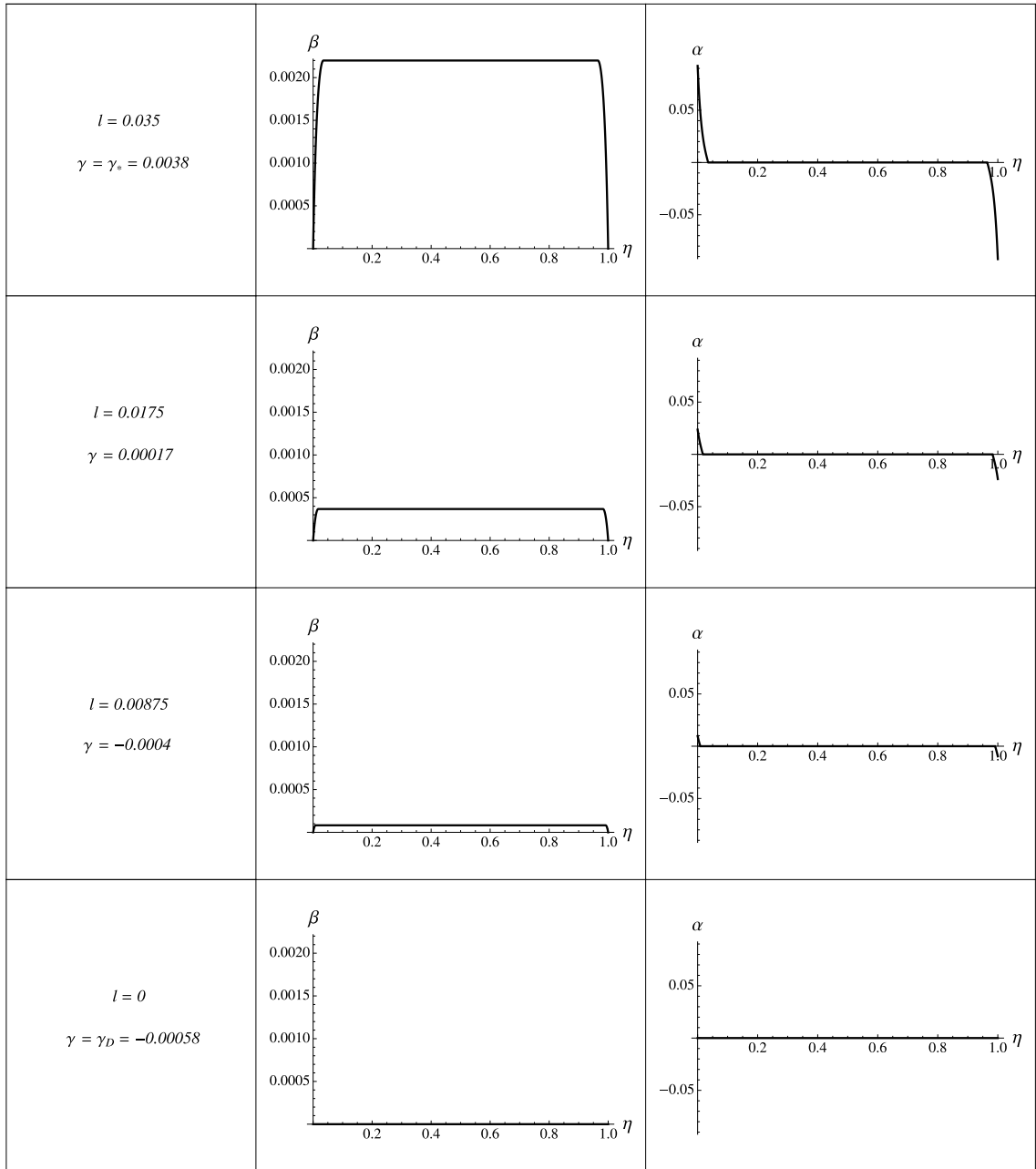


Figure 4.11: Evolution of  $\beta$  and  $\alpha$  during inverse loading CD for single-slip constrained shear of single crystal with dissipation where  $h = 1\mu\text{m}$  and  $\varphi = 30^\circ$

with  $\text{sign}\beta$  from (4.83) and  $B(l)$  from (4.63).

The normalized stress strain equation for inverse loading process CD takes the form

$$\frac{\tau}{\mu} = \gamma - \left( \gamma + \frac{\gamma_{cr}\text{sign}\beta}{\cos 2\varphi} \right) B(l) \cos^2 2\varphi. \quad (4.94)$$

Since the discontinuity of  $\beta$  means the rearrangement of dislocations, the plastic distortion  $\beta$  must be continue at every point in loading path presented in Fig. 4.8. To ensure the continuity of  $\beta$  at the onset of plastic flow (point C),  $\gamma_l$  at point B

$$(\gamma_l)_B = \gamma^* - \frac{\gamma_{cr}\text{sign}\beta}{\cos 2\varphi} \quad (4.95)$$

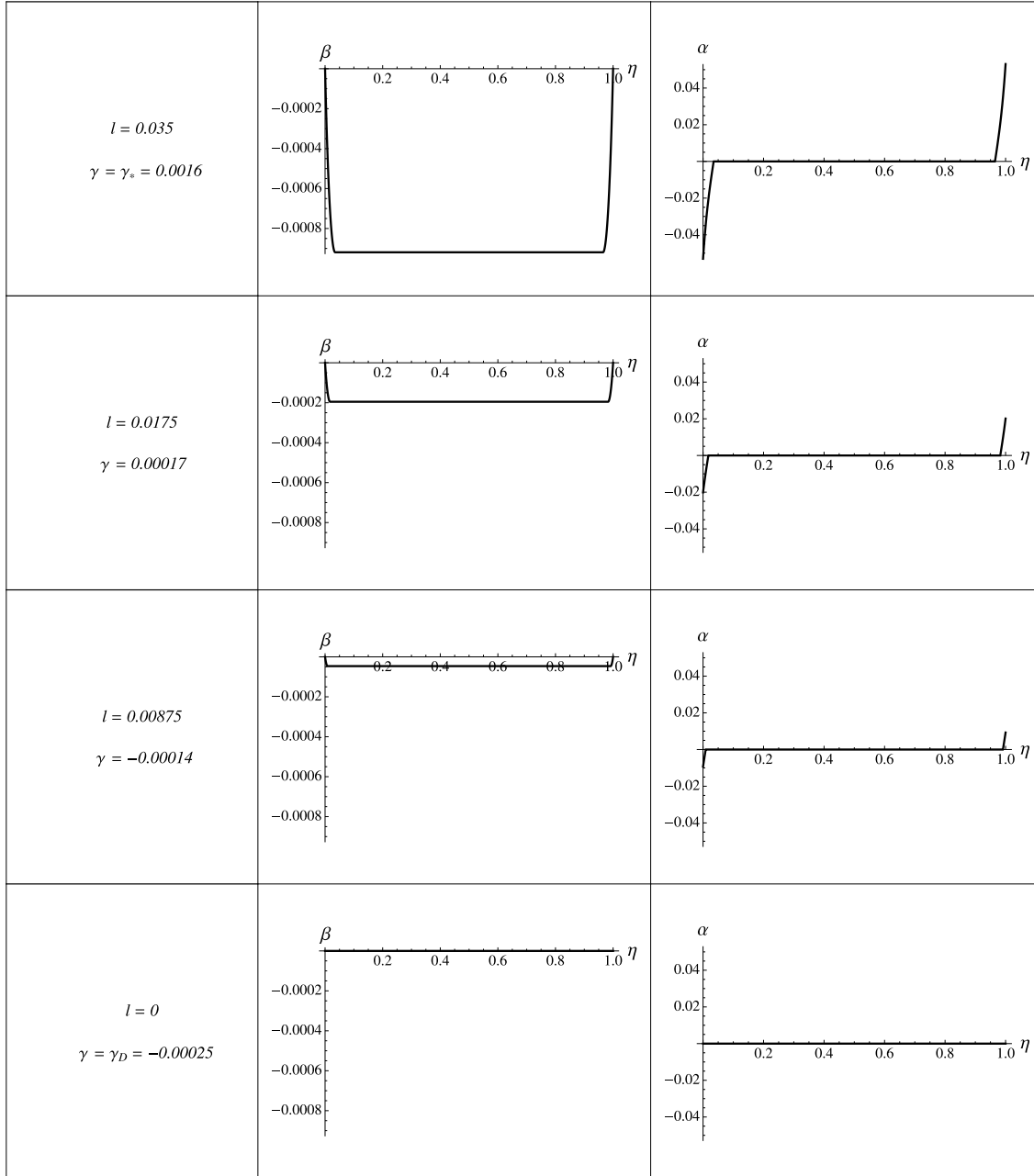


Figure 4.12: Evolution of  $\beta$  and  $\alpha$  during inverse loading CD for single-slip constrained shear of single crystal with dissipation where  $h = 1\mu\text{m}$  and  $\varphi = 60^\circ$

must be equal to  $\gamma_l$  at point C

$$(\gamma_u)_C = \gamma_* + \frac{\gamma_{cr} \text{sign} \beta}{\cos 2\varphi}. \quad (4.96)$$

In consequence the onset of plastic flow (point C) happens at

$$\gamma_* = \gamma^* - \frac{2\gamma_{cr} \text{sign} \beta}{\cos 2\varphi},$$

with  $\text{sign} \beta$  from (4.83).

In the course of inverse loading CD (decreasing  $\gamma$ ), Fig. 4.11 and Fig. 4.12 show the plots of plastic distortion ( $\beta(\eta)$ ) and dislocation density ( $\alpha(\eta)$ ) distributions along the height of the

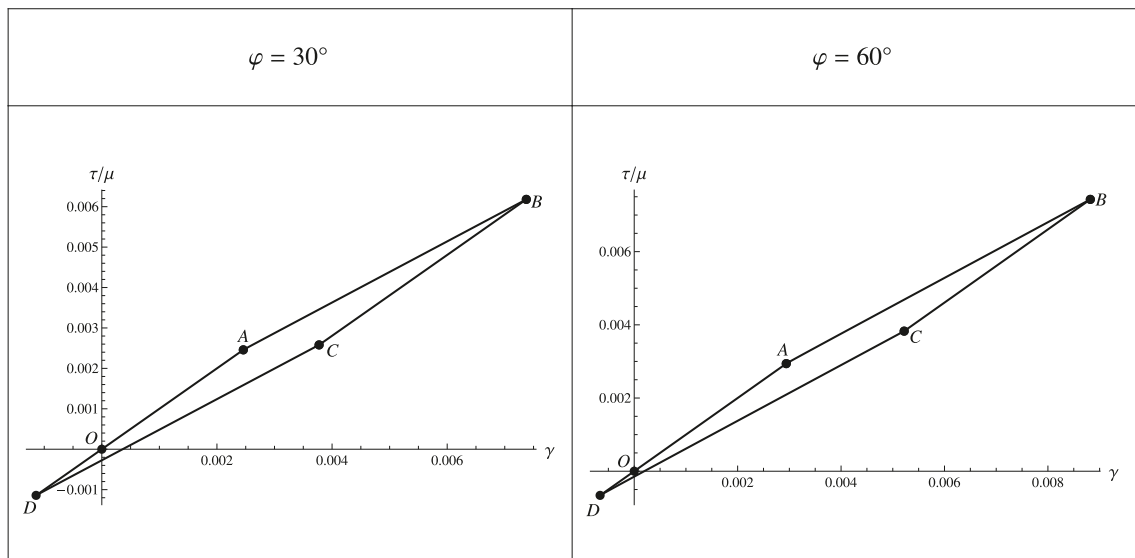


Figure 4.13: Normalized shear stress versus shear strain curves of single-slip constrained shear at non-zero dissipation of single crystal by solving the effective energy minimization (4.72), for  $\varphi = 30^\circ$  and  $\varphi = 60^\circ$

crystal ( $h = 1\mu\text{m}$ ) for single slip system undergoing plane constrained shear with energy dissipation at  $\varphi = 30^\circ$  and  $\varphi = 60^\circ$ , respectively.

Finally, for loading path DE, the crystal is loaded again by increasing  $\gamma$  from  $\gamma_D$  to zero. For this loading path the crystal deforms again elastically and  $\dot{\beta} = 0$ . Thus the value of  $\beta$  remains the same as in point D which is equal to zero. The continuity of  $\beta$  must be guaranteed also at point D. For that reason,  $\gamma_u$  at point D

$$(\gamma_u)_D = \gamma_D + \frac{\gamma_{cr}\text{sign}\beta}{\cos 2\varphi},$$

must be equivalent to  $\gamma_l$  at point A

$$(\gamma_l)_A = \gamma_{en} - \frac{\gamma_{cr}\text{sign}\beta}{\cos 2\varphi}.$$

With  $\gamma_{en}$  from (4.82), we obtain the value of  $\gamma$  at point D, namely

$$\gamma_D = \gamma_{en} - \frac{2\gamma_{cr}\text{sign}\beta}{\cos 2\varphi}.$$

The normalized stress strain equation for loading case DE takes the same form as in (4.85).

It is also interesting for this case to plot the normalized stress strain equations described in (4.85), (4.89), (4.90) and (4.94) following the closed loading path shown in Fig. 4.8. For plotting the normalized stress strain curve, we take the critical resolved shear stress  $K = 0.02367$  thus  $\gamma_c = K/\mu = 0.0009$ , and  $\gamma^* = 3\gamma_{en}$ , where all other parameters are kept the same. The normalized stress strain curves following the loading path of Fig. 4.8 for  $\varphi = 30^\circ$  and  $\varphi = 60^\circ$  are shown in Fig. 4.13.

It is observed from Fig. 4.13 that initially (at point O) the relation between stress and strain is linear until  $\gamma_{en}$  is reached (at point A), meaning that the straight line OA corresponds to

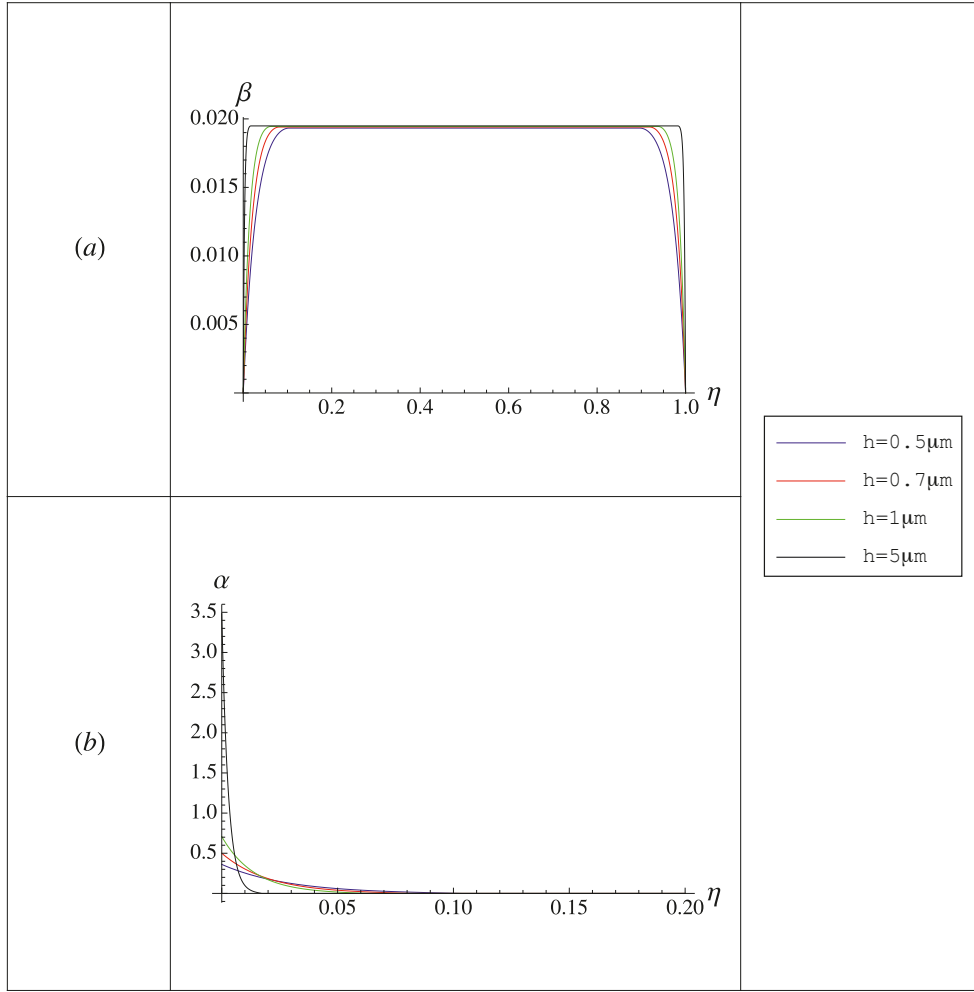


Figure 4.14: Plot of (a):  $\beta$  within the interval  $(0, 1)$  and (b):  $\alpha$  within the interval  $(0, 0.2)$  for non-zero dissipation single-slip constrained shear of single crystal at  $\varphi = 30^\circ$  and  $\gamma = 0.005$  with different crystal heights  $h$

the purely elastic loading. Beyond this point the deformation is already in the plastic region. The region AB is known as work hardening due to the dislocation pile-ups as explained by the second term of (4.89). As  $\gamma$  decreases from point B ( $\gamma = \gamma^*$ ) to point C ( $\gamma = \gamma_*$ ), during the inverse loading, the plastic distortion  $\beta = \beta^*$  is frozen. The straight line BC is parallel to the initial elastic loading path OA. As  $\gamma$  decreases further from point C to point D, the plastic distortion starts to decrease and the created dislocations annihilate. All dislocations have disappeared and  $\beta = 0$  at point D. Finally, the crystal deforms elastically with  $\beta$  remains zero as  $\gamma$  increases from point D to O.

The second term of (4.89) and (4.94) explain the size effect due to the dependency of  $B(l)$  from (4.63) on the height  $h$ . Fig. 4.14 show the distribution of  $\beta$  and  $\alpha$ , respectively, within the interval  $\eta \in (0, 1)$  at  $\varphi = 30^\circ$  and  $\gamma = 0.04$  with different crystal heights  $h$  for the dissipation case. Seeing that the saturated dislocation density from our form of energy restricts the local concentration of dislocations, the dislocation pile-ups for decreasing crystal height are forced to distribute more into the middle of crystal for both methods as can be seen in Fig. 4.14. Therefore the inner back stresses of dislocation is higher for crystal with smaller size. Thus the smaller crystal is stronger than the bigger one. The normalized stress strain curve during the loading process at  $\varphi = 30^\circ$  for the dissipation case with different height,

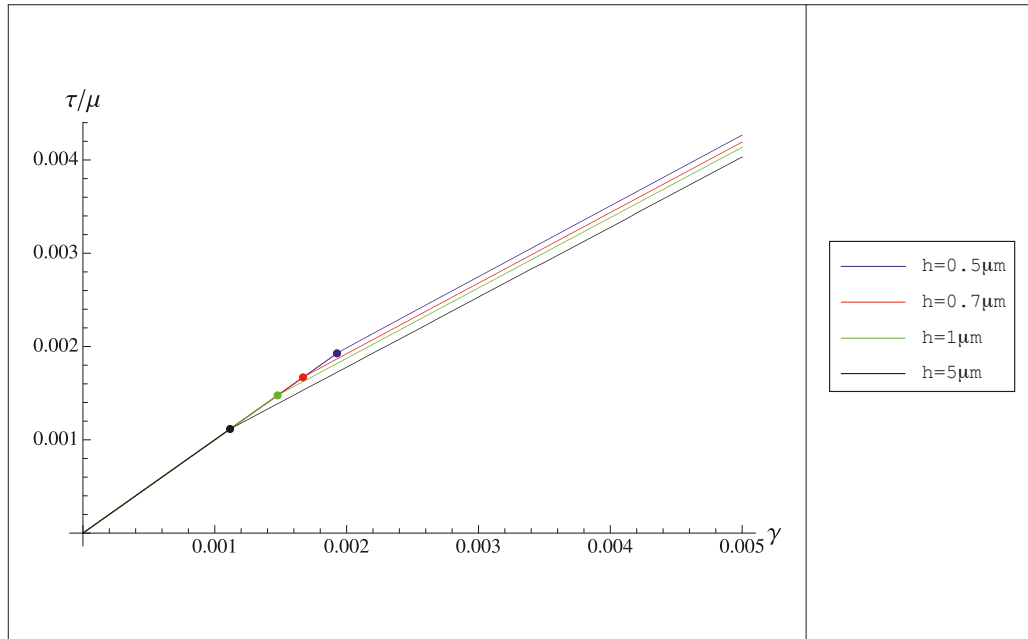


Figure 4.15: Normalized shear stress versus shear strain curves for non-zero dissipation single-slip constrained shear of single crystal at  $\varphi = 30^\circ$  with different crystal heights  $h$  throughout the loading process OAB

$h$ , of the crystal is shown in Fig. 4.15 where the dot represents the energetic threshold value for each curve. The yield stress and hardening rate increase for the effective energy minimization case for decreasing crystal size.

#### 4.4 Comparison with discrete dislocation simulations

Let us now compare our findings with the results of discrete dislocation simulations presented by Needleman and Van der Giessen [2001] and Shu et al. [2001]. By applying all of the results from section 4.2 for zero dissipation case and section 4.3 for the case with dissipation, we calculate the total shear strain profiles

$$u_{,y} = \gamma + 2 \cos 2\varphi(\beta - \langle\beta\rangle). \quad (4.97)$$

In order to compare with the discrete dislocation simulations we take  $\varphi = 60^\circ$  and  $\rho_s = 2.04 \times 10^{15}$  where we let all other material constants remain the same as in the previous simulations. From the discrete dislocation simulations, there exists the relation

$$\frac{\mu\gamma_{en}}{\tau_0} = 0.950588, \quad (4.98)$$

where  $\tau_0 = 1.9 \times 10^{-3}\mu$ . By applying (4.82) to (4.98) we obtain  $\gamma_{cr} = 0.000513$ .

Fig. 4.16 shows the comparison between the total shear strain profiles (4.97) obtained from energy minimization, effective energy minimization and from the discrete dislocation simulations reported in [Needleman and Van der Giessen, 2001, Shu et al., 2001]. The total

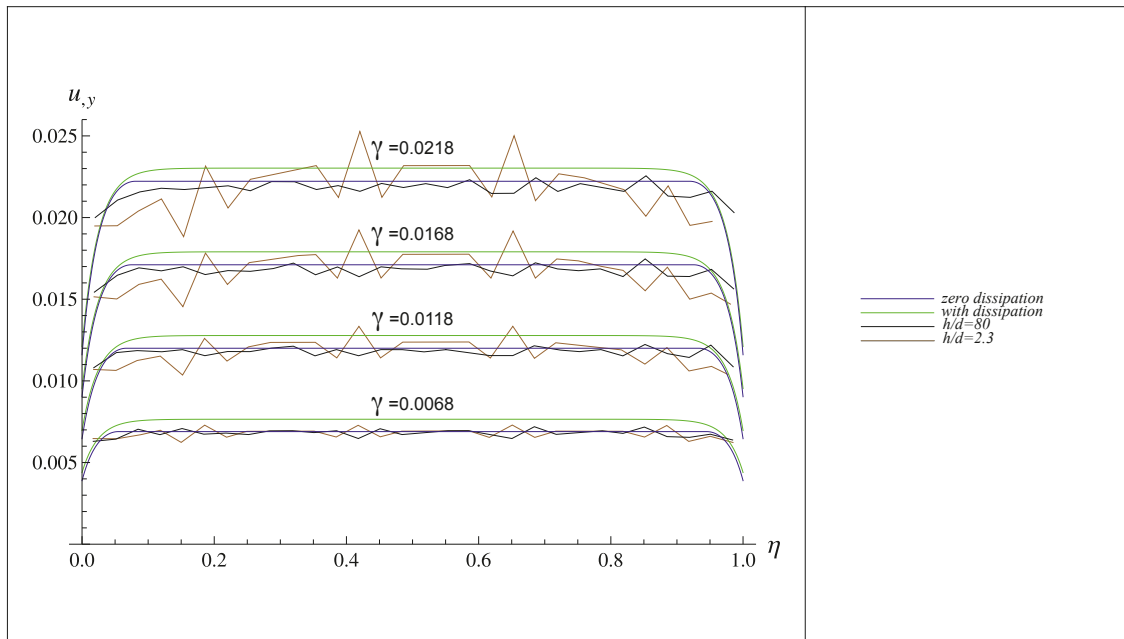


Figure 4.16: Comparison of the total shear strain profiles obtained from energy minimization, effective energy minimization and from the discrete dislocation simulations reported in [Needleman and Van der Giessen, 2001, Shu et al., 2001]

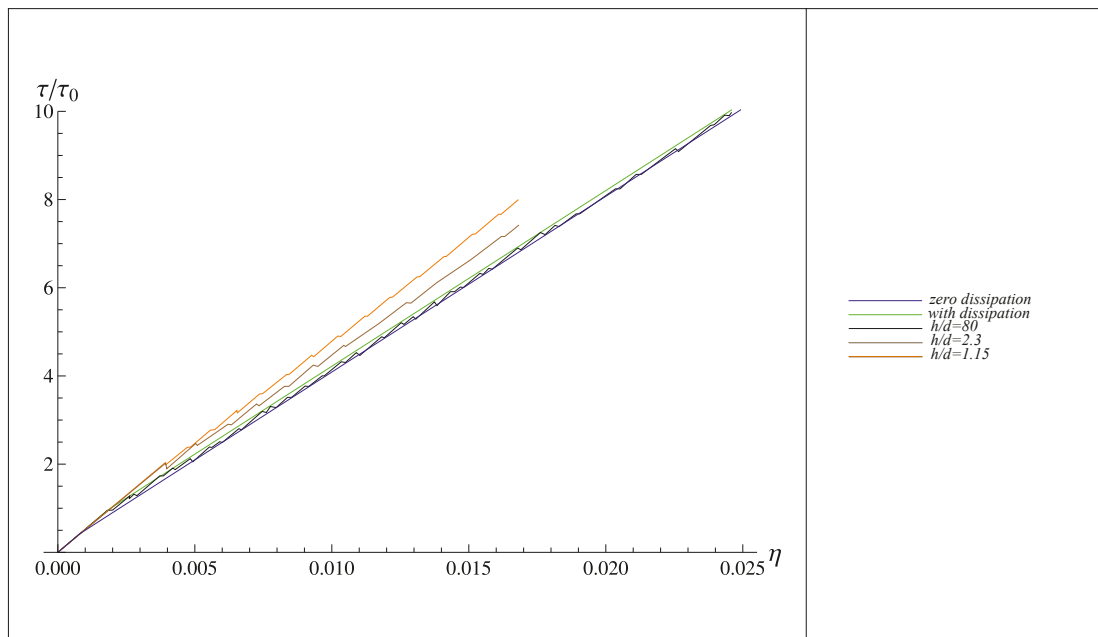


Figure 4.17: Comparison stress strain behavior of results obtained from this approach and from the discrete dislocation simulations presented in [Needleman and Van der Giessen, 2001, Shu et al., 2001]

shear strain profiles in the discrete dislocation simulations are provided for two different ratios  $h/d$ , where  $d$  is the spacing between the active slip planes. All profiles obtained from energy minimization and effective energy minimization show good agreement with the discrete dislocation simulations for  $h/d = 80$ .

Fig. 4.17 illustrates the comparison between the stress-strain curves during the loading obtained from energy minimization, from effective energy minimization, and from the discrete dislocation simulations presented in [Needleman and Van der Giessen, 2001, Shu et al., 2001]. The stress-strain curves in the discrete dislocation simulations are given for three different ratios  $h/d$ . All curves obtained from energy minimization as well as from the effective energy minimization nearly coincide with each other and show good agreement with the discrete dislocation simulations for  $h/d = 80$ .



## 5 Uniaxial extension and combined loading of single slip system

### 5.1 Energy of the crystal

Now we want to extend our previous studies to the plane-strain uniaxial extension and combined loading of a strip made up of a single crystal with one active slip system. For our approach here, we derive first the energy equation of single crystal with single slip system undergoing the combination of plane constrained shear and extension loading then later of the same crystal undergoing plane-constrained uniaxial extension.

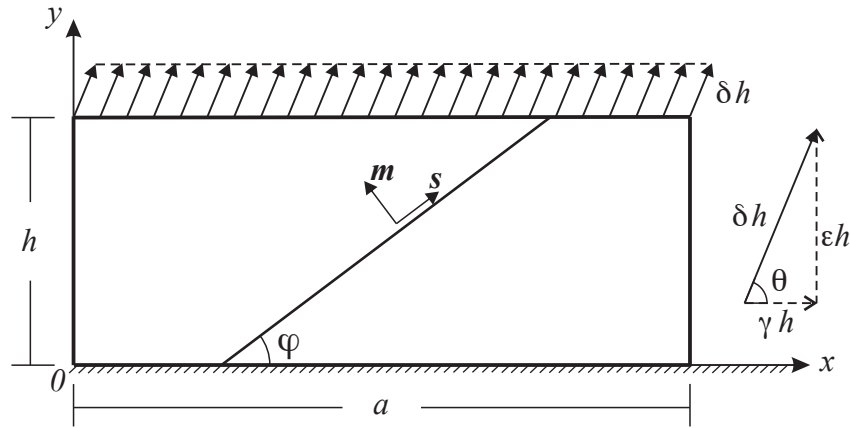


Figure 5.1: Combined deformation of uniaxial extension  $\epsilon$  and simple shear  $\gamma$  of a single crystal with one active slip system

We explain first briefly our model for this particular case of loading problem with one active slip system. We adopt the strip made up of a single crystal with the same properties as in the plane-constrained shear problems with single slip systems (see Fig. 4.1). As illustrated in Fig. 5.1, to model the grain boundary and the combined loading, the prescribed displacements

$$u(0) = 0, \quad v(0) = 0, \quad u(h) = \gamma h, \quad v(h) = \epsilon h, \quad (5.1)$$

are applied at its upper and lower boundary where  $u(y)$  and  $v(y)$  are the longitudinal and transverse displacements, respectively, with  $\gamma$  being the overall shear strain and  $\epsilon$  the overall tensile strain. We propose the total prescribed displacement  $\delta$  applied under an angle  $\theta$  so that

$$\epsilon = \delta \sin \theta \quad \text{and} \quad \gamma = \delta \cos \theta. \quad (5.2)$$

The overall strain  $\delta$  is regarded as given function of time (control parameter), so the evolution of dislocation network which accompanies the change of  $\delta$  can be studied.

The plastic distortion,  $\beta$ , plastic strain tensor,  $\epsilon_{ij}^p$ , elastic strain tensor,  $\epsilon_{ij}^e$ , and scalar dislocation density,  $\rho$ , take the same form as (4.3), (4.5), (4.6) and (4.7), respectively. On account of the boundary conditions (5.1) which prohibit the dislocations to go to the grain boundary, so that we have

$$\beta(0) = \beta(h) = 0. \quad (5.3)$$

Following the similar computation procedures already explained in detail in chapter 4 (see (4.2)-(4.22)), we can write the energy functional for combined loading case with one slip system in term of  $\beta$ , namely

$$\begin{aligned} \Psi(\beta(y)) = aL \int_0^h \mu \left[ \frac{1}{2\kappa} (\delta \sin \theta - \kappa \langle \beta \rangle \sin 2\varphi)^2 + \frac{1}{2} (\delta \cos \theta - \langle \beta \rangle \cos 2\varphi)^2 \right. \\ \left. + \frac{1}{2} (1 - \kappa) \beta^2 \sin^2 2\varphi + k \left( \frac{|\beta_{,y}| |\sin \varphi|}{b\rho_s} + \frac{1}{2} \frac{\beta_{,y}^2 \sin^2 \varphi}{(b\rho_s)^2} \right) \right] dy, \end{aligned} \quad (5.4)$$

with

$$\langle \beta \rangle = \frac{1}{h} \int_0^h \beta dy. \quad (5.5)$$

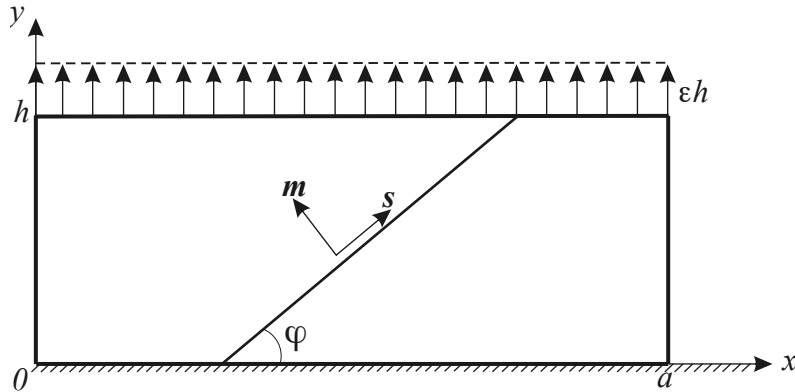


Figure 5.2: Plane-strain constrained uniaxial extension of single crystal strip with one active slip system

Now we admit again the crystal with the same properties as before but now undergoes the plane-constrained uniaxial extension as depicted in Fig. 5.2. We can consider the plane-constrained uniaxial extension as one of the special case of the previous combined loading where  $\theta = 90^\circ$ . Applying  $\theta = 90^\circ$  to (5.2) and (5.4), we obtain the total energy functional for plane-constrained uniaxial extension case in the form

$$\begin{aligned} \Psi(\beta(y)) = aL \int_0^h \mu \left[ \frac{1}{2\kappa} (\epsilon - \kappa \langle \beta \rangle \sin 2\varphi)^2 + \frac{1}{2} (\langle \beta \rangle \cos 2\varphi)^2 \right. \\ \left. + \frac{1}{2} (1 - \kappa) \beta^2 \sin^2 2\varphi + k \left( \frac{|\beta_{,y}| |\sin \varphi|}{b\rho_s} + \frac{1}{2} \frac{\beta_{,y}^2 \sin^2 \varphi}{(b\rho_s)^2} \right) \right] dy, \end{aligned} \quad (5.6)$$

obeying (5.3) with  $\langle\beta\rangle$  from (5.5). It is easy to see that the plane constrained shear case explained in chapter (4) is also considered as the special case of the combined loading where  $\theta = 0^\circ$ .

We employ the same material properties taken from Table 3.1 for all numerical computations in this chapter.

## 5.2 Dislocation nucleation and evolution at zero resistance

Analogous to the previous case (plane-constrained problem of single crystal with one active slip system), we are able to derive closed-form analytical solutions for this kind of problem. The evolution of plastic slip and the dislocation density at zero dissipation will be investigated first then later at non-zero dissipation.

### 5.2.1 Plane-constrained uniaxial extension

In the case of zero resistance where the energy dissipation is zero, the minimization of the total energy functional (5.6) under boundary conditions (5.3) is taken into account to determine  $\beta(y)$ . Again, for convenience, we apply the dimensionless quantities (4.27) to (5.6), hence the energy functional takes the dimensionless form

$$E(\beta(\eta)) = \int_0^1 \left[ \frac{1}{2\kappa} (\epsilon - \kappa\langle\beta\rangle \sin 2\varphi)^2 + \frac{1}{2} \langle\beta\rangle^2 \cos^2 2\varphi + \frac{1}{2} (1 - \kappa) \beta^2 \sin^2 2\varphi + k \left( \frac{|\beta'| |\sin \varphi|}{c} + \frac{1}{2} \frac{(\beta')^2 \sin^2 \varphi}{c^2} \right) \right] d\eta, \quad (5.7)$$

where the prime denotes differentiation with respect to  $\eta$ , and, for short, the bars over  $\bar{\beta}(\eta)$  and  $\langle\bar{\beta}(\eta)\rangle$  are dropped. The average of plastic distortion is in the form

$$\langle\beta\rangle = \int_0^1 \beta d\eta. \quad (5.8)$$

The previous results for plane constrained shear of single crystal strip with single slip system (chapter 4), demonstrates that, for the variational problem of this type, there exists a threshold value  $\epsilon_{en}$  such that when  $\epsilon < \epsilon_{en}$  no dislocations are nucleated and plastic distortion,  $\beta$ , remains zero. Near the threshold value the dislocation density must be small so that the quadratic term of  $\beta'$  in (5.7) can be ignored. In addition, the width of the boundary layer tends to zero as  $\epsilon \rightarrow \epsilon_{en}$ .

Substituting a similar minimizing sequence as that in (4.29) into the energy functional (5.7) (with the quadratic term of  $\beta'$  being removed) and ignoring all small terms of order  $\xi$  and higher, we obtain after some algebraic manipulations

$$E(\beta_m) = \frac{2k|\beta_m| |\sin \varphi|}{c} + \frac{\epsilon^2}{2\kappa} - \epsilon \sin 2\varphi \beta_m + \frac{\beta_m^2}{2}. \quad (5.9)$$

A rather simple analysis shows that for  $\varphi \in (0^\circ, 90^\circ)$ , the energy minimum is achieved at

$$\beta_m = \epsilon \sin 2\varphi - \frac{2k|\sin \varphi|}{c} > 0, \quad (5.10)$$

and for  $\varphi \in (90^\circ, 180^\circ)$  at

$$\beta_m = \epsilon \sin 2\varphi + \frac{2k|\sin \varphi|}{c} < 0, \quad (5.11)$$

if, for both cases, the following condition is fulfilled

$$\epsilon > \epsilon_{en} = \frac{2k}{c} \frac{|\sin \varphi|}{|\sin 2\varphi|}, \quad (5.12)$$

where  $c = hb\rho_s$  which shows clearly the size effect. Equivalent to the plane constrained shear cases, the energetic threshold (5.12) deviates from well known Hall-Petch relation because of the boundary conditions (5.3) which do not permit the penetration of dislocations through the grain boundaries.

Due to the fact that  $\beta'$  should change its sign on the interval  $\eta \in (0, 1)$  as a result of the boundary conditions (5.3), we employ again the minimizer following the solutions obtained in previous chapters in the form

$$\beta(\eta) = \begin{cases} \beta_1(\eta), & \text{for } \eta \in (0, l), \\ \beta_m, & \text{for } \eta \in (l, 1-l), \\ \beta_1(1-\eta), & \text{for } \eta \in (1-l, 1), \end{cases} \quad (5.13)$$

with  $\beta_m$  being a constant quantity,  $l$  the unknown boundary layer thickness ( $0 \leq l \leq 1/2$ ) and  $\beta_1(l) = \beta_m$ . The sign of  $\beta'_1$  on  $\eta \in (0, l)$  is expressed by

$$\text{sign}\beta'_1 = \begin{cases} 0, & \text{for } \varphi = 0^\circ, \\ +1, & \text{for } 0^\circ < \varphi < 90^\circ, \\ -1, & \text{for } 90^\circ < \varphi < 180^\circ, \end{cases} \quad (5.14)$$

and changes its sign to the opposite sign on the interval  $(1-l, 1)$ .

With  $\beta$  from (5.13), the dimensionless energy functional (5.7) reduces to

$$\begin{aligned} E(\beta) = & \int_0^l \left[ (1-\kappa)\beta_1^2 \sin^2 2\varphi + \frac{2k}{c} |\beta'_1| |\sin \varphi| + \frac{k}{c^2} (\beta'_1)^2 \sin^2 \varphi \right] d\eta \\ & + \frac{1}{2} (1-\kappa)(1-2l)\beta_m^2 \sin^2 2\varphi + \frac{1}{2\kappa} (\epsilon - \kappa\langle\beta\rangle \sin 2\varphi)^2 \\ & + \frac{1}{2} \langle\beta\rangle^2 \cos^2 2\varphi, \end{aligned} \quad (5.15)$$

where

$$\langle\beta\rangle = 2 \int_0^l \beta_1 d\eta + (1-2l)\beta_m. \quad (5.16)$$

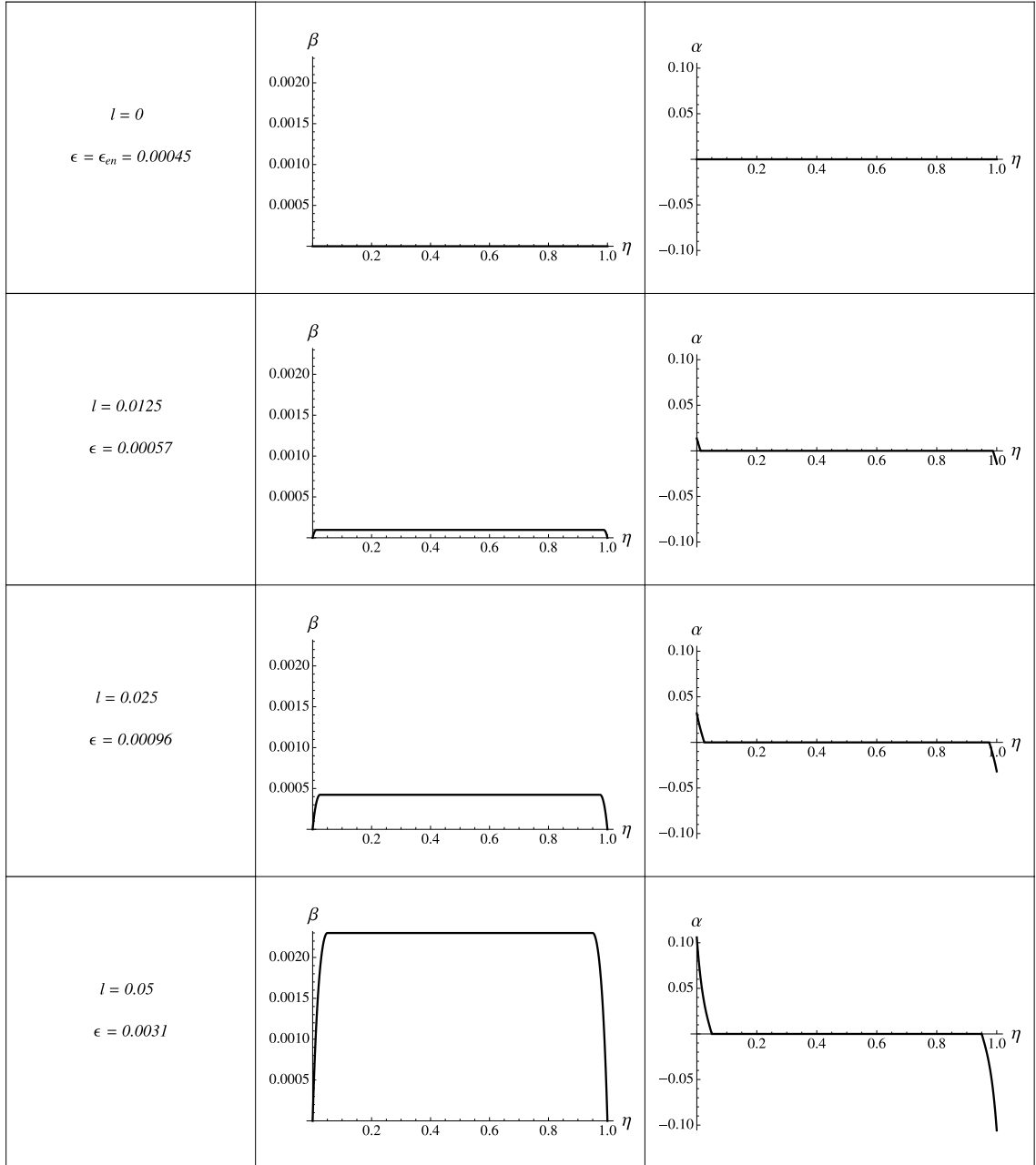


Figure 5.3: Evolution of  $\beta$  and  $\alpha$  for zero dissipation single-slip uniaxial extension of single crystal with  $h = 1\mu\text{m}$  and  $\varphi = 60^\circ$  where  $\eta = y/h$

Taking the variation of energy functional (5.15) with respect of  $\beta_1(\eta)$ ,  $l$  and  $\beta_m$ , the solution of this case reads (cf. (4.60))

$$\beta_1 = \beta_{1p}(1 - \cosh \zeta\eta + \tanh \zeta l \sinh \zeta\eta), \quad 0 \leq \eta \leq l, \quad (5.17)$$

and the constant quantity  $\beta_m$  takes the form

$$\beta_m = \beta_{1p} \left( 1 - \frac{1}{\cosh \zeta l} \right), \quad (5.18)$$

with

$$\beta_{1p} = \frac{\epsilon \sin 2\varphi - (\cos^2 2\varphi + \kappa \sin^2 2\varphi) \langle \beta \rangle}{(1 - \kappa) \sin^2 2\varphi}, \quad (5.19)$$

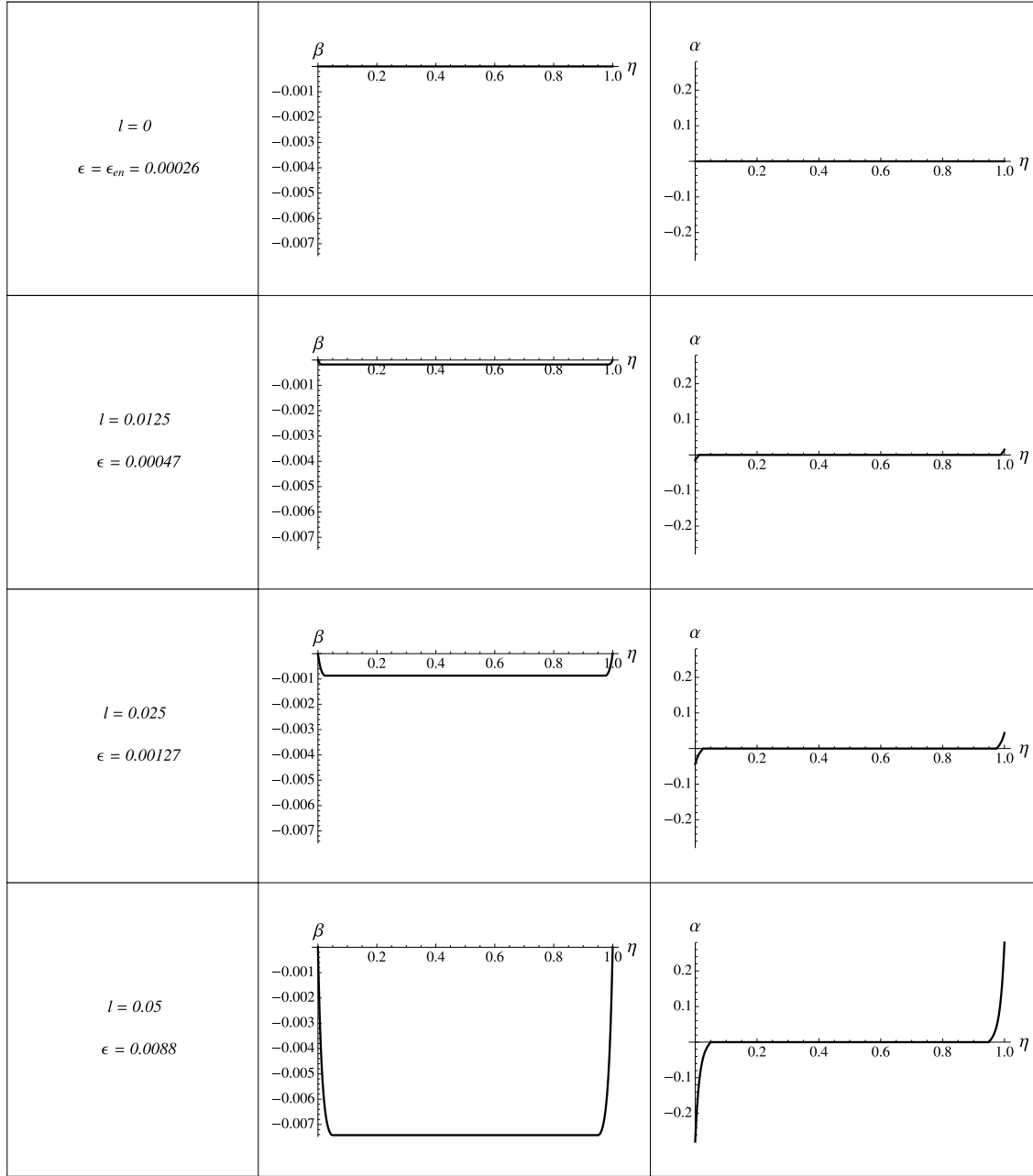


Figure 5.4: Evolution of  $\beta$  and  $\alpha$  for zero dissipation single-slip uniaxial extension of single crystal with  $h = 1\mu\text{m}$  and  $\varphi = 150^\circ$  where  $\eta = y/h$

where

$$\zeta = 2c\sqrt{\frac{1-\kappa}{k}}|\cos\varphi|. \quad (5.20)$$

The average of  $\beta$  equals

$$\langle\beta\rangle = B(l)\epsilon\sin 2\varphi, \quad (5.21)$$

with

$$B(l) = \frac{g(l)}{(1-\kappa)\sin^2 2\varphi + g(l) \times (\cos^2 2\varphi + \kappa\sin^2 \varphi)}, \quad (5.22)$$

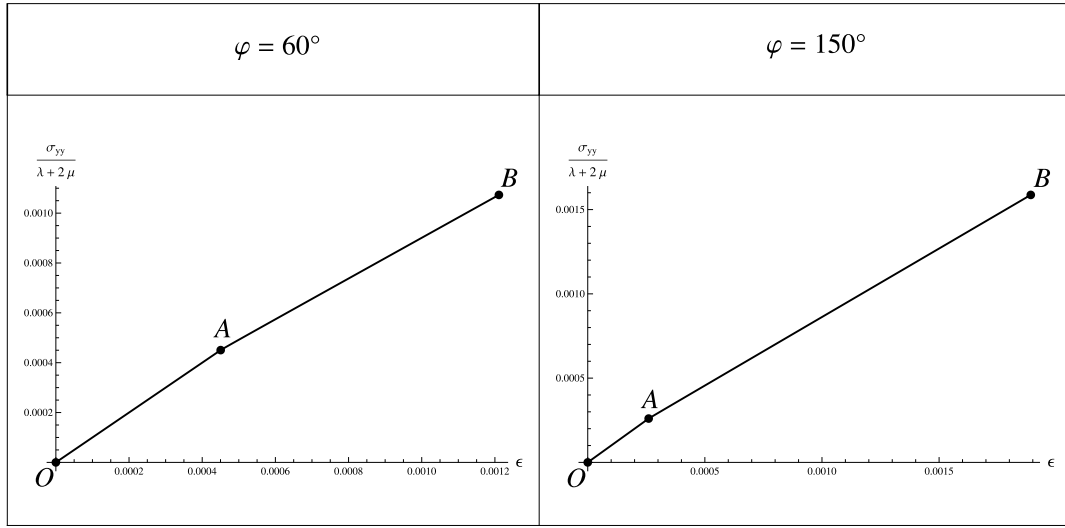


Figure 5.5: Normalized tensile stress versus strain curve for zero dissipation single-slip uni-axial extension of single crystal at  $\varphi = 60^\circ$  and  $\varphi = 150^\circ$

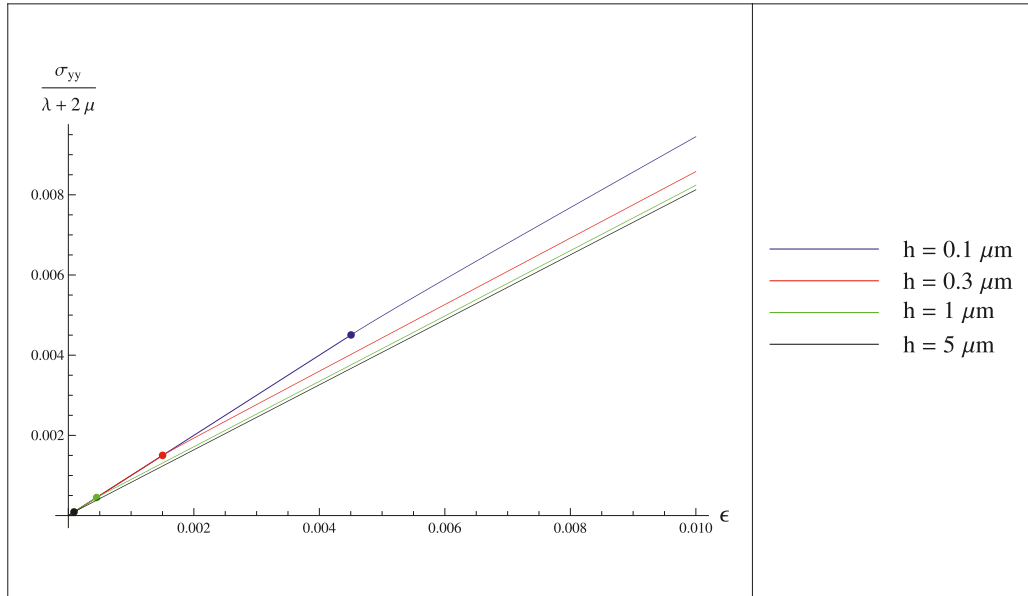


Figure 5.6: Normalized tensile stress versus strain curve for zero dissipation single-slip uni-axial extension of single crystal at  $\varphi = 60^\circ$  with different crystal heights  $h$

where

$$g(l) = 2 \left( l - \frac{\tanh \zeta l}{\zeta} \right) + \left( 1 - \frac{1}{\cosh \zeta l} \right) (1 - 2l).$$

Using above solutions (5.17) and (5.18), the normalized dislocation density,  $\alpha(\eta) = \beta' \sin \varphi$ , can be calculated and gives

$$\alpha = \begin{cases} \beta_{1p} \sin \varphi (-\zeta \sinh \zeta \eta + \zeta \tanh \zeta l \cosh \zeta \eta), & \text{for } \eta \in (0, l), \\ 0, & \text{for } \eta \in (l, 1 - l), \\ \beta_{1p} \sin \varphi (-\zeta \sinh \zeta (1 - \eta) + \zeta \tanh \zeta l \cosh \zeta (1 - \eta)), & \text{for } \eta \in (1 - l, 1). \end{cases} \quad (5.23)$$

Similar to section 4.2.2, we can also here use  $l$  as control parameter to observe the evolution

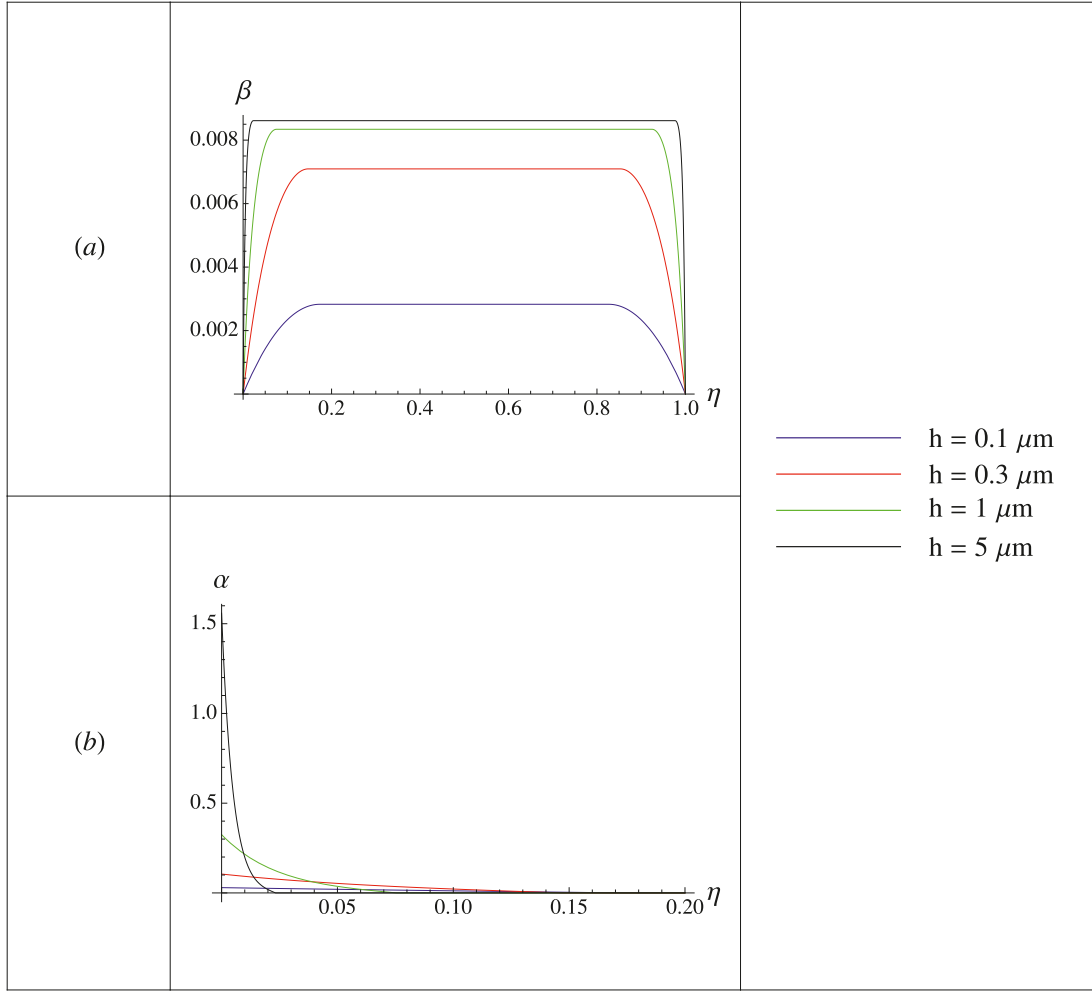


Figure 5.7: Plot of (a):  $\beta$  within the interval  $(0, 1)$  and (b):  $\alpha$  within the interval  $(0, 0.2)$  for zero dissipation single-slip uniaxial extension of single crystal at  $\varphi = 60^\circ$  and  $\gamma = 0.01$  with different crystal heights  $h$

of  $\beta$  and  $\alpha$  since increasing  $l$  means increasing  $\epsilon$  and  $\epsilon = \epsilon_{en}$  at  $l = 0$ . The equation of  $\epsilon$  as a function of  $l$  takes the form

$$\epsilon(l) = \frac{2k |\sin \varphi| \text{sign} \beta'_1 \cosh \zeta l}{c(1 - 2l) \sin 2\varphi (1 - (\cos^2 2\varphi + \kappa \sin^2 2\varphi) B(l))} \quad (5.24)$$

with  $\text{sign} \beta'_1$  from (5.14) and  $B(l)$  from (5.22).

Again similar to the previous cases of anti-plane constrained shear case and plane-constrained shear case, we have also the assumption that the tensile stress is also averagely distributed along crystal height. Therefore, the average tensile stress equation takes the form

$$\sigma_{yy} = \frac{1}{h} \int_0^h \sigma_{yy} dy, \quad (5.25)$$

or in the dimensionless form

$$\sigma_{yy} = \int_0^1 \sigma_{yy} d\eta, \quad (5.26)$$

with

$$\sigma_{yy} = \lambda \epsilon_{kk}^e + 2\mu \epsilon_{yy}^e. \quad (5.27)$$

Following the same procedure as in previous cases, the dimensionless tensile stress equation is given in the form

$$\frac{\sigma_{yy}}{\lambda + 2\mu} = \epsilon - \kappa \langle \beta \rangle \sin 2\varphi. \quad (5.28)$$

Referring to what we know, the tensile stress deforms elastically for  $\epsilon < \epsilon_{en}$  where no dislocations are nucleated and  $\beta = 0$ . For  $\epsilon \geq \epsilon_{en}$ , we apply  $\langle \beta \rangle$  from (5.21) to (5.28) to obtain the tensile stress  $\sigma_{yy}$ . The second term of (5.28) brings about the hardening due to the dislocation pile-up and describes the size effect in this model.

The evolution of plastic distortion,  $\beta(\eta)$ , and dislocation density,  $\alpha(\eta)$  through the crystal height, where  $\eta = y/h$ , for  $\varphi = 60^\circ$  and  $\varphi = 150^\circ$  are illustrated in Fig. 5.3 and Fig. 5.4, respectively. The normalized tensile stress versus strain curves for the same angles are plotted in Fig. 5.5 which shows that there are "work hardening" sections AB for  $\epsilon \geq \epsilon_{en}$  introduced by the dislocation pile-up. Since there is no residual strain during the loading in the opposite direction by decreasing  $\epsilon$ , the plastic deformation is completely reversible which means that the stress strain curves follow the same path BAO. When we approach point A, all nucleated dislocations are entirely annihilated. Fig. 5.6 shows the size effect where the yield stresses and the hardening rates mentioned in (5.12) and the second term of (5.28), respectively for different  $h$ , increase as the crystal size decreases. This can be explained by Fig. 5.7 where the saturated dislocation density,  $\rho_s$ , from our energy bounds the local concentration of dislocations so that, for decreasing  $h$ , the dislocation pile-ups are forced to distribute more into the middle of the crystal causing the increasing inner back stresses of dislocation.

### 5.2.2 Plane-constrained combined loading

If the dissipation of energy is negligible, the plastic distortion  $\beta$  minimizes the energy functional (5.4) under constraints (5.3). It is useful to introduce again the dimensionless quantities (4.27) into the energy functional (5.4) so that the energy functional reduces to

$$E(\beta) = \int_0^1 \left[ \frac{1}{2\kappa} (\delta \sin \theta - \kappa \langle \beta \rangle \sin 2\varphi)^2 + \frac{1}{2} (\delta \cos \theta - \langle \beta \rangle \cos 2\varphi)^2 + \frac{1}{2} (1 - \kappa) \beta^2 \sin^2 2\varphi + k \left( \frac{|\beta'| |\sin \varphi|}{c} + \frac{1}{2} \frac{(\beta')^2 \sin^2 \varphi}{c^2} \right) \right] d\eta, \quad (5.29)$$

with

$$\langle \beta \rangle = \int_0^1 \beta d\eta,$$

where for short the bars over  $\beta$  and  $\langle \beta \rangle$  are dropped. We minimize functional (5.29) among functions satisfying the boundary conditions (5.3).

As previous case, there exist the threshold value  $\delta_{en}$  such that the plastic deformation starts to appear when the condition  $\delta \geq \delta_{en}$  holds true. Following the same idea and procedure as in section 4.2.1, the energetic threshold value for the single slip combined loading case reads

$$\delta_{en} = \frac{2k}{c} \frac{|\sin \varphi|}{|\cos(\theta - 2\varphi)|}, \quad (5.30)$$

where  $c = hb\rho_s$ . Mention that (5.30) takes the similar form as in (4.37) and (5.12) when  $\theta = 0^\circ$  (plane-constrained shear case) and  $\theta = 90^\circ$  (uniaxial extension case), respectively.

Continuing the same procedure as in section 4.2.2, the general solutions for plastic distortion in this case are expressed by

$$\beta = \begin{cases} \beta_{1p}(1 - \cosh \zeta \eta + \tanh \zeta l \sinh \zeta \eta), & \text{for } \eta \in (0, l), \\ \beta_{1p} \left(1 - \frac{1}{\cosh \zeta l}\right), & \text{for } \eta \in (l, 1-l), \\ \beta_{1p}(1 - \cosh \zeta(1-\eta) + \tanh \zeta l \sinh \zeta(1-\eta)), & \text{for } \eta \in (1-l, 1), \end{cases} \quad (5.31)$$

where

$$\beta_{1p} = \frac{\delta \cos(\theta - 2\varphi) - (\cos^2 2\varphi + \kappa \sin^2 2\varphi) \langle \beta \rangle}{(1 - \kappa) \sin^2 2\varphi}, \quad \zeta = 2c \sqrt{\frac{1 - \kappa}{k}} |\cos \varphi|. \quad (5.32)$$

The average of plastic distortion yields

$$\langle \beta \rangle = B(l) \delta \cos(\theta - 2\varphi), \quad (5.33)$$

where

$$B(l) = \frac{g(l)}{(1 - \kappa) \sin^2 2\varphi + g(l) \times (\cos^2 2\varphi + \kappa \sin^2 2\varphi)}, \quad (5.34)$$

with

$$g(l) = 2 \left( l - \frac{\tanh \zeta l}{\zeta} \right) + \left( 1 - \frac{1}{\cosh \zeta l} \right) (1 - 2l).$$

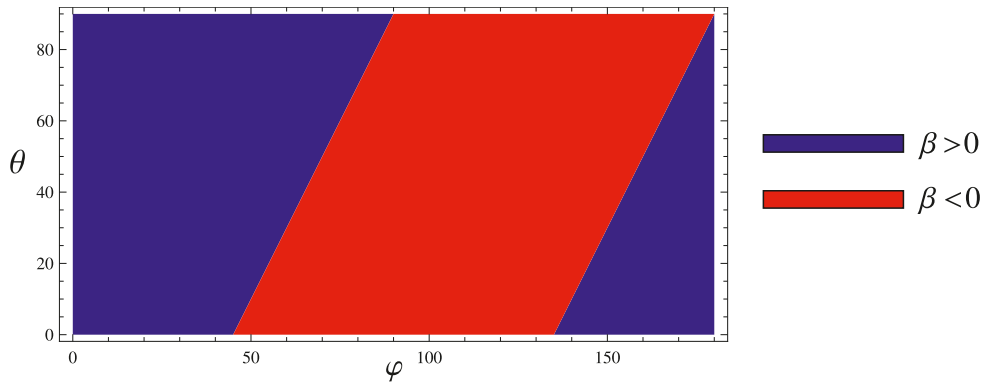


Figure 5.8: Plot  $\text{sign}\beta$  at the range  $0^\circ \leq \varphi \leq 180^\circ$  and  $0^\circ \leq \theta \leq 90^\circ$

From the threshold value derivation we found out that

$$\text{sign}\beta = \text{sign}(\cos(\theta - 2\varphi)), \quad (5.35)$$

as can be seen in Fig. 5.8, so, as a consequence, we have also the relation

$$\text{sign}\beta'_1 = \text{sign}\beta, \quad (5.36)$$

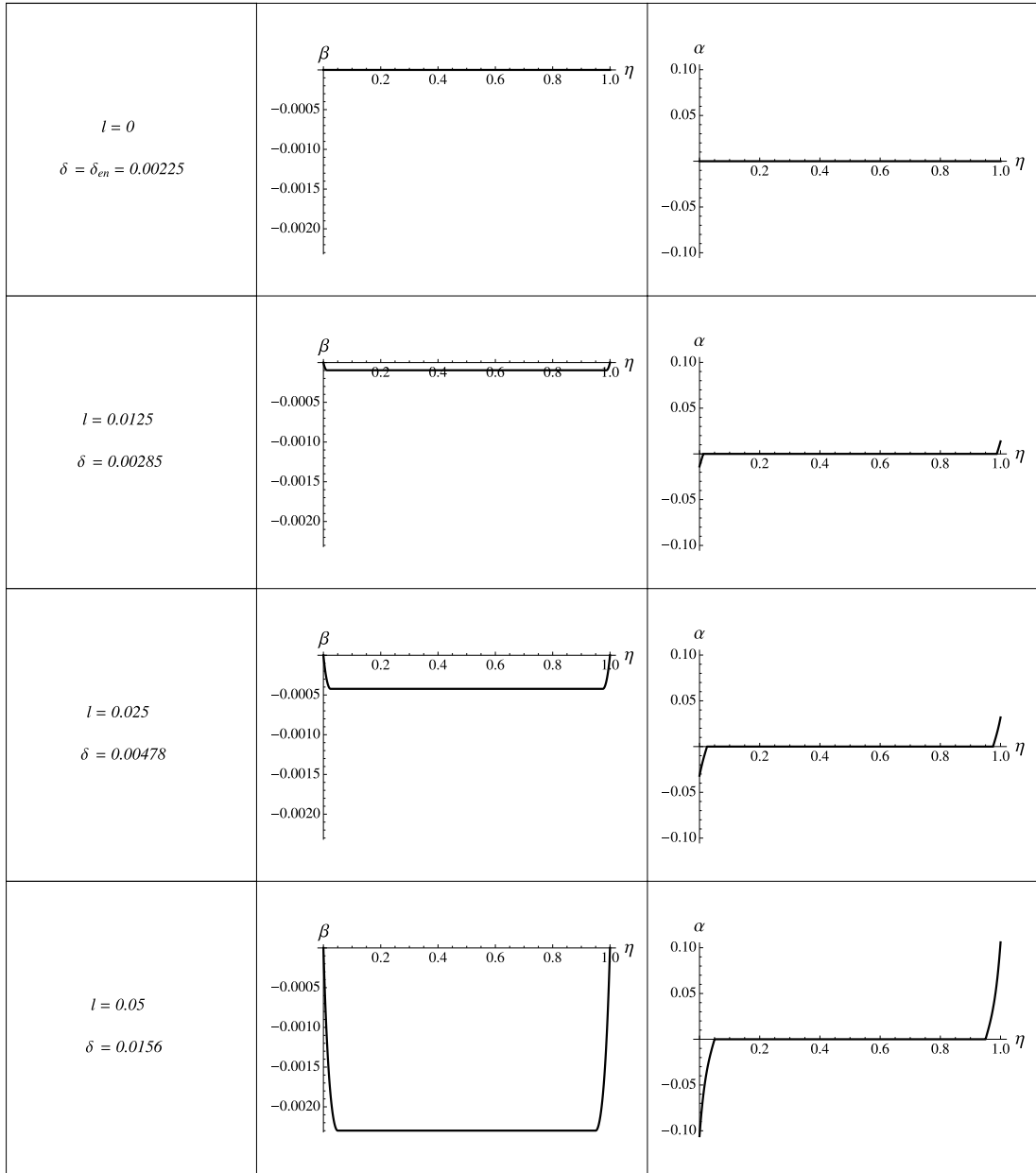


Figure 5.9: Evolution of  $\beta$  and  $\alpha$  for single slip combine loading of single crystal at zero dissipation where  $h = 1\mu\text{m}$ ,  $\varphi = 60^\circ$  and  $\theta = 20^\circ$  at increasing  $\delta$

and changes its sign to the opposite sign on the interval  $(1 - l, 1)$ . We obtain the normalized dislocation density in the form

$$\alpha = \begin{cases} \beta_{1p} \sin \varphi (-\zeta \sinh \zeta \eta + \zeta \tanh \zeta l \cosh \zeta \eta), & \text{for } \eta \in (0, l), \\ 0, & \text{for } \eta \in (l, 1 - l), \\ \beta_{1p} \sin \varphi (-\zeta \sinh \zeta (1 - \eta) + \zeta \tanh \zeta l \cosh \zeta (1 - \eta)), & \text{for } \eta \in (1 - l, 1), \end{cases} \quad (5.37)$$

Since  $\delta$  increases as  $l$  grows, as in previous cases, we can also here make use of  $l$  as the control parameter to observe the evolution of  $\beta$  and  $\alpha$ . The equation of  $\delta$  as a function of  $l$  takes the form

$$\delta(l) = \frac{2k |\sin \varphi| \text{sign} \beta'_1 \cosh \zeta l}{c(1 - 2l) \cos(\theta - 2\varphi) (1 - (\cos^2 2\varphi + \kappa \sin^2 2\varphi) B(l))}, \quad (5.38)$$

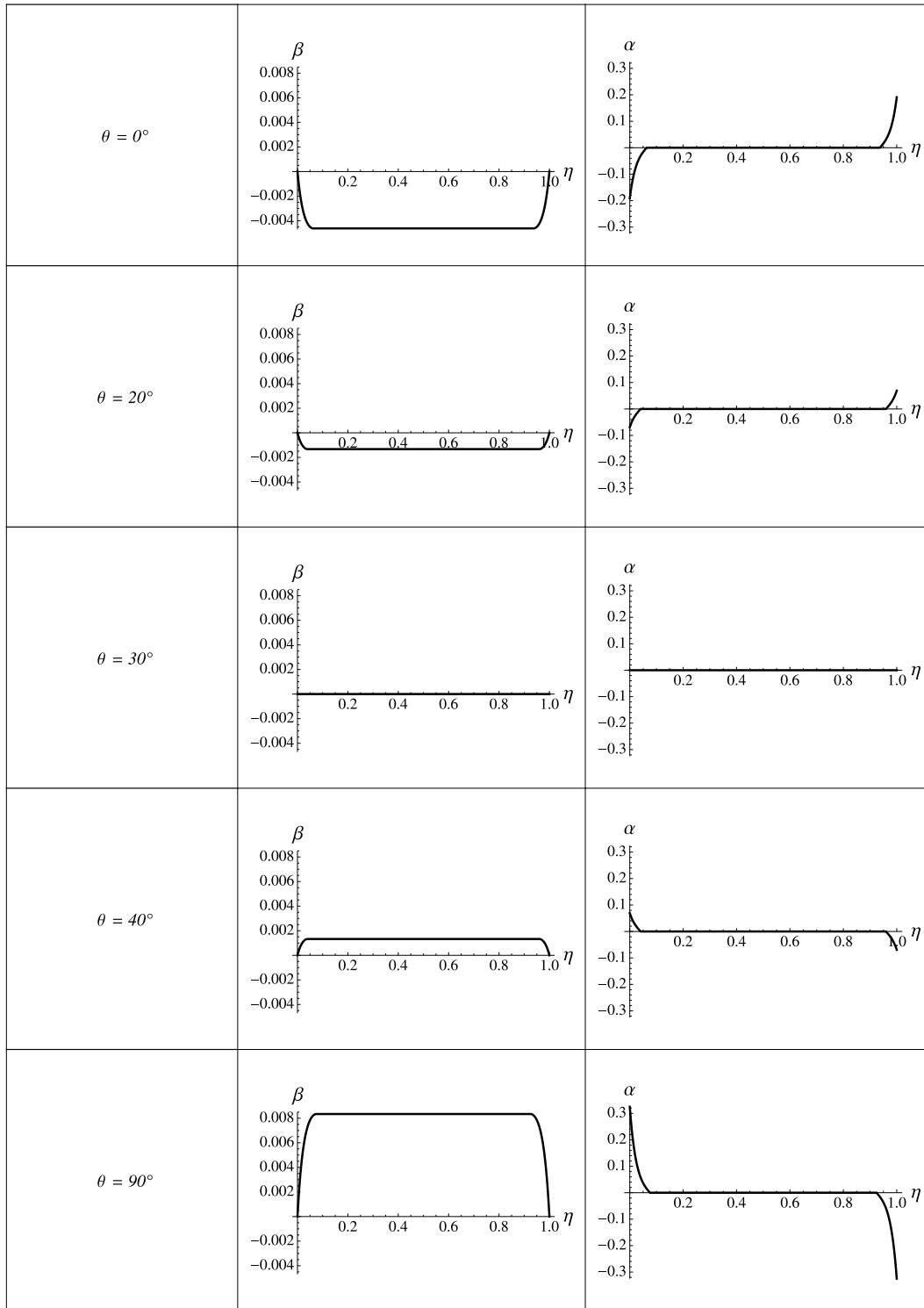


Figure 5.10: Evolution of  $\beta$  and  $\alpha$  for single slip minimization case at increasing  $\theta$  where  $\varphi = 60^\circ$  and  $\delta = 0.01$

with  $\text{sign}\beta_1^l$  from (5.36) and  $B(l)$  from (5.34).

Fig. 5.9 gives an overview of the evolution of both the plastic distortion  $\beta$  and the dimensionless dislocation density  $\alpha$  for single slip plane constrained combined loading case at zero dissipation as  $\delta$  grows where  $\varphi = 60^\circ$  and  $\theta = 20^\circ$ . The evolution of  $\beta$  and  $\alpha$  at fixed load  $\delta = 0.01$  and  $\varphi = 60^\circ$  for different angles  $\theta$  is shown in Fig. 5.10.

### 5.3 Dislocation nucleation and evolution with energy dissipation

In the case with non-zero dissipation, if the sign of  $\dot{\beta}$  does not change during the loading process, the evolution of plastic distortion,  $\beta$ , for the uniaxial extension and combined loading-deforming in single slip must be obtained from solving the variational equation (4.72) obeying boundary conditions (5.3). When  $\dot{\beta} = 0$ , the variational equation (4.26) needs not to be computed and simply replaced by  $\dot{\beta} = 0$ .

#### 5.3.1 Plane-constrained uniaxial extension

As in the plane constrained shear case, we want to find  $\beta(t, y)$  with  $\epsilon$  as the driving variable. As depicted in Fig. 5.11, in order to determine the evolution of  $\beta$ , we first increase  $\epsilon$  from zero to some value  $\epsilon^*$  (point B), then decrease to  $\epsilon_D$  (Point D) and finally increase to zero (Point E). The problem is to determine the evolution of  $\beta$  as a function of  $t$  and  $y$  where  $\beta$  is initially zero ( $\beta(0, y) = 0$ ).

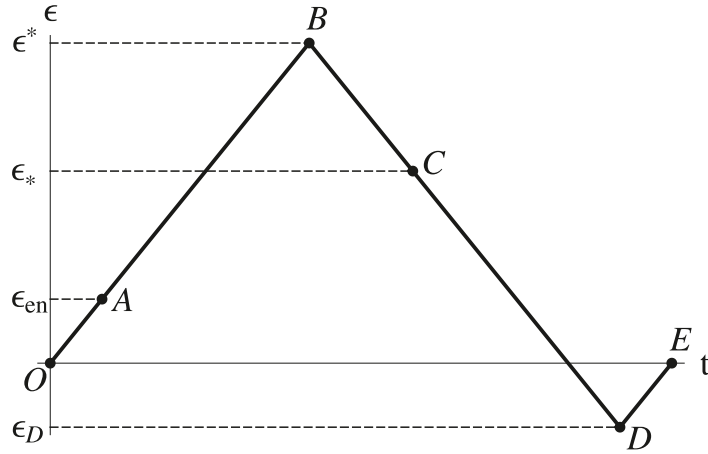


Figure 5.11: A closed loading path for plane constrained uniaxial extension of a single crystal strip with one active slip system

By first applying the energy functional (5.6) to (4.26) then applying the dimensionless quantities (4.74) to it with some algebraic manipulation and dropping the bar over  $\bar{\beta}$  for simple, the effective energy for single system for this kind of problem can be found in

$$\hat{E}(\beta) = \int_0^1 \left[ \frac{1}{2\kappa} (\epsilon_r - \kappa \langle \beta \rangle \sin 2\varphi)^2 + \frac{1}{2} \langle \beta \rangle^2 \cos^2 2\varphi + \frac{1}{2} (1 - \kappa) \beta^2 \sin^2 2\varphi + k \left( \frac{|\beta'| |\sin \varphi|}{c} + \frac{1}{2} \frac{(\beta')^2 \sin^2 \varphi}{c^2} \right) \right] d\eta, \quad (5.39)$$

with

$$\epsilon_l = \epsilon - \frac{\epsilon_{cr} \text{sign} \dot{\beta}}{\sin 2\varphi}, \quad (5.40)$$

and

$$\langle \beta \rangle = \int_0^1 \beta d\eta. \quad (5.41)$$

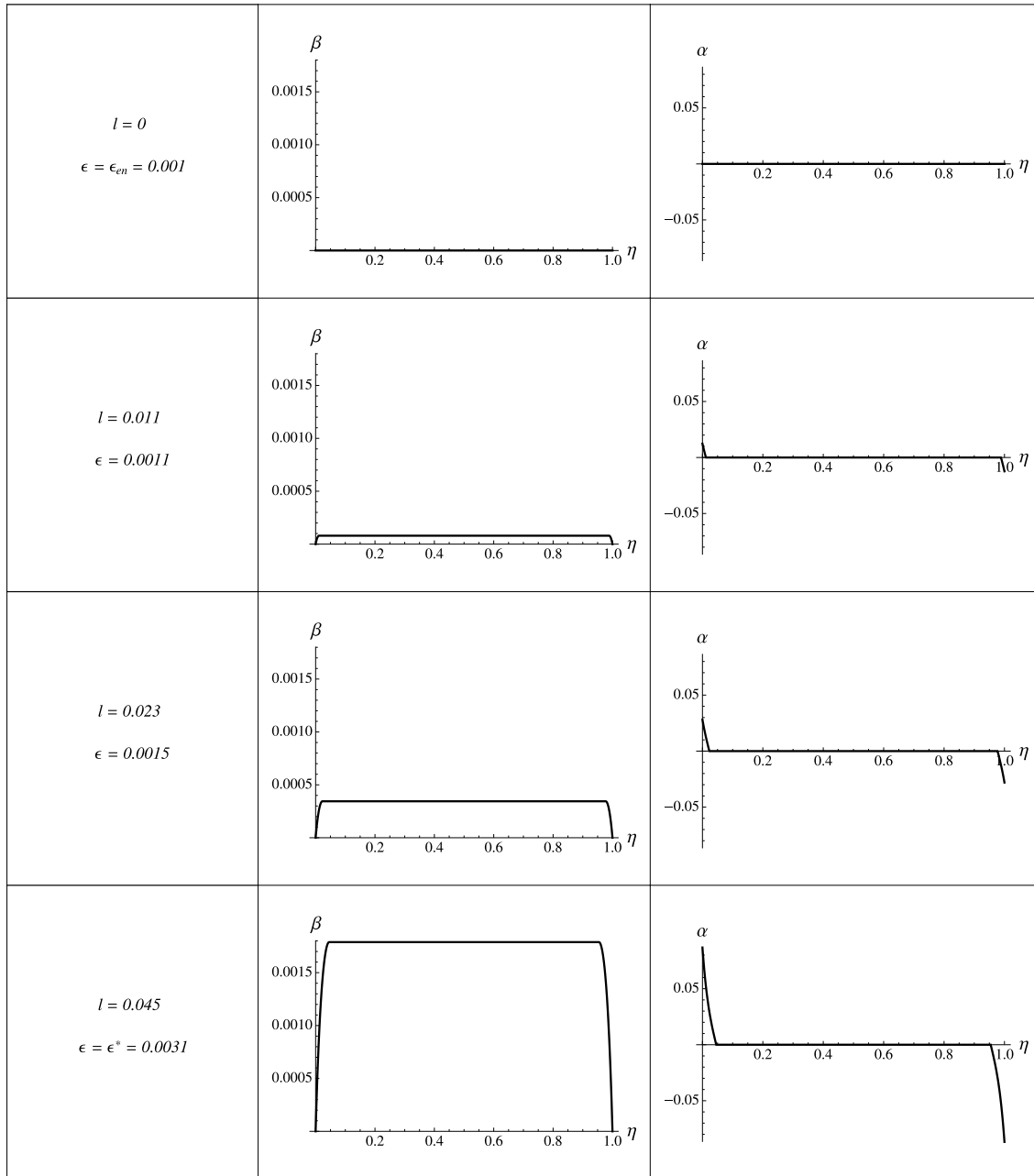


Figure 5.12: Evolution of  $\beta$  and  $\alpha$  for zero dissipation single-slip uniaxial extension of single crystal with  $h = 1\mu\text{m}$  and  $\varphi = 60^\circ$  where  $\eta = y/h$  throughout loading path AB

Mention that (5.39) has the similar form as in (5.7) but now with  $\epsilon_r$  instead of  $\epsilon$ . For finding the solutions, we adopt the similar procedure reported in section 4.3.

The energetic threshold point where the plastic deformation starts to appear in term of original length,  $h$ , is in the form

$$\epsilon_{en} = \frac{\epsilon_{cr}}{|\sin 2\varphi|} + \frac{2k}{hb\rho_s} \frac{|\sin \varphi|}{|\sin 2\varphi|}, \quad (5.42)$$

which demonstrates the size effect. From the energetic threshold value derivation we found

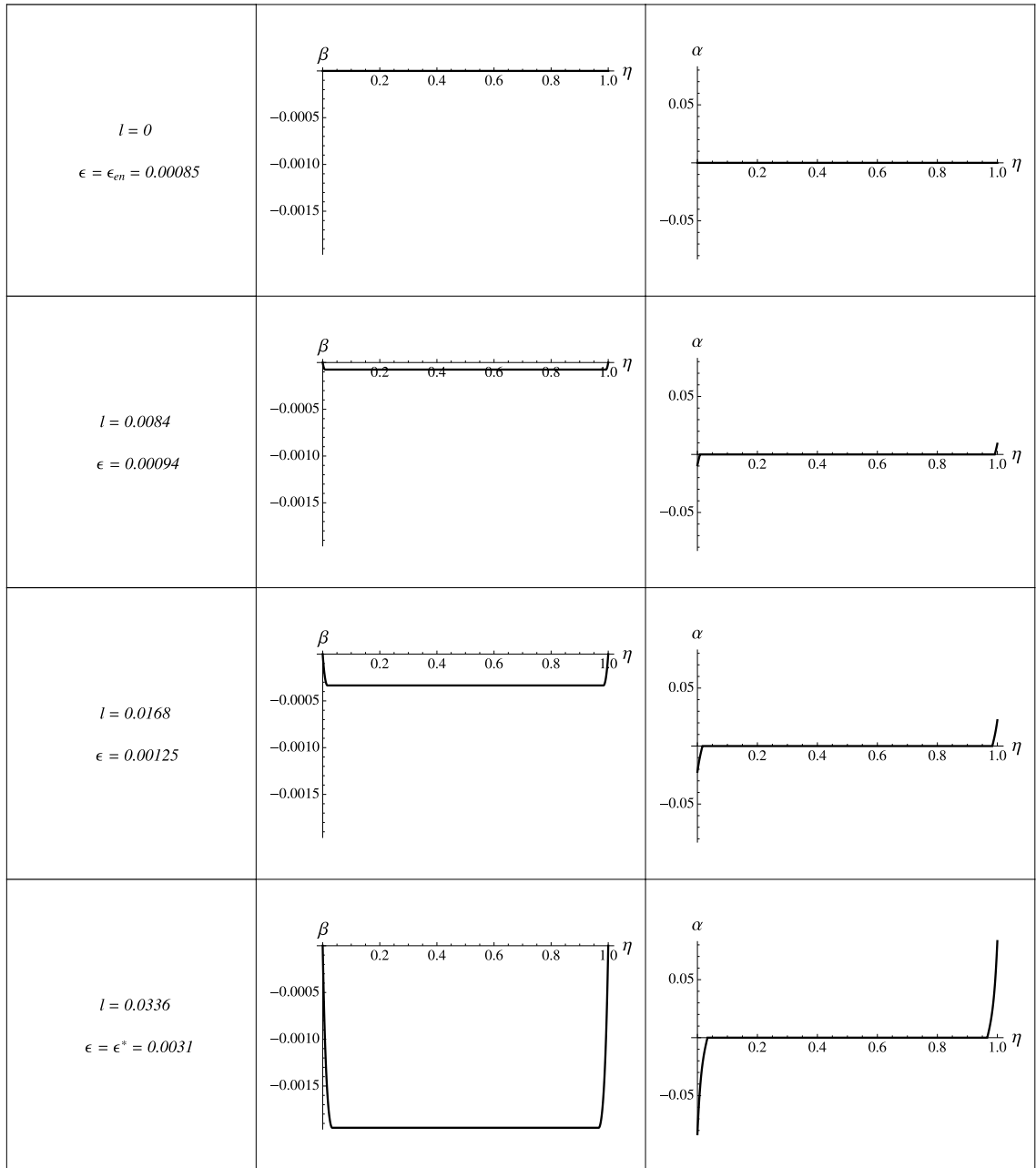


Figure 5.13: Evolution of  $\beta$  and  $\alpha$  for zero dissipation single-slip uniaxial extension of single crystal with  $h = 1\mu\text{m}$  and  $\varphi = 150^\circ$  where  $\eta = y/h$  throughout loading path AB

out

$$\text{sign}\beta = \begin{cases} 0, & \text{for } \varphi = 0^\circ, \\ +1, & \text{for } 0^\circ < \varphi < 90^\circ, \\ -1, & \text{for } 90^\circ < \varphi < 180^\circ, \end{cases} \quad (5.43)$$

so that, for interval  $\eta \in (0, l)$ , we have

$$\text{sign}\beta'_1 = \text{sign}\beta, \quad (5.44)$$

and the opposite sign for interval  $\eta \in (1 - l, 1)$ .

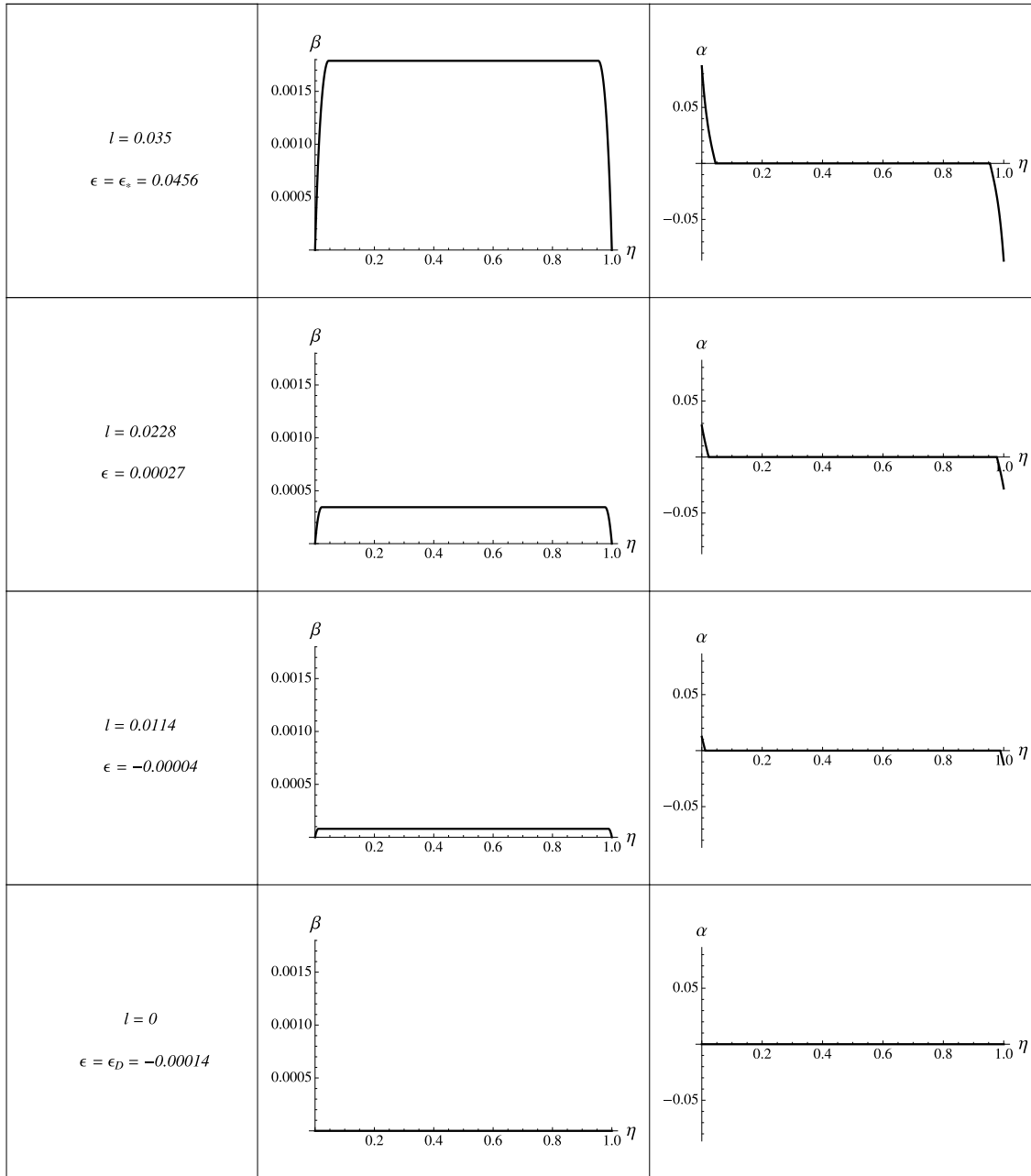


Figure 5.14: Evolution of  $\beta$  and  $\alpha$  for zero dissipation single-slip uniaxial extension of single crystal with  $h = 1\mu\text{m}$  and  $\varphi = 60^\circ$  where  $\eta = y/h$  throughout inverse loading path CD

Following the closed loading path illustrated in Fig. 5.11, we have the following conditions regarding  $\text{sign}\dot{\beta}$ , namely

1. During loading processes (increasing  $\epsilon$ ) OA and DE together with inverse loading process DE (decreasing  $\epsilon$ ), the plastic distortion,  $\beta$ , is frozen so that  $\text{sign}\dot{\beta}=0$ .
2. In the course of loading process AB we have the relation

$$\text{sign}\dot{\beta} = \text{sign}\beta. \quad (5.45)$$

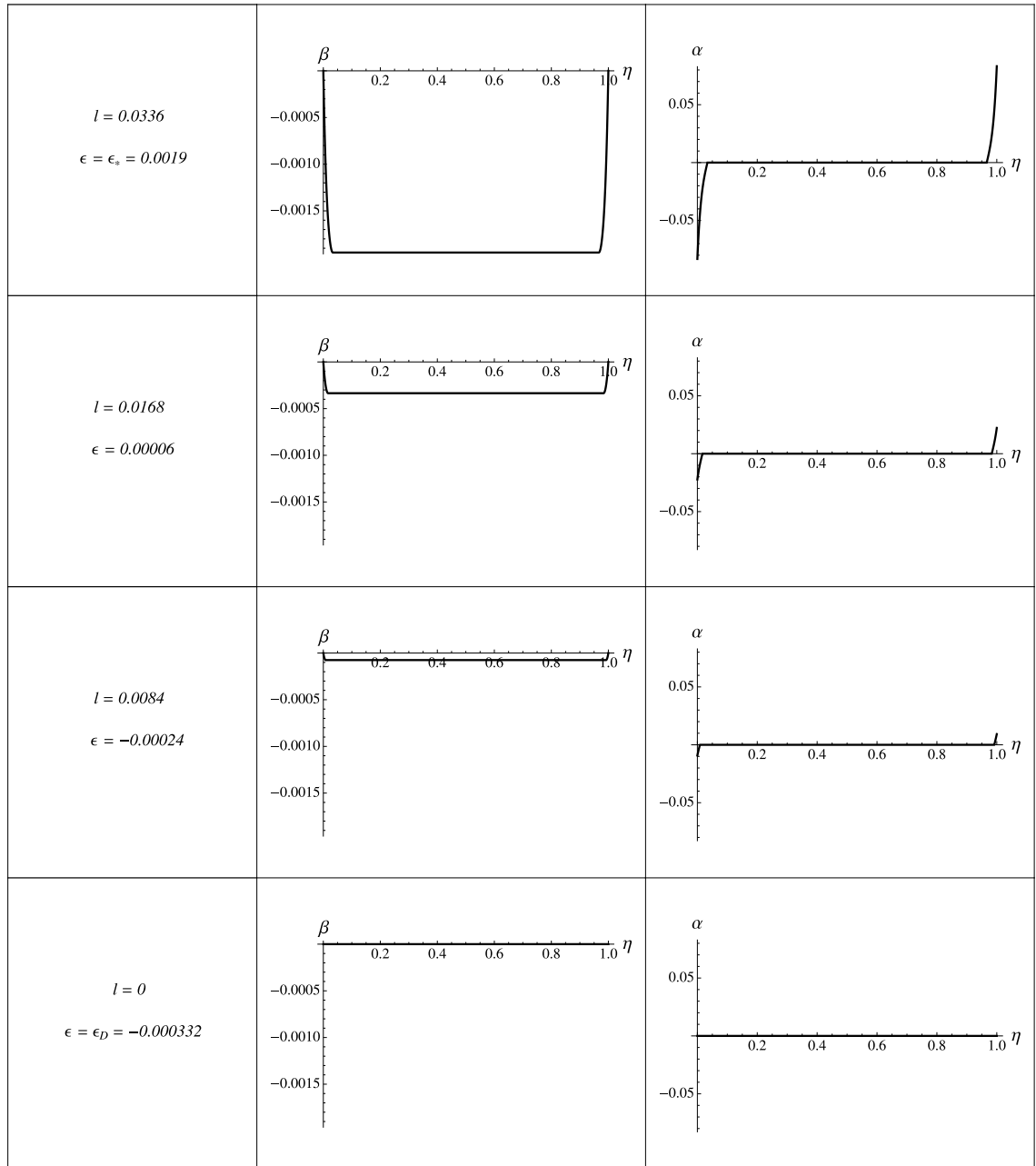


Figure 5.15: Evolution of  $\beta$  and  $\alpha$  for zero dissipation single-slip uniaxial extension of single crystal with  $h = 1\mu\text{m}$  and  $\varphi = 150^\circ$  where  $\eta = y/h$  throughout inverse loading path CD

3. The following relation valid throughout inverse loading CD

$$\text{sign}\dot{\beta} = -\text{sign}\beta. \quad (5.46)$$

For loading path AB, applying (5.45) to (5.40) to obtain

$$\epsilon_r = \epsilon(l) - \frac{\epsilon_{cr}\text{sign}\beta}{\sin 2\varphi}, \quad (5.47)$$

then to energy functional (5.39) and afterwards using the same procedure as in uniaxial extension with zero dissipation case, we obtain the similar solutions as in (5.17)-(5.23) but

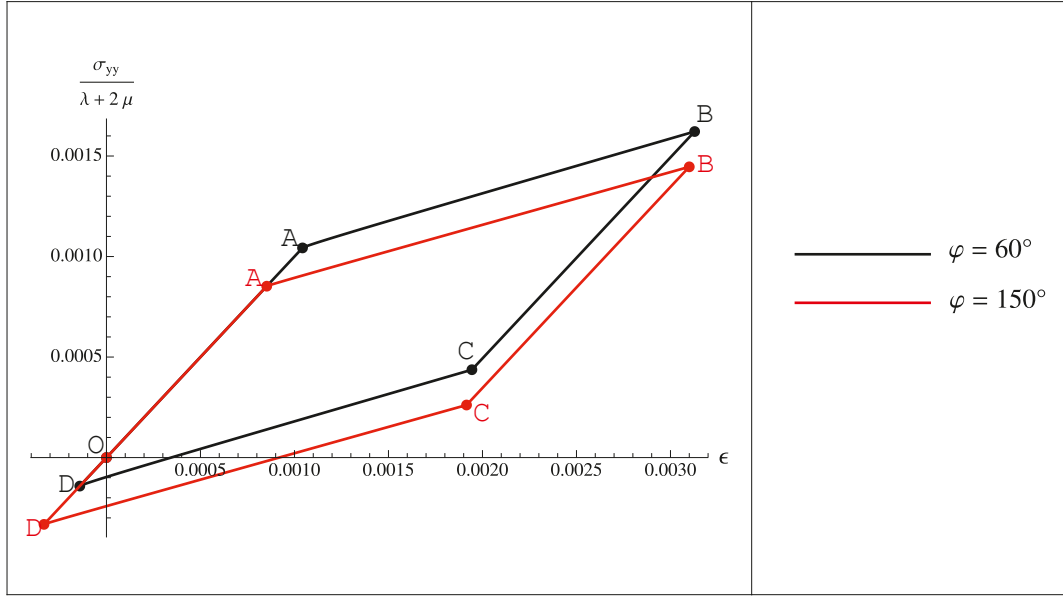


Figure 5.16: Normalized uniaxial tension stress versus strain curves of single-slip constrained shear at non-zero dissipation of single crystal, for  $\varphi = 60^\circ$  and  $\varphi = 150^\circ$

now with  $\epsilon_r$  from (5.47) replacing  $\epsilon$ . The equation of  $\epsilon$  as a function of  $l$  is given by

$$\epsilon(l) = \frac{\text{sign}\beta}{\sin 2\varphi} \left( \epsilon_{cr} + \frac{2k |\sin \varphi| \cosh \zeta l}{c(1-2l) (1 - (\cos^2 2\varphi + \kappa \sin^2 2\varphi) B(l))} \right), \quad (5.48)$$

with  $\text{sign}\beta$  from (5.43) and  $B(l)$  from (5.34). The evolution of  $\beta$  and  $\alpha$  for increasing  $l$  (hence increasing  $\epsilon$ ) in the course of loading path AB at  $\varphi = 60^\circ$  and  $\varphi = 150^\circ$  are shown in Fig. 5.12 and Fig. 5.13, respectively.

On the other hand, for inverse loading path CD, we have the similar solutions as loading path AB but now  $\epsilon_r$  takes the form as

$$\epsilon_u = \epsilon(l) + \frac{\epsilon_{cr} \text{sign}\beta}{\sin 2\varphi}, \quad (5.49)$$

with

$$\epsilon(l) = \frac{\text{sign}\beta}{\sin 2\varphi} \left( -\epsilon_{cr} + \frac{2k |\sin \varphi| \cosh \zeta l}{c(1-2l) (1 - (\cos^2 2\varphi + \kappa \sin^2 2\varphi) B(l))} \right). \quad (5.50)$$

Fig. 5.12 and Fig. 5.13, respectively, illustrate the evolution of  $\beta$  and  $\alpha$  for decreasing  $l$  during inverse loading CD at  $\varphi = 60^\circ$  and  $\varphi = 150^\circ$ .

It is interesting to compute the tensile stress  $\sigma_{yy}$  which is measurable quantity. The normalized tensile stress versus strain equations for closed loading path depicted in Fig. 5.11 are

- Loading path OA:

$$\frac{\sigma_{yy}}{\lambda + 2\mu} = \epsilon. \quad (5.51)$$

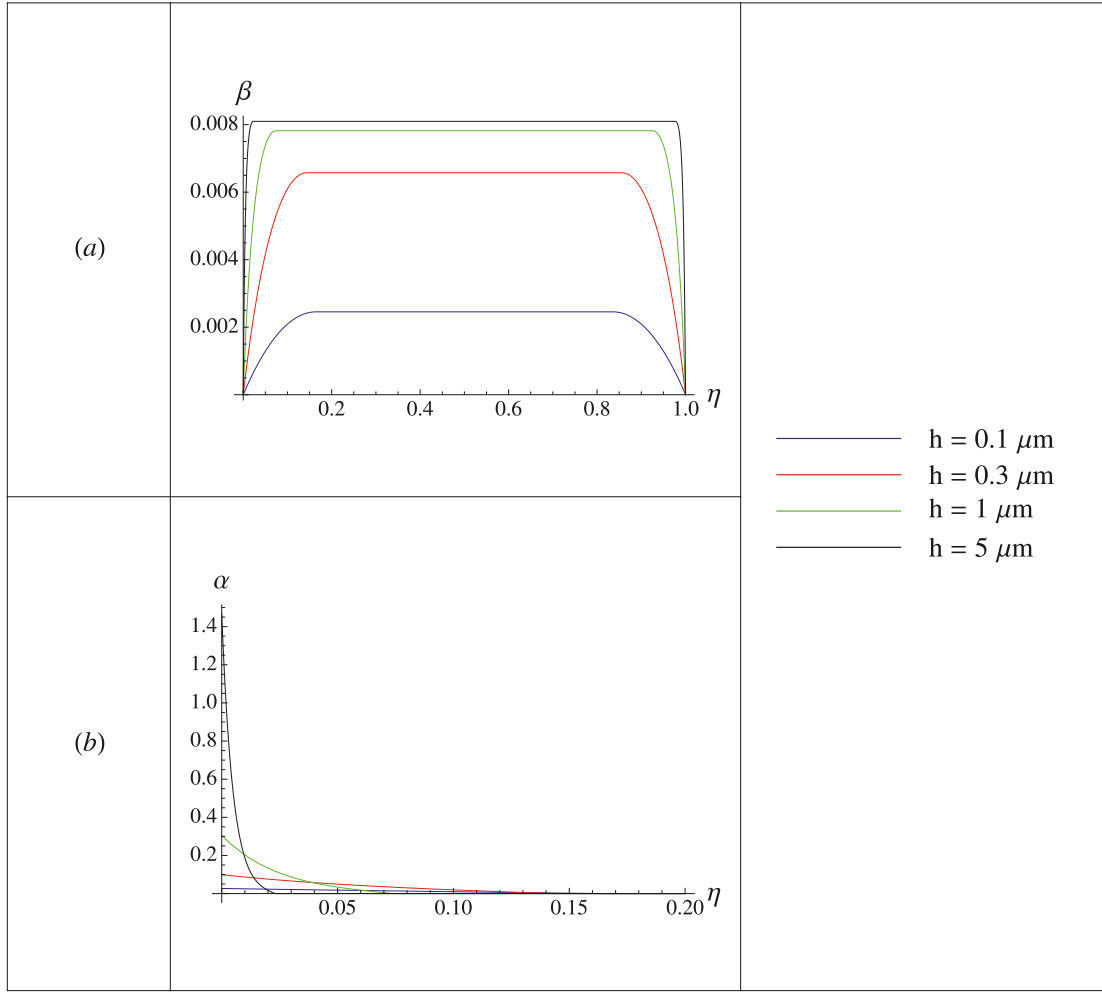


Figure 5.17: Plot of (a):  $\beta$  within the interval  $(0, 1)$  and (b):  $\alpha$  within the interval  $(0, 0.2)$  for non-zero dissipation single-slip uniaxial extension of single crystal at  $\varphi = 60^\circ$  and  $\gamma = 0.01$  with different crystal heights  $h$

- Loading path AB:

$$\frac{\sigma_{yy}}{\lambda + 2\mu} = \epsilon - \kappa \left( \epsilon - \frac{\epsilon_{cr} \text{sign} \beta}{\sin 2\varphi} \right) B(l) \sin^2 2\varphi. \quad (5.52)$$

- Loading path BC:

$$\frac{\sigma_{yy}}{\lambda + 2\mu} = \epsilon + \left( \frac{\sigma_{yy}}{\lambda + 2\mu} \right)_B - \epsilon^*, \quad (5.53)$$

where  $\left( \frac{\sigma_{yy}}{\lambda + 2\mu} \right)_B$  is the solution of (5.52) at  $\epsilon = \epsilon^*$  (point B).

- Loading path CD:

$$\frac{\sigma_{yy}}{\lambda + 2\mu} = \epsilon - \kappa \left( \epsilon + \frac{\epsilon_{cr} \text{sign} \beta}{\sin 2\varphi} \right) B(l) \sin^2 2\varphi. \quad (5.54)$$

- Loading path DE:

$$\frac{\sigma_{yy}}{\lambda + 2\mu} = \epsilon. \quad (5.55)$$

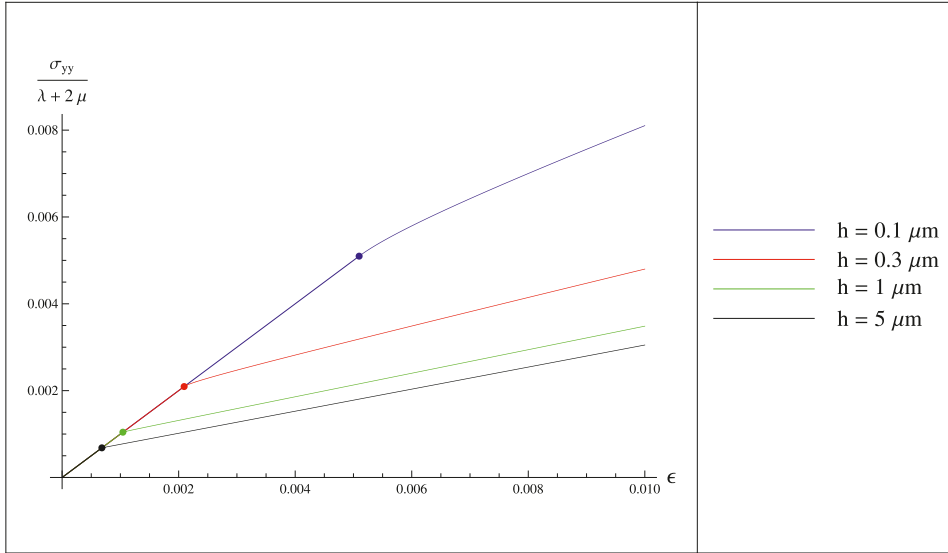


Figure 5.18: Normalized shear stress versus shear strain curve for zero dissipation single-slip uniaxial extension of single crystal at  $\varphi = 60^\circ$  and  $\gamma = 0.01$  with different crystal heights  $h$

The term  $B(l)$  in (5.52) and (5.54) is the reason for the hardening as a result of the dislocation pile-up. Therefore Eq. (5.52) and Eq. (5.54) explain the size effect in this model.

Fig. 5.16 shows the normalized tensile stress versus tensile strain curves for this case at  $\varphi = 60^\circ$  (black line) and  $\varphi = 60^\circ$  (red line) for closed loading path of Fig. 5.11, with  $\epsilon_{cr} = 0.000513$  and  $\epsilon^* = 0.031$  (point B). For increasing  $\epsilon$  from zero to  $\epsilon_{en}$ , straight line OA, corresponds to the pure elastic loading. The nucleation of dislocations starts at point A ( $\epsilon = \epsilon_{en}$ ). Line AB corresponds to the plastic deformation and the work hardening due to the dislocation pile-up is clear to be seen. During the inverse loading as  $\epsilon$  decreases from  $\epsilon^*$  (point B) to  $\epsilon_*$  (point C) the plastic distortion is frozen, namely  $\beta = \beta^*$ . As a consequence, the length of boundary layer at point B ( $l_B$ ) equals to the boundary layer at point C ( $l_C$ ) so that

$$\epsilon_* = \epsilon[l_B],$$

with  $\epsilon(l)$  from (5.50). As  $\epsilon$  decreases further from  $\epsilon_*$  to  $\epsilon_D$  (line CD), the crystal undergoes again the plastic deformation. As  $\epsilon$  is decreased along line CD, the created dislocations start to annihilate and disappear completely at point D. Hence  $\beta = 0$  ( $l_D = 0$ ) at point D and

$$\epsilon_D = \epsilon(0),$$

with  $\epsilon(l)$  from (5.50). Finally, the crystal behaves elastically for increasing  $\epsilon$  from  $\epsilon_D$  to zero. Similar to the plane-constrained shear case, we have also here the translational shift of the yield surface in the stress space (Bauschinger effect).

Fig. 5.17 illustrates the plot of plastic distortions,  $\beta$ , and dislocation densities,  $\alpha$ , for different  $h$  which explains the increasing inner back stress (due to the forced distribution of dislocations more to the middle of crystal for smaller  $h$ ) causing the size effect. Fig. 5.18 shows the plot of normalized tensile stress strain curves for different  $h$  which explains clearly the size effect. The dot at each curve in Fig. 5.18 describes the energetic yield point.

### 5.3.2 Plane-constrained combined loading

In this case with single crystal with one active slip system undergoing combined loading, we use  $\delta$  as the driving variable to find the plastic distortion  $\beta$ . Adopting similar algebraic manipulation idea as in section 5.3.1, we can write the effective energy for this case in the form

$$\hat{E}(\beta) = \int_0^1 \left[ \frac{1}{2\kappa} (\delta_r \sin \theta - \kappa \langle \beta \rangle \sin 2\varphi)^2 + \frac{1}{2} (\delta_r \cos \theta - \langle \beta \rangle \cos 2\varphi)^2 + \frac{1}{2} (1 - \kappa) \beta^2 \sin^2 2\varphi + k \left( \frac{|\beta'| |\sin \varphi|}{c} + \frac{1}{2} \frac{(\beta')^2 \sin^2 \varphi}{c^2} \right) \right] d\eta, \quad (5.56)$$

with

$$\delta_r = \delta - \frac{\delta_{cr} \text{sign} \dot{\beta}}{\cos(\theta - 2\varphi)}, \quad (5.57)$$

and

$$\langle \beta \rangle = \int_0^1 \beta d\eta. \quad (5.58)$$

Since the effective energy functional (5.56) resembles the energy functional (5.29) but now with  $\delta_r$  instead of  $\delta$ , we can obtain the similar solutions as in section 5.2.2 (Eq. (5.31) - Eq. (5.37)) with  $\delta_r$  replacing  $\delta$ .

The energetic threshold value, in term of the original length  $h$ , where the plastic deformation starts to appear yields

$$\delta_{en} = \frac{\delta_{cr}}{|\cos(\theta - 2\varphi)|} + \frac{2k}{hb\rho_s} \frac{|\sin \varphi|}{|\cos(\theta - 2\varphi)|}, \quad (5.59)$$

which exhibits the size effect. From the energetic threshold value derivation for this case we found again the similar relation with (5.35) to determine the sign of  $\beta$  for  $\beta \neq 0$ .

For  $\beta$  is frozen, during elastic deformation, we have  $\dot{\beta} = 0$ . In the course of increasing  $\delta$  (loading process), where  $\dot{\beta} \neq 0$ , we have the relation

$$\text{sign} \dot{\beta} = \text{sign} \beta.$$

The equation of  $\delta_r$  during the loading process is given by

$$\delta_r = \delta(l) - \frac{\delta_{cr} \text{sign} \dot{\beta}}{\cos(\theta - 2\varphi)}, \quad (5.60)$$

with

$$\delta(l) = \frac{\text{sign} \dot{\beta}}{\cos(\theta - 2\varphi)} \left( \delta_{cr} + \frac{2k |\sin \varphi| \cosh \zeta l}{c(1 - 2l) (1 - (\cos^2 2\varphi + \kappa \sin^2 2\varphi) B(l))} \right). \quad (5.61)$$

All along the inverse loading (decreasing  $\delta$ ), for  $\dot{\beta} \neq 0$ , we have

$$\text{sign} \dot{\beta} = -\text{sign} \beta,$$

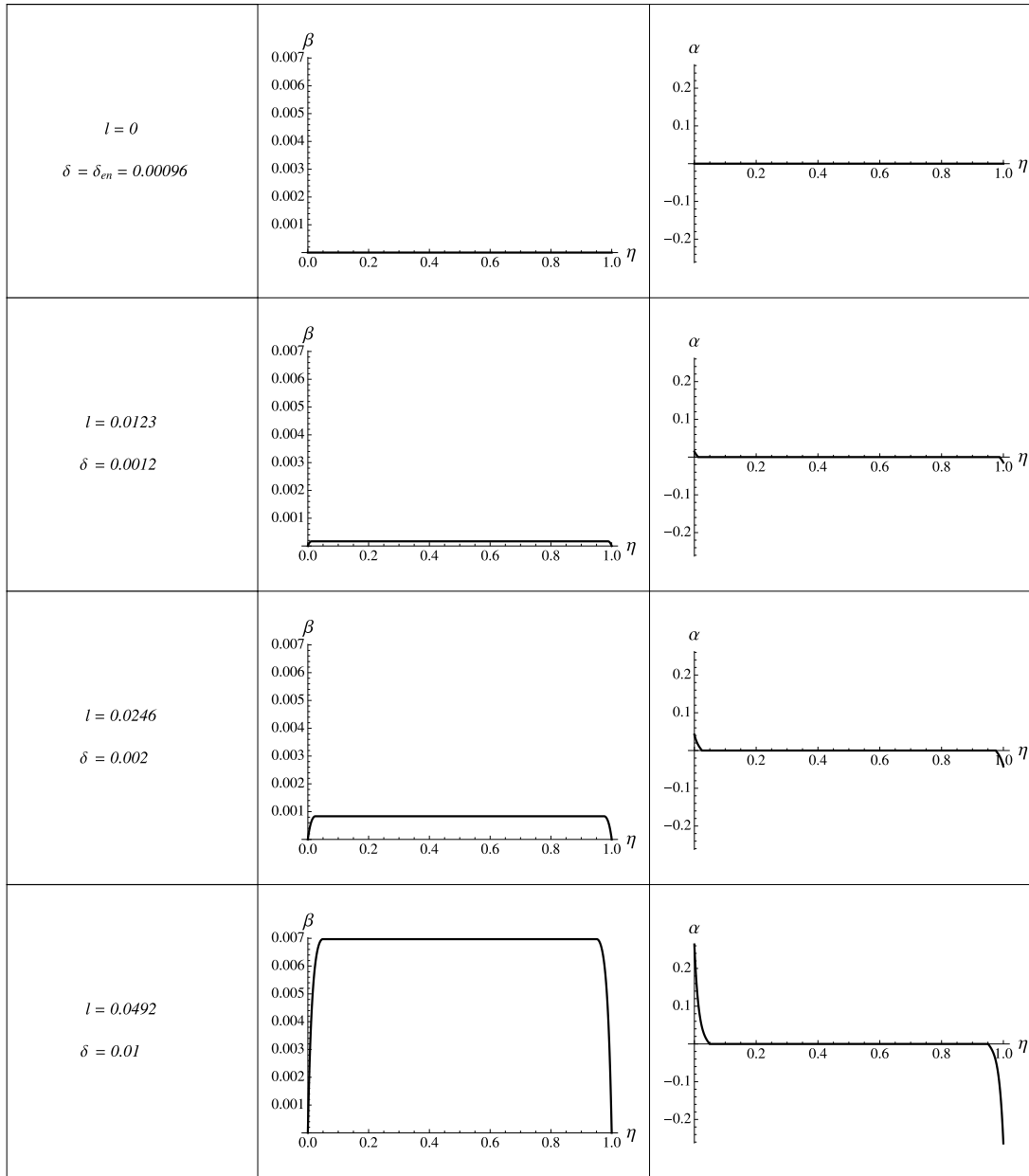


Figure 5.19: Evolution of  $\beta$  and  $\alpha$  for single slip combine loading of single crystal at non-zero dissipation in the course of increasing  $\delta$  where  $h = 1\mu\text{m}$ ,  $\varphi = 30^\circ$  and  $\theta = 20^\circ$  at increasing  $\delta$

so that

$$\delta_r = \delta(l) + \frac{\delta_{cr} \text{sign} \beta}{\cos(\theta - 2\varphi)}, \quad (5.62)$$

with

$$\delta(l) = \frac{\text{sign} \beta}{\cos(\theta - 2\varphi)} \left( -\delta_{cr} + \frac{2k |\sin \varphi| \cosh \zeta l}{c(1 - 2l) (1 - (\cos^2 2\varphi + \kappa \sin^2 2\varphi) B(l))} \right). \quad (5.63)$$

The evolution of  $\beta$  and  $\alpha$  for increasing  $\delta$  is shown in Fig. 5.19. Fig. 5.20 illustrates the evolution of  $\beta$  and  $\alpha$  in the course of loading process at  $\delta = 0.01$  for increasing  $\theta$ .

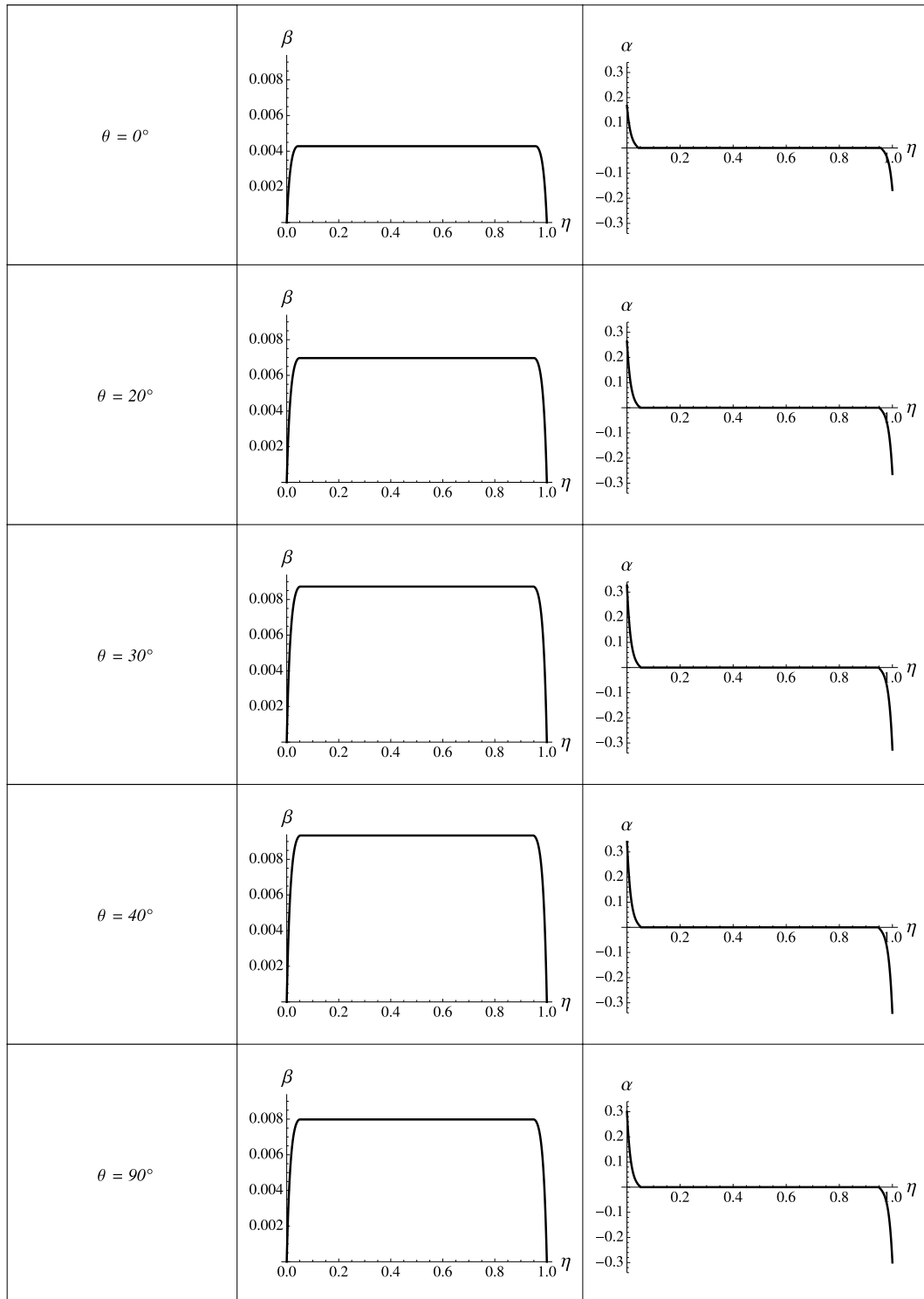


Figure 5.20: Evolution of  $\beta$  and  $\alpha$  of single crystal with one active slip system at non-zero dissipation in the course of loading at  $\delta = 0.01$  for increasing  $\theta$



## 6 Single crystals plane-constrained shear problem with double slip systems

Following the previous chapter 4, we extend the results to the plane-strain constrained shear of a single crystal strip deforming in double slip by adding the second slip system to the crystal from Fig. 4.1. Our aim is two fold. We are going first to find the solutions in closed analytical form for crystals deforming in symmetric double slip then develop numerical procedures for crystals deforming in non-symmetric double slip.

### 6.1 Energy of the crystal

We consider again the strip made up of a single crystal undergoing a plane-strain shear deformation with a rectangle cross section of width  $a$  and height  $h$  ( $0 \leq x \leq a$ ,  $0 \leq y \leq h$ ) as can be seen in Fig. 6.1. In order to realize the shear deformation, the strip is mounted in a "hard" device with the prescribed displacements:

$$u(0) = 0, \quad v(0) = 0 \quad u(h) = \gamma h, \quad v(h) = 0, \quad (6.1)$$

with  $\gamma$ ,  $u(y)$  and  $v(y)$  are the overall shear strain, the longitudinal and transverse displacements respectively. Again with the assumption that the strip length,  $L$ , is very large and the width,  $a$ , is much greater than the height,  $h$ , so that  $L \geq a \geq h$ , we can neglect the end effects and have the stresses and strains depending only on  $y$  in the central part of the strip.

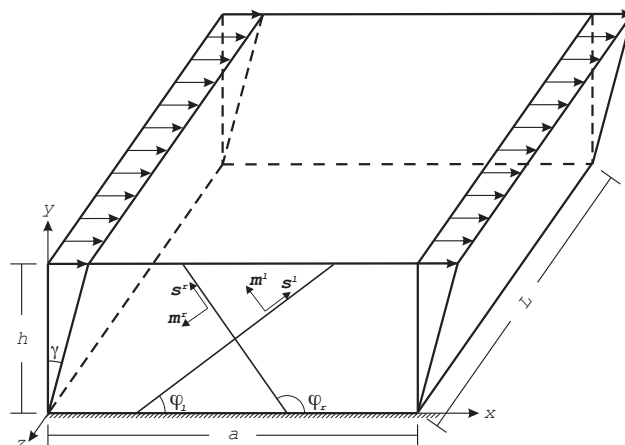


Figure 6.1: Plane-strain constrained shear of single crystal deforming in double-slip

The in-plane components of the strain tensor for the plane strain state are

$$\varepsilon_{xx} = 0, \quad \varepsilon_{xy} = \varepsilon_{yx} = \frac{1}{2}u_{,y}, \quad \varepsilon_{yy} = v_{,y} \quad (6.2)$$

For sufficiently small shear strain,  $\gamma$ , the crystal deforms elastically. On the other hand, for  $\gamma$  exceeding some critical threshold, the edge dislocation may appear in the crystal.

As shown in Fig 6.1, we denote the two slip directions perpendicular to the  $z$ -axis and inclined at an angle  $\varphi_l$  ( $0 \leq \varphi_l \leq \pi/2$ ) and  $\varphi_r$  ( $\pi/2 \leq \varphi_r \leq \pi$ ) with the  $x$ -axis by  $s^l$  and  $s^r$ , respectively, and assume that the dislocation lines are parallel to the  $z$ -axis. With  $s_i^\alpha = (\cos \varphi_\alpha, \sin \varphi_\alpha, 0)^T$  being the slip directions, and  $m_j^\alpha = (-\sin \varphi_\alpha, \cos \varphi_\alpha, 0)^T$  the normal vectors to the slip planes ( $\alpha = l, r$ ), the plastic distortion for two active slip systems,  $\beta_{ij} = \beta_l s_i^l m_j^l + \beta_r s_i^r m_j^r$ , can be written as

$$\beta_{ij} = \begin{pmatrix} -\beta_l \sin \varphi_l \cos \varphi_l - \beta_r \sin \varphi_r \cos \varphi_r & \beta_l \cos^2 \varphi_l + \beta_r \cos^2 \varphi_r \\ -\beta_l \sin^2 \varphi_l - \beta_r \sin^2 \varphi_r & \beta_l \sin \varphi_l \cos \varphi_l + \beta_r \sin \varphi_r \cos \varphi_r \end{pmatrix}. \quad (6.3)$$

We suppose that  $\beta_l$  and  $\beta_r$  depend on  $y$  only:  $\beta_l = \beta_l(y)$  and  $\beta_r = \beta_r(y)$ . It follows from the prescribed boundary conditions (6.1) that dislocations cannot penetrate the boundaries  $y = 0$  and  $y = h$ , so

$$\beta_l(0) = \beta_r(0) = \beta_l(h) = \beta_r(h) = 0. \quad (6.4)$$

The non-zero components of the plastic tensor  $\varepsilon_{ij}^p = \frac{1}{2}(\beta_{ij} + \beta_{ji})$  under the plane strain state condition are in the form

$$\begin{aligned} \varepsilon_{xx}^p &= -\frac{1}{2}(\beta_l \sin 2\varphi_l + \beta_r \sin 2\varphi_r), \\ \varepsilon_{xy}^p &= \frac{1}{2}(\beta_l \cos 2\varphi_l + \beta_r \cos 2\varphi_r), \\ \varepsilon_{yy}^p &= \frac{1}{2}(\beta_l \sin 2\varphi_l + \beta_r \sin 2\varphi_r). \end{aligned} \quad (6.5)$$

Then, by substituting (6.2) and (6.5) into  $\varepsilon_{ij}^e = \varepsilon_{ij} - \varepsilon_{ij}^p$ , the components of the elastic strain tensor can be written as

$$\begin{aligned} \varepsilon_{xx}^e &= \frac{1}{2}(\beta_l \sin 2\varphi_l + \beta_r \sin 2\varphi_r), \\ \varepsilon_{xy}^e &= \frac{1}{2}(u_{,y} - \beta_l \cos 2\varphi_l - \beta_r \cos 2\varphi_r), \\ \varepsilon_{yy}^e &= v_{,y} - \frac{1}{2}(\beta_l \sin 2\varphi_l + \beta_r \sin 2\varphi_r). \end{aligned} \quad (6.6)$$

With  $\beta_l$  and  $\beta_r$  depending only on  $y$ , the two non-zero components of dislocation density tensor [Bilby, 1955, Kröner, 1955, Nye, 1953] read

$$\begin{aligned} \alpha_{xz} &= \beta_{l,y} \sin \varphi_l \cos \varphi_l + \beta_{r,y} \sin \varphi_r \cos \varphi_r, \\ \alpha_{yz} &= \beta_{l,y} \sin^2 \varphi_l + \beta_{r,y} \sin^2 \varphi_r. \end{aligned} \quad (6.7)$$

which are the components of the resultant Burgers' vector of all edge dislocations whose dislocation lines cut the area perpendicular to the  $z$ -axis. We see the dislocations produced by two slip systems belong to two different groups: the first one with the resultant Burgers' vector showing in the direction  $s_i^l$ , the second one with the resultant Burgers' vector parallel to  $s_i^r$ . In consequence the scalar dislocation densities take the form

$$\rho_l = \frac{1}{b} |\beta_{l,y} \sin \varphi_l|, \quad \rho_r = \frac{1}{b} |\beta_{r,y} \sin \varphi_r|, \quad (6.8)$$

where  $b$  is the magnitude of the Burgers' vector.

The energy density of the dislocation network for single crystals with two active slip systems is assume to be given as

$$\Phi_m(\rho_l, \rho_r) = \mu k \left( \ln \frac{1}{1 - \frac{\rho_l}{\rho_s}} + \ln \frac{1}{1 - \frac{\rho_r}{\rho_s}} + \chi \frac{\rho_l \rho_r}{\rho_s^2} \right), \quad (6.9)$$

which consists of energies of each dislocations plus the energy of cross-slip interaction, with  $\rho_s$  being the saturated dislocation density and  $\chi$  the interaction factor.

By first applying (6.6) and (6.8) to (6.9) then to (3.11) and afterwards integrating over the volume, the total energy functional takes the form

$$\begin{aligned} \Psi(u, v, \beta_l, \beta_r) = aL \int_0^h & \left[ \frac{1}{2} \lambda v_{,y}^2 + \frac{\mu}{2} (u_{,y} - \beta_l \cos 2\varphi_l - \beta_r \cos 2\varphi_r)^2 \right. \\ & + \frac{\mu}{4} (\beta_l \sin 2\varphi_l + \beta_r \sin 2\varphi_r)^2 + \frac{\mu}{2} (2v_{,y} - \beta_l \sin 2\varphi_l - \beta_r \sin 2\varphi_r)^2 \\ & \left. + \mu k \left( \ln \frac{1}{1 - \frac{\rho_l}{\rho_s}} + \ln \frac{1}{1 - \frac{\rho_r}{\rho_s}} + \chi \frac{\rho_l \rho_r}{\rho_s^2} \right) \right] dy. \end{aligned} \quad (6.10)$$

We can again reduce the energy functional (6.10) to a functional depending on  $\beta_l(y)$  and  $\beta_r(y)$  only. Following the same procedure as in Eq. (4.11) - Eq. (4.19), we find that

$$\begin{aligned} u_{,y} &= \gamma + (\beta_l - \langle \beta_l \rangle) \cos 2\varphi_l + (\beta_r - \langle \beta_r \rangle) \cos 2\varphi_r, \\ v_{,y} &= \kappa (\beta_l - \langle \beta_l \rangle) \sin 2\varphi_l + \kappa (\beta_r - \langle \beta_r \rangle) \sin 2\varphi_r, \end{aligned} \quad (6.11)$$

where

$$\kappa = \frac{\mu}{\lambda + 2\mu},$$

and the average of  $\beta_l$  and  $\beta_r$  are defined as

$$\langle \beta_l \rangle = \frac{1}{h} \int_0^h \beta_l dy, \quad \langle \beta_r \rangle = \frac{1}{h} \int_0^h \beta_r dy. \quad (6.12)$$

Substituting the asymptotic formulas

$$\ln \frac{1}{1 - \frac{\rho_l}{\rho_s}} \cong \frac{\rho_l}{\rho_s} + \frac{1}{2} \left( \frac{\rho_l}{\rho_s} \right)^2, \quad \ln \frac{1}{1 - \frac{\rho_r}{\rho_s}} \cong \frac{\rho_r}{\rho_s} + \frac{1}{2} \left( \frac{\rho_r}{\rho_s} \right)^2, \quad (6.13)$$

and (6.11) into (6.10) then collecting the common terms, the energy functional in terms of  $\beta_l$  and  $\beta_r$  admits the form

$$\begin{aligned} \Psi(\beta_l, \beta_r) = aL \int_0^h & \mu \left[ \frac{1}{2} (\langle \beta_l \rangle \cos 2\varphi_l + \langle \beta_r \rangle \cos 2\varphi_r - \gamma)^2 \right. \\ & + \frac{\kappa}{2} (\langle \beta_l \rangle \sin 2\varphi_l + \langle \beta_r \rangle \sin 2\varphi_r)^2 + \frac{1 - \kappa}{2} (\beta_l \sin 2\varphi_l + \beta_r \sin 2\varphi_r)^2 \\ & + \frac{k}{b\rho_s} (|\beta_{l,y} \sin \varphi_l| + |\beta_{r,y} \sin \varphi_r|) + \frac{k}{2(b\rho_s)^2} (\beta_{l,y}^2 \sin^2 \varphi_l + \beta_{r,y}^2 \sin^2 \varphi_r \\ & \left. + 2\chi |\beta_{l,y} \sin \varphi_l| |\beta_{r,y} \sin \varphi_r| \right] dy, \end{aligned} \quad (6.14)$$

with  $\langle \beta_l \rangle$  and  $\langle \beta_r \rangle$  from (6.12).

## 6.2 Double slip plane-constrained shear at zero resistance

Similar to the single-slip case, the determination of  $\beta_l(y)$  and  $\beta_r(y)$  in the case of double slip constrained shear of single crystal at zero dissipation reduces to the minimization of the total energy (6.14) under the constraints (6.4).

In order to have the unique solution for this variational problem, the free energy per unit volume  $\Phi$  from (6.9) must be convex with respect to  $\beta_l$ ,  $\beta_r$ ,  $\beta'_l$  and  $\beta'_r$ . Since  $\Phi$  is convex with respect to  $\beta_l$  and  $\beta_r$ , we need to investigate the convexity of  $\Phi$  with respect to  $\beta'_l$  and  $\beta'_r$ . For this purpose let us consider the matrix

$$\begin{pmatrix} \Phi_{,\beta'_l\beta'_l} & \Phi_{,\beta'_l\beta'_r} \\ \Phi_{,\beta'_r\beta'_l} & \Phi_{,\beta'_r\beta'_r} \end{pmatrix} = k \sin^2 \varphi \begin{pmatrix} 1 & \chi \text{sign}\beta'_l \text{sign}\beta'_r \\ \chi \text{sign}\beta'_l \text{sign}\beta'_r & 1 \end{pmatrix} \quad (6.15)$$

It is noticeable that for  $\varphi \neq 0$  and  $\chi < 1$ , matrix (6.15) is positive definite. For that reason, the energy density  $\Phi$  is convex with respect to  $\beta'_l$  and  $\beta'_r$ . For  $\chi = 1$  the determinant of the matrix becomes zero and there exists the eigenvector corresponding to zero eigenvalue. Hence, the energy is no longer strictly convex for  $\chi = 1$  and one may expect non-uniqueness of the minimizer as well as some numerical instability. To prevent this instability we will assume that  $\chi < 1$ .

For the numerical simulation in this section, as in single slip case, we adopt again the material parameters from Table 3.1, with additional parameter  $\chi = 0.576$ .

### 6.2.1 Energetic threshold values

When we load a single crystal with double active slip systems, by increasing  $\gamma$ , only one slip system is activated in the beginning. Then the crystal deforms with only one slip system up to some point where the second slip system is activated. Therefore for the variational problem of this type, there exist the energetic threshold values  $\gamma_{en1}$  and  $\gamma_{en2}$  such as:

- when  $\gamma < \gamma_{en1}$ , no dislocations are nucleated and  $\beta_l = \beta_r = 0$ ,
- if  $\gamma_{en1} \leq \gamma < \gamma_{en2}$ , only one slip system is active so either the condition  $\beta_l = 0$ ,  $\beta_r \neq 0$  or the condition  $\beta_r = 0$ ,  $\beta_l \neq 0$  is true,
- while  $\gamma \geq \gamma_{en2}$ , both slip systems are fully activated with now  $\beta_l \neq 0$  and  $\beta_r \neq 0$ .

Again for convenient we introduce the following dimensionless quantities

$$E = \frac{\Psi}{\mu a L h}, \quad \eta = \frac{y}{h}, \quad \bar{\beta}_l(\eta) = \beta_l(y), \quad \bar{\beta}_r(\eta) = \beta_r(y), \quad c = h b \rho_s, \quad (6.16)$$

with  $\eta \in (0, 1)$ . Then the energy functional (6.14) in terms of these dimensionless quantities becomes

$$\begin{aligned}
E(\bar{\beta}_l, \bar{\beta}_r) = & \int_0^1 \left[ \frac{1}{2} (\langle \bar{\beta}_l \rangle \cos 2\varphi_l + \langle \bar{\beta}_r \rangle \cos 2\varphi_r - \gamma)^2 \right. \\
& + \frac{\kappa}{2} (\langle \bar{\beta}_l \rangle \sin 2\varphi_l + \langle \bar{\beta}_r \rangle \sin 2\varphi_r)^2 + \frac{1-\kappa}{2} (\bar{\beta}_l \sin 2\varphi_l + \bar{\beta}_r \sin 2\varphi_r)^2 \\
& + \frac{k}{c} (|\bar{\beta}_l' \sin \varphi_l| + |\bar{\beta}_r' \sin \varphi_r|) + \frac{k}{2c^2} ((\bar{\beta}_l')^2 \sin^2 \varphi_l + (\bar{\beta}_r')^2 \sin^2 \varphi_r \\
& \left. + 2\chi |\bar{\beta}_l' \sin \varphi_l| |\bar{\beta}_r' \sin \varphi_r| \right] d\eta, \tag{6.17}
\end{aligned}$$

with

$$\langle \bar{\beta}_l \rangle = \int_0^1 \bar{\beta}_l d\eta, \quad \langle \bar{\beta}_r \rangle = \int_0^1 \bar{\beta}_r d\eta. \tag{6.18}$$

For short we drop the bars over  $\bar{\beta}_l$ ,  $\bar{\beta}_r$ ,  $\langle \bar{\beta}_l \rangle$  and  $\langle \bar{\beta}_r \rangle$  for the future computation.

We propose two possible cases to find these energetic threshold values. The first case to find these energetic threshold values is where  $\beta_l$  appears first when we apply the load. For the second case is where  $\beta_r$  emerges first instead of  $\beta_l$  in the course of loading. Due to the similar procedure, the derivation of the first case will be given in detail then followed by the results of the second case.

For the first case, at  $\gamma_{en1} \leq \gamma < \gamma_{en2}$ , we apply  $\beta_r = 0$  in the energy functional (6.17) which gives

$$\begin{aligned}
E = & \int_0^1 \left[ \frac{1}{2} \kappa \langle \beta_l \rangle^2 \sin^2 2\varphi_l + \frac{1}{2} (\langle \beta_l \rangle \cos 2\varphi_l - \gamma)^2 + \frac{1}{2} (1-\kappa) \beta_l^2 \sin^2 2\varphi_l \right. \\
& \left. + k \left( \frac{|\beta_l'| |\sin \varphi_l|}{c} + \frac{1}{2} \frac{(\beta_l')^2 \sin^2 \varphi_l}{c^2} \right) \right] d\eta, \tag{6.19}
\end{aligned}$$

with  $\langle \beta_l \rangle$  from (6.18).

To obtain the first energetic threshold value,  $\gamma_{en1}$ , we use the same idea as in section 4.2.1 by employing the minimizing sequence in the form

$$\beta_l = \begin{cases} \frac{\beta_{lm}}{\xi} \eta, & \text{for } \eta \in (0, \xi), \\ \beta_{lm}, & \text{for } \eta \in (\xi, 1-\xi), \\ \frac{\beta_{lm}}{\xi} (1-\eta), & \text{for } \eta \in (1-\xi, 1), \end{cases} \tag{6.20}$$

where  $\beta_{lm}$  is unknown constants, and  $\xi$  is a small unknown length which tends to zero as  $\gamma \rightarrow \gamma_{en1}$ . Since  $\beta_{lm}$  is negligibly small near  $\gamma_{en1}$ , the quadratic term of energy functional (6.19) is ignored during threshold value calculation. With the last term being removed, we apply (6.20) to the energy functional (6.19) giving

$$\begin{aligned}
E(\beta_{lm}) = & \int_0^\xi \left[ (1-\kappa) \frac{\beta_{lm}}{\xi} \eta \sin^2 2\varphi_l + \frac{2k}{c} \frac{|\beta_{lm}| |\sin \varphi_l|}{\xi} \right] d\eta \\
& + \frac{1-\kappa}{2} (1-2\xi) \beta_{lm}^2 \sin^2 2\varphi_l + \frac{\kappa}{2} \langle \beta_l \rangle^2 \sin^2 2\varphi_l + \frac{1}{2} (\langle \beta_l \rangle \cos 2\varphi_l - \gamma)^2 \tag{6.21}
\end{aligned}$$

where the average of  $\beta_l$  takes the form

$$\langle \beta_l \rangle = 2 \int_0^\xi \frac{\beta_{lm}}{\xi} \eta \, d\eta + (1 - 2\xi) \beta_{lm}. \quad (6.22)$$

Integrating (6.21) and (6.22) then disregarding all small terms of order  $\xi$  and higher, we arrive at  $\langle \beta_{lm} \rangle = \beta_{lm}$  and the energy functional

$$E(\beta_{lm}) = \frac{1}{2}(\gamma - \beta_{lm} \cos 2\varphi_l)^2 + \beta_{lm}^2 \sin^2 2\varphi_l + \frac{2k}{c} |\beta_{lm}| |\sin \varphi_l|. \quad (6.23)$$

We set the partial derivatives of (6.23) with respect to  $\beta_{lm}$  equal to zero to find the minimum of the energy.

For  $\varphi_l \in (0^\circ, 45^\circ)$ , a rather simple analysis shows that the minimum of (6.23) is achieved at

$$\beta_{lm} = \frac{1}{2 \cos 2\varphi_l} \left( \gamma - \frac{2k |\sin \varphi_l|}{c \cos 2\varphi_l} \right) > 0, \quad (6.24)$$

and for  $\varphi_l \in (45^\circ, 90^\circ)$  we have

$$\beta_{lm} = \frac{1}{2 \cos 2\varphi_l} \left( \gamma + \frac{2k |\sin \varphi_l|}{c \cos 2\varphi_l} \right) < 0, \quad (6.25)$$

if and only if

$$\gamma > \gamma_{en1} = \frac{2k |\sin \varphi_l|}{c |\cos 2\varphi_l|}, \quad (6.26)$$

otherwise it is achieved at  $\beta_{lm} = 0$  (no dislocations are nucleated).

Based on the previous conditions (6.24) and (6.25) from the previous analysis, we can say that  $\beta_l > 0$  if  $\varphi_l \in (0^\circ, 45^\circ)$  and  $\beta_l < 0$  if  $\varphi_l \in (45^\circ, 90^\circ)$ . It can also be concluded that  $\text{sign} \beta_l'$  for interval  $\eta \in (0, l)$

$$\text{sign} \beta_l' = \begin{cases} 0, & \text{for } \varphi_l = 0^\circ, \\ +1, & \text{for } 0^\circ < \varphi_l < 45^\circ, \\ -1, & \text{for } 45^\circ < \varphi_l < 90^\circ, \end{cases} \quad (6.27)$$

and, due to the symmetry, will change its sign for interval  $\eta \in (1 - l, 1)$ .

Now, starting from  $\gamma_{en1}$  up to  $\gamma_{en2}$ , we have again the case with one active slip system. Therefore, following the same procedure as in section (4.2.2), we obtain the solutions for the range  $\gamma_{en1} \leq \gamma < \gamma_{en2}$ , namely

$$\beta_l = \begin{cases} \beta_{lp}(1 - \cosh \zeta \eta + \tanh \zeta l \sinh \zeta \eta), & \text{for } \eta \in (0, l), \\ \beta_{lm} = \beta_{lp} \left( 1 - \frac{1}{\cosh \zeta l} \right), & \text{for } \eta \in (l, 1 - l), \\ \beta_{lp}(1 - \cosh \zeta(1 - \eta) + \tanh \zeta l \sinh \zeta(1 - \eta)), & \text{for } \eta \in (1 - l, 1), \end{cases} \quad (6.28)$$

with

$$\beta_{lp} = \frac{\gamma \cos 2\varphi_l - (\cos^2 2\varphi_l + \kappa \sin^2 2\varphi_l) \langle \beta_l \rangle}{(1 - \kappa) \sin^2 2\varphi_l} \quad \text{and} \quad \zeta = 2c |\cos \varphi_l| \sqrt{\frac{1 - \kappa}{k}}. \quad (6.29)$$

The average of  $\beta_l$  takes the form

$$\langle \beta_l \rangle = \gamma \cos 2\varphi_l B_l(l), \quad (6.30)$$

with

$$B_l(l) = \frac{g(l)}{(1 - \kappa) \sin^2 2\varphi_l + g(l)(\cos^2 2\varphi_l + \kappa \sin^2 2\varphi_l)}, \quad (6.31)$$

and

$$g(l) = 2 \left( l - \frac{\tanh \zeta l}{\zeta} \right) + \left( 1 - \frac{1}{\cosh \zeta l} \right) (1 - 2l). \quad (6.32)$$

The equation of  $\gamma$  as a function of  $l$  takes the form

$$\gamma(l) = \frac{2k |\sin \varphi_l| \operatorname{sign} \beta_l' \cosh \zeta l}{c(1 - 2l) \cos 2\varphi_l (1 - (\cos^2 2\varphi_l + \kappa \sin^2 2\varphi_l) B_l(l))}, \quad (6.33)$$

where  $\operatorname{sign} \beta_l'$  from (6.27).

In order to find the second energetic threshold value,  $\gamma_{en2}$ , the following considerations are taken into account

- The width of boundary layer of  $\beta_r$ ,  $\xi$ , approaches zero at  $\gamma \rightarrow \gamma_{en2}$ .
- Since  $\xi \rightarrow 0$  at  $\gamma_{en2}$ , we can assume that  $\beta_l$  is linear in interval  $\eta \in (0, \xi)$  and  $\eta \in (1 - \xi, 1)$ , namely,  $\frac{\beta_l(\xi)}{\xi} \eta$  and  $\frac{\beta_l(1-\xi)}{\xi} (1 - \eta)$ , respectively. The constants  $\beta_l(\xi)$  and  $\beta_l[1 - \xi]$  are simply  $\beta_l(\eta)$  at point  $\eta = \xi$  and  $\eta = 1 - \xi$ , respectively.

Therefore we employ the following minimizing sequences for finding  $\gamma_{en2}$

$$\beta_l = \begin{cases} \frac{\beta_l(\xi)}{\xi} \eta, & \text{for } \eta \in (0, \xi), \\ \beta_l(\eta), & \text{for } \eta \in (\xi, l), \\ \beta_{lm}, & \text{for } \eta \in (l, 1 - l), \\ \beta_l(1 - \eta), & \text{for } \eta \in (1 - l, 1 - \xi), \\ \frac{\beta_l[1-\xi]}{\xi} (1 - \eta), & \text{for } \eta \in (1 - \xi, 1), \end{cases} \quad (6.34)$$

and

$$\beta_r = \begin{cases} \frac{\beta_{rm}}{\xi} \eta, & \text{for } \eta \in (0, \xi), \\ \beta_{rm}, & \text{for } \eta \in (\xi, l), \\ \beta_{rm}, & \text{for } \eta \in (l, 1 - l), \\ \beta_{rm}, & \text{for } \eta \in (1 - l, 1 - \xi), \\ \frac{\beta_{rm}}{\xi} (1 - \eta), & \text{for } \eta \in (1 - \xi, 1), \end{cases} \quad (6.35)$$

where  $\beta_{lm}$  and  $\beta_{rm}$  are unknown constants, and  $l$  is the boundary layer width of  $\beta_l$ . Since  $\beta_l(\xi)$  and  $\beta_{rm}$  are negligibly small at  $\gamma_{en2}$ , the parts of energy functional that contains the

quadratic and multiplication among these constants are ignored during  $\gamma_{en2}$  calculation. We apply (6.34) and (6.35) to the energy functional (6.17) giving

$$\begin{aligned}
E = & \int_0^\xi \left[ (1 - \kappa) \left( \frac{\beta_l(\xi)}{\xi} \eta \sin 2\varphi_l + \frac{\beta_{rm}}{\xi} \eta \sin 2\varphi_r \right)^2 \right. \\
& + \frac{2k}{c} \left( \left| \frac{\beta_l(\xi)}{\xi} \sin \varphi_l \right| + \left| \frac{\beta_{rm}}{\xi} \sin \varphi_r \right| \right) \left. \right] d\eta \\
& + \int_\xi^l \left[ (1 - \kappa) (\beta_l \sin 2\varphi_l + \beta_{rm} \sin 2\varphi_r)^2 + \frac{2k}{c} |\beta_l' \sin \varphi_l| \right. \\
& + \frac{k}{c^2} (\beta_l')^2 \sin^2 2\varphi_l \left. \right] d\eta + \frac{1}{2} (1 - \kappa) (\beta_{lm} \sin 2\varphi_l + \beta_{rm} \sin 2\varphi_r)^2 (1 - 2l) \\
& + \frac{1}{2} (\langle \beta_l \rangle \cos 2\varphi_l + \langle \beta_r \rangle \cos 2\varphi_r - \gamma)^2 \\
& + \frac{\kappa}{2} (\langle \beta_l \rangle \sin 2\varphi_l + \langle \beta_r \rangle \sin 2\varphi_r)^2, \tag{6.36}
\end{aligned}$$

with

$$\langle \beta_r \rangle = \int_0^\xi \frac{\beta_{rm}}{\xi} \eta d\eta + \beta_{rm}(1 - 2\xi), \tag{6.37}$$

where  $\beta_l$  and  $\langle \beta_l \rangle$  from the solutions (6.28) and (6.30), respectively. Taking first the variation of (6.36) with respect to  $\beta_{rm}$ , then integrating and then ignoring all of the terms that contain  $\xi$  and finally setting it equal to zero to obtain the minimum, we arrive at

$$\begin{aligned}
& \frac{2k |\sin \varphi_r| \text{sign} \beta_{rm}}{c} + \beta_{rm} + (1 - 2l)(1 - \kappa) \sin 2\varphi_l \sin 2\varphi_r \beta_{lm} \\
& - \gamma \cos 2\varphi_r + (\cos 2\varphi_l \cos 2\varphi_r + \kappa \sin 2\varphi_l \sin 2\varphi_r) \langle \beta_l \rangle \\
& + \frac{2}{\zeta} (1 - \kappa) \sin 2\varphi_l \sin 2\varphi_r \beta_{lp} (\zeta l - \tanh \zeta l) = 0, \tag{6.38}
\end{aligned}$$

where  $\beta_{lm}$  from (6.28),  $\langle \beta_l \rangle$  from (6.30),  $\beta_{lp}$  and  $\zeta$  from (6.29).

There are two possible conditions for solving Eq. (6.38). The first condition is when  $\beta_{rm} > 0$  which is fulfilled by the combination of  $\varphi_l$  and  $\varphi_r$ , for  $\gamma \geq \gamma_{en2}$ , that obey the following condition

$$\begin{aligned}
\beta_{rm} = & - \frac{2k |\sin \varphi_r|}{c} - (1 - 2l)(1 - \kappa) \sin 2\varphi_l \sin 2\varphi_r \beta_{lm} \\
& + \gamma \cos 2\varphi_r - (\cos 2\varphi_l \cos 2\varphi_r + \kappa \sin 2\varphi_l \sin 2\varphi_r) \langle \beta_l \rangle \\
& - \frac{2}{\zeta} (1 - \kappa) \sin 2\varphi_l \sin 2\varphi_r \beta_{lp} (\zeta l - \tanh \zeta l) > 0. \tag{6.39}
\end{aligned}$$

The length of boundary layer,  $l_{en2}$ , that satisfies the condition (6.39) is obtained by solving the following equation

$$\begin{aligned}
f(l_{en2}) \equiv & - \frac{2k |\sin \varphi_r|}{c} - (1 - 2l_{en2})(1 - \kappa) \sin 2\varphi_l \sin 2\varphi_r \beta_{lm}[l_{en2}] + \gamma[l_{en2}] \cos 2\varphi_r \\
& - (\cos 2\varphi_l \cos 2\varphi_r + \kappa \sin 2\varphi_l \sin 2\varphi_r) \gamma[l_{en2}] \cos 2\varphi_l B_l[l_{en2}] \\
& - \frac{2 - 1}{\zeta} (1 - \kappa) \sin 2\varphi_l \sin 2\varphi_r \beta_{lp}[l_{en2}] (\zeta l_{en2} - \tanh(\zeta l_{en2})) = 0. \tag{6.40}
\end{aligned}$$

Then, substituting back  $l_{en2}$  into (6.33) we obtain the second energetic threshold value, namely

$$\gamma_{en2} = \gamma[l_{en2}]. \quad (6.41)$$

The second condition is when  $\beta_{rm} < 0$  which is achieved at

$$\begin{aligned} \beta_{rm} = & \frac{2k |\sin \varphi_r|}{c} - (1 - 2l)(1 - \kappa) \sin 2\varphi_l \sin 2\varphi_r \beta_{lm} \\ & + \gamma \cos 2\varphi_r - (\cos 2\varphi_l \cos 2\varphi_r + \kappa \sin 2\varphi_l \sin 2\varphi_r) \langle \beta_l \rangle \\ & - \frac{2}{\zeta} (1 - \kappa) \sin 2\varphi_l \sin 2\varphi_r \beta_{lp} (\zeta l - \tanh \zeta l) < 0, \end{aligned} \quad (6.42)$$

if and only if  $\gamma \geq \gamma_{en2}$ . The second energetic threshold value,  $\gamma_{en2}$ , for this condition is given by

$$\gamma_{en2} = \gamma[l_{en2}],$$

where the boundary layer length,  $l_{en2}$ , is obtained from solving

$$\begin{aligned} f(l_{en2}) \equiv & \frac{2k |\sin \varphi_r|}{c} - (1 - 2l_{en2})(1 - \kappa) \sin 2\varphi_l \sin 2\varphi_r \beta_{lm}[l_{en2}] + \gamma[l_{en2}] \cos 2\varphi_r \\ & - (\cos 2\varphi_l \cos 2\varphi_r + \kappa \sin 2\varphi_l \sin 2\varphi_r) \gamma[l_{en2}] \cos 2\varphi_l B_l[l_{en2}] \\ & - \frac{2}{\zeta} (1 - \kappa) \sin 2\varphi_l \sin 2\varphi_r \beta_{lp}[l_{en2}] (\zeta l_{en2} - \tanh(\zeta l_{en2})) = 0. \end{aligned} \quad (6.43)$$

Mention that only one from (6.40) and (6.43) that can give the solution for  $l_{en2}$  for each combination of angles  $\varphi_l$  and  $\varphi_r$ .

By following the same procedures as shown in (6.19)-(6.43), we are able to derive the energetic threshold values ( $\gamma_{en1}$  and  $\gamma_{en2}$ ) for the second case where  $\beta_r$ , rather than  $\beta_l$ , emerges first during the loading process. The first energetic threshold value,  $\gamma_{en1}$ , for this case is expressed by

$$\gamma_{en1} = \frac{2k |\sin \varphi_r|}{c |\cos 2\varphi_r|}, \quad (6.44)$$

where  $c = hb\rho_s$ . For  $\gamma > \gamma_{en1}$ , in order to minimize the energy functional the conditions

$$\beta_{rm} = \frac{1}{2 \cos 2\varphi_r} \left( \gamma - \frac{2k |\sin \varphi_r|}{c \cos 2\varphi_r} \right) > 0,$$

for  $\varphi_l \in (0^\circ, 45^\circ)$  and

$$\beta_{rm} = \frac{1}{2 \cos 2\varphi_r} \left( \gamma + \frac{2k |\sin \varphi_r|}{c \cos 2\varphi_r} \right) < 0,$$

for  $\varphi_l \in (45^\circ, 90^\circ)$  must be fulfilled.

In the course of loading process, for interval  $\gamma_{en1} \leq \gamma < \gamma_{en2}$ , we obtain the following solution for plastic distortion, i.e.

$$\beta_r = \begin{cases} \beta_{rp}(1 - \cosh \zeta \eta + \tanh \zeta l \sinh \zeta \eta), & \text{for } \eta \in (0, l), \\ \beta_{rm} = \beta_{rp} \left( 1 - \frac{1}{\cosh \zeta l} \right), & \text{for } \eta \in (l, 1 - l), \\ \beta_{rp}(1 - \cosh \zeta(1 - \eta) + \tanh \zeta l \sinh \zeta(1 - \eta)), & \text{for } \eta \in (1 - l, 1), \end{cases} \quad (6.45)$$

where

$$\beta_{rp} = \frac{\gamma \cos 2\varphi_r - (\cos^2 2\varphi_r + \kappa \sin^2 2\varphi_r) \langle \beta_r \rangle}{(1 - \kappa) \sin^2 2\varphi_r} \quad \text{and} \quad \zeta = 2c |\cos \varphi_l| \sqrt{\frac{1 - \kappa}{k}}. \quad (6.46)$$

The average of  $\beta_r$  takes the form

$$\langle \beta_r \rangle = \gamma \cos 2\varphi_r B_r(l), \quad (6.47)$$

with

$$B_r(l) = \frac{g(l)}{(1 - \kappa) \sin^2 2\varphi_r + g(l)(\cos^2 2\varphi_r + \kappa \sin^2 2\varphi_r)}, \quad (6.48)$$

where  $g(l)$  from (6.32). The shear strain,  $\gamma$ , is given in the form

$$\gamma(l) = \frac{2k |\sin \varphi_r| \text{sign} \beta'_r \cosh \zeta l}{c(1 - 2l) \cos 2\varphi_r (1 - (\cos^2 2\varphi_r + \kappa \sin^2 2\varphi_r) B_r(l))}, \quad (6.49)$$

where  $\text{sign} \beta'_r$  for interval  $\eta \in (0, l)$  takes the form

$$\text{sign} \beta'_r = \begin{cases} 0, & \text{for } \varphi_l = 0^\circ, \\ +1, & \text{for } 0^\circ < \varphi_l < 45^\circ, \\ -1, & \text{for } 45^\circ < \varphi_l < 90^\circ. \end{cases} \quad (6.50)$$

For the situation where  $\beta_l > 0$ , the second energetic threshold value,  $\gamma_{en2}$ , is given by substituting  $l_{en2}$  to (6.49), namely

$$\gamma_{en2} = \gamma[l_{en2}],$$

where  $l_{en2}$  is obtained from solving

$$f(\text{sign} \beta_{lm} = 1, l_{en2}) = 0, \quad (6.51)$$

and the minimum of energy is achieved if

$$f(\text{sign} \beta_{lm} = 1, l) > 0,$$

if and only if  $\gamma > \gamma_{en2}$  where

$$\begin{aligned} f(\text{sign} \beta_{lm}, l) = & - \frac{2k |\sin \varphi_l| \text{sign} \beta_{lm}}{c} - (1 - 2l)(1 - \kappa) \sin 2\varphi_l \sin 2\varphi_r \beta_{rm}(l) \\ & + \gamma(l) \cos 2\varphi_l - (\cos 2\varphi_l \cos 2\varphi_r + \kappa \sin 2\varphi_l \sin 2\varphi_r) \gamma(l) \cos 2\varphi_r B_r(l) \\ & + \frac{2}{\zeta} (1 - \kappa) \sin 2\varphi_l \sin 2\varphi_r \beta_{rp}(l) (\zeta l - \tanh \zeta l), \end{aligned} \quad (6.52)$$

with  $\beta_{rm}$  from (6.45),  $\beta_{rp}$  and  $\zeta$  from (6.46).

We need first to find  $l_{en2}$  by solving the following

$$f(\text{sign} \beta_{lm} = -1, l_{en2}) = 0, \quad (6.53)$$

with  $f(\text{sign}\beta_{lm}, l)$  from (6.52), then applying  $l_{en2}$  to (6.49) to obtain  $\gamma_{en2}$  for  $\beta_l < 0$ . Similar as before, in place of achieving the minimum of the energy, the following situation must be fulfilled for  $\gamma > \gamma_{en2}$ , i.e.

$$f(\text{sign}\beta_{lm} = -1, l_{en2}) < 0.$$

Similar to the first case, only one from (6.51) and (6.53) that can give the solution for  $\gamma_{en2}$  for each combination of  $\varphi_l$  and  $\varphi_r$ .

To conclude, in the interest of finding the energetic threshold values, we choose first the case that gives the smallest  $\gamma$  among (6.26) and (6.44) to obtain  $\gamma_{en1}$ . Afterwards, to find  $\gamma_{en2}$ , we take first the equation that gives us  $l_{en2}$  either from (6.40) or (6.43) for the first case and either from (6.51) or (6.53) for the second case then apply  $l_{en2}$  to (6.33).

### 6.2.2 Symmetric double slip systems at zero dissipation

In order to derive closed-form analytical solution, let us reduce the complexity of this variational problem by analyzing the special case  $\varphi_r = \pi - \varphi_l = \pi - \varphi$  which corresponds to the symmetric double slip systems. Therefore, for brevity, it is again convenient to introduce the dimensionless quantities

$$E = \frac{\Psi}{\mu a L h}, \quad \eta = \frac{y}{h}, \quad c = hb\rho_s, \quad \bar{\beta}_l(\eta) = \beta_l(y), \quad \bar{\beta}_r(\eta) = \beta_r(y), \quad (6.54)$$

so that

$$\beta_{l,y}(y) = \frac{\bar{\beta}_l'(\eta)}{h} \quad \text{and} \quad \beta_{r,y}(y) = \frac{\bar{\beta}_r'(\eta)}{h},$$

with the dimensionless variable  $\eta$  changes on the interval (0, 1).

Consequently the energy functional (6.14) reduces to

$$\begin{aligned} E(\beta_l, \beta_r) = \int_0^1 & \left[ \frac{1}{2} \left( (\langle \beta_l \rangle + \langle \beta_r \rangle) \cos 2\varphi - \gamma \right)^2 + \frac{\kappa}{2} (\langle \beta_l \rangle - \langle \beta_r \rangle)^2 \sin^2 2\varphi \right. \\ & + \frac{1 - \kappa}{2} (\beta_l - \beta_r)^2 \sin^2 2\varphi + \frac{k |\sin \varphi| (|\beta_l'| + |\beta_r'|)}{c} \\ & \left. + \frac{k \sin^2 \varphi}{2c^2} (\beta_l'^2 + \beta_r'^2 + 2\chi |\beta_l'| |\beta_r'|) \right] d\eta, \end{aligned} \quad (6.55)$$

with

$$\langle \beta_l \rangle = \int_0^1 \beta_l d\eta \quad \text{and} \quad \langle \beta_r \rangle = \int_0^1 \beta_r d\eta, \quad (6.56)$$

where the bars over  $\bar{\beta}_l(\eta)$  and  $\bar{\beta}_r(\eta)$  are dropped for short. Then we need to minimize functional (6.55) with respect to  $\beta_l$  and  $\beta_r$  satisfying the boundary conditions (6.4).

Toward finding the energetic threshold values for the symmetric double slip systems case we apply the same procedure as presented in section (6.2.1). We found out, for this case, that both of slip systems emerge at the same time during the loading with

$$\beta_{lm} = \beta_{rm} = \beta_m, \quad (6.57)$$

which is natural to expect. As a consequence, we only have one energetic threshold value for symmetric double slip systems, namely

$$\gamma_{en} = \frac{2k |\sin \varphi|}{c \cos 2\varphi}. \quad (6.58)$$

Based on the previous analysis, we now assume that for  $\eta \in (0, 1)$

$$\beta_l(\eta) = \beta_r(\eta) = \beta(\eta) \quad \text{and} \quad \langle \beta_l \rangle = \langle \beta_r \rangle = \langle \beta \rangle \quad (6.59)$$

under the boundary conditions

$$\beta(0) = \beta[1] = 0. \quad (6.60)$$

As a consequence, the energy functional (6.55) reduces to

$$E(\beta) = \int_0^1 \left[ \frac{1}{2} (2\langle \beta \rangle \cos 2\varphi - \gamma)^2 + \frac{2k |\sin \varphi| |\beta'|}{c} + \frac{k(1 + \chi) \sin^2 \varphi (\beta')^2}{c^2} \right] d\eta. \quad (6.61)$$

Similar to the single slip problem,  $\beta'(\eta)$  should change its sign on the interval  $\eta \in (0, 1)$  following boundary conditions (6.60). Therefore we apply again the minimizer suggested in [Berdichevsky and Le, 2007] namely

$$\beta(\eta) = \begin{cases} \beta_1(\eta), & \text{for } \eta \in (0, l), \\ \beta_m, & \text{for } \eta \in (l, 1-l), \\ \beta_1(1-\eta), & \text{for } \eta \in (1-l, 1), \end{cases} \quad (6.62)$$

with  $\beta_m$  being a constant quantity and  $l$  the unknown boundary layer thickness ( $0 \leq l \leq \frac{1}{2}$ ). The sign  $\beta'_1$  on the interval  $(0, l)$  is given in the form

$$\text{sign} \beta'_1 = \begin{cases} 0, & \text{for } 0^\circ, \\ +1, & \text{for } 0^\circ < \varphi < 45^\circ, \\ -1, & \text{for } 45^\circ < \varphi < 90^\circ, \end{cases} \quad (6.63)$$

and, due to the boundary conditions (6.60),  $\text{sign} \beta'_1$  is changed to the opposite sign on the interval  $\eta \in (1-l, 1)$ . Hence the energy functional (6.61) is transformed into

$$E = \int_0^l \left[ \frac{4k |\sin \varphi| |\beta'_1|}{c} + \frac{2k(1 + \chi) \sin^2 \varphi \beta_1'^2}{c^2} \right] d\eta + \frac{1}{2} (2\langle \beta \rangle \cos 2\varphi - \gamma)^2, \quad (6.64)$$

where

$$\langle \beta \rangle = 2 \int_0^l \beta_1 d\eta + \beta_m(1 - 2l). \quad (6.65)$$

Function  $\beta_1$  must obey the boundary conditions

$$\beta_1(0) = 0, \quad \beta_1(l) = \beta_m. \quad (6.66)$$

In order to find  $\beta_1(\eta)$  and the constant,  $\beta_m$  and  $l$ , we set the variation of energy functional (6.64) with respect to the wanted variables

$$\begin{aligned} \delta E = & \int_0^l \left[ \frac{4k|\sin\varphi|\text{sign}\beta'_1}{c} + \frac{4k(1+\chi)\sin^2\varphi\beta'_1}{c^2} \right] \delta\beta'_1 d\eta \\ & + \left( \frac{2k|\sin\varphi||\beta'_1(l)|}{c} + \frac{k(1+\chi)\sin^2\varphi(\beta'_1(l))^2}{c^2} \right) \delta l \\ & + 2\cos 2\varphi(2\cos 2\varphi\langle\beta\rangle - \gamma)\langle\delta\beta\rangle, \end{aligned} \quad (6.67)$$

where the variation of (6.65) obeying (6.66)<sub>2</sub>

$$\langle\delta\beta\rangle = 2 \int_0^l \delta\beta_1 d\eta + (1-2l)\delta\beta_m. \quad (6.68)$$

Satisfying (6.66), we integrate (6.67) partially then set  $\delta E = 0$

$$\begin{aligned} \delta E = & \int_0^l \left[ 4\cos 2\varphi(2\cos\varphi\langle\beta\rangle - \gamma) - \frac{4k(1+\chi)\sin^2\varphi\beta''_1}{c^2} \right] \delta\beta_1 d\eta \\ & + \left( \frac{2k|\sin\varphi||\beta'_1(l)|}{c} + \frac{k(1+\chi)\sin^2\varphi(\beta'_1(l))^2}{c^2} \right) \delta l \\ & + \left( \frac{4k|\sin\varphi|\text{sign}\beta'_1}{c} + \frac{4k(1+\chi)\sin^2\varphi\beta'_1(l)}{c^2} \right. \\ & \left. + 2\cos 2\varphi(1-2l)(2\cos 2\varphi\langle\beta\rangle - \gamma) \right) \delta\beta_m = 0, \end{aligned} \quad (6.69)$$

where  $\delta\beta_1$ ,  $\delta\beta_m$  and  $\delta l$  are arbitrary.

From (6.69) we can see that the variation of the energy functional (6.64) with respect to  $\beta_1$  gives

$$\cos 2\varphi(2\cos\varphi\langle\beta\rangle - \gamma) - \frac{k(1+\chi)\sin^2\varphi\beta''_1}{c^2} = 0, \quad (6.70)$$

where  $\beta_1(\eta)$  is subject to the boundary conditions (6.66). The variation of Eq. (6.69) with respect to the boundary layer thickness,  $l$ , gives an additional boundary condition at  $\eta = l$

$$\beta'_1(l) = 0, \quad (6.71)$$

which means that dislocation density must be continuous. Varying the energy functional with respect to  $\beta_m$ , we obtain a condition for  $\beta_m$

$$\frac{4k|\sin\varphi|\text{sign}\beta'_1}{c} + 2\cos 2\varphi(1-2l)(2\cos 2\varphi\langle\beta\rangle - \gamma) = 0 \quad (6.72)$$

By first integrating (6.70) with boundary condition (6.71) then integrating again taking into account (6.66)<sub>1</sub> we obtain

$$\beta_1 = \frac{1}{2}(2l-\eta)\eta\beta_{1p}, \quad 0 \leq \eta \leq l, \quad (6.73)$$

where

$$\beta_{1p} = \frac{c^2 \cos 2\varphi(\gamma - 2\cos 2\varphi\langle\beta\rangle)}{k(1+\chi)\sin^2\varphi}. \quad (6.74)$$

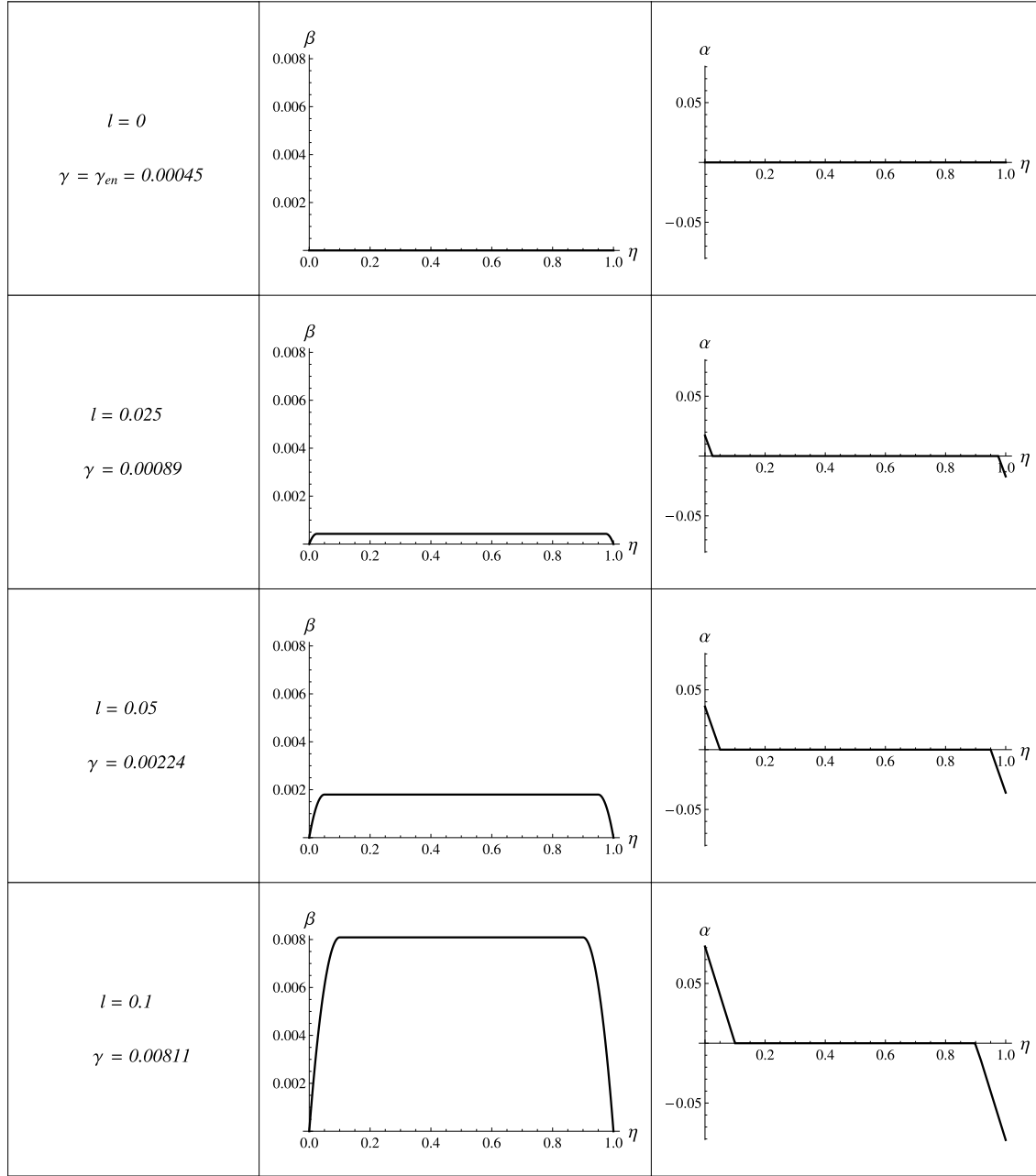


Figure 6.2: Evolution of  $\beta$  and  $\alpha$  for symmetric double-slip constrained shear of single crystal at zero dissipation where  $h = 1\mu\text{m}$  and  $\varphi = 30^\circ$  where  $\eta = y/h$

Substituting (6.73) to boundary condition (6.66)<sub>2</sub> we obtain the constant

$$\beta_m = \frac{1}{2}l^2\beta_{1p}. \quad (6.75)$$

Substituting (6.74) and (6.75) into (6.65), we get the average of plastic distortion in the form

$$\langle\beta\rangle = B(l)\gamma \cos 2\varphi \quad (6.76)$$

where

$$B(l) = \frac{l^2(3-2l)c^2}{6k(1+\chi)\sin^2\varphi + 2l^2(3-2l)c^2\cos^2 2\varphi}. \quad (6.77)$$

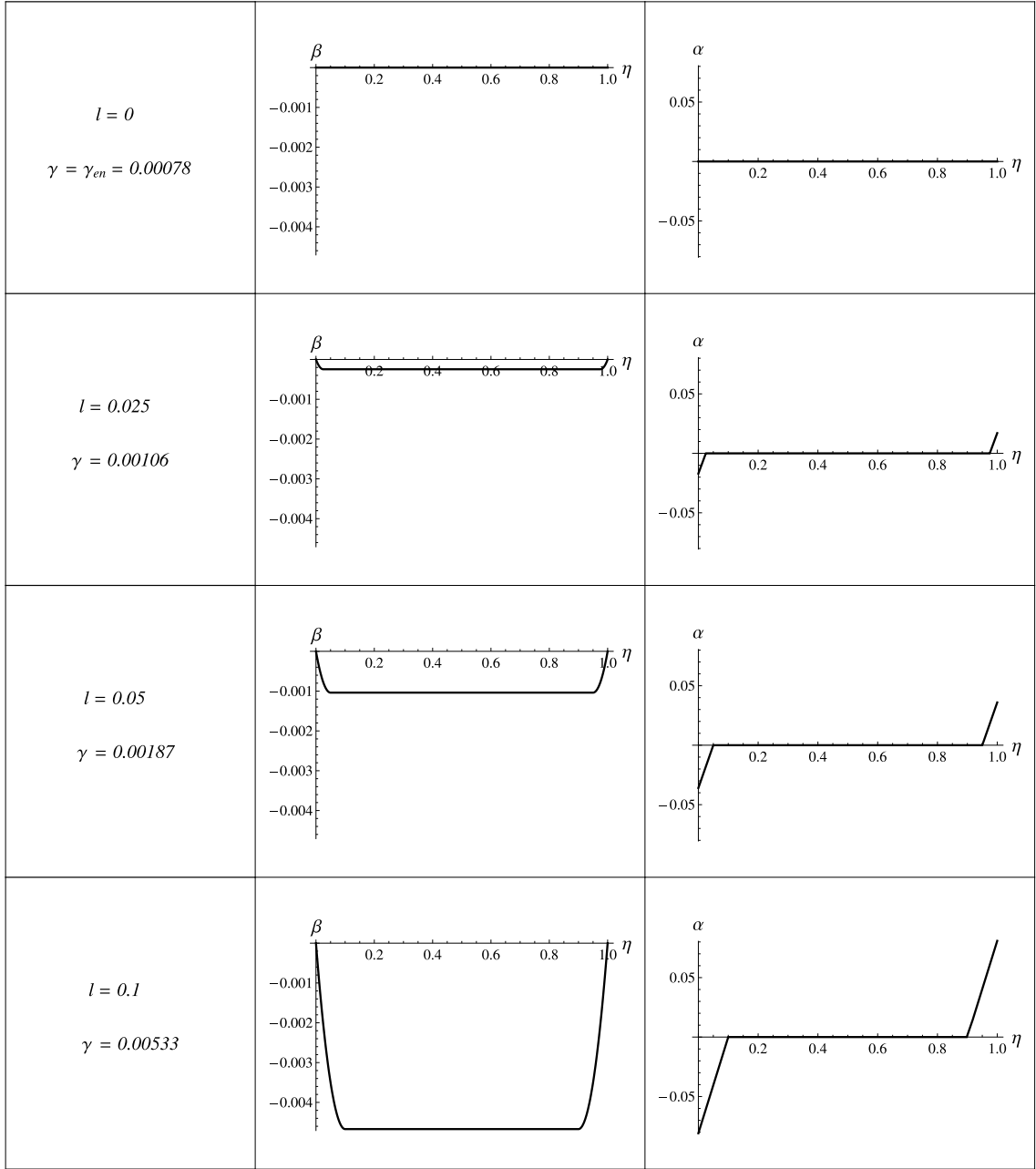


Figure 6.3: Evolution of  $\beta$  and  $\alpha$  for symmetric double-slip constrained shear of single crystal at zero dissipation where  $h = 1\mu\text{m}$  and  $\varphi = 60^\circ$  where  $\eta = y/h$

Applying (6.73) and (6.75) to the minimizing sequence (6.62) gives the general solutions for plastic distortion

$$\beta = \begin{cases} \frac{1}{2}\beta_{1p}(2l - \eta)\eta, & \text{for } \eta \in (0, l), \\ \frac{1}{2}\beta_{1p}l^2, & \text{for } \eta \in (l, 1 - l), \\ \frac{1}{2}\beta_{1p}(2l - (1 - \eta))(1 - \eta), & \text{for } \eta \in (1 - l, 1). \end{cases} \quad (6.78)$$

With (6.72) and (6.76), we obtain the equation of  $\gamma$  as a function of  $l$ , namely

$$\gamma(l) = \frac{2k|\sin\varphi|\text{sign}\beta_1'}{c(1 - 2l)\cos 2\varphi(1 - 2\cos^2 2\varphi B(l))}, \quad (6.79)$$

where  $\text{sign}\beta'_1$  from (6.63). Since  $\gamma$  increases for increasing  $l$  and  $\gamma = \gamma_{en}$  for  $l = 0$ , we can also here use  $l$  as the control parameter.

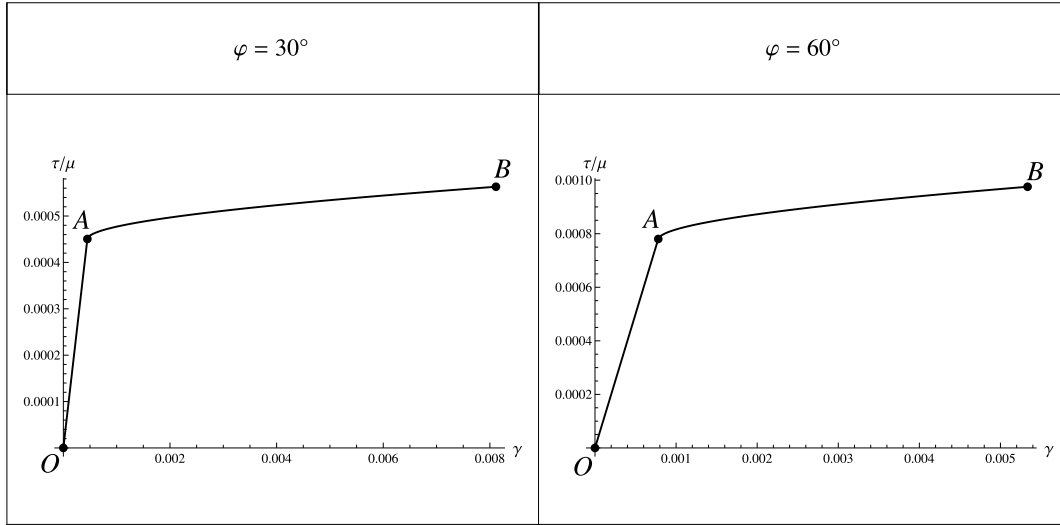


Figure 6.4: Normalized shear stress versus shear strain curve for symmetric double-slip constrained shear of single crystal at zero dissipation with  $h = 1\mu\text{m}$  when  $l$  is increased from 0 to 0.1

The dislocation densities for plane-strain constrained shear of single crystal deforming in symmetric double slip are equal

$$\alpha_l(y) = \alpha_r(y) = \beta_{,y} \sin \varphi.$$

According to (6.7), there is only one non-zero component of the resultant Burgers vector of all dislocations in the  $y$ -direction namely

$$\alpha_{yz} = 2\beta_{,y} \sin^2 \varphi.$$

As a consequence, couples of dislocations near the boundaries form "super" dislocations with the Burgers vector in the  $y$ -direction.

The normalized dislocation density for symmetric double slip systems is given in the form

$$\alpha(\eta) = \beta' \sin \varphi. \quad (6.80)$$

Substituting (6.78) into (6.80) gives the distribution of normalized dislocation density in the crystal namely

$$\alpha = \begin{cases} (l - \eta)\beta_{1p}, & \text{for } \eta \in (0, l), \\ 0, & \text{for } \eta \in (l, 1 - l), \\ -(l - (1 - \eta))\beta_{1p}, & \text{for } \eta \in (1 - l, 1), \end{cases} \quad (6.81)$$

where  $\beta_{1p}$  from (6.74).

Fig. 6.2 and Fig. 6.3 show the evolution of  $\beta(\eta)$  and  $\alpha(\eta)$  with increasing  $l$  (hence  $\gamma$  increases) for  $\varphi = 30^\circ$  and  $\varphi = 60^\circ$ , respectively. Again we notice the dislocation free zone in the middle of the crystal and dislocation pile-up near the crystal boundary.

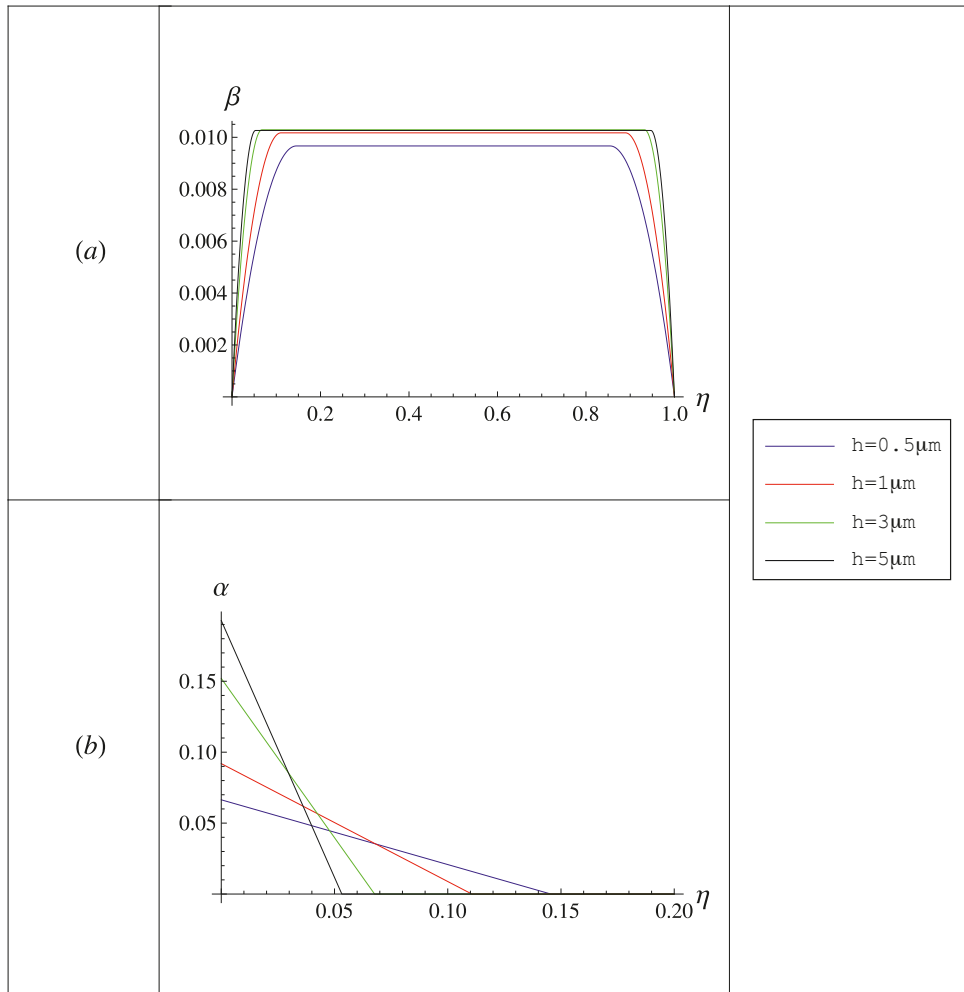


Figure 6.5: Evolution of  $\beta$  within the interval  $\eta \in (0, 1)$  and  $\alpha$  within the interval  $\eta \in (0, 0.2)$  for zero dissipation symmetric double-slip constrained shear of single crystal at  $\varphi = 30^\circ$  and  $\gamma = 0.01$  with different crystal heights  $h$

The normalized shear stress as function of shear strain is written in the form

$$\tau = \mu(\gamma - 2\langle\beta\rangle \cos 2\varphi). \quad (6.82)$$

As we know that the plastic distortion,  $\beta$ , remains zero and no dislocations are nucleated for  $\gamma < \gamma_{en}$ , thus the shear stress as function of shear strain takes the form

$$\tau = \mu\gamma.$$

With  $\langle\beta\rangle$  from (6.76), we can now compute the shear stress for  $\gamma < \gamma_{en}$ . Fig. 6.4 shows the normalized shear stress versus shear strain (OAB for  $\varphi = 30^\circ$  and OA'B' for  $\varphi = 60^\circ$ ). We observe that Fig. 6.4 has the similar behavior to the single-slip constrained shear in the zero dissipation case (see section 3.3.2).

Fig. 6.5 illustrates the evolution of plastic distortion,  $\beta$ , and normalized dislocation density,  $\alpha$ , with changing height,  $h$ , and Fig. 6.6 demonstrates the stress strain curve for different  $h$  wherenthe dot at each curve represents the starting point of plastic deformation. Both Fig. 6.5 and Fig. 6.6 admit the same characteristic as in the single slip system and clearly show the size effect. It is obvious from Fig. 6.6 that the smaller crystal is stronger than the bigger one.

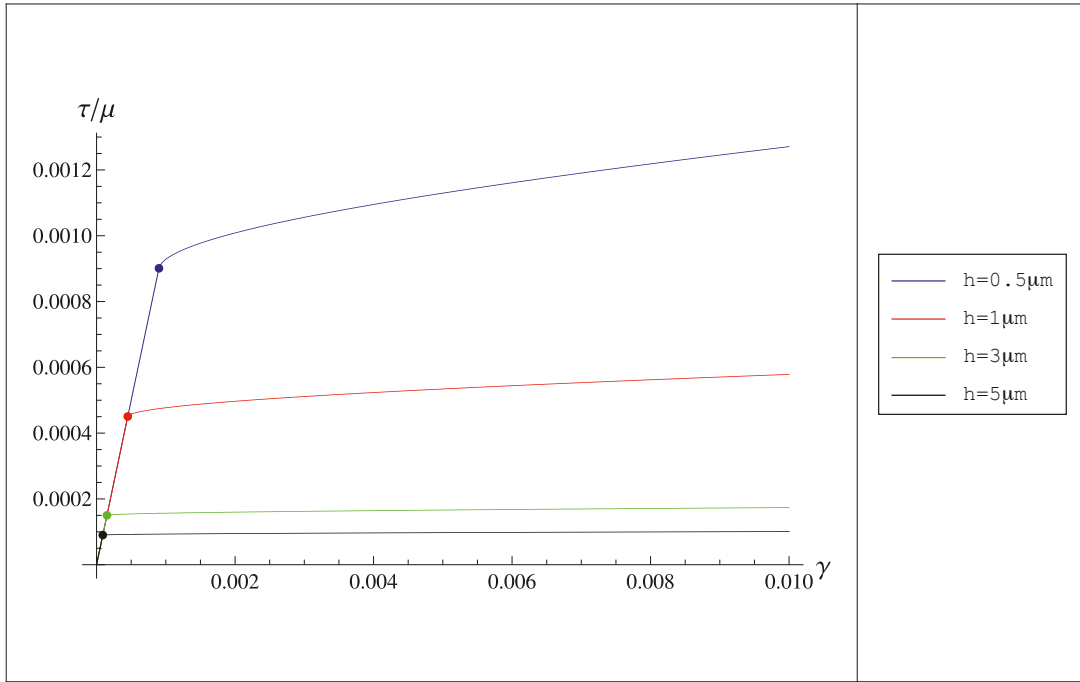


Figure 6.6: Normalized shear stress versus shear strain curves for zero dissipation symmetric double-slip constrained shear of single crystal at  $\varphi = 30^\circ$  with different crystal heights  $h$

### 6.2.3 General double slip systems case at zero dissipation

As we know from the physical point of view that for the case of double slip systems, one of the slip system is activated first as  $\gamma$  is increased during the loading process. Initially for  $\gamma < \gamma_{en1}$ , the plastic distortions,  $\beta_l$  and  $\beta_r$ , are zero and the crystal deforms elastically. As a consequence, we have the normalized stress strain equation in the linear form, such as

$$\frac{\tau}{\mu} = \gamma. \quad (6.83)$$

After  $\gamma$  reaches  $\gamma_{en1}$ , one of the slip system becomes active (either  $\beta_l$  or  $\beta_r$ ) and the newly nucleated dislocations start to appear to minimize the energy. When we increase  $\gamma$  further up to  $\gamma_{en2}$ , the crystal deforms plastically with only one active slip system. Therefore in this interval of loading we obtain the solutions (6.28)-(6.33) and

$$\frac{\tau}{\mu} = \gamma - \langle \beta_l \rangle \cos 2\varphi_l, \quad (6.84)$$

for the case where  $\beta_l$  emerges first and if  $\beta_r$  appears first we have the solutions from (6.45)-(6.49) together with

$$\frac{\tau}{\mu} = \gamma - \langle \beta_r \rangle \cos 2\varphi_r. \quad (6.85)$$

The procedures to determine  $\gamma_{en1}$  and  $\gamma_{en2}$  are explained in detail in section (6.2.1).

Fig. (6.7) illustrates the evolution of plastic distortions and dislocation densities for  $\gamma_{en1} \leq \gamma \leq \gamma_{en2}$  at  $\varphi_l = 35^\circ$  and  $\varphi_r = 165^\circ$ . By cause of the different orientations of the two active slip systems, one of the slip system may stay passive even at  $\gamma > \gamma_{en1}$ . We observed this

phenomena in Fig.6.7 where plastic distortion of one slip system is already well-developed but still passive for the other slip system. Due to the cross-slip interaction between two slip systems, the dislocation activity on one slip system hinders the dislocation activity on the other slip system near the grain boundary.

For crystal having non-symmetric active slip systems, an analytical solution does not seem feasible for  $\gamma > \gamma_{en2}$ . Therefore we employ a numerical solution by means of a finite element procedure.

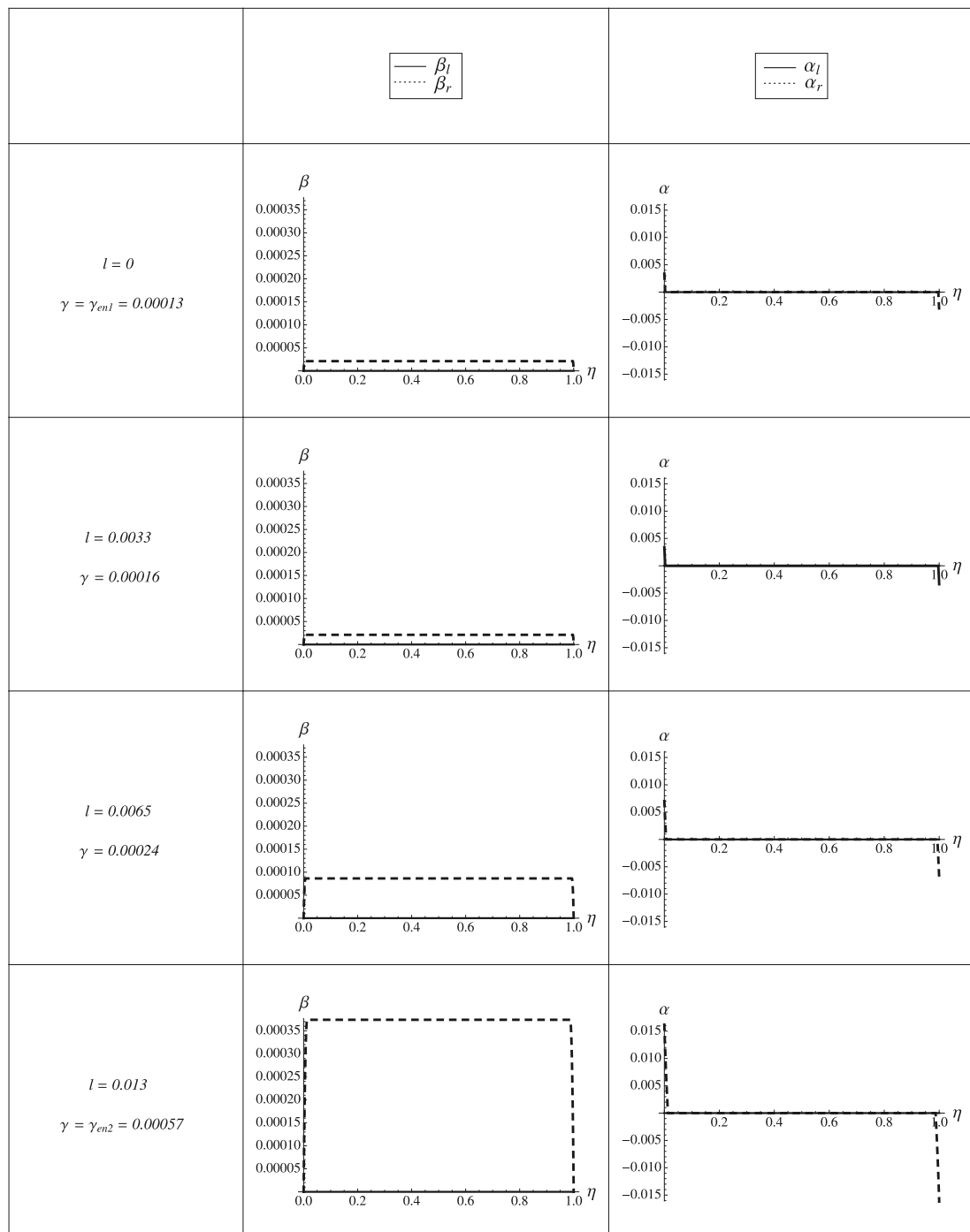


Figure 6.7: Evolution of plastic distortions ( $\beta_l$  and  $\beta_r$ ) and dislocation densities ( $\alpha_l$  and  $\alpha_r$ ) at  $\varphi_l = 35^\circ$  and  $\varphi_r = 165^\circ$  for  $\gamma_{en1} \leq \gamma \leq \gamma_{en2}$  where  $h = 1 \mu\text{m}$ .

For the purpose of numerical minimization it is convenient to non-dimensionalize the energy functional (6.14) by multiplying both sides of (6.14) by  $1/aLh\mu\gamma^3$  so that we obtain

$$\begin{aligned} \frac{\Psi(\beta_l, \beta_r)}{aLh\mu\gamma^3} &= \int_0^h \left[ \frac{1}{2} \left( \frac{\langle \beta_l \rangle}{\gamma} \cos 2\varphi_l + \frac{\langle \beta_r \rangle}{\gamma} \cos 2\varphi_r - 1 \right)^2 \right. \\ &\quad + \frac{\kappa}{2} \left( \frac{\langle \beta_l \rangle}{\gamma} \sin 2\varphi_l + \frac{\langle \beta_r \rangle}{\gamma} \sin 2\varphi_r \right)^2 + \frac{1-\kappa}{2} \left( \frac{\beta_l}{\gamma} \sin 2\varphi_l + \frac{\beta_r}{\gamma} \sin 2\varphi_r \right)^2 \\ &\quad + \frac{k}{\gamma^2 b \rho_s} (|\beta_{l,y} \sin \varphi_l| + |\beta_{r,y} \sin \varphi_r|) + \frac{k}{2(\gamma b \rho_s)^2} (\beta_{l,y}^2 \sin^2 \varphi_l + \beta_{r,y}^2 \sin^2 \varphi_r \\ &\quad \left. + 2\chi |\beta_{l,y} \sin \varphi_l| |\beta_{r,y} \sin \varphi_r| \right) \frac{dy}{h\gamma}. \end{aligned}$$

Therefore we suggest the dimensionless quantities for this numerical computation in the form

$$\begin{aligned} E &= \frac{\Psi}{aLh\mu\gamma^3}, \quad \eta = \frac{y}{h\gamma}, \quad H = \frac{1}{\gamma}, \quad c = hb\rho_s, \\ m &= \frac{k}{\gamma^2}, \quad \bar{\beta}_l(\eta) = \frac{\beta_l(y)}{\gamma}, \quad \bar{\beta}_r(\eta) = \frac{\beta_r(y)}{\gamma}, \end{aligned} \quad (6.86)$$

so that

$$\bar{\beta}'_l(\eta) = h\beta_{l,y}(y) \quad \text{and} \quad \bar{\beta}'_r(\eta) = h\beta_{r,y}(y), \quad (6.87)$$

and the dimensionless variable  $\eta$  changes in interval  $(0, H)$ . The dimensionless energy now takes the form (for shorts, the bars over  $\bar{\beta}_l(\eta)$  and  $\bar{\beta}_r(\eta)$  are dropped)

$$\begin{aligned} E(\beta_l, \beta_r) &= \int_0^H \left[ \frac{1}{2} (1-\kappa) (\beta_l \sin 2\varphi_l + \beta_r \sin 2\varphi_r)^2 \right. \\ &\quad + \frac{1}{2} \kappa (\langle \beta_l \rangle \sin 2\varphi_l + \langle \beta_r \rangle \sin 2\varphi_r)^2 \\ &\quad + \frac{1}{2} (\langle \beta_l \rangle \cos 2\varphi_l + \langle \beta_r \rangle \cos 2\varphi_r - 1)^2 + \frac{m}{c} \left( |\beta'_l \sin \varphi_l| + |\beta'_r \sin \varphi_r| \right) \\ &\quad \left. + \frac{m}{2c^2} \left( (\beta'_l)^2 \sin^2 \varphi_l + (\beta'_r)^2 \sin^2 \varphi_r + 2\chi |\beta'_l \sin \varphi_l| |\beta'_r \sin \varphi_r| \right) \right] d\eta, \end{aligned} \quad (6.88)$$

with the average of plastic distortions

$$\langle \beta_l \rangle = \frac{1}{H} \int_0^H \beta_l d\eta \quad \text{and} \quad \langle \beta_r \rangle = \frac{1}{H} \int_0^H \beta_r d\eta. \quad (6.89)$$

Based on the analysis of dislocation pile-up obtained here and in [Berdichevsky and Le, 2007], we assume  $\beta_l$  and  $\beta_r$  to be constant in the middle layer. This means that the nucleated dislocations pile-up at the boundaries, leaving the center dislocation-free and forming thin boundary layers. Furthermore, we assume  $\beta_l$  and  $\beta_r$  to be symmetric as has been found for symmetric double slip system before. Therefore we seek the minimizers in the form

$$\beta_l(\eta) = \begin{cases} \beta_l(\eta), & \text{for } \eta \in (0, l), \\ \beta_{lm}, & \text{for } \eta \in (l, H-l), \\ \beta_l(1-\eta), & \text{for } \eta \in (H-l, H), \end{cases} \quad (6.90)$$

and

$$\beta_r(\eta) = \begin{cases} \beta_r(\eta), & \text{for } \eta \in (0, l), \\ \beta_{rm}, & \text{for } \eta \in (l, H - l), \\ \beta_r(1 - \eta), & \text{for } \eta \in (H - l, H), \end{cases} \quad (6.91)$$

with  $\beta_{lm}$  and  $\beta_{rm}$  being a constant quantities and  $l$  the unknown boundary layer thickness ( $0 \leq l \leq \frac{H}{2}$ ). The major advantage of formulating the numerical problem this way lies in the small number of degrees of freedom needed for minimization. Functions  $\beta_l$  and  $\beta_r$  are subjected to boundary conditions

$$\beta_l(0) = \beta_r(0) = 0, \quad \beta_l(l) = \beta_{lm}, \quad \beta_r(l) = \beta_{rm}. \quad (6.92)$$

Assigning the energy functional (6.88) to (6.90) and (6.91), we get

$$\begin{aligned} E = \int_0^l & \left[ (1 - k)(\beta_l \sin 2\varphi_l + \beta_r \sin 2\varphi_r)^2 + \frac{2m}{c} \left( |\beta'_l \sin \varphi_l| + |\beta'_r \sin \varphi_r| \right) \right. \\ & \left. + \frac{m}{c^2} \left( (\beta'_l)^2 \sin^2 \varphi_l + (\beta'_r)^2 \sin^2 \varphi_r + 2\chi |\beta'_l \sin \varphi_l| |\beta'_r \sin \varphi_r| \right) \right] d\eta \\ & + \frac{H}{2} \left( \kappa (\langle \beta_l \rangle \sin 2\varphi_l + \langle \beta_r \rangle \sin 2\varphi_r)^2 + (\langle \beta_l \rangle \cos 2\varphi_l + \langle \beta_r \rangle \cos 2\varphi_r - 1)^2 \right) \\ & + \frac{1 - \kappa}{2} (H - 2l)(\beta_{lm} \sin 2\varphi_l + \beta_{rm} \sin \varphi_r)^2, \end{aligned} \quad (6.93)$$

with

$$\begin{aligned} \langle \beta_l \rangle &= \frac{1}{H} \left( \int_0^l 2\beta_l d\eta + \beta_{lm}(H - 2l) \right), \\ \langle \beta_r \rangle &= \frac{1}{H} \left( \int_0^l 2\beta_r d\eta + \beta_{rm}(H - 2l) \right). \end{aligned} \quad (6.94)$$

Based on the minimizing sequences (6.90) and (6.91), we employed linear elements to model  $\beta_l$  and  $\beta_r$  over the height of the crystal under consideration as sketch in Fig 6.8 with  $c$  and  $d$  being the degrees of freedom for one element.

To model each boundary layer with  $n$  elements, we need  $2n + 2$  degrees of freedom at nodes plus the unknown boundary layer thickness  $l$ . Boundary conditions yield the constraints

$$c_0 = d_0 = c_{2n+2} = d_{2n+2} = 0. \quad (6.95)$$

With  $j$  being the element number, the discretization form of the total energy functional



coordinate  $\eta$  are replaced by the approximated parameters  $\tilde{\beta}_l$  and  $\tilde{\beta}_r$  depending on the natural coordinates  $\xi$ . The relation between physical and natural coordinates is shown in Fig. 6.9.

Let us assume that we have a linear equation for one element (see Fig. 6.9) in the form

$$\eta = a\xi + b, \quad (6.98)$$

where  $a$  and  $b$  being some arbitrary constants. First we substitute  $\xi = -1$  into (6.98) to obtain

$$\eta = \eta_{j-1} = -a + b, \quad (6.99)$$

then we apply  $\xi = 1$  to (6.98) to get

$$\eta = \eta_j = a + b. \quad (6.100)$$

By subtracting and adding (6.99) and (6.100), we acquire

$$a = \frac{\eta_j - \eta_{j-1}}{2}, \quad b = \frac{\eta_j + \eta_{j-1}}{2}. \quad (6.101)$$

Afterward we substitute (6.101) into the differential of (6.98) to get

$$d\eta = \frac{\Delta}{2}d\xi, \quad (6.102)$$

where

$$\Delta = \eta_j - \eta_{j-1} = \frac{l}{n}. \quad (6.103)$$

Eq. (6.102) describes the relationship between the corresponding differential line elements  $d\eta$  and  $d\xi$ .

For the systematic representation of approximation (shape) functions of finite elements of similar geometry, shape functions are defined in the natural parameter space  $\xi$ . As the result, all approximated variables are also defined in the natural parameter space. The linear shape functions are presented in the form

$$N_1(\xi) = \frac{1}{2}(1 - \xi), \quad N_2(\xi) = \frac{1}{2}(1 + \xi). \quad (6.104)$$

The derivative of the shape functions (6.104) are given in the form

$$N_{1;\xi}(\xi) = -\frac{1}{2}, \quad N_{2;\xi}(\xi) = \frac{1}{2}, \quad (6.105)$$

with  $(\bullet)_{;\xi}$  denotes differentiation with respect to  $\xi$ .

The approximation of plastic distortions takes the form

$$\begin{aligned} (\beta_l)_j(\xi) &\approx (\tilde{\beta}_l)_j(\xi) = N_1(\xi)c_{j-1} + N_2(\xi)c_j \\ (\beta_r)_j(\xi) &\approx (\tilde{\beta}_r)_j(\xi) = N_1(\xi)d_{j-1} + N_2(\xi)d_j. \end{aligned} \quad (6.106)$$

From (6.102) and (6.106), the approximation of the derivatives of  $\beta_l(\xi)$  and  $\beta_r(\xi)$  with respect to  $\eta$  are

$$\begin{aligned} (\beta'_l)_j(\xi) &\approx (\tilde{\beta}'_l)_j(\xi) = \frac{2}{\Delta} \left( N_{1;\xi}(\xi)c_{j-1} + N_{2;\xi}(\xi)c_j \right), \\ (\beta'_r)_j(\xi) &\approx (\tilde{\beta}'_r)_j(\xi) = \frac{2}{\Delta} \left( N_{1;\xi}(\xi)d_{j-1} + N_{2;\xi}(\xi)d_j \right), \end{aligned} \quad (6.107)$$

with  $\Delta$  from (6.103) and prime being the derivation with respect to  $\eta$ .

Finally by applying equations (6.104)-(6.107) to (6.96) we obtain the discretized dimensionless energy

$$\begin{aligned}
E(c_j, d_j, l) = & \frac{1}{3n} l(1 - \kappa) \sum_{j=1}^n \left[ \sin 2\varphi_l \sin 2\varphi_r \left( c_{j-1}(2d_{j-1} + d_j) + c_j(d_{j-1} + 2d_j) \right) \right. \\
& \left. + \sin^2 2\varphi_l (c_{j-1}^2 + c_{j-1}c_j + c_j^2) + \sin^2 2\varphi_r (d_{j-1}^2 + d_{j-1}d_j + d_j^2) \right] \\
& + \frac{2m}{c} \sum_{j=1}^n \left[ |\sin \varphi_l (c_j - c_{j-1})| + |\sin \varphi_r (d_j - d_{j-1})| \right] \\
& + \frac{mn}{lc^2} \sum_{j=1}^n \left[ \sin^2 \varphi_l (c_j - c_{j-1})^2 + \sin^2 \varphi_r (d_j - d_{j-1})^2 \right. \\
& \left. + 2\chi |\sin \varphi_l (c_j - c_{j-1})| |\sin \varphi_r (d_j - d_{j-1})| \right] \\
& + \frac{H}{2} \kappa (\langle \beta_l \rangle \sin 2\varphi_l + \langle \beta_r \rangle \sin 2\varphi_r)^2 \\
& + \frac{H}{2} (\langle \beta_l \rangle \cos 2\varphi_l + \langle \beta_r \rangle \cos 2\varphi_r - 1)^2 \\
& + \frac{1}{2} (1 - \kappa) (H - 2l) (c_n \sin 2\varphi_l + d_n \sin 2\varphi_r)^2, \tag{6.108}
\end{aligned}$$

with

$$\begin{aligned}
\langle \beta_l \rangle &= \frac{1}{H} \left( \frac{l}{n} \sum_{j=1}^n (c_{j-1} + c_j) + c_n (H - 2l) \right), \\
\langle \beta_r \rangle &= \frac{1}{H} \left( \frac{l}{n} \sum_{j=1}^n (d_{j-1} + d_j) + d_n (H - 2l) \right). \tag{6.109}
\end{aligned}$$

Minimizing Eq. (6.108) with respect to variables  $(c_j, d_j, l)$  and with additional constraint

$$0 \leq l \leq \frac{H}{2},$$

we obtain the numerical solutions for  $\beta_l$  and  $\beta_r$ .

Applying Eq. (6.107) to

$$(\alpha_l)_j = (\beta_l^l)_j \sin \varphi_l \quad \text{and} \quad (\alpha_r)_j = (\beta_r^l)_j \sin \varphi_r, \tag{6.110}$$

with  $j$  being the element number, gives us the discretization of normalized dislocation densities, namely

$$(\alpha_l)_j = \begin{cases} \frac{n \sin \varphi_l}{l} (c_j - c_{j-1}), & \text{for } \eta \in (0, l), \\ 0, & \text{for } \eta \in (l, H - l), \\ -\frac{n \sin \varphi_l}{l} (c_j - c_{j-1}), & \text{for } \eta \in (H - l, H), \end{cases} \tag{6.111}$$

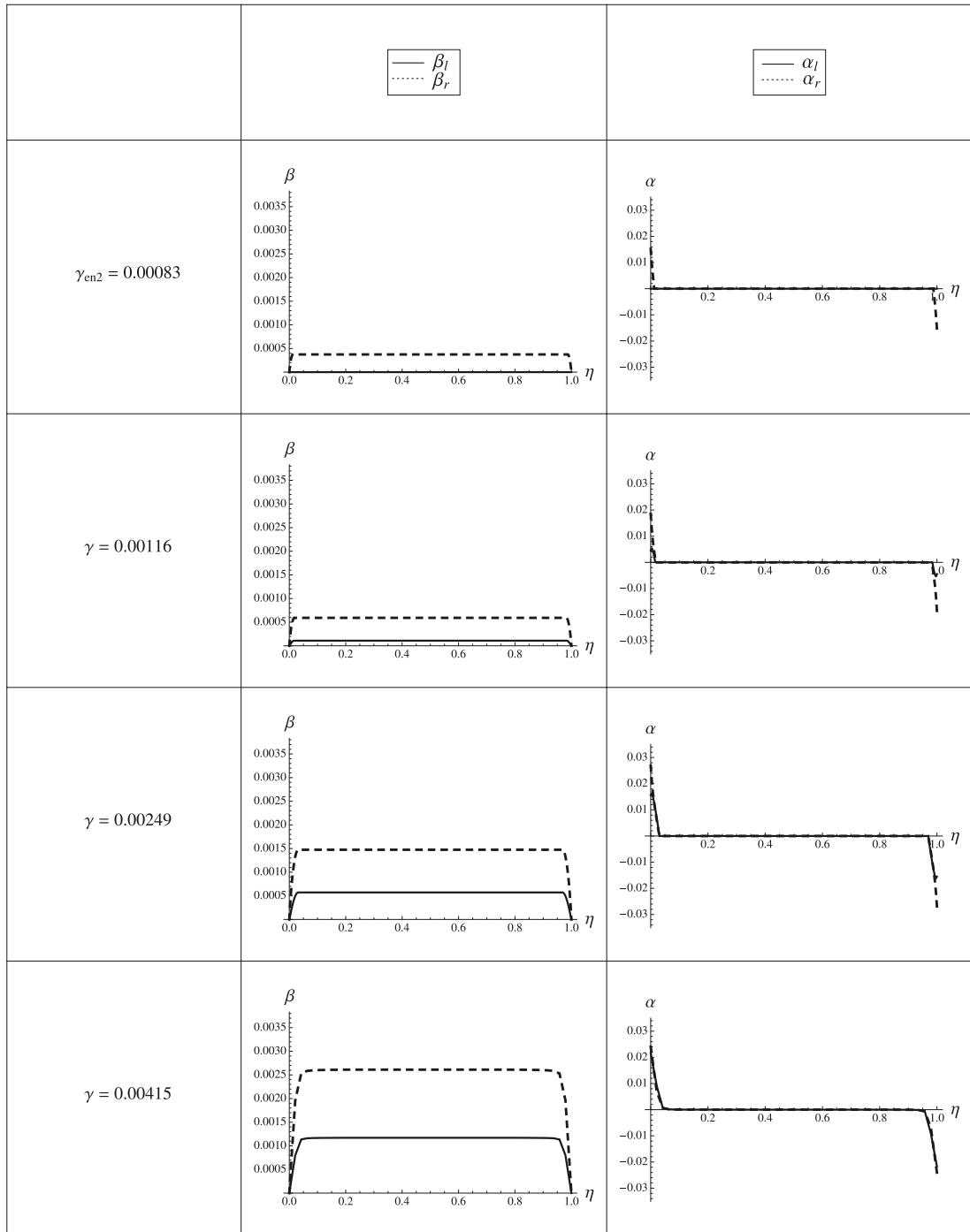


Figure 6.10: Evolution of  $\beta_l$  and  $\beta_r$  together with  $\alpha_l$  and  $\alpha_r$  for general case double-slip constrained shear of single crystal at zero dissipation where  $h = 1 \mu\text{m}$ ,  $\varphi_l = 35^\circ$  and  $\varphi_r = 165^\circ$  at  $\gamma \geq \gamma_{en2}$

and

$$(\alpha_r)_j = \begin{cases} \frac{n \sin \varphi_r}{l} (d_j - d_{j-1}), & \text{for } \eta \in (0, l), \\ 0, & \text{for } \eta \in (l, H - l), \\ -\frac{n \sin \varphi_r}{l} (d_j - d_{j-1}), & \text{for } \eta \in (H - l, H). \end{cases} \quad (6.112)$$

For the normalized shear stress and strain relation, the discretized form of the average plastic

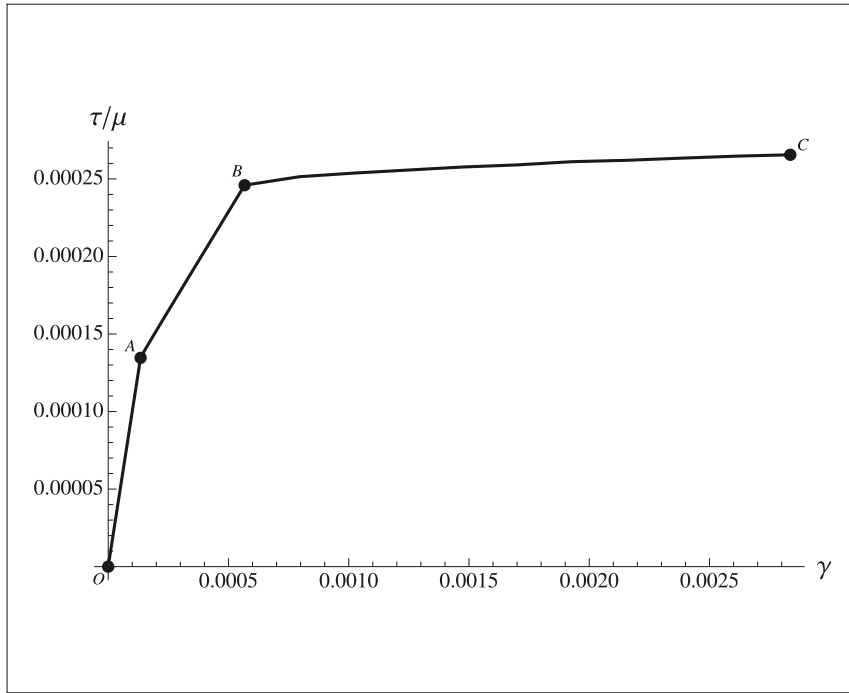


Figure 6.11: Normalized shear stress versus shear strain curve for general case double-slip constrained shear of single crystal at zero dissipation at  $\varphi_l = 35^\circ$  and  $\varphi_r = 165^\circ$  with  $h = 1 \mu\text{m}$

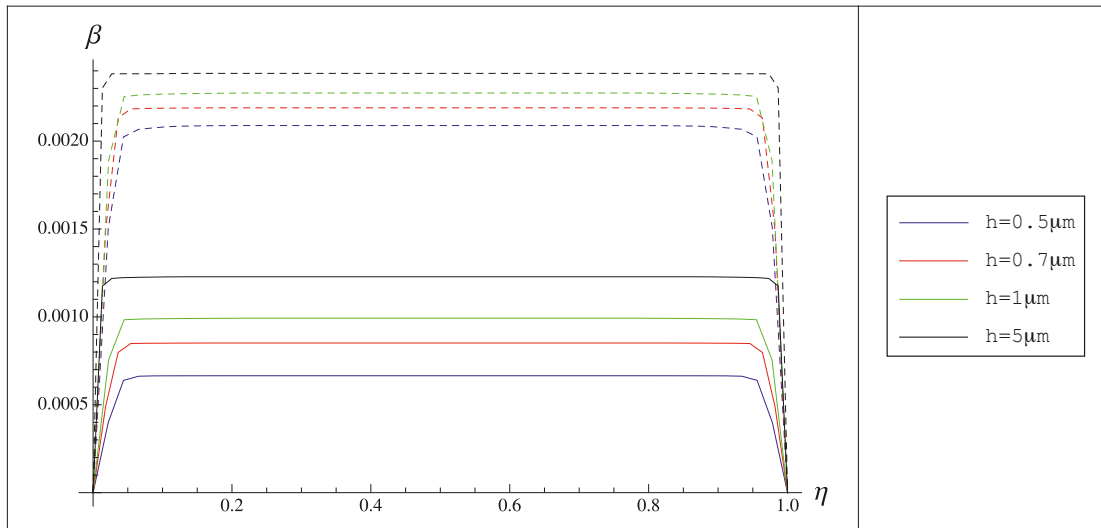


Figure 6.12: Evolution of  $\beta_l$  (continuous lines) and  $\beta_r$  (dashed lines) within the interval  $\eta \in (0, 1)$  for zero dissipation double-slip constrained shear of single crystal at  $\varphi_l = 35^\circ$ ,  $\varphi_r = 165^\circ$  and  $\gamma = 0.01$  with different crystal heights  $h$

distortions takes the form

$$\frac{\tau}{\mu} = \gamma - (\langle \beta_l \rangle \cos 2\varphi_l + \langle \beta_r \rangle \cos 2\varphi_r), \quad (6.113)$$

with  $\langle \beta_l \rangle$  and  $\langle \beta_r \rangle$  from (6.109).

For numerical example we apply 10 elements for each boundary layer. In order to plot the results in the same way as in previous cases, after the computation, we need to multiply  $\eta$ ,

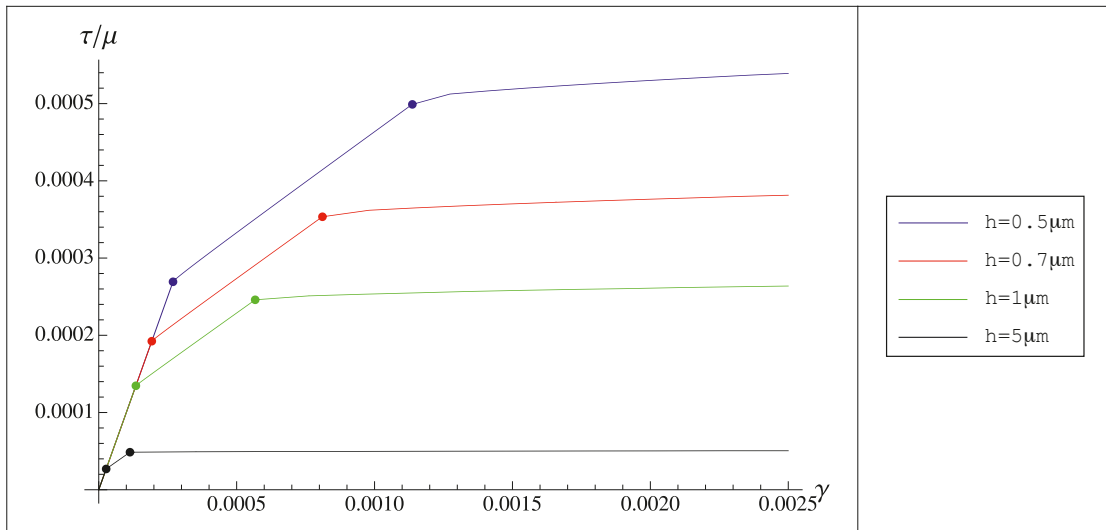


Figure 6.13: Normalized shear stress versus shear strain curves for zero dissipation double-slip constrained shear of single crystal at  $\varphi_l = 35^\circ$  and  $\varphi_r = 165^\circ$  with different crystal heights  $h$

$H$  and all the results from the computation ( $\beta_l, \beta_r, \alpha_l$  and  $\alpha_r$ ) with  $\gamma$ . And so for plotting the results, we now have  $\eta \in (0, 1)$  and  $H = 1$ .

Fig. 6.10 outlines the plots of the evolution of plastic distortions ( $\beta_l, \beta_r$ ) together with the evolution of dislocation densities ( $\alpha_l, \alpha_r$ ) at  $\varphi_l = 35^\circ$  and  $\varphi_r = 165^\circ$  for  $\gamma \geq \gamma_{en2}$  where  $h = 1 \mu\text{m}$ . The normalized stress-strain curve for the general case where the dissipation of energy is negligible for  $\varphi_l = 35^\circ$  and  $\varphi_r = 165^\circ$  is illustrated in Fig. 6.11. The linear line OA is the plot of (6.83) where line AB is the plot either from (6.84) or (6.84) (see section (6.2.1) for the explanation of the case determination). Line BC is the plot of (6.113) where both slip systems are already activated. The lines AB and BC explain the work hardening sections due to the dislocation pile-up. Because there is no dissipation of energy, the stress strain curve follows the same path CBAO as we unload by decreasing  $\gamma$ . Fig. 6.12 and Fig. 6.13 illustrate the plots of plastic distortions ( $\beta_l$  and  $\beta_r$ ) and normalized stress strain curves with different  $h$ , respectively, which explain the size effect with the same reason explained in section 3.3.2. The left dot of each curve explains the first energetic yield point where only one slip system is active and the right dot describes the second energetic yield point where both slip systems become active.

To confirm the correctness of the numerical simulation, we need to compare the results in the special case of symmetric double slip between the analytical solutions found in section 6.2.2 and numerical solutions (with the largest relative error less than 0.6 %).

### 6.3 Double slip plane-constrained shear at non-zero dissipation

In the case of non-zero dissipation, similar to the single slip system case, the evolution of  $\beta_l$  and  $\beta_r$  must be obtained from solving

$$\delta\Psi + aL \left( \int_0^h \frac{\partial D}{\partial \dot{\beta}_l} \delta\beta_l dy + \int_0^h \frac{\partial D}{\partial \dot{\beta}_r} \delta\beta_r dy \right) = 0, \quad (6.114)$$

under boundary conditions (6.4), where  $\Psi$  from (6.14). The simplest dissipation potential can be proposed as follows

$$D = K \left( |\dot{\beta}_l| + |\dot{\beta}_r| \right), \quad (6.115)$$

with  $K$  being positive constant called critical resolved shear stress of the crystal, and the dot above a function denoting its time derivative. Note that the cross-slip interaction leading to the latent hardening can also be taken into account by adding some cross terms in (6.115). Due to the complexity of such models with latent hardening, we will not consider them in our work here.

For  $\dot{\beta}_l \neq 0$  and  $\dot{\beta}_r \neq 0$ , we assume that the signs of  $\dot{\beta}_l$  and  $\dot{\beta}_r$  do not change during the plastic deformation, ergo the variational equation (6.114) can be written as

$$\delta\hat{\Psi} = 0, \quad (6.116)$$

with  $\hat{\Psi}$  being the effective energy where the terms originating from dissipation are added to the energy functional (6.14), namely

$$\hat{\Psi} = \Psi + aL \int_0^h \left( \frac{\partial D}{\partial \dot{\beta}_l} \dot{\beta}_l + \frac{\partial D}{\partial \dot{\beta}_r} \dot{\beta}_r \right) dy. \quad (6.117)$$

For  $\dot{\beta}_l = 0$  or  $\dot{\beta}_r = 0$  the corresponding equation (6.114) does not have to be satisfied which simply replaced by the equations  $\dot{\beta}_r = 0$  or  $\dot{\beta}_l = 0$ . Applying (6.14) and (6.115) to (6.117), the effective energy functional is now expressed by

$$\begin{aligned} \hat{\Psi} = aL\mu \int_0^h & \left[ \frac{1}{2}(1 - \kappa)(\beta_l \sin 2\varphi_l + \beta_r \sin 2\varphi_r)^2 + \frac{\kappa}{2}(\langle \beta_l \rangle \sin 2\varphi_l + \langle \beta_r \rangle \sin 2\varphi_r)^2 \right. \\ & + \frac{1}{2}(\langle \beta_l \rangle \cos 2\varphi_l + \langle \beta_r \rangle \cos 2\varphi_r - \gamma)^2 + \frac{k}{b\rho_s}(|\beta_{l,y} \sin \varphi_l| + |\beta_{r,y} \sin \varphi_r|) \\ & + \frac{k}{2(b\rho_s)^2}(\beta_{l,y}^2 \sin^2 \varphi_l + \beta_{r,y}^2 \sin^2 \varphi_r + 2\chi|\beta_{l,y} \sin \varphi_l||\beta_{r,y} \sin \varphi_r|) \\ & \left. + \frac{K}{\mu} \left( (\text{sign}\dot{\beta}_l) \beta_l + (\text{sign}\dot{\beta}_r) \beta_r \right) \right] dy. \quad (6.118) \end{aligned}$$

Analogous to the zero dissipation case, we introduce the following dimensionless quantities

$$\begin{aligned} \hat{E} &= \frac{\hat{\Psi}}{\mu a L h}, \quad \eta = \frac{y}{h}, \quad \bar{\beta}_l(\eta) = \beta_l(y), \quad \bar{\beta}_r(\eta) = \beta_r(y), \\ c &= hb\rho_s \quad \text{and} \quad \gamma_{cr} = \frac{K}{\mu}, \quad (6.119) \end{aligned}$$

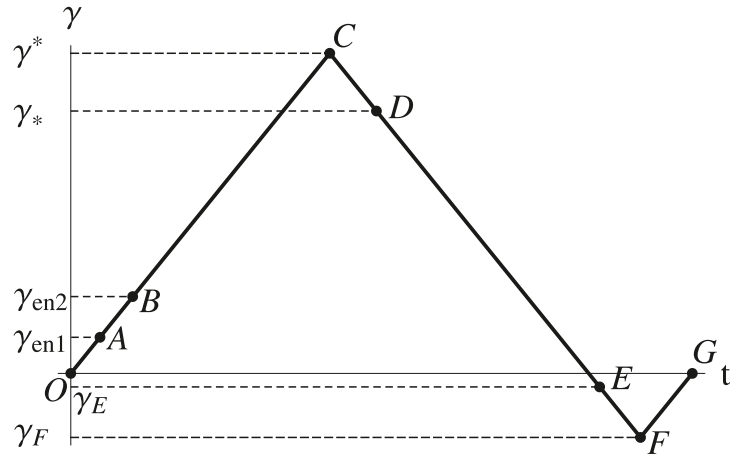


Figure 6.14: A closed loading path for plane-constrained shear problem with two active slip systems

with  $\eta \in (0, 1)$ . We may reduce the functional (6.118) using the dimensionless variables (6.119), namely

$$\begin{aligned} \hat{E} = \int_0^1 & \left[ \frac{1}{2}(1 - \kappa)(\beta_l \sin 2\varphi_l + \beta_r \sin 2\varphi_r)^2 + \frac{\kappa}{2}(\langle \beta_l \rangle \sin 2\varphi_l + \langle \beta_r \rangle \sin 2\varphi_r)^2 \right. \\ & + \frac{1}{2}(\langle \beta_l \rangle \cos 2\varphi_l + \langle \beta_r \rangle \cos 2\varphi_r - \gamma)^2 + \frac{k}{c}(|\beta'_l \sin \varphi_l| + |\beta'_r \sin \varphi_r|) \\ & + \frac{k}{2c^2}((\beta'_l)^2 \sin^2 \varphi_l + (\beta'_r)^2 \sin^2 \varphi_r + 2\chi|\beta'_l \sin \varphi_l||\beta'_r \sin \varphi_r|) \\ & \left. + \gamma_{cr} \left( (\text{sign} \dot{\beta}_l) \beta_l + (\text{sign} \dot{\beta}_r) \beta_r \right) \right] d\eta, \end{aligned} \quad (6.120)$$

where the bars over  $\bar{\beta}_l$  and  $\bar{\beta}_r$  are ignored for short and  $\langle \bar{\beta}_l \rangle$  and  $\langle \bar{\beta}_r \rangle$  are similar to (6.18)

We need to determine  $\beta_l(t, \eta)$  and  $\beta_r(t, \eta)$  with  $\gamma$  as the driving variable. Considering the loading path as shown in Fig. 6.14, we increase  $\gamma$  first from zero to  $\gamma^*$  (OC), then decrease it to  $\gamma_F$  (CF), and afterward increase it again to zero (FG). As in the single slip problem, we assume also the rate independence of dissipation so that the rate of change of  $\gamma(t)$  will not influence the results. We need now to determine the evolution of  $\beta_l$  and  $\beta_r$  as function of  $t$  and  $\eta$  where  $\beta_l = 0$  and  $\beta_r = 0$  at  $t = 0$ .

For plotting the results, we employ again the same material parameters as in the case with no dissipation with addition  $\gamma_{cr} = 0.0009$ .

### 6.3.1 Energetic threshold values

From the previous analysis of the case with zero dissipation we know already that for this kind of problem the energetic threshold values,  $\gamma_{en1}$  and  $\gamma_{en2}$ , are present. The plastic distortions,  $\beta_l$  and  $\beta_r$ , are initially equal to zero and the dislocation nucleation is not exist when  $\gamma < \gamma_{en1}$ . For the interval  $\gamma_{en1} \leq \gamma < \gamma_{en2}$ , the crystal deforms in single slip and afterwards, for  $\gamma \geq \gamma_{en2}$ , both slip systems are fully activated. We adopt the same procedures presented in section (6.2.1) to obtain both energetic threshold values.

We now consider the first case where  $\beta_l$  appears at  $\gamma = \gamma_{en1}$  and then  $\beta_r$  emerges at  $\gamma = \gamma_{en2}$ . We denote for the first case ( $\beta_l$  appears first)

$$\begin{aligned} \beta_e(\eta) &= \beta_l(\eta), & \beta_f(\eta) &= \beta_r(\eta), & \beta_{em} &= \beta_{lm}, & \beta_{fm} &= \beta_{rm}, \\ \langle \beta_e \rangle &= \langle \beta_l \rangle, & \langle \beta_f \rangle &= \langle \beta_r \rangle, & \varphi_e &= \varphi_l, & \varphi_f &= \varphi_r. \end{aligned} \quad (6.121)$$

The first energetic threshold value,  $\gamma_{en1}$ , in term of original height,  $h$ , is given in the form

$$\gamma_{en1} = \frac{\gamma_{cr}}{|\cos 2\varphi_e|} + \frac{2k}{hb\rho_s} \frac{|\sin \varphi_e|}{|\cos 2\varphi_e|}. \quad (6.122)$$

For every  $\gamma \geq \gamma_{en1}$ , the following conditions

$$\gamma \cos 2\varphi_e - \gamma_{cr} - \frac{2k |\sin \varphi_e|}{c} > 0, \quad (6.123)$$

for  $\beta_e > 0$  and

$$\gamma \cos 2\varphi_e + \gamma_{cr} + \frac{2k |\sin \varphi_e|}{c} < 0, \quad (6.124)$$

for  $\beta_e < 0$  must be fulfilled.

When  $\gamma$  is increased further in the range  $\gamma_{en1} \leq \gamma < \gamma_{en2}$ , the plastic distortion is evolved in one active slip system with the solutions

$$\beta_e = \begin{cases} \beta_p(1 - \cosh \zeta \eta + \tanh \zeta l \sinh \zeta \eta), & \text{for } \eta \in (0, l), \\ \beta_{em} = \beta_p \left(1 - \frac{1}{\cosh \zeta l}\right), & \text{for } \eta \in (l, 1-l), \\ \beta_p(1 - \cosh \zeta(1-\eta) + \tanh \zeta l \sinh \zeta(1-\eta)), & \text{for } \eta \in (1-l, 1), \end{cases} \quad (6.125)$$

where

$$\beta_p = \frac{\gamma_l \cos 2\varphi_e - (\cos^2 2\varphi_e + \kappa \sin^2 2\varphi_e) \langle \beta_e \rangle}{(1 - \kappa) \sin^2 2\varphi_e} \quad \text{and} \quad \zeta = 2c |\cos \varphi_l| \sqrt{\frac{1 - \kappa}{k}}, \quad (6.126)$$

with

$$\gamma_l = \gamma - \frac{\gamma_{cr} \text{sign} \dot{\beta}_e}{\cos 2\varphi_e}, \quad (6.127)$$

where during the loading

$$\text{sign} \dot{\beta}_e = \begin{cases} 0, & \text{for } \varphi_e = 0^\circ, \\ +1, & \text{for } 0^\circ < \varphi_e < 45^\circ, \\ -1, & \text{for } 45^\circ < \varphi_e < 90^\circ. \end{cases} \quad (6.128)$$

From (6.128), during the loading process (increasing  $\gamma$ ), we found out that

$$\text{sign} \dot{\beta}_e = \text{sign} \beta_e = \text{sign} \beta'_e. \quad (6.129)$$

The average of plastic distortion takes the form

$$\langle \beta_e \rangle = \gamma_l \cos 2\varphi_e B_e(l), \quad (6.130)$$

with

$$B_e(l) = \frac{g(l)}{(1 - \kappa) \sin^2 2\varphi_e + g(l)(\cos^2 2\varphi_e + \kappa \sin^2 2\varphi_e)}, \quad (6.131)$$

and

$$g(l) = 2 \left( l - \frac{\tanh \zeta l}{\zeta} \right) + \left( 1 - \frac{1}{\cosh \zeta l} \right) (1 - 2l). \quad (6.132)$$

The equation of  $\gamma$  in term of  $l$  takes the form

$$\gamma(l) = \frac{\text{sign}(\beta_e)}{\cos 2\varphi_e} \left( \gamma_{cr} + \frac{2k |\sin \varphi_e| \cosh \zeta l}{c(1 - 2l) (1 - (\cos^2 2\varphi_e + \kappa \sin^2 2\varphi_e) B_e(l))} \right). \quad (6.133)$$

We need first to find  $l_{en2}$  by either

$$f(\text{sign}\beta_{fm} = 1, l_{en2}) = 0, \quad (6.134)$$

for  $\beta_f > 0$ , or

$$f(\text{sign}\beta_{fm} = -1, l_{en2}) = 0, \quad (6.135)$$

for  $\beta_f < 0$ , then substituting the newly found  $l_{en2}$  into (6.133) to obtain  $\gamma_{en2}$  where

$$\begin{aligned} f(\text{sign}\beta_{fm}, l) = & - \frac{2k |\sin \varphi_f| \text{sign}\beta_{fm}}{c} - (1 - 2l)(1 - \kappa) \sin 2\varphi_e \sin 2\varphi_f \beta_{em}(l) \\ & - (\cos 2\varphi_e \cos 2\varphi_f + \kappa \sin 2\varphi_e \sin 2\varphi_f) \langle \beta_e \rangle (l) \\ & + \frac{2}{\zeta} (1 - \kappa) \sin 2\varphi_e \sin 2\varphi_f \beta_p(l) (\zeta l - \tanh \zeta l) \\ & + \gamma(l) \cos 2\varphi_f - \gamma_{cr} \text{sign}\dot{\beta}_f, \end{aligned} \quad (6.136)$$

with  $\text{sign}\dot{\beta}_f = \text{sign}\beta_{fm}$  in the course of increasing  $\gamma$ ,  $\beta_{em}$  from (6.125),  $\beta_p$  from (6.126) and  $\langle \beta_e \rangle$  from (6.130). Mention that only one equation from (6.134) and (6.135) that gives  $l_{en2}$  so that we can also determine the sign of  $\beta_f$ .

Considering the second case where  $\beta_r$  being first activated at  $\gamma = \gamma_{en1}$  then  $\beta_l$  at  $\gamma = \gamma_{en2}$ , we obtain  $\gamma_{en1}$  and  $\gamma_{en2}$  by substituting

$$\begin{aligned} \beta_e(\eta) = \beta_r(\eta), \quad \beta_f(\eta) = \beta_l(\eta), \quad \beta_{em} = \beta_{rm}, \quad \beta_{fm} = \beta_{lm}, \\ \langle \beta_e \rangle = \langle \beta_r \rangle, \quad \langle \beta_f \rangle = \langle \beta_l \rangle, \quad \varphi_e = \varphi_r, \quad \varphi_f = \varphi_l, \end{aligned} \quad (6.137)$$

into Eqs. (6.122)-(6.136).

### 6.3.2 Symmetric double slip systems at non-zero dissipation

As in section (6.2.2), with regard to derive closed-form analytical solution it is convenient to analyze the evolution of  $\beta_l$  and  $\beta_r$  in the special case of symmetric double slip systems where

$$\varphi_r = \pi - \varphi_l = \pi - \varphi. \quad (6.138)$$

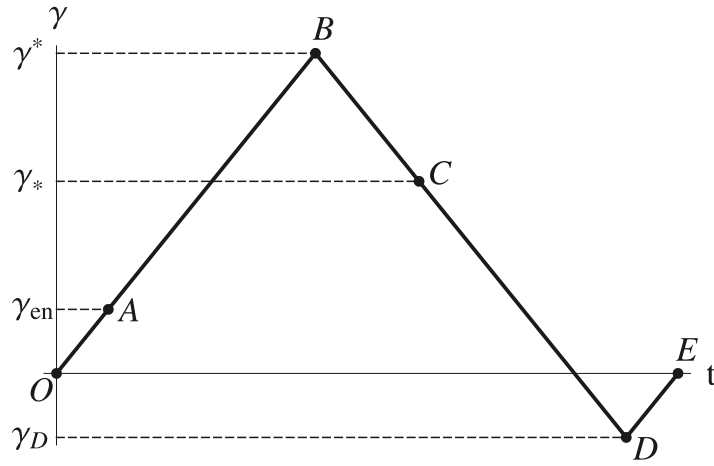


Figure 6.15: A closed loading path for plane-constrained shear problem with symmetric double slip systems

Applying (6.138) to the effective energy functional (6.120) then following the procedures to find the energetic threshold values presented in section (6.3.1), we found out that both slip systems are activated at the same time at

$$\gamma_{en} = \frac{\gamma_{cr}}{|\cos 2\varphi|} + \frac{2k}{c} \frac{|\sin \varphi|}{|\cos 2\varphi|}, \quad (6.139)$$

and have the relation

$$\beta_{lm} = \beta_{rm}.$$

Consequently we can denote

$$\beta_l(\eta) = \beta_r(\eta) = \beta \quad \text{and} \quad \langle \beta_l \rangle = \langle \beta_r \rangle = \langle \beta \rangle, \quad (6.140)$$

under the boundary conditions

$$\beta(0) = \beta[1] = 0. \quad (6.141)$$

Thus, after doing some algebraic manipulation and omitting the unnecessary terms for the variational computation, the effective energy functional (6.120) is changed into

$$\hat{E}(\beta) = \int_0^1 \left[ \frac{1}{2} (2\langle \beta \rangle \cos 2\varphi - \gamma_l)^2 + \frac{2k|\sin \varphi||\beta'|}{c} + \frac{k(1+\chi)\sin^2 \varphi (\beta')^2}{c^2} \right] d\eta, \quad (6.142)$$

with

$$\langle \beta \rangle = \int_0^1 \beta d\eta, \quad (6.143)$$

and

$$\gamma_l = \gamma - \frac{\gamma_{cr} \text{sign} \dot{\beta}}{\cos 2\varphi}. \quad (6.144)$$

Since we have now only one  $\beta$ , we need to change the loading path (6.14) into the one shown in Fig. (6.15).

In the beginning of loading process, the plastic distortion,  $\beta$ , is equal to zero along the loading path OA from Fig. (6.15) until  $\gamma$  reaches the energetic threshold value  $\gamma_{en}$ . Geometrically necessary dislocations start to emerge when the situation  $\gamma \geq \gamma_{en}$  (loading path AB) holds true. Hence the plastic distortion,  $\beta$ , is no longer zero and starts to evolve throughout loading path AB with

$$\text{sign}\dot{\beta} = \text{sign}\beta. \quad (6.145)$$

The meaning of (6.145) is that we have constantly increasing  $\beta$  for  $\beta > 0$  and constantly decreasing  $\beta$  for  $\beta < 0$  as  $\gamma$  grows. From the derivation of the energetic threshold value we found out

$$\text{sign}\beta = \begin{cases} 0, & \text{for } \varphi_e = 0^\circ, \\ +1, & \text{for } 0^\circ < \varphi_e < 45^\circ, \\ -1, & \text{for } 45^\circ < \varphi_e < 90^\circ. \end{cases} \quad (6.146)$$

With the assumption that there exist a dislocation-free zone in the middle of the crystal and  $\text{sign}\beta'$  should be changed in  $\eta \in (0, 1)$  as a result of boundary conditions (6.141), we employ again the minimizer (6.62) obeying (6.66) and the relation between  $\text{sign}\beta'(\eta)$  with  $\varphi$  from (6.63). Hence the effective energy (6.142) now can be written in the form

$$\hat{E} = \int_0^l \left[ \frac{4k|\sin\varphi||\beta'_1|}{c} + \frac{2k(1+\chi)\sin^2\varphi\beta_1'^2}{c^2} \right] d\eta + \frac{1}{2}(2\langle\beta\rangle\cos 2\varphi - \gamma_l)^2, \quad (6.147)$$

with

$$\gamma_l = \gamma - \frac{\gamma_{cr}\text{sign}\beta}{\cos 2\varphi}. \quad (6.148)$$

where  $\text{sign}\beta$  from (6.146) and

$$\langle\beta\rangle = 2 \int_0^l \beta_1 d\eta + (1-2l)\beta_m. \quad (6.149)$$

We intend to find  $\beta_1$ ,  $\beta'$  and the boundary layer thickness  $l$ . Since (6.147) has a similar form as (6.64), we can obtain here all of the same solutions as in (6.73)-(6.78) but now with  $\gamma_l$  from (6.148) replacing  $\gamma$ . The equation of  $\gamma$  as a function of  $l$  is given in the form

$$\gamma(l) = \frac{\gamma_{cr}\text{sign}\beta}{\cos 2\varphi} + \frac{2k|\sin\varphi|\text{sign}\beta}{c(1-2l)\cos 2\varphi(1-2\cos^2 2\varphi B(l))}. \quad (6.150)$$

with  $\text{sign}\beta$  from (6.146). The distribution of normalized dislocation density for this case has the similar form as in (6.81). Fig. (6.16) shows the distribution and evolution of plastic distortion,  $\beta$ , and dislocation density,  $\alpha$ , in the course of loading for the crystal with  $h = 1 \mu\text{m}$  at  $\varphi = 30^\circ$ .

After arriving at  $\gamma = \gamma^*$  (point B), for the inverse loading process taking after loading path BC, we decrease  $\gamma$  up to point C ( $\gamma = \gamma_*$ ). During this loading path, the condition  $\dot{\beta} = 0$  holds true and the dissipation potential,  $D$ , vanishes so that the crystal deforms elastically. The plastic distortion  $\beta = \beta^*$  and dislocation density  $\alpha = \alpha^*$  stay the same up to some point where the plastic deformation begins (point C).

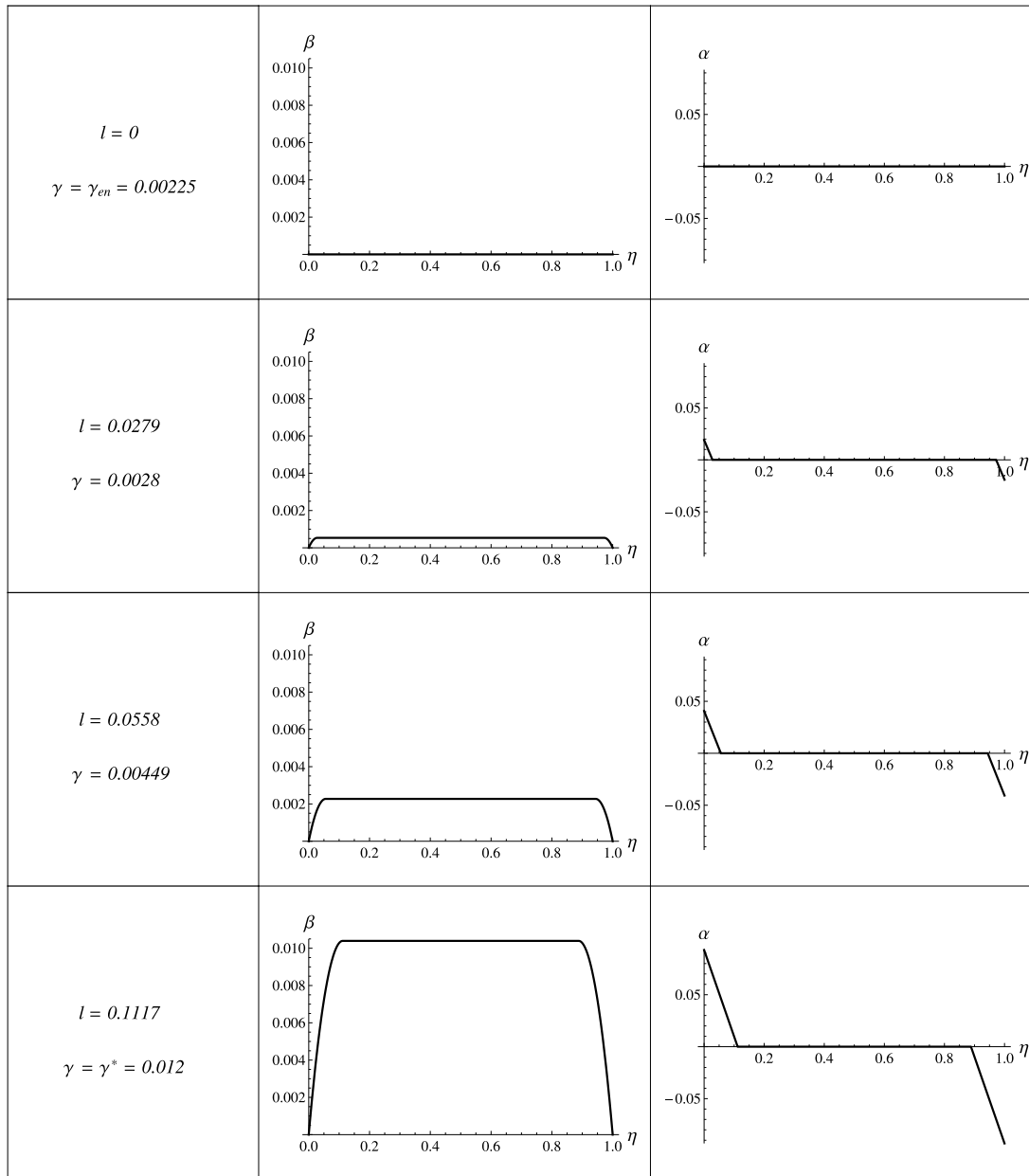


Figure 6.16: Evolution of  $\beta$  and  $\alpha$  for the case of symmetric double slip systems with dissipation during the loading process as  $\gamma$  increases at  $\varphi = 30^\circ$  where  $h = 1 \mu\text{m}$ .

Start from point C, we decrease further  $\gamma$  so that the plastic distortion,  $\beta$ , begins to evolve towards zero at point D. In this inverse loading path CD, since we have constantly decreasing  $\beta$  for  $\beta > 0$  and steadily increasing  $\beta$  as  $\beta < 0$ , we have

$$\text{sign} \dot{\beta} = -\text{sign} \beta, \quad (6.151)$$

where  $\text{sign} \beta$  from (6.146). The effective energy for inverse loading case can now be written as

$$\hat{E} = \int_0^l \left[ \frac{4k |\sin \varphi| |\beta'_1|}{c} + \frac{2k(1 + \chi) \sin^2 \varphi \beta_1'^2}{c^2} \right] d\eta + \frac{1}{2} (2\langle \beta \rangle \cos 2\varphi - \gamma_u)^2, \quad (6.152)$$

with  $\langle \beta \rangle$  from (6.149) and

$$\gamma_u = \gamma + \frac{\gamma_{cr} \text{sign} \beta}{\cos 2\varphi}. \quad (6.153)$$

We can now compute the general solutions for the inverse loading case by following the same procedure as in loading process, where  $\gamma_u$  from (6.153) is used instead of  $\gamma_l$  for the entire computation and

$$\gamma(l) = -\frac{\gamma_{cr} \operatorname{sign}\beta}{\cos 2\varphi} + \frac{2k|\sin\varphi|\operatorname{sign}\beta}{c(1-2l)\cos 2\varphi(1-2\cos^2 2\varphi B(l))}. \quad (6.154)$$

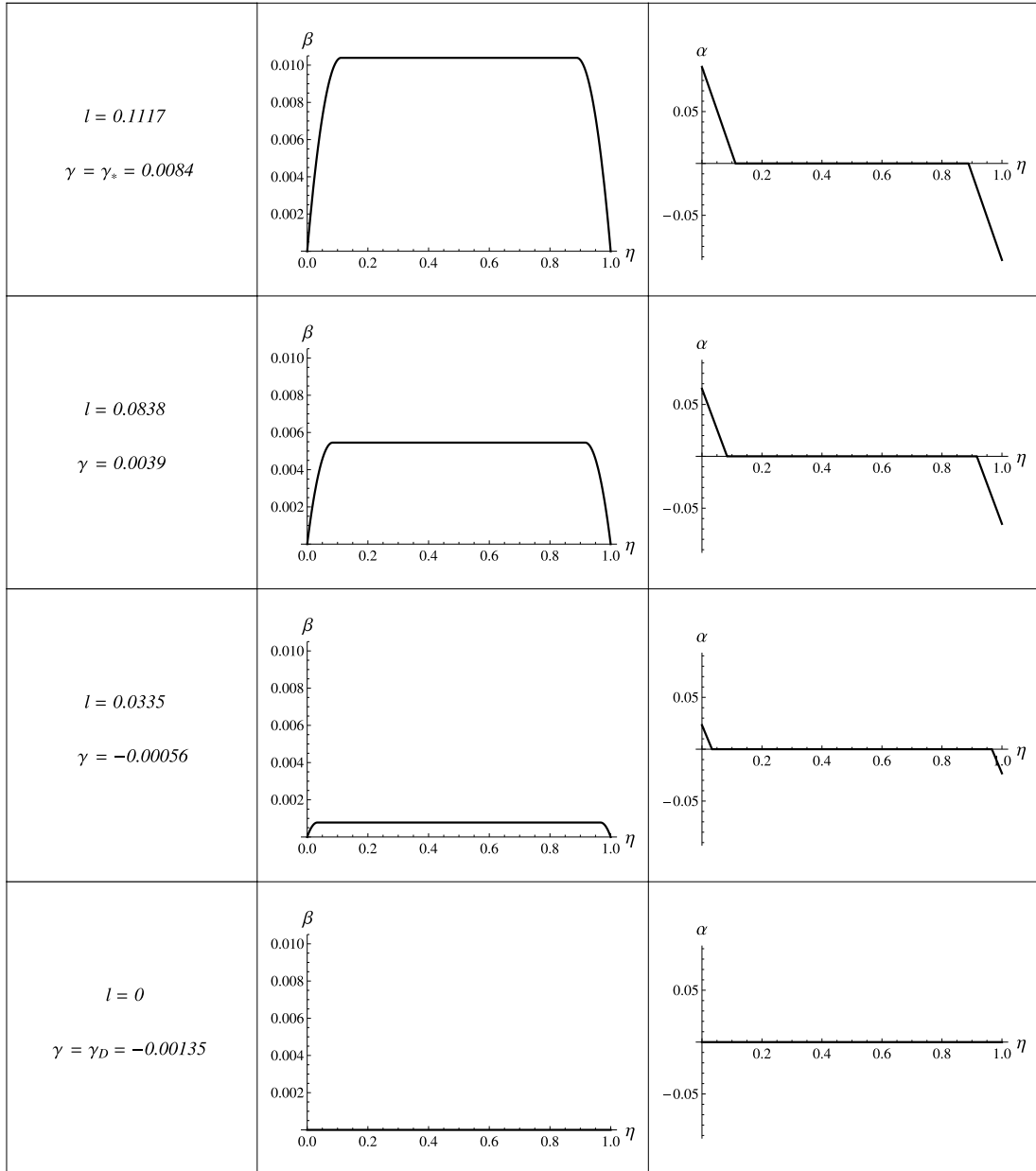


Figure 6.17: Evolution of  $\beta$  and  $\alpha$  for the case of symmetric double slip systems with dissipation in the course of inverse loading process at  $\varphi = 30^\circ$  where  $h = 1 \mu\text{m}$ .

In order to guarantee that  $\beta$  is continuous at point C, since  $\beta$  is constant during loading path BC, the average of plastic distortions  $\langle\beta\rangle$  at point B must be equal to  $\langle\beta\rangle$  at point C. Since  $\langle\beta\rangle$  is proportional to  $\gamma_l$  and also to  $\gamma_u$ , we have the condition that  $\gamma_r$  at point B, namely

$$(\gamma_l)_B = \gamma^* \cos 2\varphi - \gamma_{cr} \operatorname{sign}\beta$$

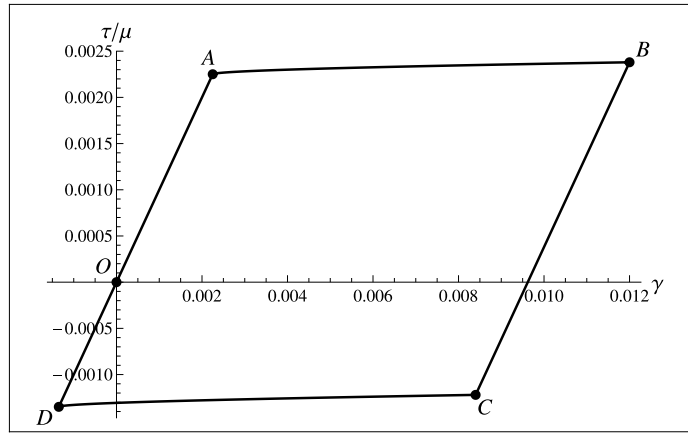


Figure 6.18: Normalized shear stress versus shear strain curve of single-slip constrained shear at non-zero dissipation of single crystal for  $\varphi = 30^\circ$  and  $h = 1 \mu\text{m}$

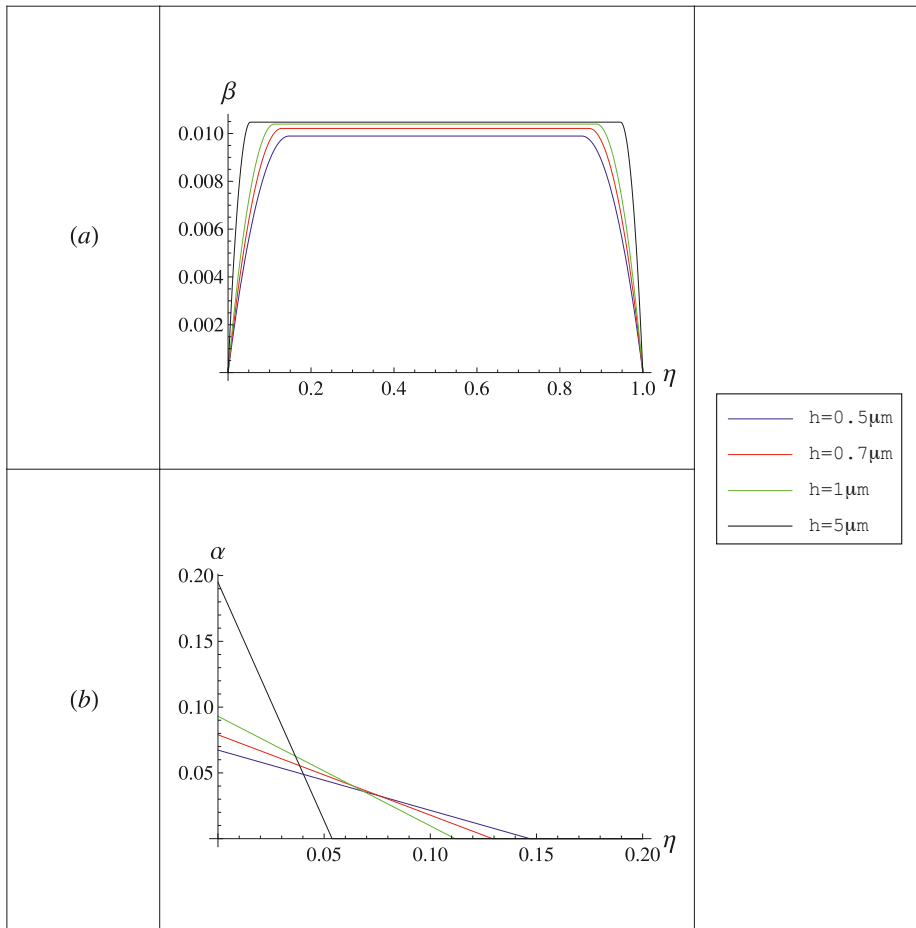


Figure 6.19: Plot of  $\beta$  within the interval  $\eta \in (0, 1)$  and  $\alpha$  within the interval  $\eta \in (0, 0.2)$  at  $\varphi = 30^\circ$  and  $\gamma = 0.012$  with different crystal heights  $h$  for the symmetric double slip system case with non-zero dissipation

must be equal to  $\gamma_u$  at point C, i.e.

$$(\gamma_u)_C = \gamma_* \cos 2\varphi + \gamma_{cr} \text{sign}\beta.$$

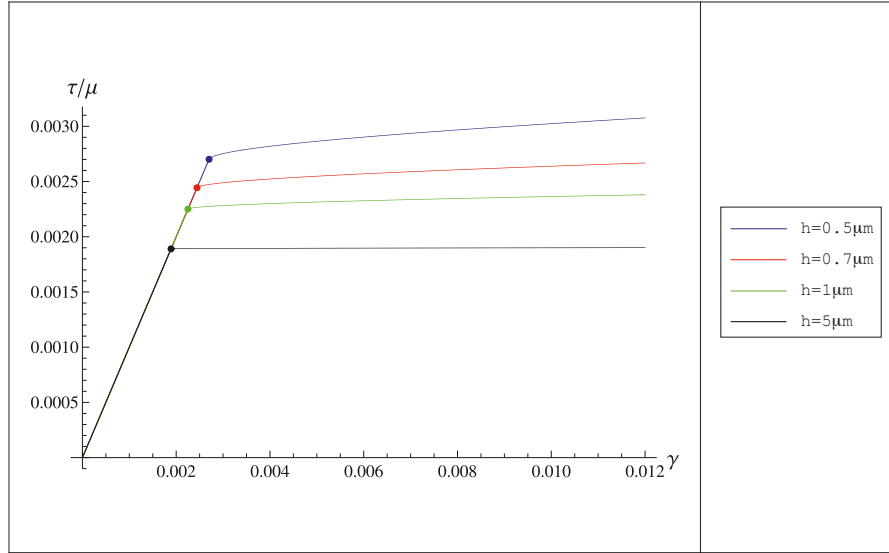


Figure 6.20: Normalized shear stress versus shear strain curve at  $\varphi = 30^\circ$  with different crystal heights  $h$  during the loading for symmetric double slip systems case with dissipation

Accordingly, the beginning point of the plastic flow (point C) is at

$$\gamma_* = \gamma^* - \frac{2\gamma_{cr} \text{sign}\beta}{\cos 2\varphi},$$

with  $\text{sign}\beta$  from (6.146). The evolution of  $\beta$  and  $\alpha$  for decreasing  $\gamma$  during inverse loading process at  $h = 1 \mu\text{m}$  and  $\varphi = 30^\circ$  is depicted in Fig. (6.17).

Then we load the crystal again along the loading path DE by increasing  $\gamma$  further from  $\gamma_D$  to zero. During this phase, the crystal deforms elastically and  $\beta$  remains zero. Similar to point C, to assure the continuity of  $\beta$  at point D, the condition  $\gamma_u$  at point D must be equivalent with  $\gamma_l$  at point A. Therefrom, with  $\gamma_{en}$  from (6.139), we have

$$\gamma_D = \gamma_{en} - \frac{2\gamma_{cr} \text{sign}\beta}{\cos 2\varphi}.$$

Following the closed loading path depicted in Fig. 6.15, we plot the normalized shear strain equation

$$\frac{\tau}{\mu} = \gamma - 2\gamma_l B(l) \cos^2 2\varphi, \quad (6.155)$$

for loading case and

$$\frac{\tau}{\mu} = \gamma - 2\gamma_u B(l) \cos^2 2\varphi, \quad (6.156)$$

for inverse loading case, where  $\gamma_l$  from (6.148),  $\gamma_u$  from (6.153) and  $B(l)$  from (6.77), as illustrated in Fig.6.18. We took  $\gamma_{cr} = 0.0009$ ,  $\gamma^* = 0.012$  and  $\varphi = 30^\circ$  in addition to other material parameters similar to the previous case. From Fig.6.18 we can observe that, during the loading, the crystal deforms elastically up to the point where  $\gamma_{en}$  is achieved (point A). Start from point A, the increase of strain is not linear again with the increase of stress and

the plastic deformation begins. We observe again the work hardening region AB on account of the dislocation pile-ups explained by the last term of (6.155).

In the course of inverse loading, the plastic distortion  $\beta = \beta^*$  stays constant when  $\gamma$  decreases from point B ( $\gamma = \gamma^*$ ) to point C ( $\gamma = \gamma_*$ ). Line BC which is parallel to the line OA shows the elastic deformation. Plastic distortion begins to decrease and the nucleated dislocations starts to annihilate when we decrease  $\gamma$  further from point C to point D. There is no dislocation anymore at point D and  $\beta = 0$ . Lastly, as  $\gamma$  increases from point D to O, the crystal deforms elastically and  $\beta = 0$  is frozen. In this closed cycle OABCDO dissipation is present only along lines AB and CD. We have also here the Bauschinger effect where lines DA and BC are parallel and of the same length.

The effect of the different crystal heights  $h$  for the case with dissipation are outlined in Fig. 6.19 and Fig. 6.20. The distribution of  $\beta$  and  $\alpha$  along the crystal height for  $\varphi = 30^\circ$  and  $\gamma = 0.012$  are shown in Fig. 6.19. Considering the restriction of local concentration of dislocations due to the saturated dislocation density of the energy, similar to the single slip case, the distribution of dislocation pile-up for decreasing  $h$  are forced more into the middle of the crystal for this case causing higher inner back stresses of dislocation. As a consequence, the crystal becomes stronger for smaller size.

Fig. 6.20 illustrates the normalized stress strain curves for this case at different crystal height  $h$ . We observe that, with decreasing  $h$ , the hardening rate increases. The increasing energetic yield points are shown in dots in Fig. 6.20.

### 6.3.3 General double slip systems case with energy dissipation

In this general case, all of the solutions will be derived following the loading path presented in Fig. (6.14). For better understanding, we will compute the numerical examples for each loading path by employing the same material parameters as in the case with zero dissipation together with  $\gamma_{cr} = 0.0009$ ,  $h = 1 \mu\text{m}$ ,  $\varphi_l = 35^\circ$  and  $\varphi_r = 155^\circ$ .

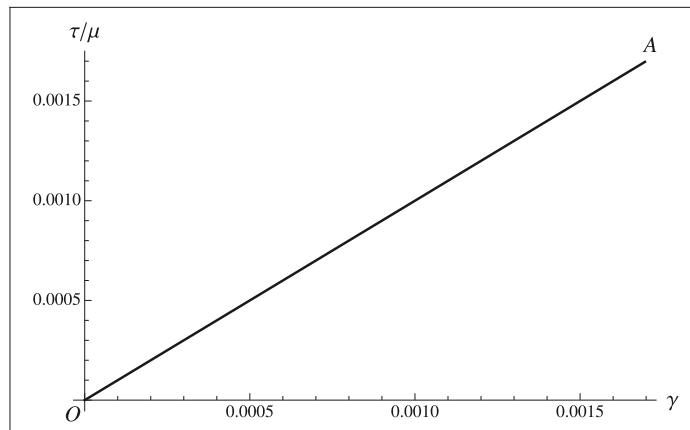


Figure 6.21: Normalized shear stress versus shear strain curve for loading path OA at  $\varphi_l = 35^\circ$  and  $\varphi_r = 155^\circ$  where  $h = 1 \mu\text{m}$

In the beginning, we have an elastic deformation in the course of loading path OA since

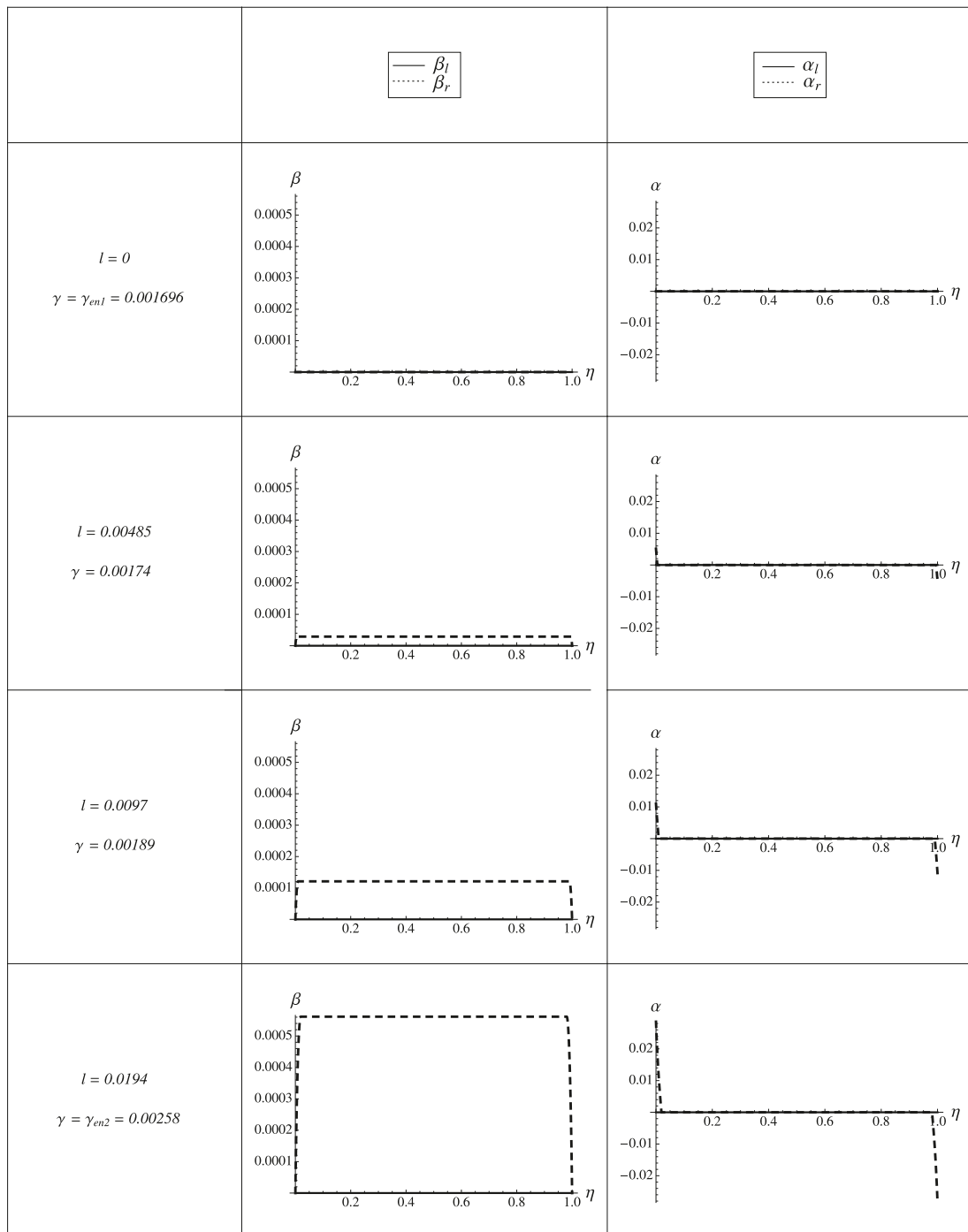


Figure 6.22: Evolution of plastic distortions and dislocation densities for loading path AB as  $\gamma$  increased at  $\varphi_l = 35^\circ$  and  $\varphi_r = 155^\circ$  where  $h = 1 \mu\text{m}$ .

$\dot{\beta}_l$  and  $\dot{\beta}_r$  equal to zero. Therefore, similar to the previous case of symmetric double slip systems,  $\beta_l$  and  $\beta_r$  remain zero as we increase  $\gamma$  from zero to  $\gamma_{en1}$ . The normalized shear stress versus shear strain equation for this loading path takes the form

$$\frac{\tau}{\mu} = \gamma, \quad (6.157)$$

which is depicted in Fig. (6.21).

At point A ( $\gamma = \gamma_{en1}$ ), geometrically necessary dislocations start to appear on one slip

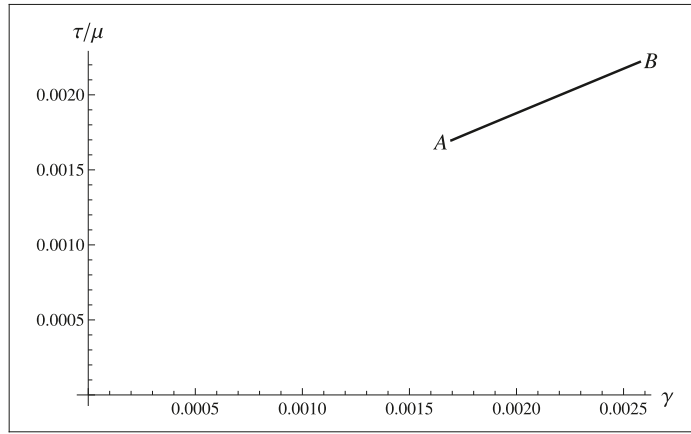


Figure 6.23: Normalized shear stress versus shear strain curve for loading path AB at  $\varphi_l = 35^\circ$  and  $\varphi_r = 155^\circ$  where  $h = 1 \mu\text{m}$

system. Therefore, if we increase  $\gamma$  further in interval  $\gamma_{en1} \leq \gamma < \gamma_{en2}$  (loading path AB) the crystal is now subjected to plastic deformation with only one active slip system with the solutions described in (6.125)-(6.133). The second slip system is activated at  $\gamma = \gamma_{en2}$  (point B). The shear stress and strain equation is presented by

$$\frac{\tau}{\mu} = \gamma - \langle \beta_e \rangle \cos 2\varphi_e, \quad (6.158)$$

with  $\langle \beta_e \rangle$  from (6.130). The procedures to determine  $\gamma_{en1}$ ,  $\gamma_{en2}$ ,  $\text{sign}\beta_l$ ,  $\text{sign}\beta_r$  and which slip system is activated first can be seen in section (6.3.1).

For numerical example of loading path AB, we apply the material parameters mentioned in the beginning of this section to the solutions above. In this case, the crystal undergoes the plastic deformation with one active slip system where  $\beta_r > 0$  and  $\beta_l = 0$  throughout loading path AB. Fig. (6.22) and Fig. (6.23) illustrate the evolution of  $\beta_r$  and  $\beta_l$  for increasing  $\gamma$  and the plot of normalized shear stress versus shear strain equation, respectively. The second slip system becomes active at  $\gamma_{en2}$  (point B) with  $\beta_l > 0$ .

Analogous to the the previous general double slip systems case with no dissipation, since both slip systems are already active, the problem cannot be solved anymore analytically for loading path BC and inverse loading DE. Therefore we apply the same finite element procedure derived in section (6.2.3).

Due to the dissipation of energy, the stress strain curve during loading and inverse loading will not go through the same path. Hence in order to be able to get the proper computation results for negative  $\gamma$  during the inverse loading we need to change slightly the dimensionless variables (6.86) into

$$\begin{aligned} \hat{E} &= \frac{\hat{\Psi}}{aLh\mu|\gamma|^3}, \quad \eta = \frac{y}{h|\gamma|}, \quad H = \frac{1}{|\gamma|}, \quad \gamma_{cr} = \frac{K}{\mu} \\ m &= \frac{k}{\gamma^2}, \quad \bar{\beta}_l(\eta) = \frac{\beta_l(y)}{|\gamma|}, \quad \bar{\beta}_r(\eta) = \frac{\beta_r(y)}{|\gamma|}, \quad c = hb\rho_s, \end{aligned} \quad (6.159)$$

with  $\bar{\beta}'_l(\eta)$  and  $\bar{\beta}'_r(\eta)$  similar to (6.87).

We may transform the functional (6.118) using the dimensionless variables (6.159) to

$$\begin{aligned} \hat{E} = \int_0^H & \left[ \frac{1}{2}(1 - \kappa)(\beta_l \sin 2\varphi_l + \beta_r \sin 2\varphi_r)^2 + \frac{\kappa}{2}(\langle \beta_l \rangle \sin 2\varphi_l + \langle \beta_r \rangle \sin 2\varphi_r)^2 \right. \\ & + \frac{1}{2}(\langle \beta_l \rangle \cos 2\varphi_l + \langle \beta_r \rangle \cos 2\varphi_r - \text{sign}\gamma)^2 + \frac{m}{c}(|\beta'_l \sin \varphi_l| + |\beta'_r \sin \varphi_r|) \\ & + \frac{m}{2c^2}((\beta'_l)^2 \sin^2 \varphi_l + (\beta'_r)^2 \sin^2 \varphi_r + 2\chi|\beta'_l \sin \varphi_l||\beta'_r \sin \varphi_r|) \\ & \left. + \frac{\gamma_{cr}}{|\gamma|} (\beta_l \text{sign}\dot{\beta}_l + \beta_r \text{sign}\dot{\beta}_r) \right] d\eta, \end{aligned} \quad (6.160)$$

where the bars over  $\bar{\beta}_l$  and  $\bar{\beta}_r$  are ignored for short and  $\langle \beta_l \rangle$  and  $\langle \beta_r \rangle$  are similar to (6.89).

For the sake of plotting the results in the same way with the analytic problems (single slip and symmetric double slip system), all the results from the simulation ( $\beta_l$ ,  $\beta_r$ ,  $\alpha_l$ ,  $\alpha_r$ ) together with  $\eta$  and  $H$  from (6.86) are multiplied by  $|\gamma|$  after numerical computation. Consequently, for plotting the results,  $\eta \in (0, 1)$  and  $H = 1$ .

Due to the constantly increasing  $\beta_l$  and  $\beta_r$  for positive  $\beta_l$  and  $\beta_r$  and also constantly decreasing  $\beta_l$  and  $\beta_r$  for negative  $\beta_l$  and  $\beta_r$  throughout loading path BC, we have

$$\text{sign}\dot{\beta}_l = \text{sign}\beta_l \quad \text{and} \quad \text{sign}\dot{\beta}_r = \text{sign}\beta_r, \quad (6.161)$$

where  $\text{sign}\beta_l$  and  $\text{sign}\beta_r$  have been determined from the previous loading path AB.

We apply Eq. (6.161) as well as the same minimizing sequences (see (6.90) and (6.91)) along with linear elements model outlined in Fig. 6.8 to the functional (6.160). Therefore, the discretized form of the effective energy during the loading becomes

$$\hat{E} = \frac{l}{3n}(1 - \kappa) \sum_{j=1}^n Q_1 + \frac{2m}{c} \sum_{j=1}^n Q_2 + \frac{mn}{lc^2} \sum_{j=1}^n Q_3 + \frac{l\gamma_{cr}}{n|\gamma|} \sum_{j=1}^n Q_4 + Q_5 + Q_6 + Q_7, \quad (6.162)$$

where

$$\begin{aligned} Q_1 &= \sin 2\varphi_l \sin 2\varphi_r \left( c_{j-1}(2d_{j-1} + d_j) + c_j(d_{j-1} + 2d_j) \right) \\ &\quad + \sin^2 2\varphi_l (c_{j-1}^2 + c_{j-1}c_j + c_j^2) + \sin^2 2\varphi_r (d_{j-1}^2 + d_{j-1}d_j + d_j^2), \\ Q_2 &= |\sin 2\varphi_l| |a_i - a_{i-1}| + |\sin 2\varphi_r| |b_i - b_{i-1}| \\ Q_3 &= \sin^2 \varphi_l (c_j - c_{j-1})^2 + \sin^2 \varphi_r (d_j - d_{j-1})^2 \\ &\quad + 2\chi |\sin \varphi_l (c_j - c_{j-1})| |\sin \varphi_r (d_j - d_{j-1})|, \\ Q_4 &= (c_i + c_{i-1}) \text{sign}\beta_l + (d_i + d_{i-1}) \text{sign}\beta_r \\ Q_5 &= \frac{H}{2} \kappa (\sin 2\varphi_l \langle \beta_l \rangle + \sin 2\varphi_r \langle \beta_r \rangle)^2 \\ &\quad + \frac{H}{2} (\cos 2\varphi_l \langle \beta_l \rangle + \cos 2\varphi_r \langle \beta_r \rangle - \text{sign}\gamma)^2, \\ Q_6 &= \frac{1 - \kappa}{2} (H - 2l)(c_n \sin 2\varphi_l + d_n \sin 2\varphi_r)^2, \\ Q_7 &= \frac{\gamma_{cr}}{|\gamma|} (H - 2l)(c_n \text{sign}\beta_l + d_n \text{sign}\beta_r). \end{aligned} \quad (6.163)$$

with

$$\begin{aligned}\langle\beta_l\rangle &= \frac{1}{H} \left( \frac{l}{n} \sum_{j=1}^n (c_{j-1} + c_j) + c_n(H - 2l) \right), \\ \langle\beta_r\rangle &= \frac{1}{H} \left( \frac{l}{n} \sum_{j=1}^n (d_{j-1} + d_j) + d_n(H - 2l) \right).\end{aligned}\quad (6.164)$$

Minimizing Eq. (6.162) with respect to variables  $(c_j, d_j, l)$  and with additional constraint

$$0 \leq l \leq \frac{H}{2},$$

we obtain the numerical solutions for  $\beta_l$  and  $\beta_r$ .

The discretized form of dislocation densities can be written as

$$(\alpha_l)_j = \begin{cases} \frac{n \sin \varphi_l}{l} (c_j - c_{j-1}), & \text{for } \eta \in (0, l), \\ 0, & \text{for } \eta \in (l, H - l), \\ -\frac{n \sin \varphi_l}{l} (c_j - c_{j-1}), & \text{for } \eta \in (H - l, H), \end{cases}\quad (6.165)$$

and

$$(\alpha_r)_j = \begin{cases} \frac{n \sin \varphi_r}{l} (d_j - d_{j-1}), & \text{for } \eta \in (0, l), \\ 0, & \text{for } \eta \in (l, H - l), \\ -\frac{n \sin \varphi_r}{l} (d_j - d_{j-1}), & \text{for } \eta \in (H - l, H), \end{cases}\quad (6.166)$$

where  $j$  being the element number. For the normalized shear stress and strain relation, the discretized form of the average plastic distortions (6.164) are applied to

$$\frac{\tau}{\mu} = \gamma - (\langle\beta_l\rangle \cos 2\varphi_l + \langle\beta_r\rangle \cos 2\varphi_r).\quad (6.167)$$

Continuing the previous example from loading path AB, we increase  $\gamma$  further up to some point C where  $\gamma = \gamma^* > \gamma_{en2}$ . Fig. (6.24) explains the evolution of plastic distortions ( $\beta_l$  and  $\beta_r$ ) and dislocation densities ( $\alpha_l$  and  $\alpha_r$ ) as  $\gamma$  grows throughout the loading path BC. The plot of the normalized shear stress and shear strain relation for loading path AB with  $\gamma^* = 0.0129$  is depicted in Fig. (6.25).

After reaching point C ( $\gamma = \gamma^*$ ), we load the crystal in the opposite direction (inverse loading) by decreasing  $\gamma$  from point C to point D ( $\gamma = \gamma_*$ ). In the course of inverse loading CD, the plastic distortions,  $\beta_l$  and  $\beta_r$ , remain constant and the crystal is subjected to elastic deformation. Therefore we have linear shear stress and strain relation for this loading path, namely

$$\frac{\tau}{\mu} = \gamma - \gamma^* + \left( \frac{\tau}{\mu} \right)_{\gamma^*},\quad (6.168)$$

where  $(\tau/\mu)_{\gamma^*}$  is the solution of (6.167) at  $\gamma = \gamma^*$ .

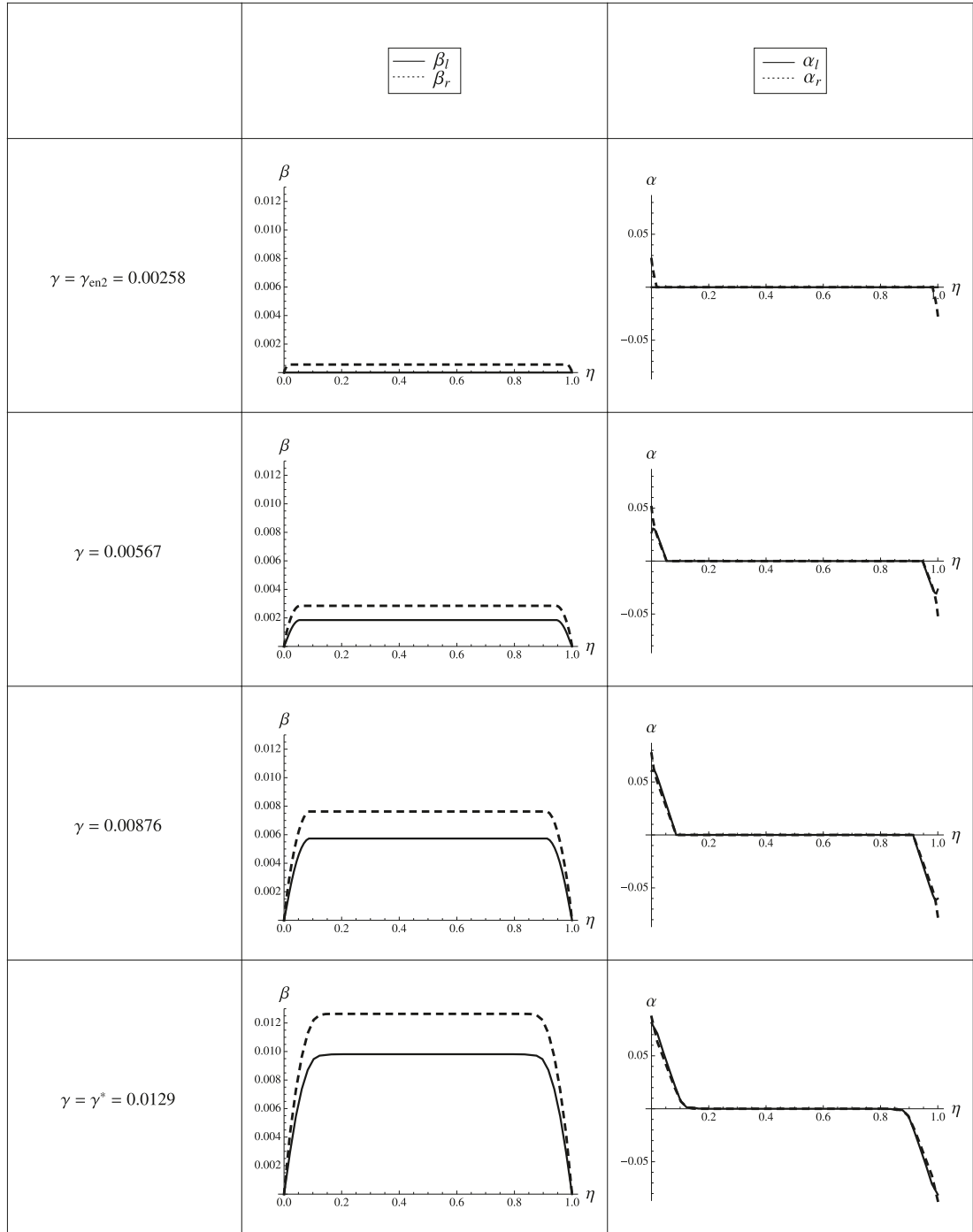


Figure 6.24: Evolution of plastic distortions and dislocation densities as  $\gamma$  grows for loading path BC at  $\varphi_l = 35^\circ$  and  $\varphi_r = 155^\circ$  where  $h = 1 \mu\text{m}$ .

Then, for loading path DE when  $\gamma$  is decreased up to  $\gamma = \gamma_D$ , we apply again the same numerical procedure as in loading path BC but now with

$$\text{sign} \dot{\beta}_l = -\text{sign} \beta_l \quad \text{and} \quad \text{sign} \dot{\beta}_r = -\text{sign} \beta_r, \quad (6.169)$$

instead of (6.161). For that reason, the discretized form of the effective energy all along the inverse loading reduces to

$$\hat{E} = \frac{l}{3n}(1-\kappa) \sum_{j=1}^n Q_1 + \frac{2m}{c} \sum_{j=1}^n Q_2 + \frac{mn}{lc^2} \sum_{j=1}^n Q_3 - \frac{l\gamma_{cr}}{n|\gamma|} \sum_{j=1}^n Q_4 + Q_5 + Q_6 - Q_7, \quad (6.170)$$

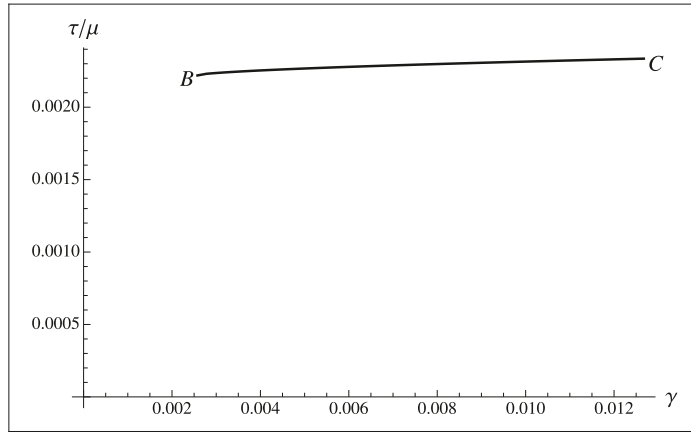


Figure 6.25: Normalized shear stress versus shear strain curve for loading path BC at  $\varphi_l = 35^\circ$  and  $\varphi_r = 155^\circ$  where  $h = 1 \mu\text{m}$

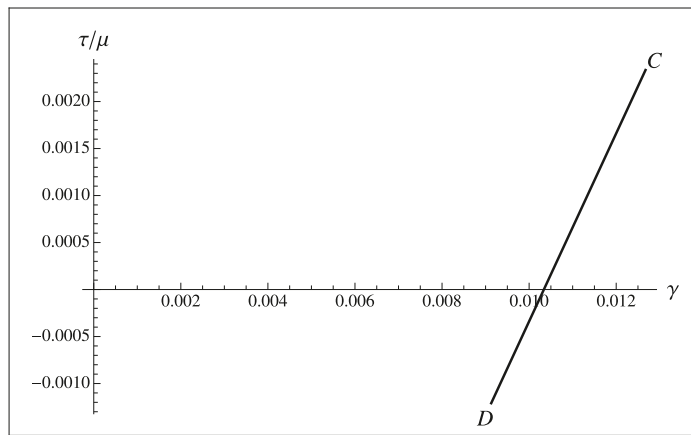


Figure 6.26: Normalized shear stress versus shear strain curve for loading path CD at  $\varphi_l = 35^\circ$  and  $\varphi_r = 155^\circ$  where  $h = 1 \mu\text{m}$

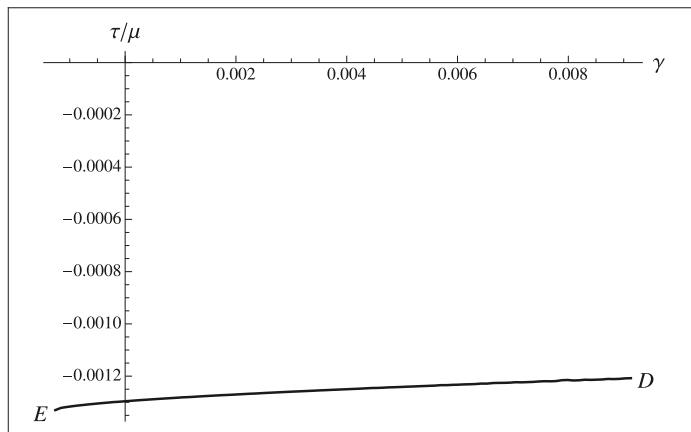


Figure 6.27: Normalized shear stress versus shear strain curve for loading path DE at  $\varphi_l = 35^\circ$  and  $\varphi_r = 155^\circ$  where  $h = 1 \mu\text{m}$

where  $Q_1$ - $Q_7$  from (6.163). To obtain the numerical solutions for  $\beta_l$  and  $\beta_r$ , we take the minimization of Eq. (6.170) with respect to variables  $(c_j, d_j, l)$  with additional constraint  $0 \leq l \leq \frac{H}{2}$ . The discretized shear stress and shear strain relation takes the similar form as in (6.168) and the discretized dislocation densities is analogous to (6.165) and (6.166).

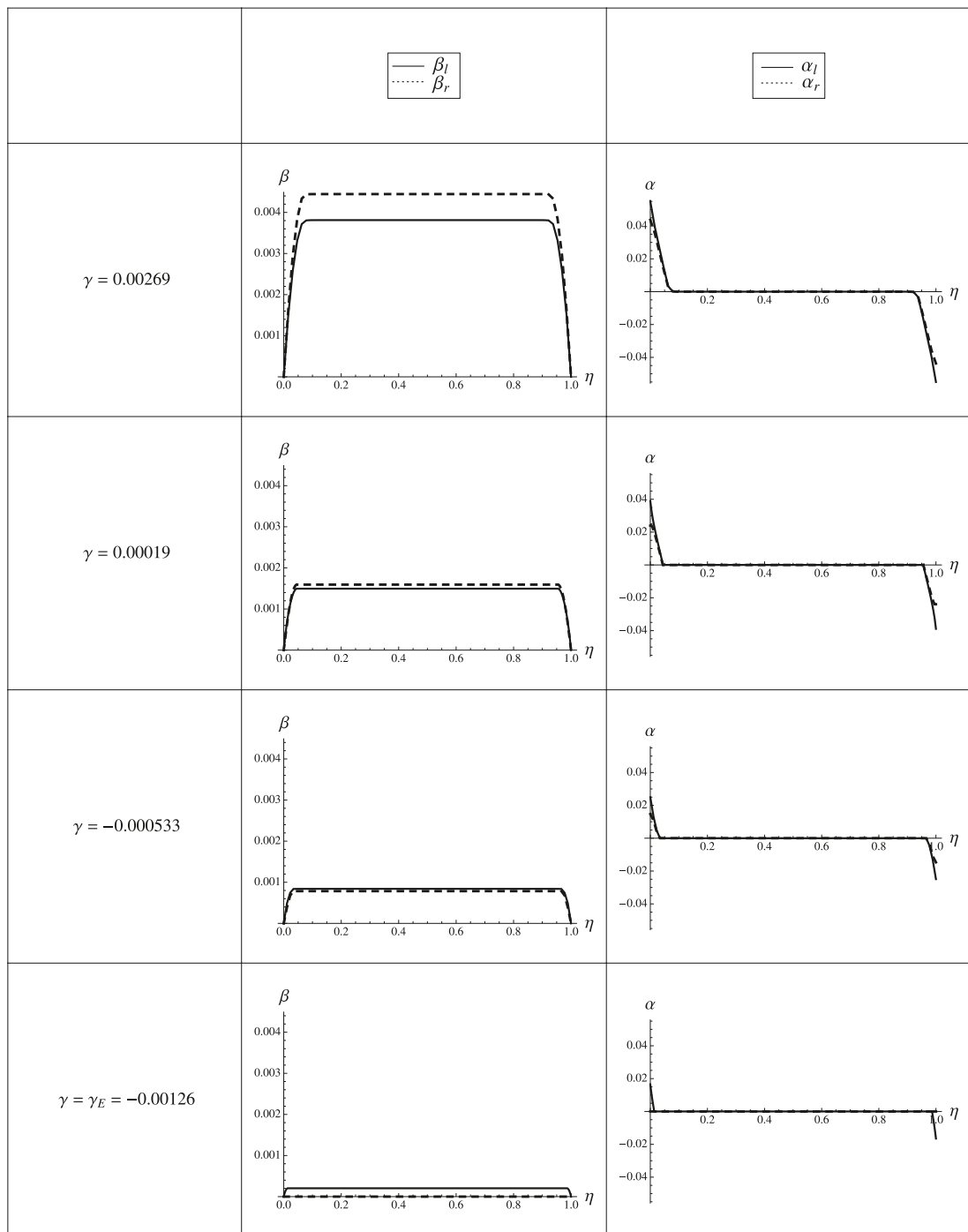


Figure 6.28: Evolution of plastic distortions and dislocation densities as  $\gamma$  decreases for loading path DE at  $\varphi_l = 35^\circ$  and  $\varphi_r = 155^\circ$  where  $h = 1 \mu\text{m}$ .

By plotting (6.168) and (6.167) at some interval of  $\gamma$  then finding the intersection between these two lines, we are able to determine  $\gamma_*$  (point D). Fig. 6.26 illustrates the normalized shear stress and shear strain curves for loading path CD.

To determine point E ( $\gamma = \gamma_E$ ) where one of the slip systems disappears, we have to consider the following cases:

1. Considering that  $\beta_r$  disappears at point E, we apply (6.121) and the condition  $\text{sign} \dot{\beta}_f =$

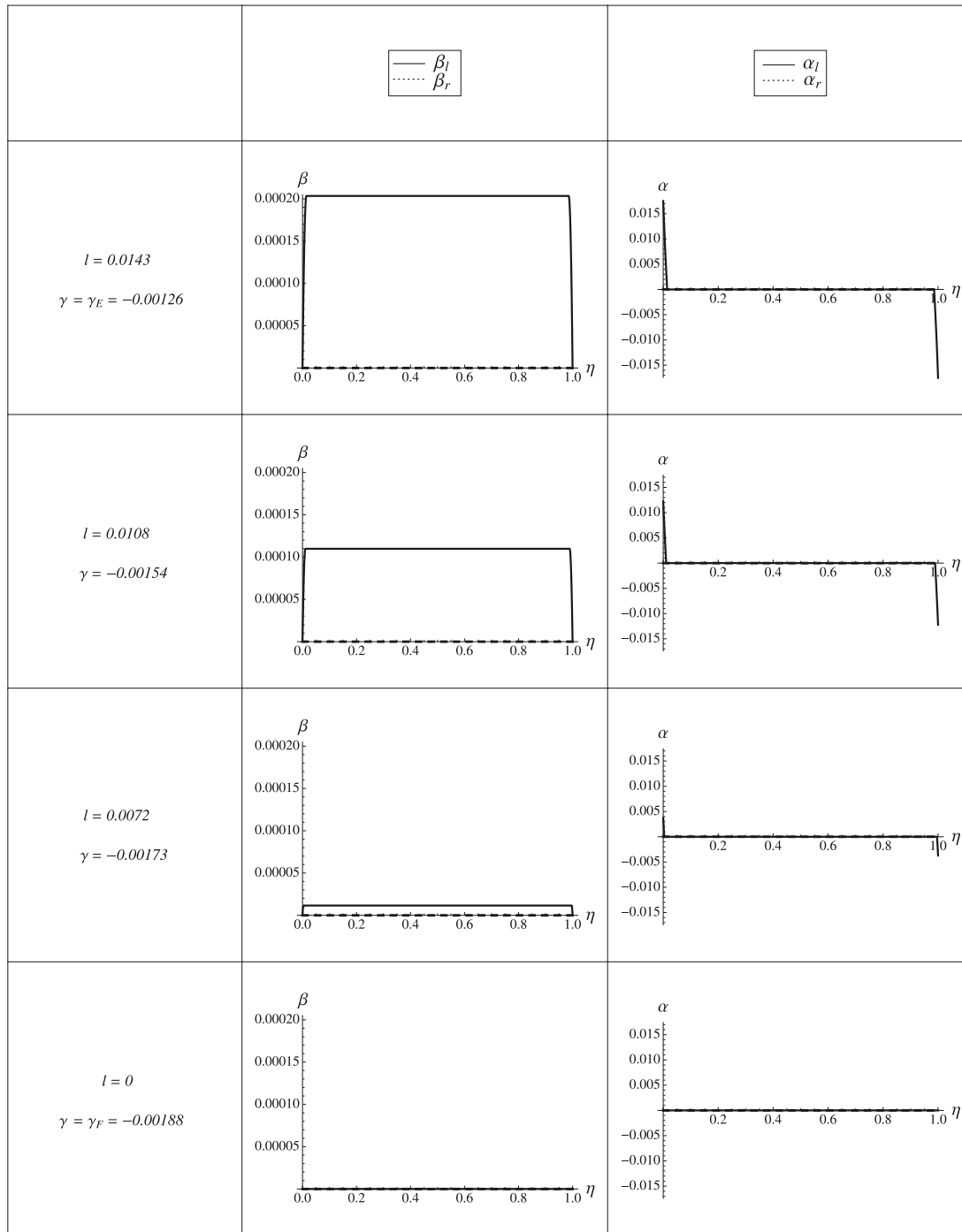


Figure 6.29: Evolution of plastic distortions and dislocation densities as  $\gamma$  decreases for loading path EF at  $\varphi_l = 35^\circ$  and  $\varphi_r = 155^\circ$  where  $h = 1 \mu\text{m}$ .

–  $\text{sign}\beta_{fm}$  to (6.125)-(6.133) and (6.136) then solve (6.134) for  $\beta_l > 0$  and (6.135) for  $\beta_l < 0$  in order to find  $\gamma_E$ .

2. If  $\beta_l$  vanishes at point E, the relation (6.137) and the condition  $\text{sign}\dot{\beta}_f = -\text{sign}\beta_{fm}$  are assigned to (6.125)-(6.133) together with (6.136) before solving (6.134) for  $\beta_r > 0$  and (6.135) for  $\beta_r < 0$  in place of finding  $\gamma_E$ .

The evolution of plastic distortions and dislocation densities as  $\gamma$  decreases is shown in

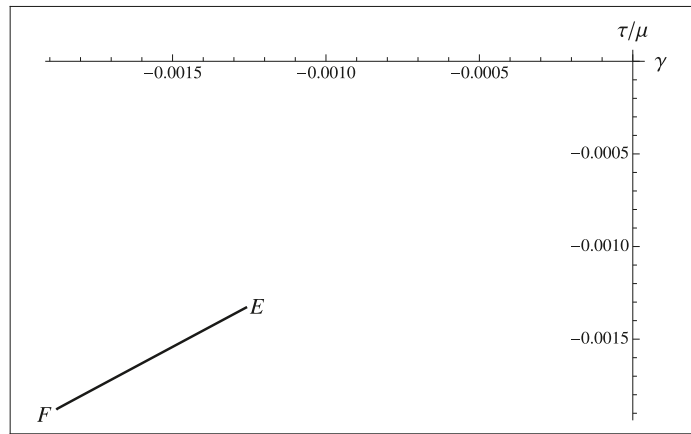


Figure 6.30: Normalized shear stress versus shear strain curve for loading path EF at  $\varphi_l = 35^\circ$  and  $\varphi_r = 150^\circ$  where  $h = 1 \mu\text{m}$

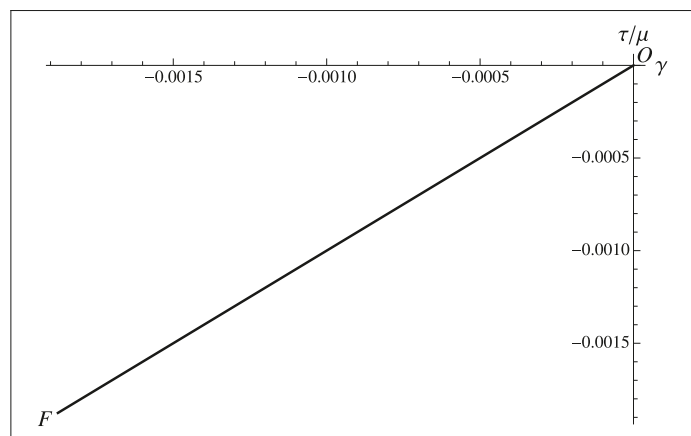


Figure 6.31: Normalized shear stress versus shear strain curve for loading path FG at  $\varphi_l = 35^\circ$  and  $\varphi_r = 150^\circ$  where  $h = 1 \mu\text{m}$

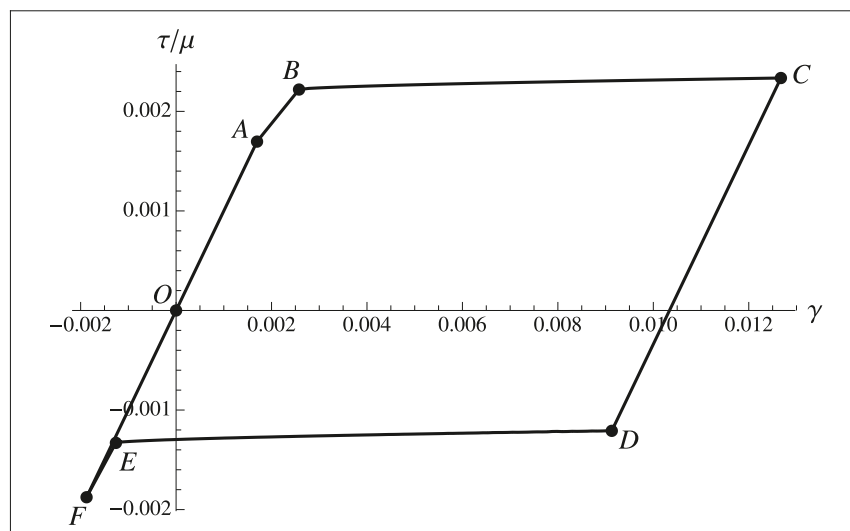


Figure 6.32: Normalized shear stress versus shear strain curve of general double slip constrained shear at non-zero dissipation of single crystal for  $\varphi_l = 35^\circ$  and  $\varphi_r = 155^\circ$  where  $h = 1 \mu\text{m}$

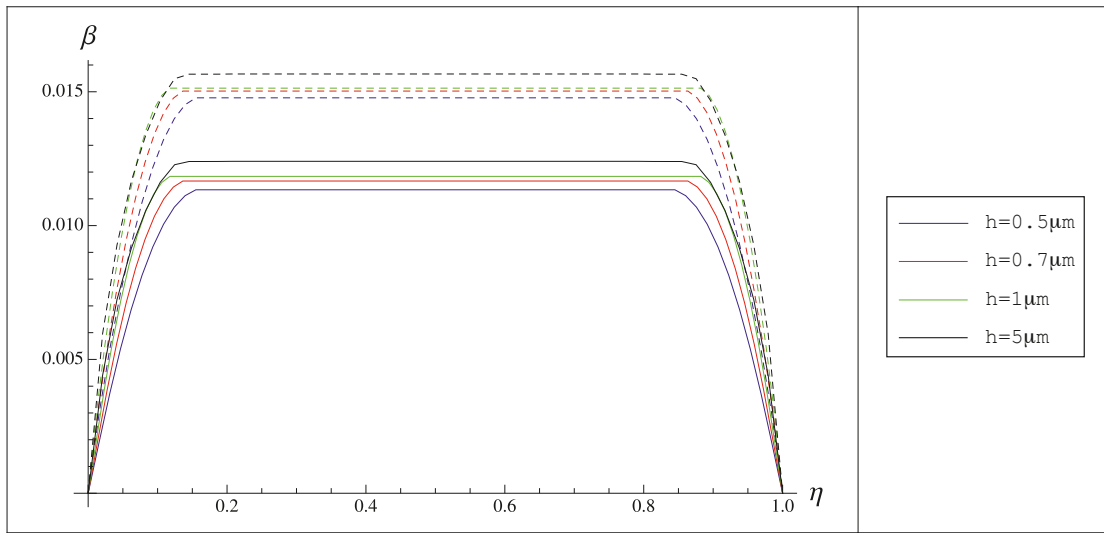


Figure 6.33: Evolution of  $\beta_l$  (continuous lines) and  $\beta_r$  (dashed lines) within the interval  $\eta \in (0, 1)$  during the loading process (increasing  $\gamma$ ) for double-slip constrained shear with dissipation of single crystal at  $\varphi_l = 35^\circ$ ,  $\varphi_r = 155^\circ$  and  $\gamma = 0.015$  with different crystal heights  $h$

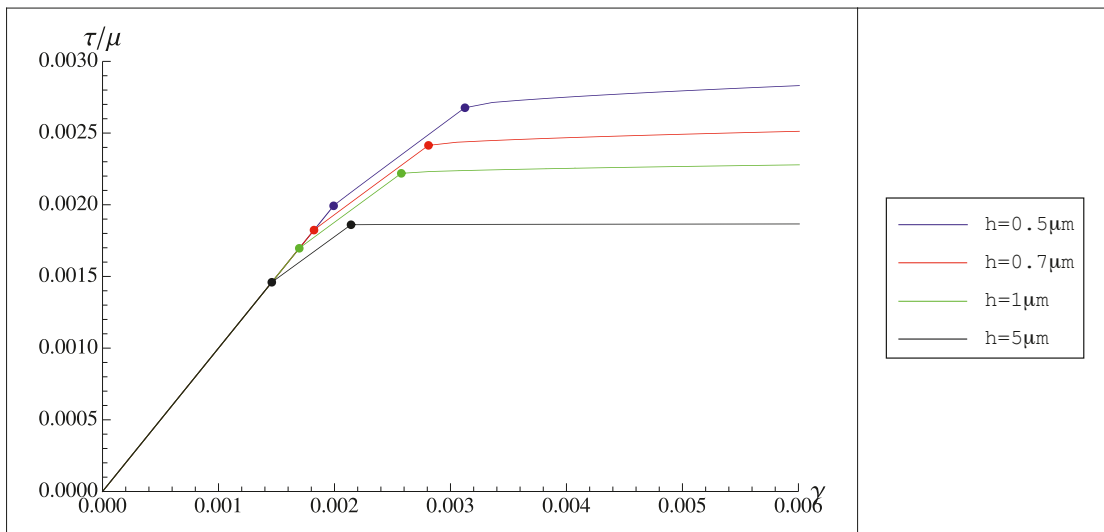


Figure 6.34: Normalized shear stress versus shear strain curves for zero dissipation symmetric double-slip constrained shear of single crystal at  $\varphi_l = 35^\circ$  and  $\varphi_r = 155^\circ$  with different crystal heights  $h$

Fig. 6.28. Since  $\beta_r$  appears first and has higher plastic distortion's rate than  $\beta_l$  ( $\text{sign}\dot{\beta}_r > \text{sign}\dot{\beta}_l$ ) as we increase  $\gamma$  for loading process, then it is also true that for the same slip system, it has higher plastic distortion's rate throughout inverse loading by decreasing  $\gamma$ . Therefore, if we decrease  $\gamma$  further,  $\beta_r$  will disappear first at point E ( $\gamma = \gamma_E$ ) as can be observed in Fig. 6.28. The normalized shear stress and shear strain curve is plotted in Fig. 6.27.

Afterwards, we decrease  $\gamma$  from point E ( $\gamma = \gamma_E$ ) to point F ( $\gamma = \gamma_F$ ). The crystal once again deforms in single slip system throughout this inverse loading EF. The solutions for

this case are obtained by replacing  $\gamma_l$  with

$$\gamma_u = \gamma + \frac{\gamma_{cr} \text{sign} \dot{\beta}_e}{\cos 2\varphi_e},$$

for the entire solutions (6.125)-(6.133) before applying (6.121) for the case when we have only  $\beta_l$  and (6.137) for  $\beta_r$ . We take the same form of equation as in (6.158) but now with  $\gamma_u$  instead of  $\gamma_l$  to obtain the shear stress and strain equation. While  $\gamma$  decreasing along this loading path EF, the created dislocations annihilate and completely disappear at point F.

Finally,  $\gamma$  is increased again from  $\gamma_F$  to zero (loading path FG). The crystal behaves elastically during this loading path so that  $\beta = 0$  and the shear stress and strain equation being identical to (6.157). Similar to the symmetric double slip systems with dissipation case, to ensure the continuity of  $\beta$  at point F, the condition  $\gamma_u$  at point F must be the same with  $\gamma_l$  at point A. Therefore we have

$$\gamma_F = \frac{\gamma_{cr}}{|\cos 2\varphi_l|} + \frac{2k |\sin 2\varphi_l|}{c |\cos 2\varphi_l|} - \frac{2\gamma_{cr} \text{sign} \beta_l}{\cos 2\varphi_l}, \quad (6.171)$$

for the case with  $\beta_l$  and

$$\gamma_F = \frac{\gamma_{cr}}{|\cos 2\varphi_r|} + \frac{2k |\sin 2\varphi_r|}{c |\cos 2\varphi_r|} - \frac{2\gamma_{cr} \text{sign} \beta_r}{\cos 2\varphi_r}, \quad (6.172)$$

for the case with  $\beta_r$ .

Fig. 6.30 and Fig. 6.31 illustrate the normalized shear stress and shear stress equation for loading path EF and FG, respectively. The evolution of  $\beta_l$  and  $\alpha_l$  for decreasing  $\gamma$  during inverse loading path EF can be seen in Fig. 6.29. Finally by combining Fig. 6.21, Fig. 6.23, Fig. 6.25, Fig. 6.26, Fig. 6.27, Fig. 6.30 and Fig. 6.31, we are able to plot the complete cycle of the normalized shear stress and shear strain curve following loading path depicted in Fig. 6.14 as can be seen in Fig. 6.32. The evolution of plastic distortions ( $\beta_l$  and  $\beta_r$ ) and the normalized shear stress strain curves for different  $h$  are shown in Fig. 6.33 and Fig. 6.34, respectively. Fig. 6.34 shows clearly the size effect. The left dots in Fig. 6.34 describe the first energetic yield points and the right dots describe the second energetic yield points.

## 6.4 Comparison with discrete dislocation simulations

Now we compare the result of our study with discrete dislocation simulations results reported in Needleman and Van der Giessen [2001] and Shu et al. [2001]. For comparison, the total strain profile

$$u_{,y} = \gamma + 2 \cos 2\varphi (\beta - \langle \beta \rangle), \quad (6.173)$$

needs to be computed for symmetric double slip systems with zero dissipation and with dissipation cases (see section (6.2.2) and section (6.3.2), respectively).

For comparison we use the same material parameters as in previous section at  $\varphi = 60^\circ$ . The comparison of total the strain profiles (6.173) between our findings with discrete dislocation simulations is shown in Fig. 6.35. The total strain profiles from discrete dislocation

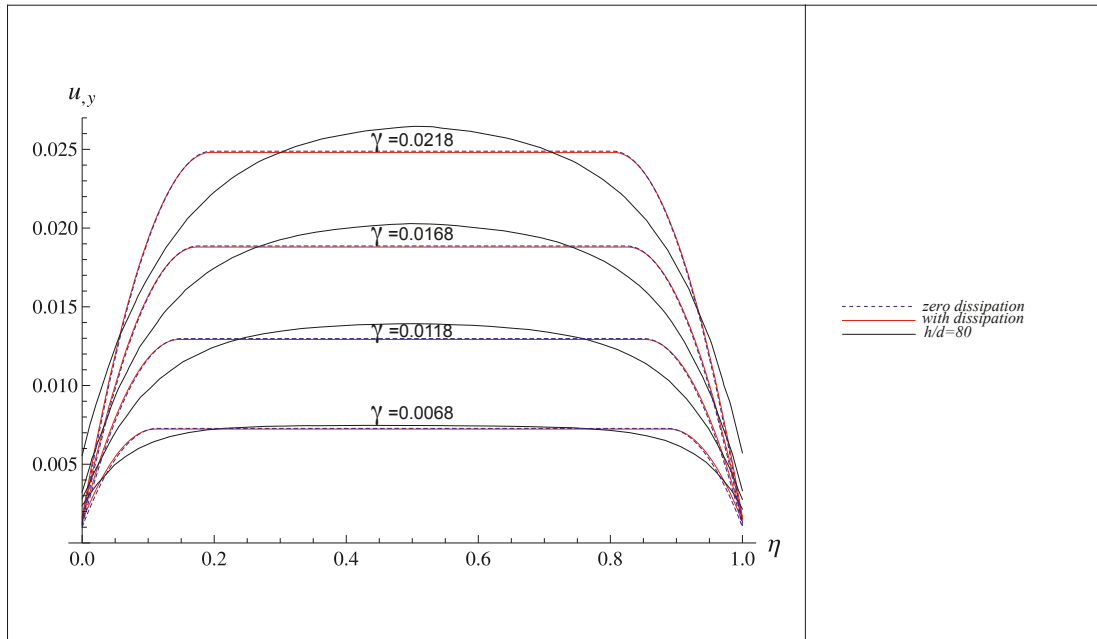


Figure 6.35: Comparison of the total shear strain profiles obtained from zero and non-zero dissipation symmetric double slip systems cases and from the discrete dislocation simulations reported in [Needleman and Van der Giessen, 2001, Shu et al., 2001]

simulations has the profile  $h/d = 80$ , where  $h$  being the crystal height and  $d$  being the spacing between the active slip planes. A somewhat larger discrepancy between the shear strain profiles obtained from our study with discrete approach is perhaps due to the rather low  $h/d = 80$  taken to simulate these curves in [Needleman and Van der Giessen, 2001, Shu et al., 2001].

The stress strain curves during the loading obtained from our study and discrete dislocation simulations in [Needleman and Van der Giessen, 2001, Shu et al., 2001] are outlined in Fig. 6.36. In order to compare with discrete dislocations simulation we choose  $\gamma_{en} = 0.00144$ ,  $\varphi = 60^\circ$ ,  $\tau_0 = 1.9 \cdot 10^{-3} \mu$  in addition to the other material parameters similar to the previous sections. The stress strain curves in the discrete dislocations simulation are given for four different ratios  $h/d$ . It is seen that reasonably good agreement between the discrete and the effective energy minimization is observed at  $h/d = 160$ .

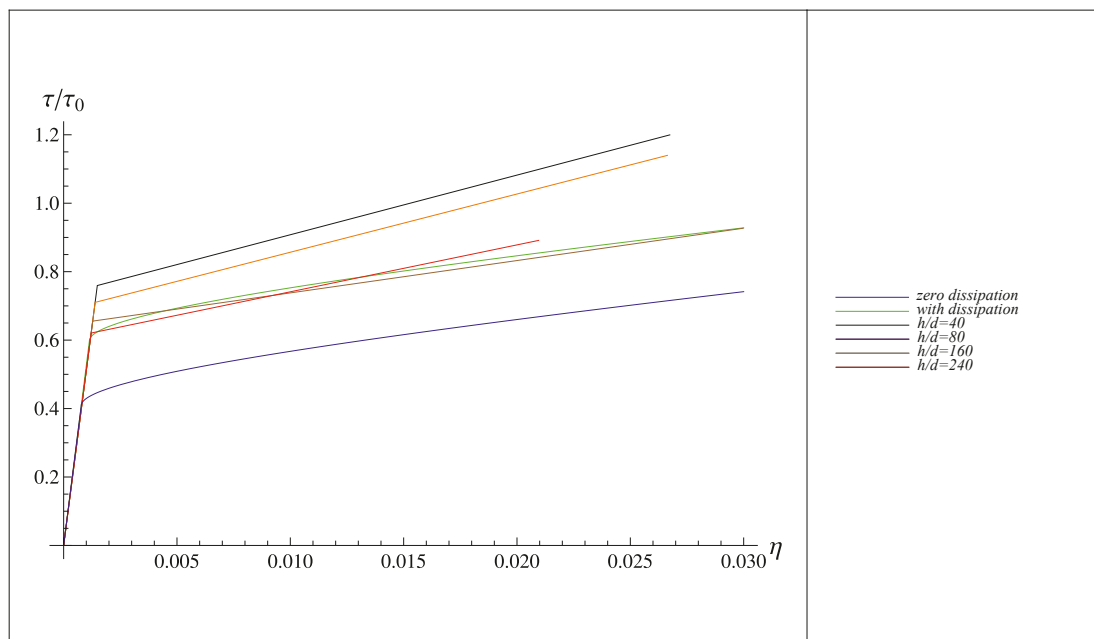


Figure 6.36: Comparison stress strain behavior of results obtained from this approach and from the discrete dislocation simulations presented in [Needleman and Van der Giessen, 2001, Shu et al., 2001]



## 7 Uniaxial extension and combined loading of two active slip systems

### 7.1 Energy of the crystal

Following our previous studies of the plane-constrained shear problem deforming in double slip systems, let us now complete our study by investigating the particular problems of plane-constrained uniaxial extension and combined loading of a single crystal strip with two active slip systems. Similar to the single slip system (see section 5.1), we derive first the energy equation for combined loading then for plane-constrained uniaxial extension of single crystal with double slip systems.

To realize this particular problem of combined loading, we place the single crystal with two active slip systems on a hard device with prescribed displacements at its upper and lower sides, namely

$$u(0) = 0, \quad v(0) = 0, \quad u(h) = \gamma h, \quad v(h) = \epsilon h, \quad (7.1)$$

with  $u(y)$  and  $v(y)$  being the longitudinal and transverse displacements, respectively, with  $\gamma$  being the overall shear strain and  $\epsilon$  the overall tensile strain. We suggest the following relation

$$\epsilon = \delta \sin \theta \quad \text{and} \quad \gamma = \delta \cos \theta, \quad (7.2)$$

where  $\delta$  being the total prescribed displacement applied under an angle  $\theta$ . Fig. 7.1 explains

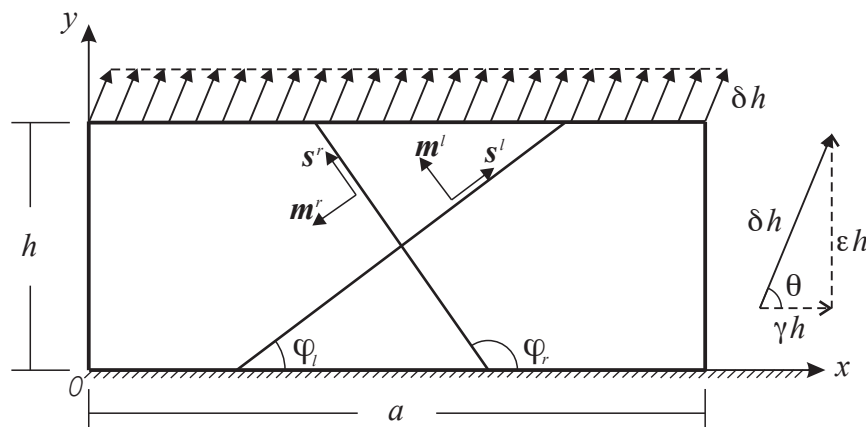


Figure 7.1: Combined deformation of uniaxial extension  $\epsilon$  and simple shear  $\gamma$  of a single crystal with two active slip systems

the combined loading case with double slip systems with  $s_i^\alpha = (\cos \varphi_\alpha, \sin \varphi_\alpha, 0)$  being the slip directions, and  $m_j^\alpha = (-\sin \varphi_\alpha, \cos \varphi_\alpha, 0)$  being the normal vectors to the slip planes ( $\alpha = l, r$ ).

Since the computation procedure is already explained in detail in section 6.1, the derivation and computation for the whole section will be presented in brief only. The energy functional in terms of  $\beta_l$  and  $\beta_r$  admits the form

$$\begin{aligned} \Psi(\beta_l(y), \beta_r(y)) = & aL \int_0^h \mu \left[ \frac{1}{2\kappa} \left( \delta \sin \theta - \kappa(\langle \beta_l \rangle \cos 2\varphi_l + \langle \beta_r \rangle \cos 2\varphi_r) \right)^2 \right. \\ & + \frac{1}{2} (\delta \cos \theta - \langle \beta_l \rangle \cos 2\varphi_l - \langle \beta_r \rangle \cos 2\varphi_r)^2 \\ & + \frac{1-\kappa}{2} (\beta_l \sin 2\varphi_l + \beta_r \sin 2\varphi_r)^2 + \frac{k}{b\rho_s} (|\beta_{l,y} \sin \varphi_l| + |\beta_{r,y} \sin \varphi_r|) \\ & \left. + \frac{k(\beta_{l,y}^2 \sin^2 \varphi_l + \beta_{r,y}^2 \sin^2 \varphi_r + 2\chi |\beta_{l,y} \sin \varphi_l| |\beta_{r,y} \sin \varphi_r|)}{2(b\rho_s)^2} \right] dy, \end{aligned} \quad (7.3)$$

with

$$\langle \beta_l \rangle = \frac{1}{h} \int_0^h \beta_l dy \quad \text{and} \quad \langle \beta_r \rangle = \frac{1}{h} \int_0^h \beta_r dy. \quad (7.4)$$

Considering the prescribed boundary conditions (7.1), dislocations are not able to go through the boundaries  $y = 0$  and  $y = h$ , which serve as the obstacles to dislocation motion, hence

$$\beta_l(0) = \beta_r(0) = \beta_l(h) = \beta_r(h) = 0. \quad (7.5)$$

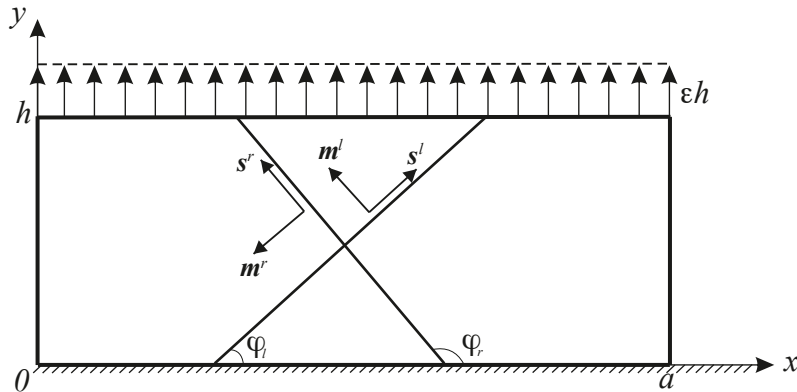


Figure 7.2: Plane-constrained uniaxial extension of single crystal strip with two active slip systems

For realizing the plane-constrained uniaxial extension for the same crystal deforming in double slip systems as depicted in Fig. 7.2, we apply  $\theta = 90^\circ$  to (7.2) then to (7.1). Following the same procedure as before, the total energy functional for plane-constrained uniaxial

extension for double slip system takes the form

$$\begin{aligned} \Psi(\beta_l(y), \beta_r(y)) = aL \int_0^h \mu \left[ \frac{1}{2\kappa} \left( \epsilon - \kappa(\langle \beta_l \rangle \cos 2\varphi_l + \langle \beta_r \rangle \cos 2\varphi_r) \right)^2 \right. \\ + \frac{1}{2} (\langle \beta_l \rangle \cos 2\varphi_l + \langle \beta_r \rangle \cos 2\varphi_r)^2 + \frac{1-\kappa}{2} (\beta_l \sin 2\varphi_l + \beta_r \sin 2\varphi_r)^2 \\ + \frac{k}{b\rho_s} (|\beta_{l,y} \sin \varphi_l| + |\beta_{r,y} \sin \varphi_r|) + \frac{k}{2(b\rho_s)^2} (\beta_{l,y}^2 \sin^2 \varphi_l + \beta_{r,y}^2 \sin^2 \varphi_r \\ \left. + 2\chi |\beta_{l,y} \sin \varphi_l| |\beta_{r,y} \sin \varphi_r| \right] dy, \end{aligned} \quad (7.6)$$

which objects to (7.5) where  $\langle \beta_l \rangle$  and  $\langle \beta_r \rangle$  from (7.4).

Analogous to the previous chapter for the case where the dissipation of energy is negligible (see section 6.2), in order to determine the plastic distortions ( $\beta_l$  and  $\beta_r$ ), we admit the minimization under the boundary conditions (7.5) of the total energy functionals (7.6) and (7.3) for plane-constrained uniaxial extension and combined loading, respectively.

When the resistance to dislocation motion cannot be neglected, the energy minimization is substituted by the variational formulation (6.114) where  $\Psi$  from (7.6) for plane-constrained uniaxial extension case and from (7.3) for combined loading case. We apply again here the simplest model of dissipation potential proposed in (6.115). Similar to the previous case of plane-constrained shear deforming in double slip system, considering the complexity of the model, we will not take into account the cross-slip interaction in (6.115) leading to the latent hardening. Since we assume also here, for the case of  $\dot{\beta}_l \neq 0$  and  $\dot{\beta}_r \neq 0$ , that  $\text{sign}\dot{\beta}_l$  and  $\text{sign}\dot{\beta}_r$  are constant over the plastic deformation, the variational equation (6.114) can now be replaced by the minimization of the effective energy,  $\hat{\Psi}$ , i.e.

$$\delta \hat{\Psi} = 0, \quad (7.7)$$

where

$$\hat{\Psi} = \Psi + aL \int_0^h K \left( \left( \text{sign}\dot{\beta}_l \right) \beta_l + \left( \text{sign}\dot{\beta}_r \right) \beta_r \right) dy. \quad (7.8)$$

When  $\dot{\beta}_l = 0$  or  $\dot{\beta}_r = 0$ , the variational equation (6.114) needs not to be computed and simply replaced by  $\dot{\beta}_l = 0$  or  $\dot{\beta}_r = 0$ .

Accordingly, the effective energy for the case of plane-constrained uniaxial extension is in the form

$$\begin{aligned} \hat{\Psi}(\beta_l(y), \beta_r(y)) = aL \int_0^h \mu \left[ \frac{1}{2\kappa} \left( \epsilon - \kappa(\langle \beta_l \rangle \cos 2\varphi_l + \langle \beta_r \rangle \cos 2\varphi_r) \right)^2 \right. \\ + \frac{1}{2} (\langle \beta_l \rangle \cos 2\varphi_l + \langle \beta_r \rangle \cos 2\varphi_r)^2 + \frac{1-\kappa}{2} (\beta_l \sin 2\varphi_l + \beta_r \sin 2\varphi_r)^2 \\ + \frac{k}{b\rho_s} (|\beta_{l,y} \sin \varphi_l| + |\beta_{r,y} \sin \varphi_r|) + \frac{k}{2(b\rho_s)^2} (\beta_{l,y}^2 \sin^2 \varphi_l + \beta_{r,y}^2 \sin^2 \varphi_r \\ \left. + 2\chi |\beta_{l,y} \sin \varphi_l| |\beta_{r,y} \sin \varphi_r|) + \frac{K}{\mu} \left( \left( \text{sign}\dot{\beta}_l \right) \beta_l + \left( \text{sign}\dot{\beta}_r \right) \beta_r \right) \right] dy, \end{aligned} \quad (7.9)$$

and for combined loading

$$\begin{aligned}
\hat{\Psi}(\beta_l(y), \beta_r(y)) = & aL \int_0^h \mu \left[ \frac{1}{2\kappa} \left( \delta \sin \theta - \kappa (\langle \beta_l \rangle \cos 2\varphi_l + \langle \beta_r \rangle \cos 2\varphi_r) \right)^2 \right. \\
& + \frac{1}{2} (\delta \cos \theta - \langle \beta_l \rangle \cos 2\varphi_l - \langle \beta_r \rangle \cos 2\varphi_r)^2 \\
& + \frac{1-\kappa}{2} (\beta_l \sin 2\varphi_l + \beta_r \sin 2\varphi_r)^2 + \frac{k}{b\rho_s} (|\beta_{l,y} \sin \varphi_l| + |\beta_{r,y} \sin \varphi_r|) \\
& + \frac{k(\beta_{l,y}^2 \sin^2 \varphi_l + \beta_{r,y}^2 \sin^2 \varphi_r + 2\chi |\beta_{l,y} \sin \varphi_l| |\beta_{r,y} \sin \varphi_r|)}{2(b\rho_s)^2} \\
& \left. + \frac{K}{\mu} \left( (\text{sign} \dot{\beta}_l) \beta_l + (\text{sign} \dot{\beta}_r) \beta_r \right) \right] dy. \tag{7.10}
\end{aligned}$$

In this chapter, we work first with the case of plane-constrained uniaxial extension then later with combined loading case. To guarantee the existence and uniqueness of the minimizer we must have the convexity of the energy density  $\Phi$  with respect to  $\beta_l$  and  $\beta_r$ . Therefore, following the explanation on section 6.2, we assume that  $\chi < 1$ . In addition to the interaction factor  $\chi = 0.576$  we employ again the same material parameters shown in Table 3.1 for all numerical computations.

## 7.2 Plane-constrained uniaxial extension

### 7.2.1 Energetic threshold values

Based on the same idea as the previous case of plane-constrained shear with double slip systems, for both cases of zero and non-zero energy dissipation, we have here also different points of activation for each of the two slip systems. As a consequence we admit two energetic threshold values,  $\epsilon_{en1}$  and  $\epsilon_{en2}$ , where

- no dislocations nucleation at  $\epsilon < \epsilon_{en1}$ ,
- the first slip system is activated at  $\epsilon = \epsilon_{en1}$  and the crystal deforms in single slip system for interval  $\epsilon_{en1} \leq \epsilon < \epsilon_{en2}$ ,
- and finally the second slip system becomes active at  $\epsilon = \epsilon_{en2}$ .

We first derive the energetic threshold value for the case with zero dissipation then afterwards with the case of non-zero dissipation.

For computing the threshold values for zero dissipation case, it is convenient to introduce to (7.6) the characters with subscript  $e$ ,  $(\star)_e$ , for slip system with angle  $\varphi_e$  and with subscript,

$f$  ( $\star$ ) $_f$ , for slip system with angle  $\varphi_f$ . Therefore the energy functional (7.6) becomes

$$\begin{aligned} \Psi(\beta_e(y), \beta_f(y)) = aL \int_0^h \mu \left[ \frac{1}{2\kappa} \left( \epsilon - \kappa(\langle \beta_e \rangle \cos 2\varphi_e + \langle \beta_f \rangle \cos 2\varphi_f) \right)^2 \right. \\ + \frac{1}{2} (\langle \beta_e \rangle \cos 2\varphi_e + \langle \beta_f \rangle \cos 2\varphi_f)^2 + \frac{1-\kappa}{2} (\beta_e \sin 2\varphi_e + \beta_f \sin 2\varphi_f)^2 \\ + \frac{k}{b\rho_s} (|\beta_{e,y} \sin \varphi_e| + |\beta_{f,y} \sin \varphi_f|) + \frac{k}{2(b\rho_s)^2} (\beta_{e,y}^2 \sin^2 \varphi_e + \beta_{f,y}^2 \sin^2 \varphi_f \\ \left. + 2\chi |\beta_{e,y} \sin \varphi_e| |\beta_{f,y} \sin \varphi_f| \right] dy, \end{aligned} \quad (7.11)$$

with

$$\langle \beta_e \rangle = \frac{1}{h} \int_0^h \beta_e dy \quad \text{and} \quad \langle \beta_f \rangle = \frac{1}{h} \int_0^h \beta_f dy. \quad (7.12)$$

Then we introduce to (7.11) and (7.12) the following dimensionless quantities

$$E = \frac{\Psi}{\mu a L h}, \quad \eta = \frac{y}{h}, \quad \bar{\beta}_e(\eta) = \beta_e(\eta), \quad \bar{\beta}_f(\eta) = \beta_f(\eta), \quad c = hb\rho_s, \quad (7.13)$$

with  $\eta \in (0, 1)$  to get

$$\begin{aligned} E(\beta_e(\eta), \beta_f(\eta)) = \int_0^1 \left[ \frac{1}{2\kappa} \left( \epsilon - \kappa(\langle \beta_e \rangle \cos 2\varphi_e + \langle \beta_f \rangle \cos 2\varphi_f) \right)^2 \right. \\ + \frac{1}{2} (\langle \beta_e \rangle \cos 2\varphi_e + \langle \beta_f \rangle \cos 2\varphi_f)^2 + \frac{1-\kappa}{2} (\beta_e \sin 2\varphi_e + \beta_f \sin 2\varphi_f)^2 \\ + \frac{k}{c} (|\beta'_e \sin \varphi_e| + |\beta'_f \sin \varphi_f|) + \frac{k}{2c^2} ((\beta'_e)^2 \sin^2 \varphi_e + (\beta'_f)^2 \sin^2 \varphi_f \\ \left. + 2\chi |\beta'_e \sin \varphi_e| |\beta'_f \sin \varphi_f| \right] d\eta, \end{aligned} \quad (7.14)$$

with

$$\langle \beta_e \rangle = \int_0^1 \beta_e d\eta \quad \text{and} \quad \langle \beta_f \rangle = \int_0^1 \beta_f d\eta, \quad (7.15)$$

where the bars over  $\bar{\beta}_e$ ,  $\bar{\beta}_f$ ,  $\langle \bar{\beta}_e \rangle$  and  $\langle \bar{\beta}_f \rangle$  are dropped for short.

So now we have the condition where the slip system with angle  $\varphi_e$  is always activated first at  $\epsilon = \epsilon_{en1}$  then the second slip system with angle  $\varphi_r$  at  $\epsilon = \epsilon_{en2}$ . As a consequence, if, during the loading,  $\beta_l$  becomes active first at  $\epsilon = \epsilon_{en1}$  then  $\beta_r$  at  $\epsilon = \epsilon_{en2}$ , we apply to (7.14) and (7.15) the following relations

$$\begin{aligned} \beta_e(\eta) = \beta_l(\eta), \quad \beta_f(\eta) = \beta_r(\eta), \quad \varphi_e = \varphi_l, \quad \varphi_f = \varphi_r, \\ \langle \beta_e \rangle = \langle \beta_l \rangle, \quad \langle \beta_f \rangle = \langle \beta_r \rangle. \end{aligned} \quad (7.16)$$

On the other way around, when  $\beta_r$  is activated first before  $\beta_l$  we apply

$$\begin{aligned} \beta_e(\eta) = \beta_r(\eta), \quad \beta_f(\eta) = \beta_l(\eta), \quad \varphi_e = \varphi_r, \quad \varphi_f = \varphi_l, \\ \langle \beta_e \rangle = \langle \beta_r \rangle, \quad \langle \beta_f \rangle = \langle \beta_l \rangle, \end{aligned} \quad (7.17)$$

to (7.14) and (7.15).

The following conditions

$$\epsilon \sin 2\varphi_e - \frac{2k |\sin \varphi_e|}{c} > 0, \quad (7.18)$$

for  $\beta_e > 0$  and

$$\epsilon \sin 2\varphi_e + \frac{2k |\sin \varphi_e|}{c} < 0, \quad (7.19)$$

for  $\beta_e < 0$  must be true for every  $\epsilon \geq \epsilon_{en1}$ , where the first energetic threshold value takes the form

$$\epsilon_{en1} = \frac{2k |\sin \varphi_e|}{c |\sin 2\varphi_e|}, \quad (7.20)$$

with  $c = hb\rho_s$ .

From the derivation of  $\epsilon_{en1}$  we obtain the relation

$$\text{sign}\beta_e = \begin{cases} 0, & \text{for } \varphi_e = 0^\circ, \\ +1, & \text{for } 0^\circ < \varphi_e < 90^\circ, \\ -1, & \text{for } 90^\circ < \varphi_e < 180^\circ. \end{cases} \quad (7.21)$$

For this reason the sign of  $\beta'_e$  for  $\eta \in (0, l)$  takes the form

$$\text{sign}\beta'_e = \text{sign}\beta_e, \quad (7.22)$$

and changes its sign for  $\eta \in (0, 1 - l)$ .

Seeing that only one slip system is active in the course of loading process at interval  $\epsilon_{en1} \leq \epsilon < \epsilon_{en2}$ , we obtain the solutions

$$\beta_e = \begin{cases} \beta_p(1 - \cosh \zeta\eta + \tanh \zeta l \sinh \zeta\eta), & \text{for } \eta \in (0, l), \\ \beta_{em} = \beta_p \left(1 - \frac{1}{\cosh \zeta l}\right), & \text{for } \eta \in (l, 1 - l), \\ \beta_p(1 - \cosh \zeta(1 - \eta) + \tanh \zeta l \sinh \zeta(1 - \eta)), & \text{for } \eta \in (1 - l, 1), \end{cases} \quad (7.23)$$

where

$$\beta_p = \frac{\epsilon \sin 2\varphi_e - (\cos^2 2\varphi_e + \kappa \sin^2 2\varphi_e) \langle \beta_e \rangle}{(1 - \kappa) \sin^2 2\varphi_e} \quad \text{and} \quad \zeta = 2c |\cos \varphi_l| \sqrt{\frac{1 - \kappa}{k}}. \quad (7.24)$$

The normalized dislocation density reads

$$\alpha_e = \begin{cases} \beta_p \sin \varphi_e (-\zeta \sinh \zeta\eta + \zeta \tanh \zeta l \cosh \zeta\eta), & \text{for } \eta \in (0, l), \\ 0, & \text{for } \eta \in (l, 1 - l), \\ \beta_p \sin \varphi_e (-\zeta \sinh \zeta(1 - \eta) + \zeta \tanh \zeta l \cosh \zeta(1 - \eta)), & \text{for } \eta \in (1 - l, 1). \end{cases} \quad (7.25)$$

The average of plastic distortion is given in the form

$$\langle \beta_e \rangle = \epsilon \sin 2\varphi_e B_e(l), \quad (7.26)$$

with

$$B_e(l) = \frac{g(l)}{(1 - \kappa) \sin^2 2\varphi_e + g(l)(\cos^2 2\varphi_e + \kappa \sin^2 2\varphi_e)}, \quad (7.27)$$

and

$$g(l) = 2 \left( l - \frac{\tanh \zeta l}{\zeta} \right) + \left( 1 - \frac{1}{\cosh \zeta l} \right) (1 - 2l). \quad (7.28)$$

The equation of  $\epsilon$  in term of the boundary layer length,  $l$ , takes the form

$$\epsilon(l) = \frac{2k |\sin \varphi_e| \text{sign} \beta'_e \cosh \zeta l}{c(1 - 2l) \sin 2\varphi_e (1 - (\cos^2 2\varphi_e + \kappa \sin^2 2\varphi_e) B_e(l))}, \quad (7.29)$$

where  $\text{sign} \beta'_e$  from (7.22). The normalized tensile stress versus strain equation takes the form

$$\frac{\sigma_{yy}}{\lambda + 2\mu} = \epsilon (1 - \kappa B_e(l) \sin^2 2\varphi_e). \quad (7.30)$$

For finding the second energetic threshold value,  $\epsilon_{en2}$ , we need first to find the length of boundary layer at this point,  $l_{en2}$ , then apply it to (7.29) so that

$$\epsilon_{en2} = \epsilon(l_{en2}). \quad (7.31)$$

In order to find  $l_{en2}$  we need to solve

$$f(\text{sign} \beta_{fm} = 1, l_{en2}) = 0, \quad (7.32)$$

for  $\beta_f > 0$  and

$$f(\text{sign} \beta_{fm} = -1, l_{en2}) = 0, \quad (7.33)$$

where

$$\begin{aligned} f(\text{sign} \beta_{fm}, l) = & - \frac{2k |\sin \varphi_f| \text{sign} \beta_{fm}}{c} - (1 - 2l)(1 - \kappa) \sin 2\varphi_e \sin 2\varphi_f \beta_{em}(l) \\ & + \epsilon(l) \sin 2\varphi_f - (\cos 2\varphi_e \cos 2\varphi_f + \kappa \sin 2\varphi_e \sin 2\varphi_f) \epsilon(l) \sin 2\varphi_e B_e(l) \\ & + \frac{2}{\zeta} (1 - \kappa) \sin 2\varphi_e \sin 2\varphi_f \beta_p(l) (\zeta l - \tanh \zeta l), \end{aligned} \quad (7.34)$$

with  $\epsilon(l)$  from (7.29),  $\beta_{em}$  from (7.23),  $\beta_p$  from (7.24) and  $B_e(l)$  from (7.27). Mention that only one from Eq. (7.32) and Eq. (7.33) that gives the solution for  $l_{en2}$ .

For the case where the energy dissipation cannot be ignored, by applying first  $(\star)_e$ ,  $(\star)_f$ , the dimensionless quantities (7.13) and

$$\frac{K}{\mu} = \epsilon_{cr},$$

to (7.9) then doing the algebraic manipulation, the effective energy (7.9) is now reduced to

$$\begin{aligned} \hat{E}(\beta_e, \beta_f) = & \int_0^1 \left[ \frac{1}{2\kappa} \left( \epsilon_l - \kappa (\langle \beta_e \rangle \cos 2\varphi_e + \langle \beta_f \rangle \cos 2\varphi_f) \right)^2 \right. \\ & + \frac{1}{2} (\langle \beta_e \rangle \cos 2\varphi_e + \langle \beta_f \rangle \cos 2\varphi_f)^2 + \frac{1 - \kappa}{2} (\beta_e \sin 2\varphi_e + \beta_f \sin 2\varphi_f)^2 \\ & + \frac{k}{c} (|\beta'_l \sin \varphi_l| + |\beta'_r \sin \varphi_r|) + \frac{k}{2c^2} ((\beta'_l)^2 \sin^2 \varphi_l + (\beta'_r)^2 \sin^2 \varphi_r \\ & \left. + 2\chi |\beta'_l \sin \varphi_l| |\beta'_r \sin \varphi_r| \right] d\eta, \end{aligned} \quad (7.35)$$

where

$$\epsilon_l = \epsilon - \frac{\epsilon_{cr} \text{sign}\dot{\beta}_e}{\sin 2\varphi_e}. \quad (7.36)$$

Since the effective energy (7.35) has the similar form with (7.14) but now with  $\epsilon_l$  instead of  $\epsilon$ , we can again adopt the complete procedures of the zero dissipation case to obtain both of the energetic threshold values.

The first energetic threshold value in term of original height,  $h$ , is presented by

$$\epsilon_{en1} = \frac{\epsilon_{cr}}{|\sin 2\varphi_e|} + \frac{2k}{hb\rho_s} \frac{|\sin \varphi_e|}{|\epsilon 2\varphi_e|}. \quad (7.37)$$

From this derivation, we found out that  $\text{sign}\dot{\beta}_e$  is similar to (7.21). We have also here the sign of  $\dot{\beta}_e$  for the loading process (increasing  $\epsilon$ ) in the form

$$\text{sign}\dot{\beta}_e = \text{sign}\beta'_e = \text{sign}\beta_e, \quad (7.38)$$

with  $\text{sign}\beta_e$  from (7.21). Therefore, for increasing  $\epsilon$ , Eq. (7.36) can now be written as

$$\epsilon_l = \epsilon - \frac{\epsilon_{cr} \text{sign}\beta_e}{\sin 2\varphi_e}. \quad (7.39)$$

All along the interval  $\epsilon_{en1} \leq \epsilon < \epsilon_{en2}$ , the crystal deforms in single slip where  $\beta_e \neq 0$  and  $\beta_f = 0$ . Therefore we have the solutions in the similar form as in (7.23)-(7.28) but with  $\epsilon_l$  from (7.39) replacing  $\epsilon$ . The tensile strain,  $\epsilon$ , as a function of  $l$  takes the form

$$\epsilon(l) = \frac{\text{sign}\beta_e}{\sin 2\varphi_e} \left( \epsilon_{cr} + \frac{2k |\sin \varphi_e| \cosh \zeta l}{c(1-2l) (1 - (\cos^2 2\varphi_e + \kappa \sin^2 2\varphi_e) B_e(l))} \right). \quad (7.40)$$

The normalized tensile stress versus strain for the case with dissipation reads

$$\frac{\sigma_{yy}}{\lambda + 2\mu} = \epsilon - \kappa \epsilon_l B(l) \sin^2 2\varphi_e, \quad (7.41)$$

where  $\epsilon_l$  from (7.39).

To find  $\epsilon_{en2}$  we follow again the same procedure as in (7.31) -(7.33) with

$$\begin{aligned} f(\text{sign}\beta_{fm}, l) = & - \frac{2k |\sin \varphi_f| \text{sign}\beta_{fm}}{c} - (1-2l)(1-\kappa) \sin 2\varphi_e \sin 2\varphi_f \beta_{em}(l) \\ & - (\cos 2\varphi_e \cos 2\varphi_f + \kappa \sin 2\varphi_e \sin 2\varphi_f) \epsilon(l) \sin 2\varphi_e B_e(l) \\ & + \frac{2}{\zeta} (1-\kappa) \sin 2\varphi_e \sin 2\varphi_f \beta_p(l) (\zeta l - \tanh \zeta l) \\ & + \epsilon(l) \sin 2\varphi_f - \epsilon_{cr} \text{sign}\dot{\beta}_f, \end{aligned} \quad (7.42)$$

where  $\text{sign}\dot{\beta}_f = \text{sign}\beta_{fm}$ .

### 7.2.2 Symmetric double slip systems

If the dissipation of energy can be neglected, the determination of  $\beta_l(y)$  and  $\beta_r(y)$  reduces to the minimization of the total energy (7.6). The variational problem has a unique solution due to the convexity of  $\Psi$  with respect to  $\beta_l$ ,  $\beta_r$ ,  $\beta_{l,y}$  and  $\beta_{r,y}$ . To be able to obtain the closed analytical solutions we analyze first the variational problem with symmetric double slip system where  $\varphi_r = \pi - \varphi_l = \pi - \varphi$ .

Putting into use the dimensionless quantities (6.54), for the case with zero dissipation, we rewrite the functional (7.6) in the form

$$E(\beta_l(\eta), \beta_r(\eta)) = \int_0^1 \left[ \frac{1}{2} (1 - \kappa) \sin^2 2\varphi (\beta_l - \beta_r)^2 + \frac{k(|\beta'_l| + |\beta'_r|) |\sin \varphi|}{c} + \frac{k \sin^2 \varphi (\beta_l'^2 + \beta_r'^2 + 2\chi |\beta'_l| |\beta'_r|)}{c^2} \right] d\eta + \frac{1}{2} \cos^2 2\varphi (\langle \beta_l \rangle + \langle \beta_r \rangle)^2 + \frac{1}{2\kappa} \left( \epsilon - \kappa \sin 2\varphi (\langle \beta_l \rangle - \langle \beta_r \rangle) \right)^2, \quad (7.43)$$

where, for simple, the bars over  $\bar{\beta}_l(\eta)$  and  $\bar{\beta}_r(\eta)$  are dropped with

$$\langle \beta_l \rangle = \int_0^1 \beta_l d\eta, \quad \text{and} \quad \langle \beta_r \rangle = \int_0^1 \beta_r d\eta. \quad (7.44)$$

We minimize functional (7.43) among  $\beta_l$  and  $\beta_r$  satisfying the boundary conditions

$$\beta_l(0) = \beta_r(0) = \beta_l[1] = \beta_r[1] = 0. \quad (7.45)$$

From the threshold values derivation we found out that for symmetric double slip systems both slip systems are activated at the same time at

$$\epsilon_{en} = \frac{2k |\sin \varphi|}{c |\sin 2\varphi|}, \quad (7.46)$$

with  $c = hb\rho_s$ . We have also the relation

$$\beta_l(\eta) = -\beta_r(\eta) = \beta(\eta) \quad \text{and} \quad \langle \beta_l \rangle = -\langle \beta_r \rangle = \langle \beta \rangle, \quad (7.47)$$

for  $\eta \in (0, 1)$  under the boundary conditions

$$\beta(0) = \beta[1] = 0. \quad (7.48)$$

Accordingly, the energy functional (7.6) reduces to

$$E(\beta(\eta)) = \int_0^1 \left[ 2\beta^2 (1 - \kappa) \sin^2 2\varphi + \frac{2k|\beta'| |\sin \varphi|}{c} + \frac{k(1 + \chi) \sin^2 \varphi \beta'^2}{c^2} \right] d\eta + \frac{1}{2\kappa} (\epsilon - 2\kappa \sin 2\varphi \langle \beta \rangle)^2, \quad (7.49)$$

with

$$\langle \beta \rangle = \int_0^1 \beta d\eta. \quad (7.50)$$

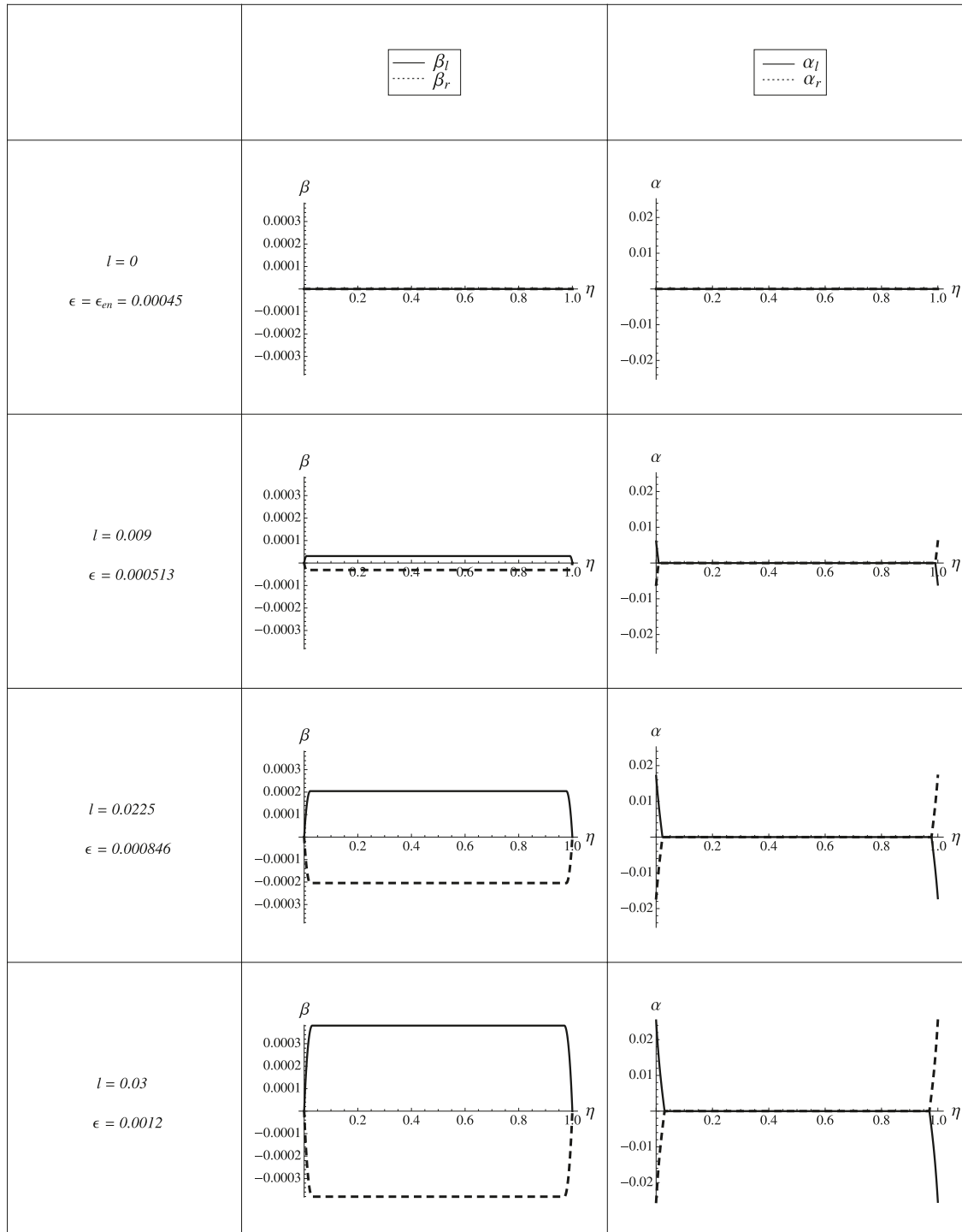


Figure 7.3: Evolution of  $\beta$  and  $\alpha$  for zero dissipation symmetric double-slip uniaxial extension of single crystal with  $h = 1 \mu\text{m}$  and  $\varphi = 60^\circ$  where  $\eta = y/h$

Since now we have only one  $\beta$ , we can follow the same procedure explained in section 5.2.1 to find the solutions and obtain

$$\beta = \begin{cases} \beta_{1p}(1 - \cosh \zeta \eta + \tanh \zeta l \sinh \zeta \eta), & \text{for } \eta \in (0, l), \\ \beta_m = \beta_{1p} \left(1 - \frac{1}{\cosh \zeta l}\right), & \text{for } \eta \in (l, 1 - l), \\ \beta_{1p}(1 - \cosh \zeta(1 - \eta) + \tanh \zeta l \sinh \zeta(1 - \eta)), & \text{for } \eta \in (1 - l, 1), \end{cases} \quad (7.51)$$

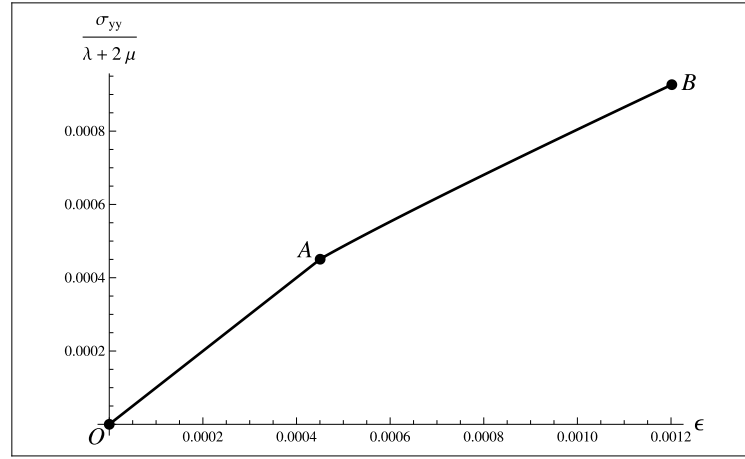


Figure 7.4: Normalized tensile stress versus tensile strain curve for symmetric double-slip uni-axial extension of single crystal at zero dissipation with  $\varphi = 60^\circ$  and  $h = 1 \mu\text{m}$

with

$$\beta_{1p} = \frac{\epsilon - 2\kappa\langle\beta\rangle \sin 2\varphi}{2(1 - \kappa) \sin 2\varphi}, \quad (7.52)$$

where

$$\zeta = 2c\sqrt{\frac{2(1 - \kappa)}{k(1 + \chi)}} |\cos \varphi|. \quad (7.53)$$

The average of  $\beta$  reads

$$\langle\beta\rangle = B(l)\epsilon, \quad (7.54)$$

where

$$B(l) = \frac{g(l)}{2 \sin 2\varphi (1 - \kappa + \kappa g(l))}, \quad (7.55)$$

with

$$g(l) = 2 \left( l - \frac{\tanh \zeta l}{\zeta} \right) + \left( 1 - \frac{1}{\cosh \zeta l} \right) (1 - 2l).$$

The equation to determine  $\epsilon$  in term of  $l$  reads

$$\epsilon(l) = \frac{2k(\text{sign}\beta) |\sin \varphi| \cosh \zeta l}{c(1 - 2l) \sin 2\varphi (1 - 2\kappa \sin 2\varphi B(l))}, \quad (7.56)$$

where

$$\text{sign}\beta = \begin{cases} 0, & \text{for } \varphi = 0^\circ, \\ +1, & \text{for } 0^\circ < \varphi < 90^\circ, \\ -1, & \text{for } 90^\circ < \varphi < 180^\circ. \end{cases} \quad (7.57)$$

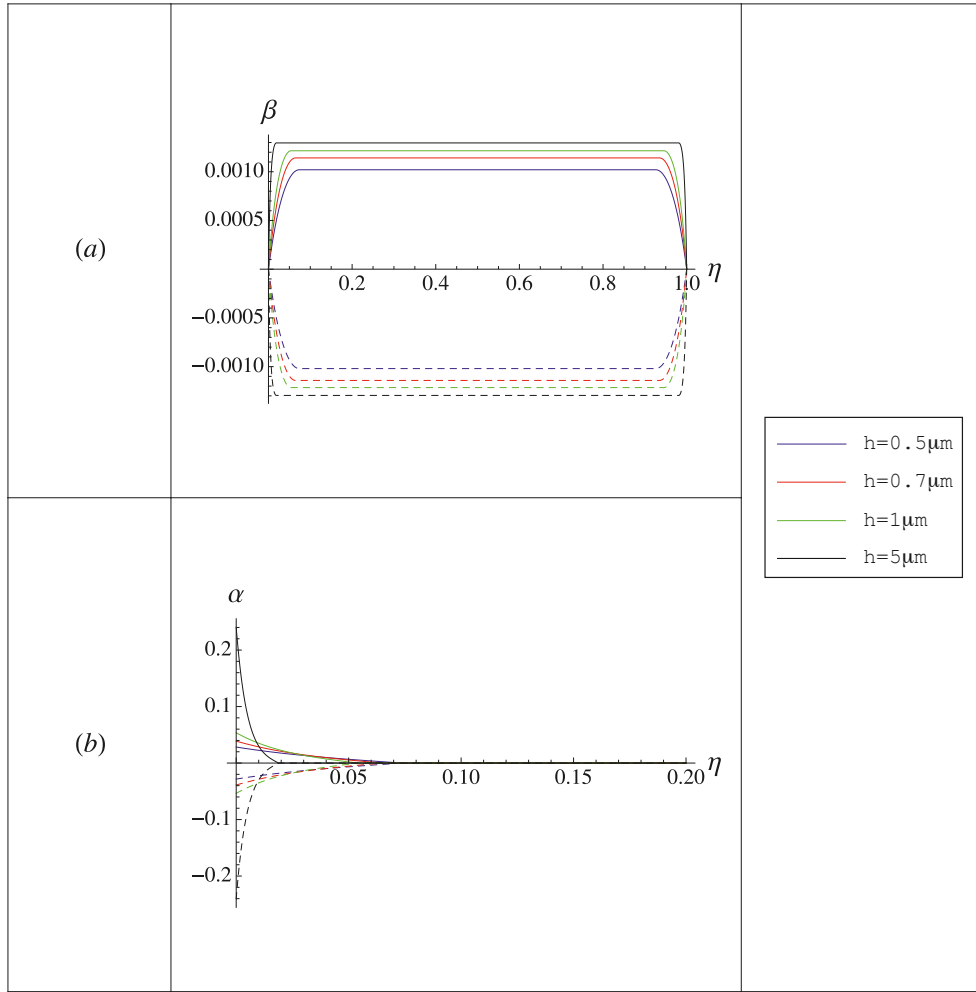


Figure 7.5: Evolution of  $\beta_l$  (continuous lines) and  $\beta_r$  (dashed lines) within the interval  $\eta \in (0, 1)$  together with  $\alpha_l$  (continuous lines) and  $\alpha_r$  (dashed lines) within the interval  $\eta \in (0, 0.2)$  for zero dissipation symmetric double-slip plane-constrained uniaxial extension of single crystal at  $\varphi = 60^\circ$  and  $\epsilon = 0.003$  with different crystal heights  $h$

For the symmetric double slip we have

$$\rho_l = -\rho_r = \frac{\beta_{,y} \sin \varphi}{b}.$$

The resultant Burgers vector of all dislocations has only one non-zero component in the  $x$ -direction, namely

$$\alpha_{xz} = \beta_{,y} \sin 2\varphi.$$

On that account, couples of dislocations close-by the boundaries form "super" dislocations with the Burgers vector in the  $x$ -direction. The normalized dislocation density

$$\alpha = \beta' \sin \varphi,$$

can be computed using the solutions (7.51), namely

$$\alpha = \begin{cases} \beta_{1p} \sin \varphi (-\zeta \sinh \zeta \eta + \zeta \tanh \zeta l \cosh \zeta \eta), & \text{for } \eta \in (0, l), \\ 0, & \text{for } \eta \in (l, 1-l), \\ \beta_{1p} \sin \varphi (-\zeta \sinh \zeta (1-\eta) + \zeta \tanh \zeta l \cosh \zeta (1-\eta)), & \text{for } \eta \in (1-l, 1). \end{cases} \quad (7.58)$$

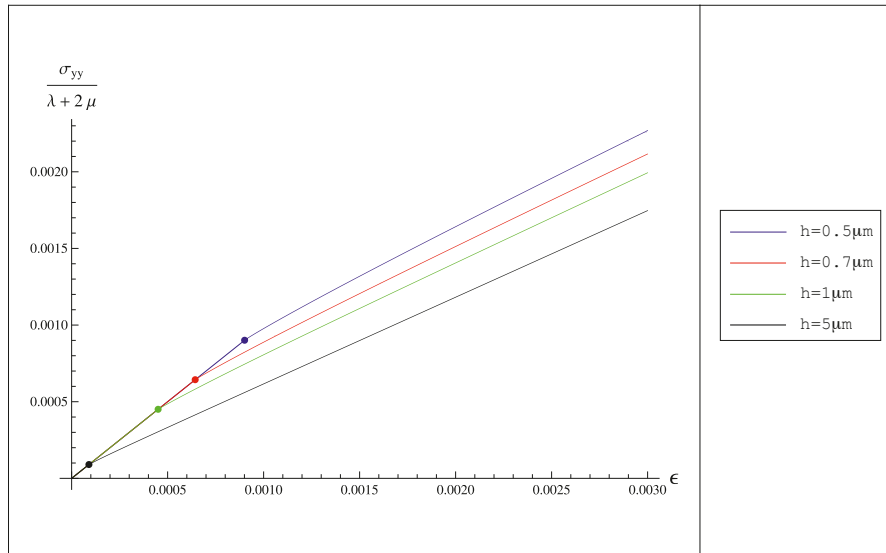


Figure 7.6: Normalized tensile stress versus tensile strain curves for zero dissipation symmetric double-slip plane-constrained uniaxial extension of single crystal at  $\varphi = 60^\circ$  with different crystal heights  $h$

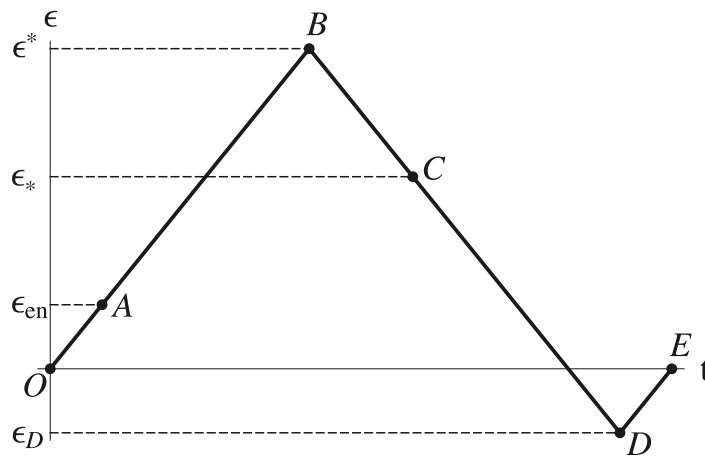


Figure 7.7: A closed loading path for plane constrained uniaxial extension of a single crystal strip with symmetric double slip systems

Fig. 7.3 shows the evolution of  $\beta(\eta)$  and  $\alpha(\eta)$  at zero dissipation for symmetric double slip at  $\varphi = 30^\circ$  as  $\epsilon$  increases, where  $\eta = y/h$ . By plotting the following equation

$$\frac{\sigma_{yy}}{\lambda + 2\mu} = \epsilon - 2\kappa \sin 2\varphi \langle \beta \rangle,$$

the normalized tensile stress versus tensile strain curve OAB for the same slip system is shown in Fig. 7.4. We observe the work hardening phenomenon and the reversibility of the stress-strain curve as previously. Fig. 7.5 shows the evolution of  $\beta_l$  and  $\beta_r$  at  $\varphi = 60^\circ$  and  $\epsilon = 0.003$  for various number of  $h$ . The size effect on the present result due to the dislocations pile-up can be observed in Fig. 7.6 where the stress strain curves for different crystal heights at  $\varphi = 60^\circ$  are plotted where the dots express the energetic yield points.

For the case of symmetric double slip system with energy dissipation, we found out here

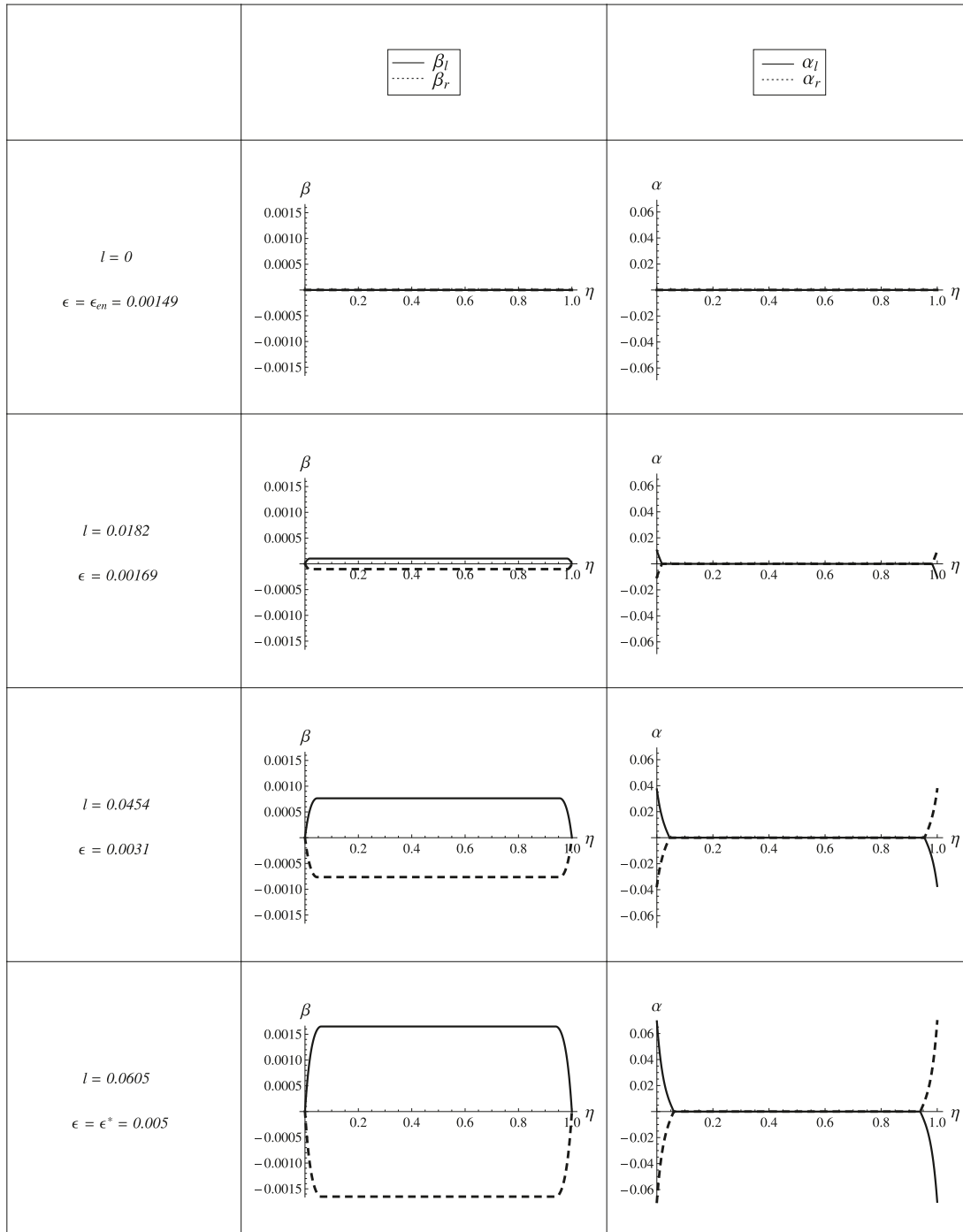


Figure 7.8: Evolution of  $\beta$  and  $\alpha$  for the case of symmetric double slip systems for plane-constrained uniaxial extension of a single crystal strip with dissipation during the loading process as  $\epsilon$  increases at  $\varphi = 60^\circ$  where  $h = 1 \mu\text{m}$ .

that the condition (7.47) obeying (7.48) is also true. Therefore, since we have only one  $\beta$ , the determination of  $\beta(\eta)$  for  $\beta \neq 0$  reduces to the minimization of dimensionless effective energy

$$\delta \hat{E} = 0, \quad (7.59)$$

where the effective energy,  $\hat{E}$ , reads

$$\hat{E} = E + \int_0^1 2\epsilon_{cr}(\text{sign}\dot{\beta})\beta \, d\eta, \quad (7.60)$$

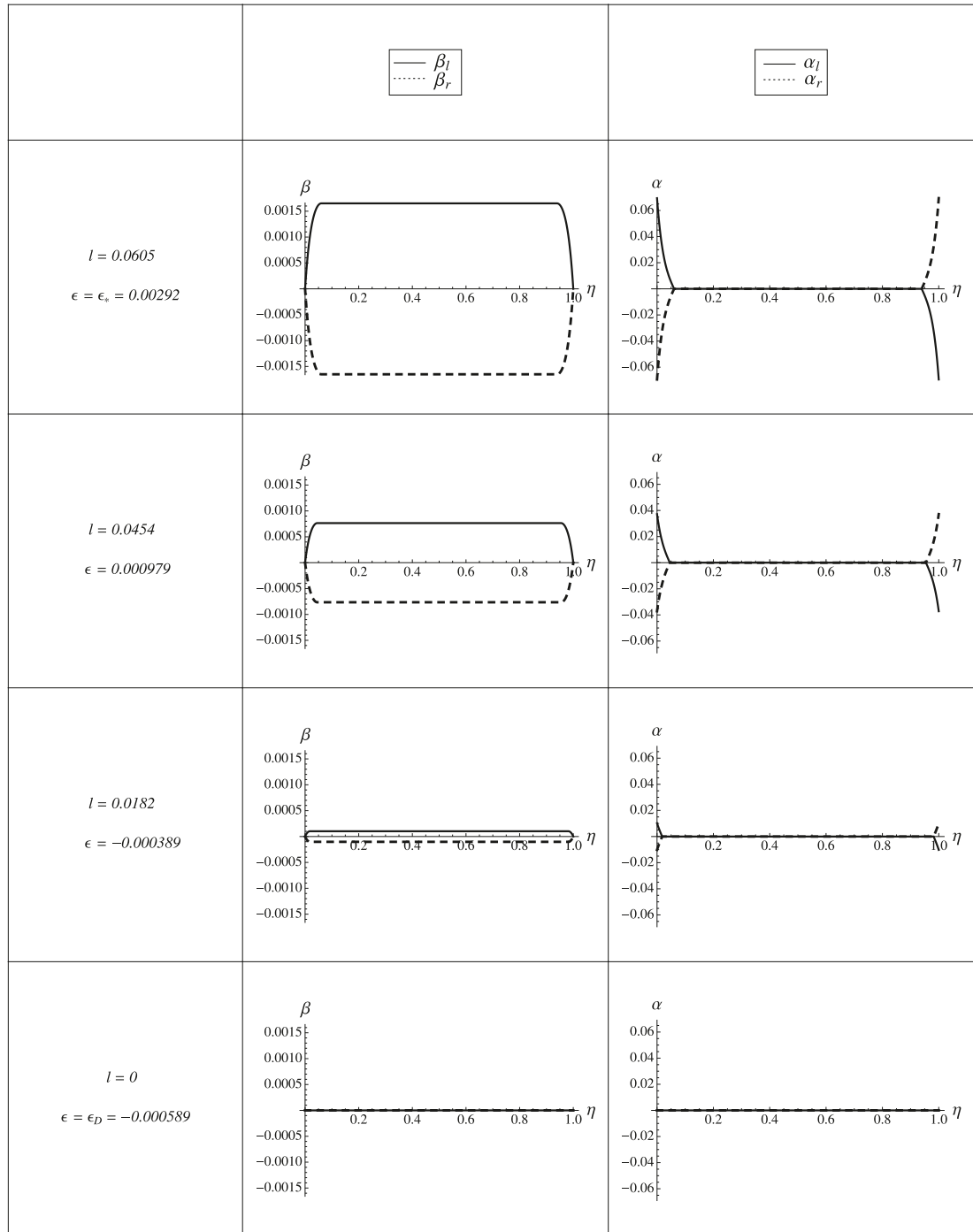


Figure 7.9: Evolution of  $\beta$  and  $\alpha$  for the case of symmetric double slip systems for plane-constrained uniaxial extension of a single crystal strip with dissipation during the inverse loading process as  $\epsilon$  decreases at  $\varphi = 60^\circ$  where  $h = 1 \mu\text{m}$ .

with  $E$  form (7.49).

Applying the energy functional (7.49) to (7.60), the dimensionless effective energy for sym-

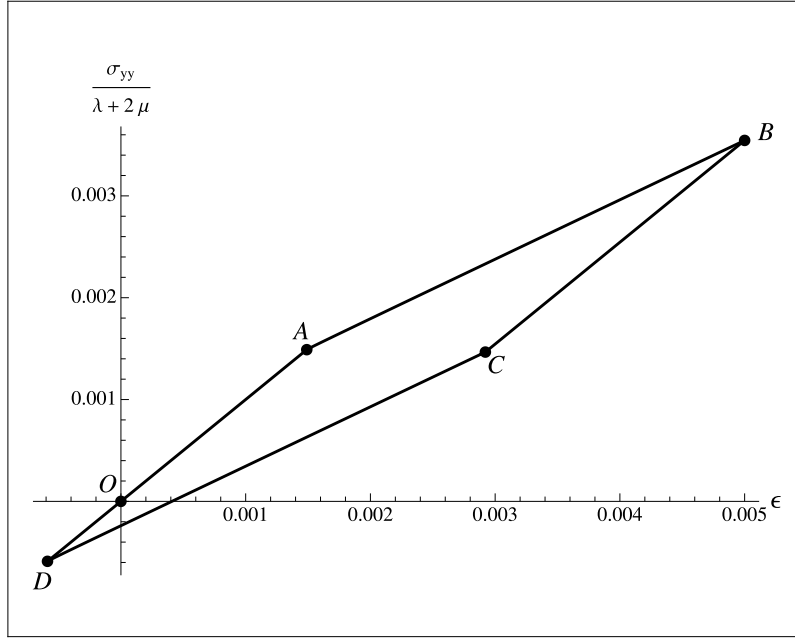


Figure 7.10: Plot of  $\beta$  within the interval  $\eta \in (0, 1)$  and  $\alpha$  within the interval  $\eta \in (0, 0.2)$  at  $\varphi = 60^\circ$  and  $\epsilon = 0.005$  with different crystal heights  $h$  for the symmetric double slip systems uniaxial extension case with non-zero dissipation

metric double slip plane-constrained uniaxial extension case can be written as

$$E(\beta(\eta)) = \int_0^1 \left[ 2\beta^2(1 - \kappa) \sin^2 2\varphi + \frac{2k|\beta'| |\sin \varphi|}{c} + \frac{k(1 + \chi) \sin^2 \varphi \beta'^2}{c^2} \right] d\eta + \frac{1}{2\kappa} (\epsilon_l - 2\kappa \sin 2\varphi \langle \beta \rangle)^2, \quad (7.61)$$

with

$$\epsilon_l = \epsilon - \frac{\epsilon_{cr} \text{sign} \dot{\beta}}{\sin 2\varphi}, \quad (7.62)$$

where  $\langle \beta \rangle$  from (7.50).

Our aim is to find  $\beta[t, \eta]$  with  $\epsilon$  as the driving variable as shown in Fig. 7.7. For loading path OA, the crystal undergoes elastic deformation and  $\dot{\beta} = 0$  as long as  $\epsilon < \epsilon_{en1}$ . Since the plastic distortion,  $\beta$ , is initially zero, we have  $\beta = 0$  and the normalized tensile stress strain equation

$$\frac{\sigma_{yy}}{\lambda + 2\mu} = \epsilon. \quad (7.63)$$

in the course of loading path OA.

The geometrically necessary dislocations start to appear at point A where

$$\epsilon_{en} = \frac{\epsilon_{cr}}{|\sin 2\varphi|} + \frac{2k}{c} \frac{|\sin \varphi|}{|\sin 2\varphi|}, \quad (7.64)$$

with  $c = hb\rho_s$  which demonstrates the size effect. Therefore the crystal is now subjected to plastic deformation throughout the loading path AB. All along this loading path we have

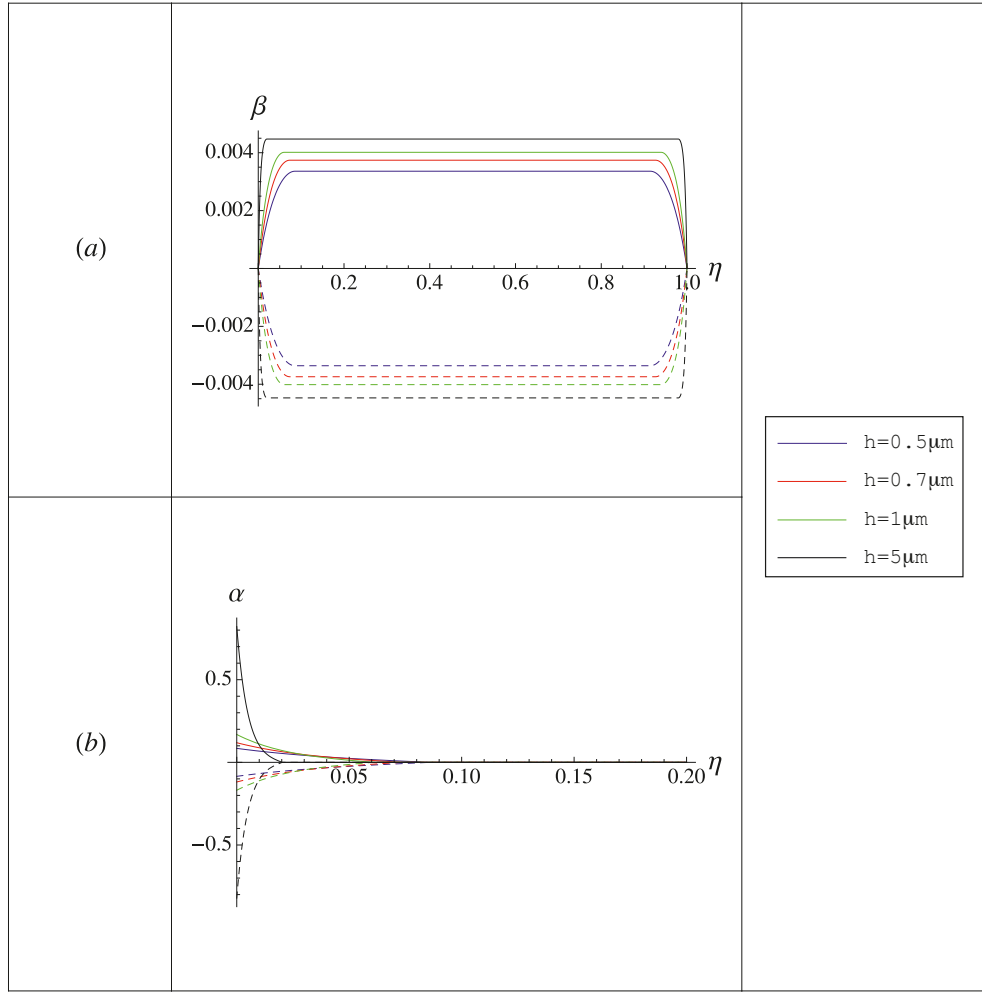


Figure 7.11: Evolution of  $\beta_l$  (continuous lines) and  $\beta_r$  (dashed lines) within the interval  $\eta \in (0, 1)$  together with  $\alpha_l$  (continuous lines) and  $\alpha_r$  (dashed lines) within the interval  $\eta \in (0, 0.2)$  for the case of symmetric double-slip plane-constrained uniaxial extension of single crystal with energy dissipation at  $\varphi = 60^\circ$  and  $\epsilon = 0.005$  for different crystal heights  $h$

either constantly increasing  $\beta$  ( $\dot{\beta} > 0$ ) or constantly decreasing  $\beta$  ( $\dot{\beta} < 0$ ) as  $\epsilon$  increases so that

$$\text{sign} \dot{\beta} = \text{sign} \beta, \quad (7.65)$$

where  $\text{sign} \beta$  from (7.57).

When  $\epsilon$  is increased from point A to point B, in order to determine the evolution of plastic distortion  $\beta$  we need to solve (7.59) with the effective energy from (7.61) where, for loading path AB, we have

$$\epsilon_l = \epsilon - \frac{\epsilon_{cr} \text{sign} \beta}{\sin 2\varphi}. \quad (7.66)$$

Due to the similar form of (7.61) and (7.49), we obtain for this case the resembling solutions as in (7.51)-(7.55) but now with  $\epsilon_l$  from (7.66) replacing  $\epsilon$  where

$$\epsilon(l) = \frac{\text{sign} \beta}{\sin 2\varphi} \left( \epsilon_{cr} + \frac{2k |\sin \varphi| \cosh \zeta l}{c(1-2l)(1-2\kappa \sin 2\varphi B(l))} \right). \quad (7.67)$$

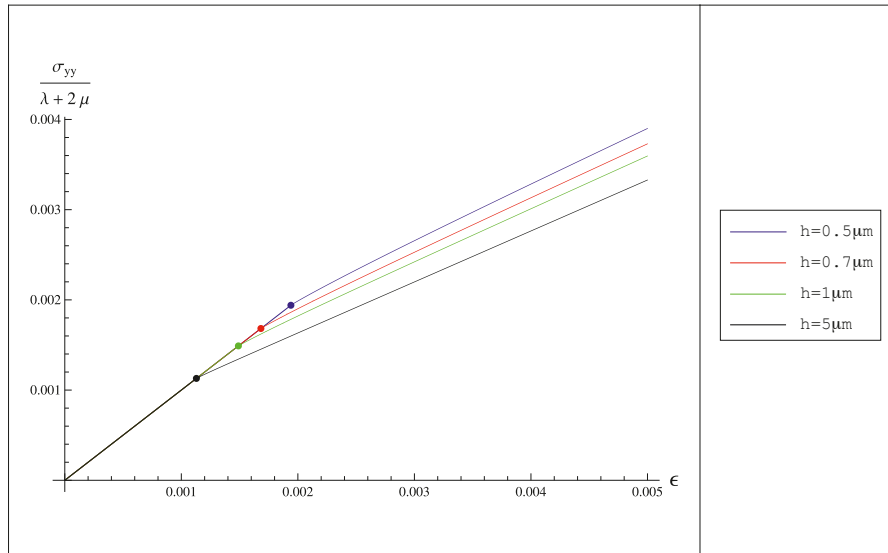


Figure 7.12: Normalized tensile stress versus tensile strain curve at  $\varphi = 60^\circ$  with different crystal heights  $h$  during the loading for symmetric double slip systems uniaxial extension case with dissipation

The normalized dislocation density is identical with (7.58). The normalized tensile stress versus tensile strain equation for loading path AB reads

$$\frac{\sigma_{yy}}{\lambda + 2\mu} = \epsilon(l) - 2\kappa \left( \epsilon(l) - \frac{\epsilon_{cr} \text{sign}\beta}{\sin 2\varphi} \right) B(l) \sin 2\varphi. \quad (7.68)$$

Then, as we decrease  $\epsilon$  from point B to point C, the crystal deforms again elastically so that  $\beta$  frozen ( $\dot{\beta} = 0$ ). The tensile stress versus tensile strain equation for inverse loading BC takes the form

$$\frac{\sigma_{yy}}{\lambda + 2\mu} = \epsilon + \left( \frac{\sigma_{yy}}{\lambda + 2\mu} \right)_B - \epsilon^*, \quad (7.69)$$

where  $\left( \frac{\sigma_{yy}}{\lambda + 2\mu} \right)_B$  is the solution of (7.68) at  $\epsilon = \epsilon^*$  (point B).

When  $\epsilon$  is further decreased from point C to point D, the crystal undergoes again to plastic deformation and the nucleated dislocations start to annihilate and completely disappear at point D. During this inverse loading process we have the relation

$$\text{sign}\dot{\beta} = -\text{sign}\beta. \quad (7.70)$$

We minimize the effective energy (7.61) but now instead of  $\epsilon_l$  we employ

$$\epsilon_u = \epsilon + \frac{\epsilon_{cr} \text{sign}\beta}{\sin 2\varphi}. \quad (7.71)$$

We obtain again the analogous solutions to (7.51)-(7.55) and (7.58) but now with  $\epsilon_u$  from (7.71) replacing  $\epsilon$  where

$$\epsilon(l) = -\frac{\text{sign}\beta}{\sin 2\varphi} \left( \epsilon_{cr} - \frac{2k |\sin \varphi| \cosh \zeta l}{c(1 - 2l)(1 - 2\kappa \sin 2\varphi B(l))} \right). \quad (7.72)$$

The normalized tensile stress equation for inverse loading CD takes the form

$$\frac{\sigma_{yy}}{\lambda + 2\mu} = \epsilon(l) - 2\kappa \left( \epsilon(l) + \frac{\epsilon_{cr} \text{sign}\beta}{\sin 2\varphi} \right) B(l) \sin 2\varphi. \quad (7.73)$$

Finally, we load again the crystal by increasing  $\epsilon$  from point D to point E. The crystal is now subjected to elastic deformation and  $\dot{\beta} = 0$ . Since the previously nucleated dislocations are now completely annihilated at point D, the plastic distortion,  $\beta$ , is equal to zero and remain the same in the course of loading path DE. The tensile stress versus strain equation for loading path DE is analogous to (7.63).

The continuity of  $\beta$  must be ensured for the whole closed loading path illustrated in Fig. 7.7. Therefore similar idea as in section 6.3.2 is adopted here to obtain the value of  $\epsilon$  at points C and D.

By using the same material properties as the previous zero dissipation case in addition to  $\epsilon_{cr} = 0.0008$ , we are able to compute results above numerically. The plots that illustrate the constantly increasing  $\beta$  and  $\alpha$  in the course of loading path AB as  $\epsilon$  increases and the steadily decreasing  $\beta$  and  $\alpha$  throughout inverse loading CD as  $\epsilon$  decreases for the case with  $\varphi = 60^\circ$  are shown in Fig. 7.8 and Fig. 7.9, respectively. The tensile stress and strain curve following loading path depicted in Fig. 7.7 for the same example which has the similar characteristic with plane-constrained shear case deforming in symmetric double slip system (see section 6.3.2) is shown in Fig. 7.10. To explain the size effect, we plot the material with the same combination of angle and properties as the previous examples for different crystal height,  $h$ , as depicted in Fig. 7.11 (distribution of plastic distortions and dislocation densities) and Fig. 7.12 (tensile stress versus tensile strain curves).

### 7.2.3 General double slip systems case

We first work with zero dissipation plane-constrained uniaxial extension of single crystal strip. Equivalent to the plane-constrained shear case deforming in non-symmetric double slip systems, as explained in detail in section 7.2.1, the first slip system becomes active at  $\epsilon = \epsilon_{en1}$  then the second slip system at  $\epsilon = \epsilon_{en2}$ . As the crystal deforms in single slip at interval  $\epsilon_{en1} \leq \epsilon < \epsilon_{en2}$ , we obtain the solutions from (7.23)-(7.30). The evolution of plastic distortions and dislocation densities for both slip systems at  $\varphi_l = 65^\circ$  and  $\varphi_r = 120^\circ$  in interval  $\epsilon_{en1} \leq \epsilon < \epsilon_{en2}$  are shown in Fig. 7.13. It can be observed from Fig. 7.13 that the slip system with  $\varphi_r$  is the only active slip system all along  $\epsilon_{en1} \leq \epsilon < \epsilon_{en2}$ .

Analytical solutions are not feasible for the case with  $\epsilon \geq \epsilon_{en2}$ . Henceforward we employ again the finite element procedure similar to section 6.2.3. For the purpose of numerical minimization it is useful to introduce the following dimensionless quantities

$$\begin{aligned} E &= \frac{\Psi}{aLh\mu\epsilon^3}, \quad \eta = \frac{y}{h\epsilon}, \quad H = \frac{1}{\epsilon}, \quad c = hb\rho_s, \\ m &= \frac{k}{\epsilon^2}, \quad \bar{\beta}_l(\eta) = \frac{\beta_l(y)}{\epsilon}, \quad \bar{\beta}_r(\eta) = \frac{\beta_r(y)}{\epsilon}, \end{aligned} \quad (7.74)$$

where

$$\bar{\beta}'_l(\eta) = h\beta_{l,y}(y) \quad \text{and} \quad \bar{\beta}'_r(\eta) = h\beta_{r,y}(y), \quad (7.75)$$

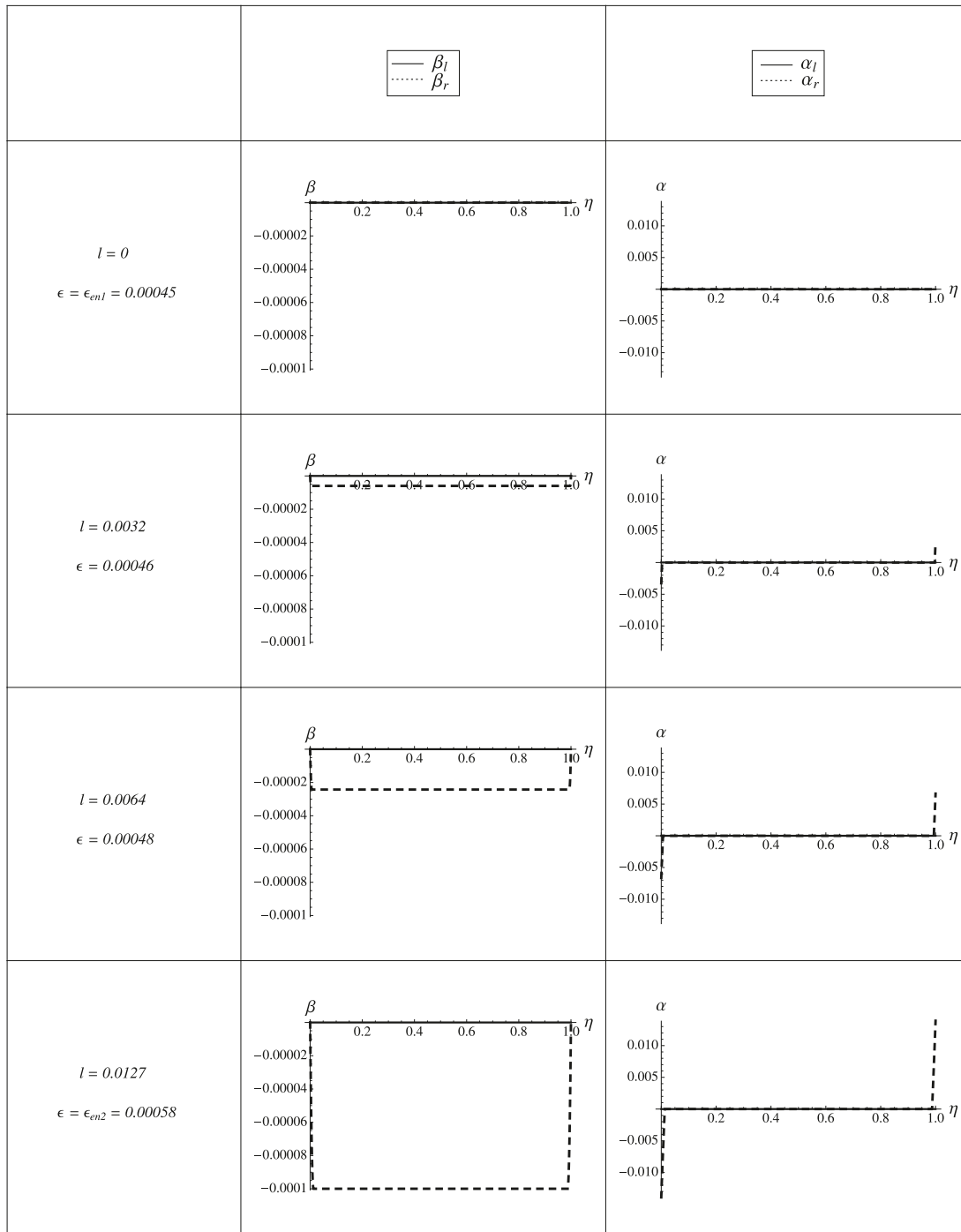


Figure 7.13: Evolution of plastic distortions ( $\beta_l$  and  $\beta_r$ ) and dislocation densities ( $\alpha_l$  and  $\alpha_r$ ) for general double slip uniaxial extension case with zero dissipation at  $\varphi_l = 65^\circ$  and  $\varphi_r = 120^\circ$  in interval  $\epsilon_{en1} \leq \epsilon < \epsilon_{en2}$  where  $h = 1 \mu\text{m}$ .

and  $\eta \in (0, H)$ . The functional (7.6) is now transformed into

$$\begin{aligned}
 E(\bar{\beta}_l(\eta), \bar{\beta}_r(\eta)) = & \int_0^H \left[ \frac{1}{2\kappa} \left( 1 - \kappa(\langle \bar{\beta}_l \rangle \cos 2\varphi_l + \langle \bar{\beta}_r \rangle \cos 2\varphi_r) \right)^2 \right. \\
 & + \frac{1}{2} (\langle \bar{\beta}_l \rangle \cos 2\varphi_l + \langle \bar{\beta}_r \rangle \cos 2\varphi_r)^2 + \frac{1 - \kappa}{2} (\bar{\beta}_l \sin 2\varphi_l + \frac{\bar{\beta}_r}{\epsilon} \sin 2\varphi_r)^2 \\
 & + \frac{m}{c} (|\bar{\beta}'_l \sin \varphi_l| + |\bar{\beta}'_r \sin \varphi_r|) + \frac{m}{2c^2} (\bar{\beta}'_l{}^2 \sin^2 \varphi_l + \bar{\beta}'_r{}^2 \sin^2 \varphi_r \\
 & \left. + 2\chi |\bar{\beta}'_l \sin \varphi_l| |\bar{\beta}'_r \sin \varphi_r| \right] d\eta, \tag{7.76}
 \end{aligned}$$

where

$$\langle \bar{\beta}_l \rangle = \frac{1}{H} \int_0^H \bar{\beta}_l d\eta \quad \text{and} \quad \langle \bar{\beta}_r \rangle = \frac{1}{H} \int_0^H \bar{\beta}_r d\eta.$$

The bars over  $\bar{\beta}_l$ ,  $\bar{\beta}_r$ ,  $\langle \bar{\beta}_l \rangle$  and  $\langle \bar{\beta}_r \rangle$  will be ignored in the future computation for short.

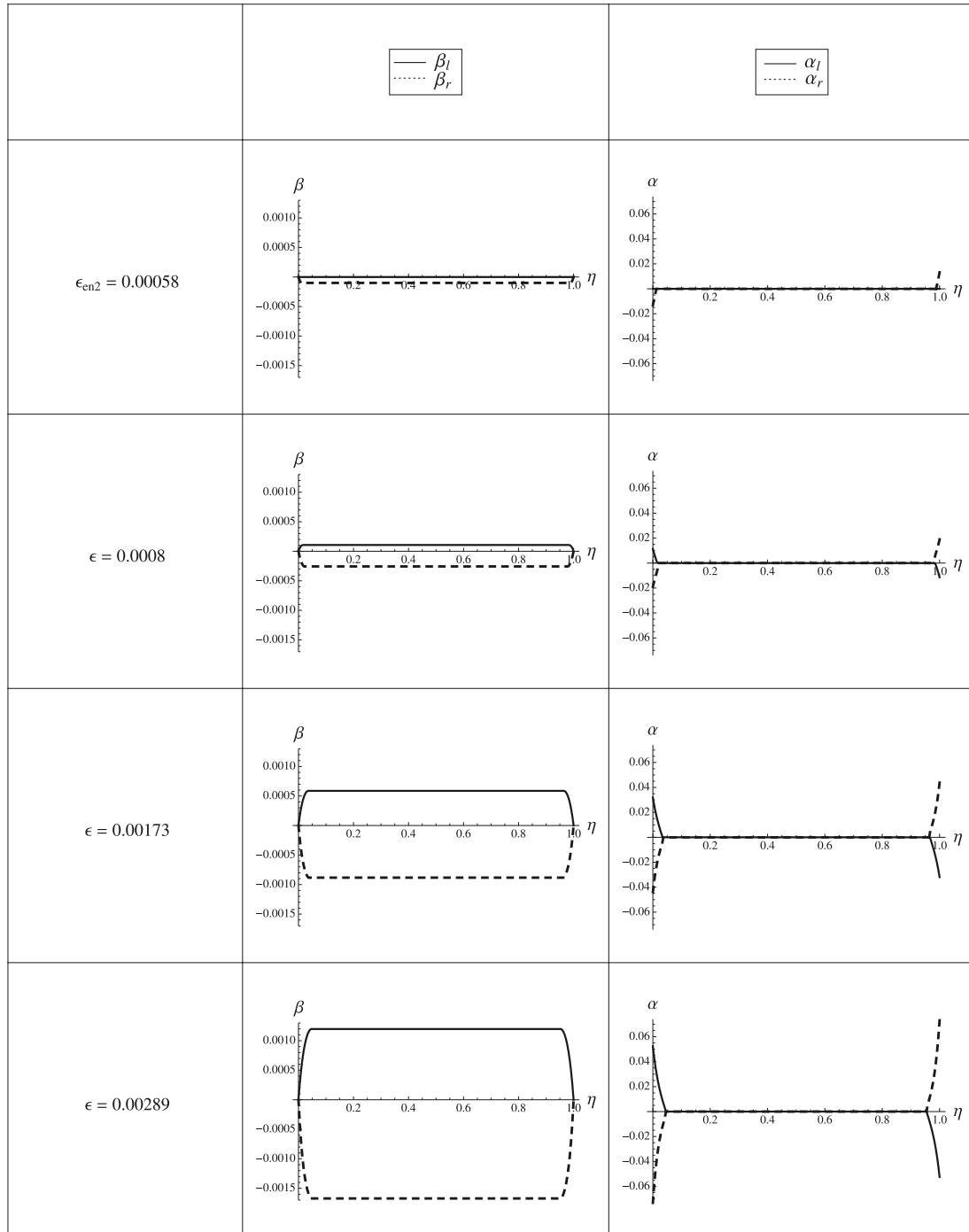


Figure 7.14: Evolution of  $\beta_l$  and  $\beta_r$  together with  $\alpha_l$  and  $\alpha_r$  for general case double slip plane-constrained uniaxial extension of single crystal at zero dissipation where  $h = 1 \mu\text{m}$ ,  $\varphi_l = 65^\circ$  and  $\varphi_r = 120^\circ$  at  $\epsilon \geq \epsilon_{en2}$

Based upon the previous analysis we employ again the following two assumptions:

- no dislocations at the center of the crystal hence  $\beta_l$  and  $\beta_r$  are constant in the middle layer
- the nucleated dislocations pile-up at the boundaries.

Consequently, we apply again the minimizers as in (6.90) and (6.91) to energy functional (7.76). In order to work with the finite element model to compute the numerical solution by energy minimization as shown in Fig. 6.8, we adopt the same discretization method used in section 6.2.3. As a result, the discretized dimensionless energy can be written now as

$$\begin{aligned}
E(c_j, d_j, l) = & \frac{1}{3n} l(1 - \kappa) \sum_{j=1}^n \left[ \sin 2\varphi_l \sin 2\varphi_r \left( c_{j-1}(2d_{j-1} + d_j) + c_j(d_{j-1} + 2d_j) \right) \right. \\
& \left. + \sin^2 2\varphi_l (c_{j-1}^2 + c_{j-1}c_j + c_j^2) + \sin^2 2\varphi_r (d_{j-1}^2 + d_{j-1}d_j + d_j^2) \right] \\
& + \frac{2m}{c} \sum_{j=1}^n \left[ |\sin \varphi_l (c_j - c_{j-1})| + |\sin \varphi_r (d_j - d_{j-1})| \right] \\
& + \frac{mn}{lc^2} \sum_{j=1}^n \left[ \sin^2 \varphi_l (c_j - c_{j-1})^2 + \sin^2 \varphi_r (d_j - d_{j-1})^2 \right. \\
& \left. + 2\chi |\sin \varphi_l (c_j - c_{j-1})| |\sin \varphi_r (d_j - d_{j-1})| \right] \\
& + \frac{1}{2} (1 - \kappa) (H - 2l) (c_n \sin 2\varphi_l + d_n \sin 2\varphi_r)^2 \\
& + \frac{H}{2\kappa} (\epsilon - \kappa \langle \beta_l \rangle \sin 2\varphi_l + \kappa \langle \beta_r \rangle \sin 2\varphi_r)^2 \\
& + \frac{H}{2} (\langle \beta_l \rangle \cos 2\varphi_l + \langle \beta_r \rangle \cos 2\varphi_r)^2, \tag{7.77}
\end{aligned}$$

where

$$\begin{aligned}
\langle \beta_l \rangle = & \frac{1}{H} \left( \frac{l}{n} \sum_{j=1}^n (c_{j-1} + c_j) + c_n (H - 2l) \right), \\
\langle \beta_r \rangle = & \frac{1}{H} \left( \frac{l}{n} \sum_{j=1}^n (d_{j-1} + d_j) + d_n (H - 2l) \right). \tag{7.78}
\end{aligned}$$

To obtain the numerical solutions for  $\beta_l$  and  $\beta_r$ , we need to minimize Eq. (7.77) with respect to  $c_j$ ,  $d_j$  and  $l$  with the additional constraint  $0 \leq l \leq H/2$ . The discretization of normalized dislocation densities are given in the form

$$(\alpha_l)_j = \begin{cases} \frac{n \sin \varphi_l}{l} (c_j - c_{j-1}), & \text{for } \eta \in (0, l), \\ 0, & \text{for } \eta \in (l, H - l), \\ -\frac{n \sin \varphi_l}{l} (c_j - c_{j-1}), & \text{for } \eta \in (H - l, H), \end{cases} \tag{7.79}$$

and

$$(\alpha_r)_j = \begin{cases} \frac{n \sin \varphi_r}{l} (d_j - d_{j-1}), & \text{for } \eta \in (0, l), \\ 0, & \text{for } \eta \in (l, H - l), \\ -\frac{n \sin \varphi_r}{l} (d_j - d_{j-1}), & \text{for } \eta \in (H - l, H), \end{cases} \tag{7.80}$$

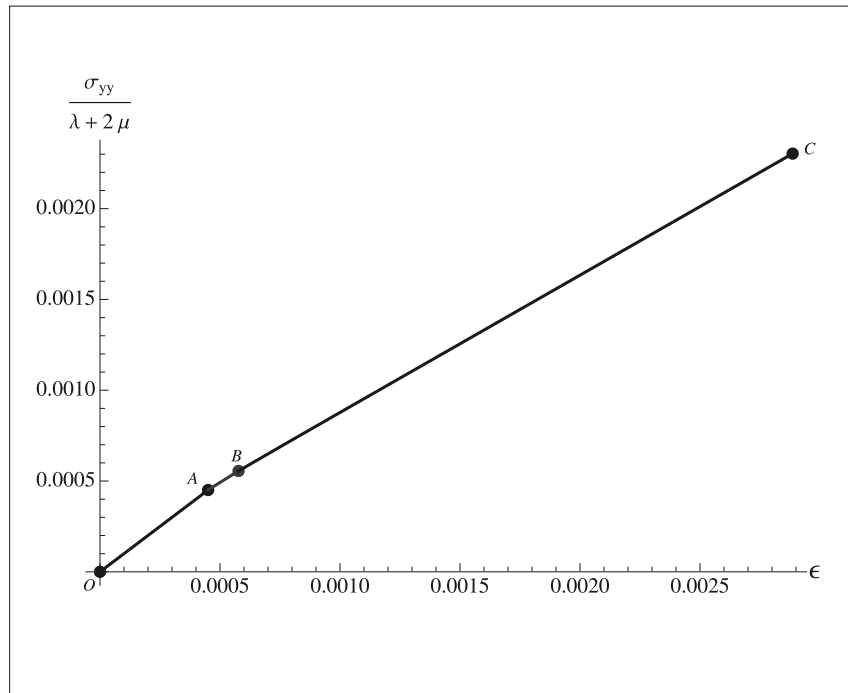


Figure 7.15: Normalized tensile stress versus tensile strain curve for general double-slip uniaxial extension of single crystal at zero dissipation at  $\varphi_l = 65^\circ$  and  $\varphi_r = 120^\circ$  with  $h = 1\mu\text{m}$

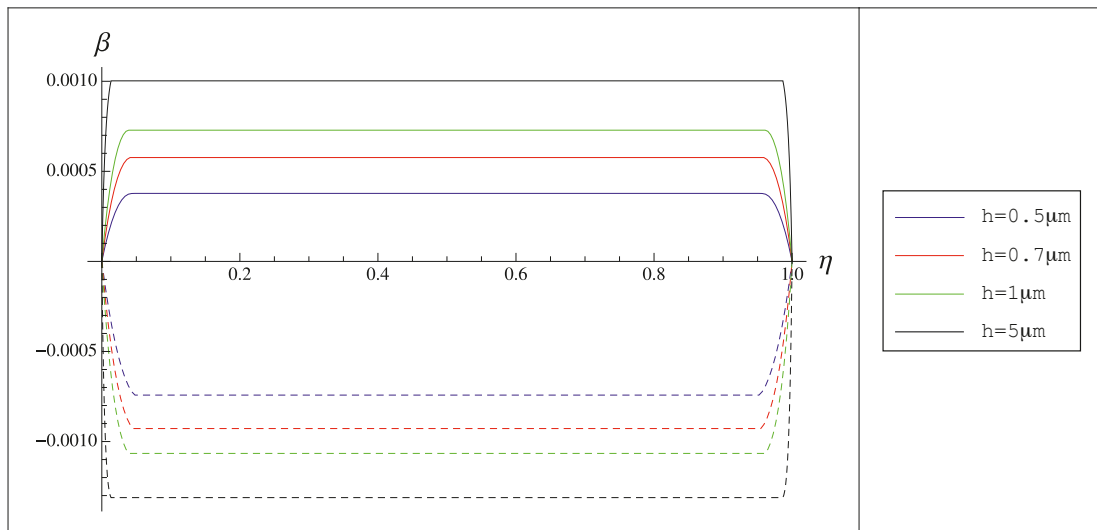


Figure 7.16: Evolution of  $\beta_l$  (continuous lines) and  $\beta_r$  (dashed lines) within the interval  $\eta \in (0, 1)$  for zero dissipation double slip plane-constrained uniaxial extension of single crystal at  $\varphi_l = 65^\circ$ ,  $\varphi_r = 120^\circ$  and  $\gamma = 0.01$  with different crystal heights  $h$

with  $j$  representing the element number.

For the numerical simulation, we employ the same material parameters as before and work with 10 elements for each boundary layer. In place of obtaining the same plotting range as in symmetric case, after numerical computation, we multiply  $H$ ,  $\eta$  and all of the computation results ( $\beta_l$ ,  $\beta_r$ ,  $\alpha_l$  and  $\alpha_r$ ) by  $\epsilon$  so that  $\epsilon \in (0, 1)$  and  $H = 1$ . Fig.7.14 illustrates the evolution

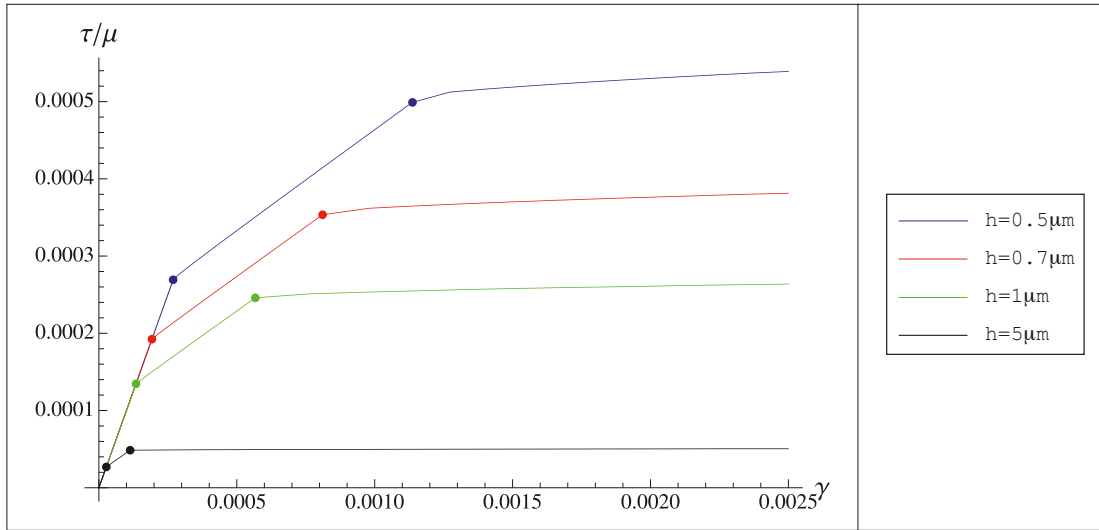


Figure 7.17: Normalized tensile stress versus tensile strain curves for zero dissipation double slip plane-constrained uniaxial extension of single crystal at  $\varphi_l = 65^\circ$  and  $\varphi_r = 120^\circ$  with different crystal heights  $h$

of plastic distortions and dislocation densities with increasing  $\epsilon$  for the case with  $\varphi_l = 65^\circ$  and  $\varphi_r = 120^\circ$  where  $h = 1\mu\text{m}$  at  $\epsilon \geq \epsilon_{en2}$ . The evolution of plastic distortions ( $\beta_l$  and  $\beta_r$ ) and dislocation densities  $\alpha_l$  and  $\alpha_r$  can be obtained easily for an arbitrary combination of angles.

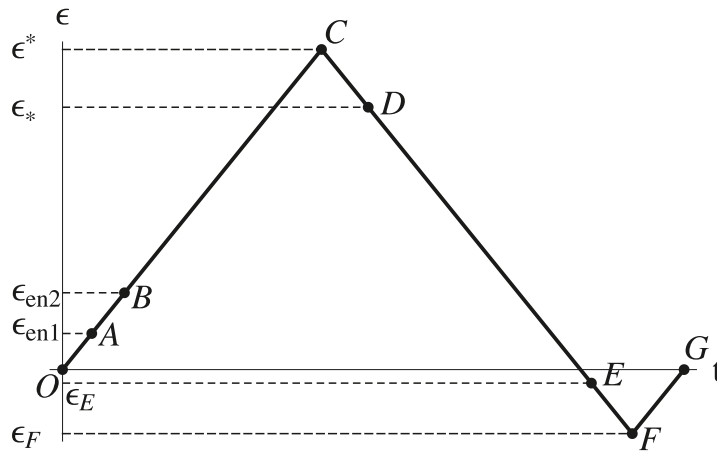


Figure 7.18: A closed loading path for plane-constrained uniaxial extension problem with two active slip systems

The normalized tensile stress and strain relation is expressed by

$$\frac{\sigma_{yy}}{\lambda + 2\mu} = \epsilon - \kappa(\langle\beta_l\rangle \sin 2\varphi_l + \langle\beta_r\rangle \sin 2\varphi_r), \quad (7.81)$$

with  $\langle\beta_l\rangle$  and  $\langle\beta_r\rangle$  from (7.78). Fig. 7.15 illustrates the stress-strain curve corresponding to (7.81) for  $\varphi_l = 65^\circ$  and  $\varphi_r = 120^\circ$ . The work hardening sections AB and BC by reason of the dislocation pile-up can be observed in Fig. 7.15. To illustrate the size effect with the same cause explained in section 3.3.2 we plot the plastic distortion and normalized tensile stress versus tensile strain curves for different crystal height,  $h$ , as can be seen in Fig. 7.16 and Fig. 7.17, respectively.

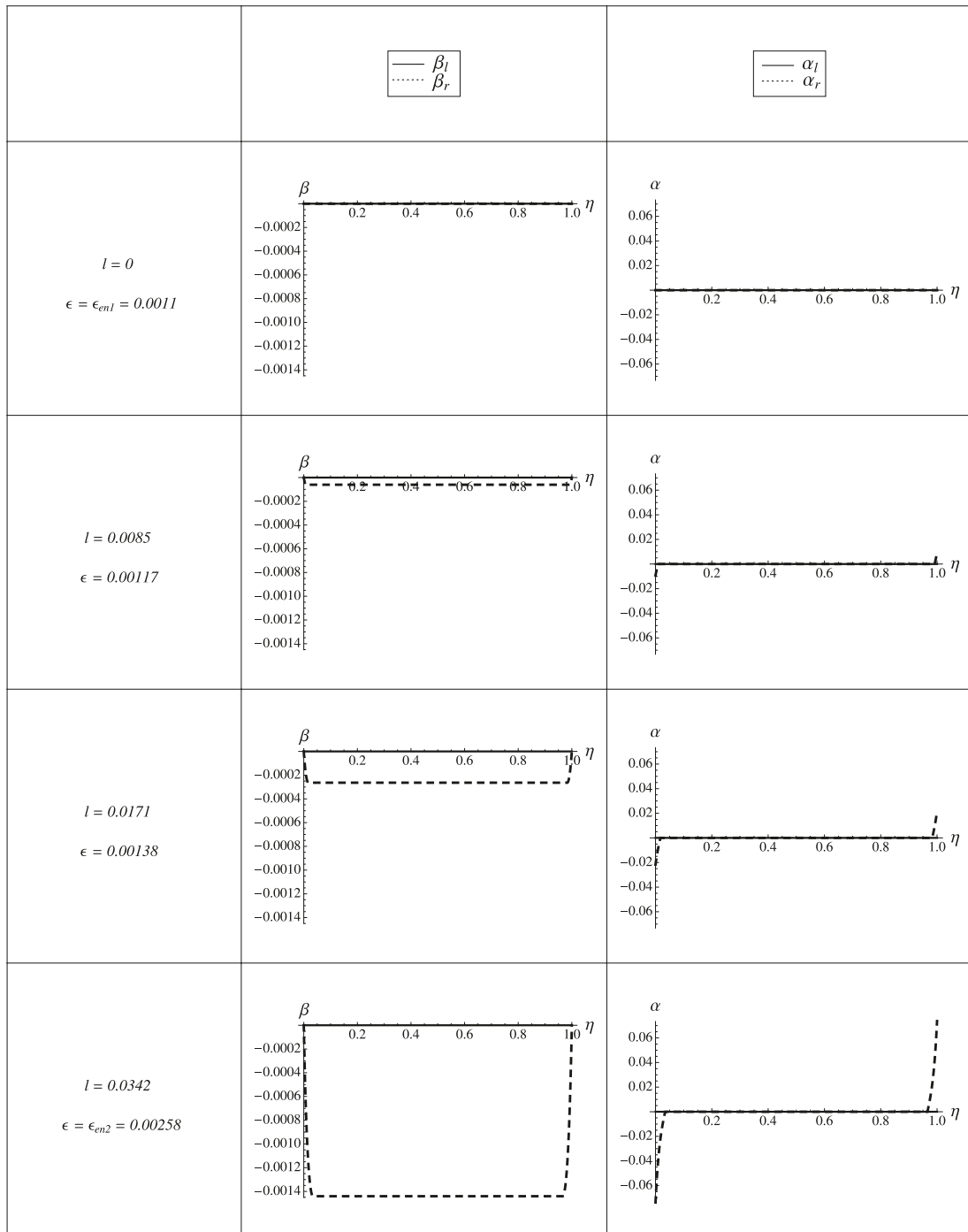


Figure 7.19: Evolution of plastic distortions and dislocation densities for loading path AB as  $\epsilon$  increased at  $\varphi_l = 20^\circ$  and  $\varphi_r = 140^\circ$  where  $h = 1 \mu\text{m}$ .

In the case of non-zero dissipation, the plastic distortions,  $\beta_l$  and  $\beta_r$  minimize the effective energy (7.9) under constraints (7.5). We need to determine the evolution of  $\beta_l$  and  $\beta_r$  with  $\epsilon$  as the driving variable following the closed loading path illustrated in Fig. 7.18.

The plastic distortions  $\beta_l$  and  $\beta_r$  are initially zero (point A). The rate of plastic distortions,  $\dot{\beta}_l$  and  $\dot{\beta}_r$ , equal to zero consequently  $\beta_l$  and  $\beta_r$  remain zero throughout this loading path OA. One slip system becomes active, hence geometrically necessary dislocations start to nucleate, at the first energetic threshold value,  $\epsilon_{en1}$  from (7.37) (point A) where the other

slip system remains passive. As a consequence, the crystal is now deforming in single slip system as we increase  $\epsilon$  from point A to point B with the solutions in similar form as (7.23)-(7.29) but now  $\epsilon$  being replaced by  $\epsilon_l$  from (7.39). The second slip system becomes active at point B where  $\epsilon = \epsilon_{en2}$ . The way to obtain  $\epsilon_{en2}$  can be seen in section 7.2.1. For plotting the results numerically, we use  $\epsilon_{cr} = 0.0008$  in addition to the same material parameter as zero dissipation case. The evolution of plastic distortions and dislocation densities for loading path AB at  $\varphi_l = 20^\circ$  and  $\varphi_r = 140^\circ$  can be observed in Fig. 7.20.

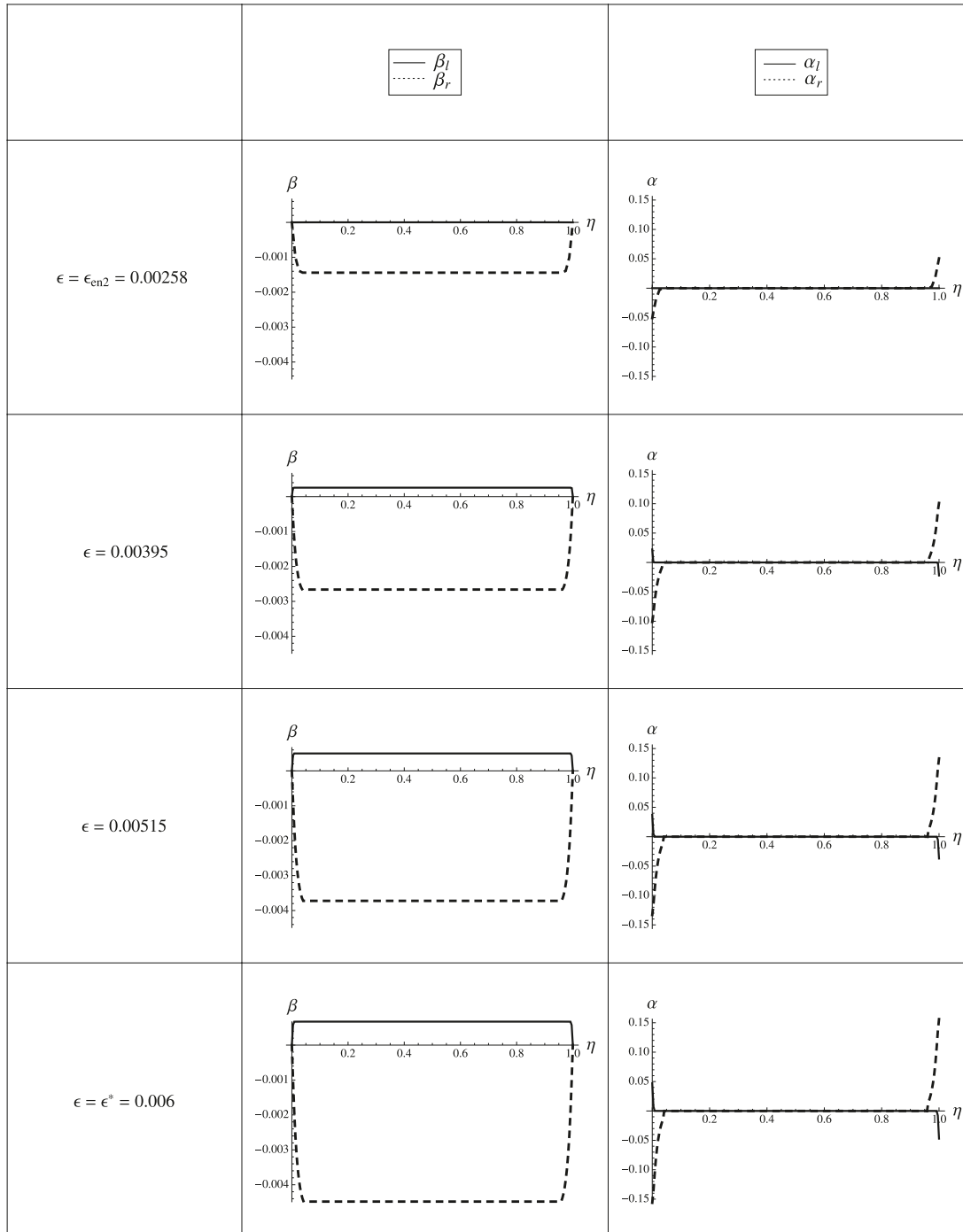


Figure 7.20: Evolution of plastic distortions and dislocation densities as  $\epsilon$  grows for loading path BC at  $\varphi_l = 20^\circ$  and  $\varphi_r = 140^\circ$  where  $h = 1 \mu\text{m}$ .

When  $\epsilon$  is increased further from point B to point C ( $\epsilon \geq \epsilon_{en2}$ ), the problem has to be solved numerically by employing the finite element procedure explained in section 6.2.3.

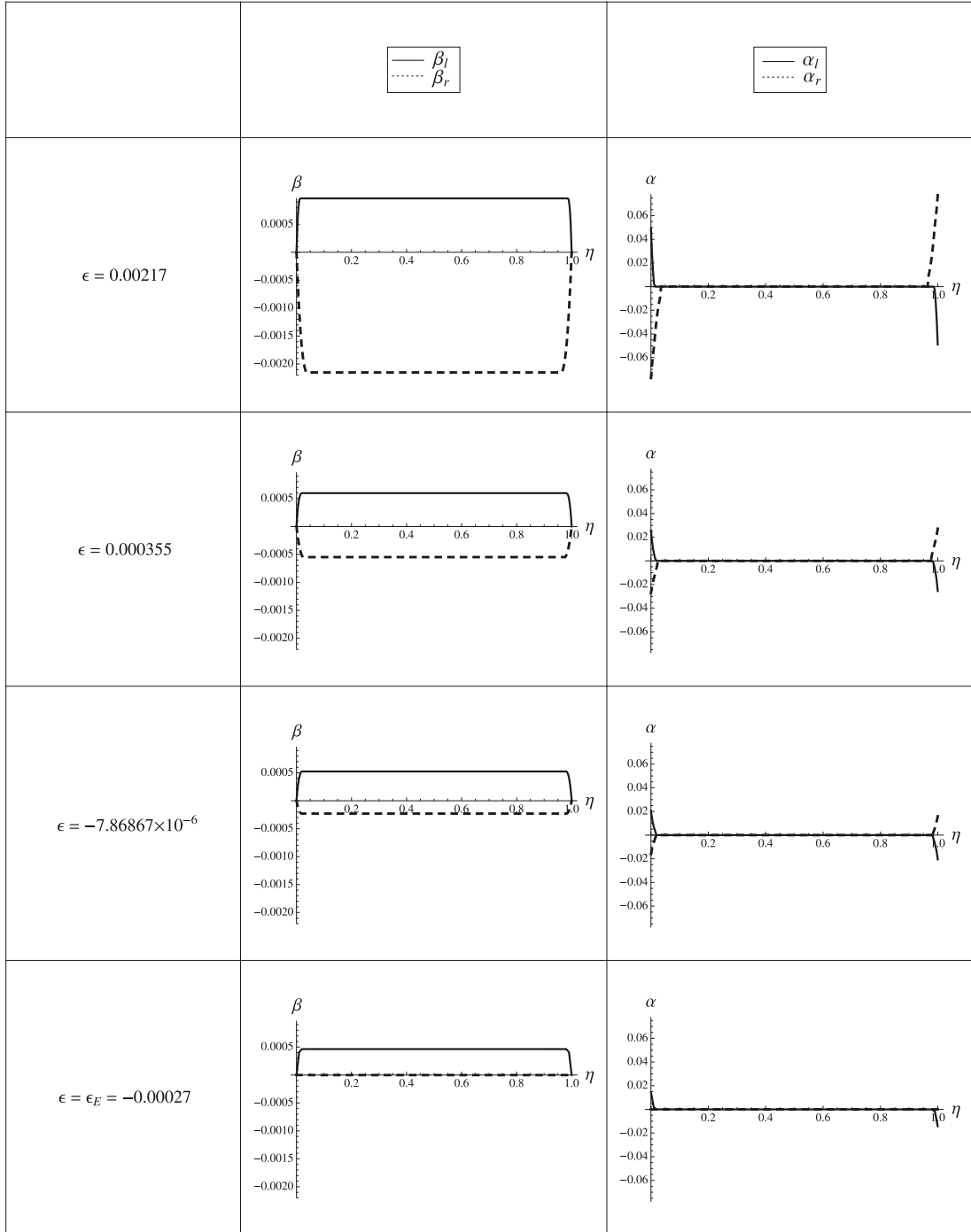


Figure 7.21: Evolution of plastic distortions and dislocation densities as  $\epsilon$  decreases for loading path DE at  $\varphi_l = 20^\circ$  and  $\varphi_r = 140^\circ$  where  $h = 1 \mu\text{m}$ .

Following the same idea as in section 6.3.3, in order to obtain the proper computation results using negative value of  $\epsilon$ , it is convenient also here to introduce to the effective energy (7.9) the dimensionless quantities

$$\begin{aligned}
 \hat{E} &= \frac{\hat{\Psi}}{aLh\mu|\epsilon|^3}, \quad \eta = \frac{y}{h|\epsilon|}, \quad H = \frac{1}{|\epsilon|}, \quad \epsilon_{cr} = \frac{K}{\mu} \\
 m &= \frac{k}{\epsilon^2}, \quad \bar{\beta}_l(\eta) = \frac{\beta_l(y)}{|\epsilon|}, \quad \bar{\beta}_r(\eta) = \frac{\beta_r(y)}{|\epsilon|}, \quad c = hb\rho_s,
 \end{aligned} \tag{7.82}$$

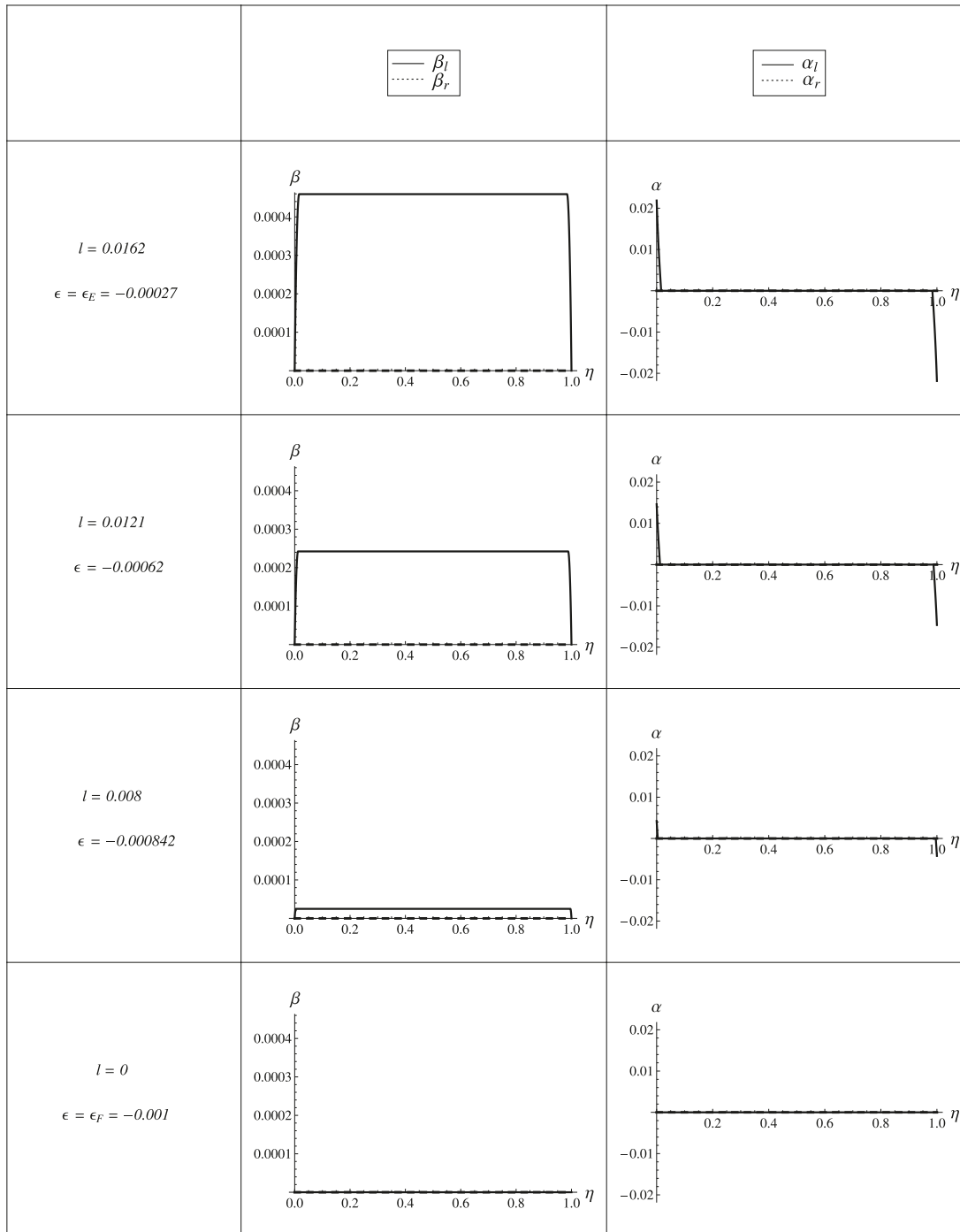


Figure 7.22: Evolution of plastic distortions and dislocation densities as  $\epsilon$  decreases for loading path EF at  $\varphi_l = 20^\circ$  and  $\varphi_r = 140^\circ$  where  $h = 1 \mu\text{m}$ .

with  $\bar{\beta}'_l(\eta)$  and  $\bar{\beta}'_r(\eta)$  similar to (7.75) where  $\eta \in (0, H)$ . During this loading path BC, for increasing  $\epsilon$  we have the following relations

$$\text{sign} \dot{\beta}'_l = \text{sign} \beta_l \quad \text{and} \quad \text{sign} \dot{\beta}'_r = \text{sign} \beta_r, \quad (7.83)$$

where  $\text{sign} \beta_l$  and  $\text{sign} \beta_r$  are known from previous loading path AB. The discretized form of the dimensionless effective energy of the uniaxial extension deforming in general double

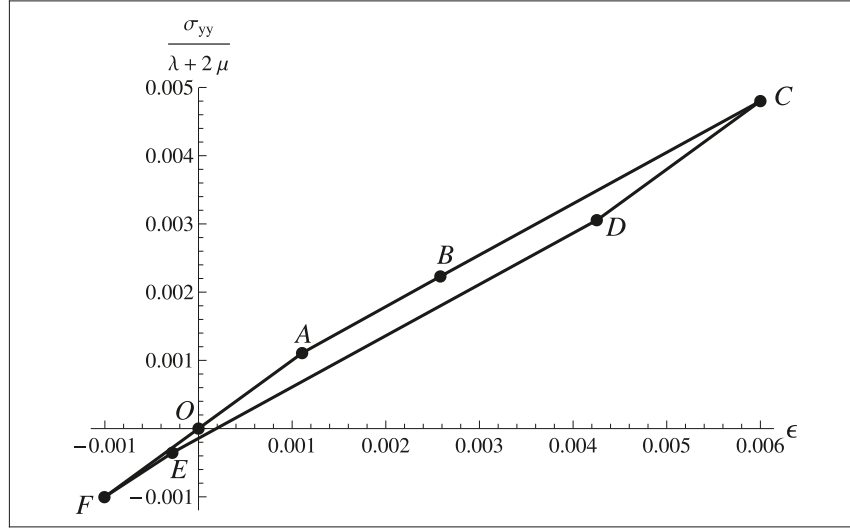


Figure 7.23: Normalized tensile stress versus tensile strain curve of general double slip plane-constrained uniaxial extension at non-zero dissipation of single crystal for  $\varphi_l = 20^\circ$  and  $\varphi_r = 140^\circ$  where  $h = 1 \mu\text{m}$

slip systems for loading case BC reads

$$\hat{E} = \frac{l}{3n}(1-\kappa) \sum_{j=1}^n Q_1 + \frac{2m}{c} \sum_{j=1}^n Q_2 + \frac{mn}{lc^2} \sum_{j=1}^n Q_3 + \frac{l\epsilon_{cr}}{n|\epsilon|} \sum_{j=1}^n Q_4 + Q_5 + Q_6 + Q_7, \quad (7.84)$$

where

$$\begin{aligned} Q_1 &= \sin 2\varphi_l \sin 2\varphi_r \left( c_{j-1}(2d_{j-1} + d_j) + c_j(d_{j-1} + 2d_j) \right) \\ &\quad + \sin^2 2\varphi_l (c_{j-1}^2 + c_{j-1}c_j + c_j^2) + \sin^2 2\varphi_r (d_{j-1}^2 + d_{j-1}d_j + d_j^2), \\ Q_2 &= |\sin 2\varphi_l| |a_i - a_{i-1}| + |\sin 2\varphi_r| |b_i - b_{i-1}| \\ Q_3 &= \sin^2 \varphi_l (c_j - c_{j-1})^2 + \sin^2 \varphi_r (d_j - d_{j-1})^2 \\ &\quad + 2\chi |\sin \varphi_l (c_j - c_{j-1})| |\sin \varphi_r (d_j - d_{j-1})|, \\ Q_4 &= (c_i + c_{i-1}) \text{sign} \beta_l + (d_i + d_{i-1}) \text{sign} \beta_r \\ Q_5 &= \frac{H}{2\kappa} (\text{sign} \epsilon - \kappa (\sin 2\varphi_l \langle \beta_l \rangle + \sin 2\varphi_r \langle \beta_r \rangle))^2 \\ &\quad + \frac{H}{2} (\cos 2\varphi_l \langle \beta_l \rangle + \cos 2\varphi_r \langle \beta_r \rangle)^2, \\ Q_6 &= \frac{1-\kappa}{2} (H - 2l)(c_n \sin 2\varphi_l + d_n \sin 2\varphi_r)^2, \\ Q_7 &= \frac{\epsilon_{cr}}{|\epsilon|} (H - 2l)(c_n \text{sign} \beta_l + d_n \text{sign} \beta_r), \end{aligned} \quad (7.85)$$

with  $\langle \beta_l \rangle$  and  $\langle \beta_r \rangle$  has the similar form as (7.78). The discretized form of dislocation densities  $(\alpha_l)_j$  and  $(\alpha_r)_j$  with  $j$  being the element number adopt the identical form as in (7.79) and (7.80). To plot the normalized tensile stress versus tensile strain for general double slip system case, numerical procedures are employed to the following equation, i.e.

$$\frac{\sigma_{yy}}{\lambda + 2\mu} = \epsilon - \kappa (\langle \beta_l \rangle \sin 2\varphi_l + \langle \beta_r \rangle \sin 2\varphi_r).$$

Again for plotting the results in the same way as in symmetric case, we multiply  $\beta_l$ ,  $\beta_r$ ,  $\alpha_l$ ,  $\alpha_r$ ,  $\eta$  and  $H$  by  $|\epsilon|$ . Fig. 7.20 illustrates the evolution of plastic distortions and dislocation densities throughout loading path BC for  $\varphi_l = 20^\circ$ ,  $\varphi_r = 140^\circ$ .

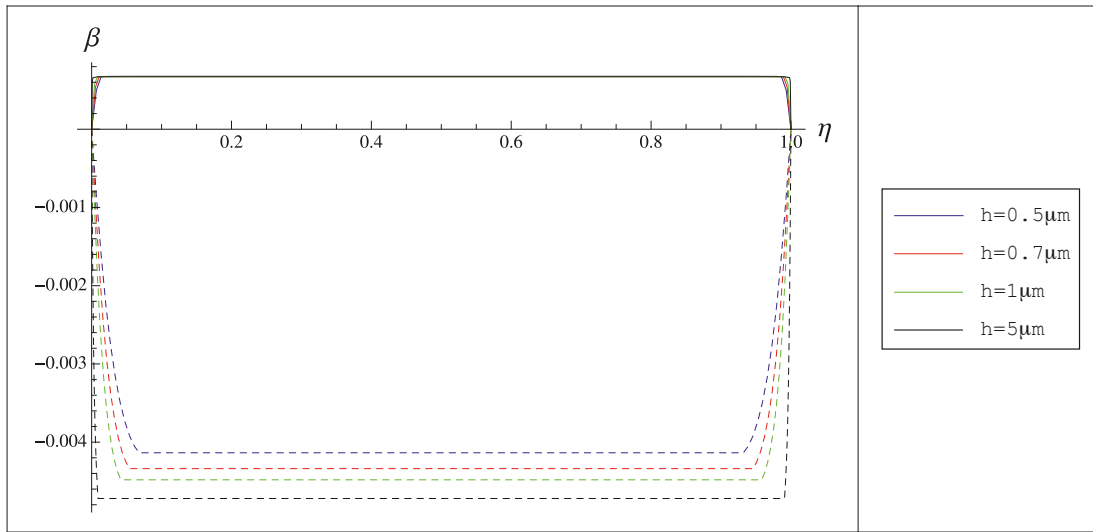


Figure 7.24: Evolution of  $\beta_l$  (continuous lines) and  $\beta_r$  (dashed lines) within the interval  $\eta \in (0, 1)$  during the loading process (increasing  $\gamma$ ) for double slip plane-constrained uniaxial extension with dissipation of single crystal at  $\varphi_l = 20^\circ$ ,  $\varphi_r = 140^\circ$  and  $\epsilon = 0.006$  with different crystal heights  $h$

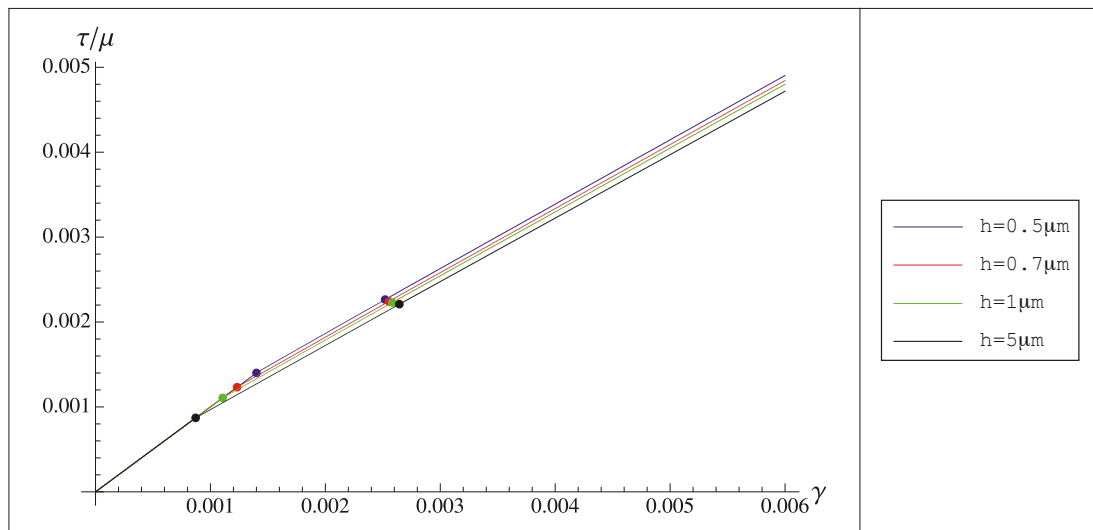


Figure 7.25: Normalized tensile stress versus tensile strain curve of general double slip plane-constrained uniaxial extension at non-zero dissipation of single crystal for  $\varphi_l = 20^\circ$  and  $\varphi_r = 140^\circ$  with different crystal heights  $h$

After reaching point C, we load the crystal in the opposite direction by decreasing  $\epsilon$ . In the course of inverse loading CD, the plastic distortions,  $\beta_l$  and  $\beta_r$ , are frozen ( $\dot{\beta}_l = 0$  and  $\dot{\beta}_r = 0$ ) so that the crystal is subjected again to elastic deformation. When we decrease  $\epsilon$  further up to point E, The crystal undergoes again the plastic deformation and the nucleated

dislocations start to annihilate. As we have two active slip systems throughout inverse loading DE, we need to employ again the finite element procedure as in loading path BC. For inverse loading case we have the relation

$$\text{sign}\dot{\beta}_l = -\text{sign}\beta_l \quad \text{and} \quad \text{sign}\dot{\beta}_r = -\text{sign}\beta_r, \quad (7.86)$$

hence the discretized form of effective energy for inverse loading DE reads

$$\hat{E} = \frac{l}{3n}(1-\kappa) \sum_{j=1}^n Q_1 + \frac{2m}{c} \sum_{j=1}^n Q_2 + \frac{mn}{lc^2} \sum_{j=1}^n Q_3 - \frac{l\epsilon_{cr}}{n|\epsilon|} \sum_{j=1}^n Q_4 + Q_5 + Q_6 - Q_7, \quad (7.87)$$

with  $Q_1$ - $Q_7$  from (7.85). The normalized tensile stress versus strain equation and dislocation densities take the same form as in loading path BC. The evolution of plastic distortions and dislocation densities for loading path DE at  $\varphi_l = 20^\circ$  and  $\varphi_r = 140^\circ$  is shown in Fig. 7.21.

At point E, the nucleated dislocations disappear completely from one slip system so that only one slip system remains active during loading path EF. Adopting the same idea as in loading path AB, for convenient, we denote here

- $(\star)_f$  belongs to the slip system that becomes non active at point E
- $(\star)_e$  is associated with the still active slip system throughout inverse loading EF.

If  $\beta_r$  disappears at point E we apply the condition (7.16) to the solutions and on the other hand if  $\beta_l$  vanishes at point E, (7.17) has to be assigned to the solutions. Therefore we obtain the similar solutions as loading path AB but now replacing  $\epsilon_l$  with

$$\epsilon_u = \epsilon + \frac{\epsilon_{cr} \text{sign}\beta_e}{\sin 2\varphi_e}, \quad (7.88)$$

where

$$\epsilon(l) = \frac{\text{sign}\beta_e}{\sin 2\varphi_e} \left( -\epsilon_{cr} + \frac{2k |\sin \varphi_e| \cosh \zeta l}{c(1-2l) (1 - (\cos^2 2\varphi_e + \kappa \sin^2 2\varphi_e) B_e(l))} \right). \quad (7.89)$$

The detail explanation of the procedure to determine the still active slip system can be seen in section 6.3.3. Fig. 7.21 illustrates the evolution of plastic distortions and dislocation densities for loading path DE at  $\varphi_l = 20^\circ$  and  $\varphi_r = 140^\circ$ .

At point F, all nucleated dislocations are now completely disappear from the crystal so that  $\beta_l = 0$  and  $\beta_r = 0$ . When we increase again  $\epsilon$  from point F to point G ( $\epsilon = 0$ ), the plastic distortions,  $\beta_l$  and  $\beta_r$ , remain zero and the crystal is subjected again to elastic deformation.

The plot of normalized tensile stress versus tensile strain for  $\varphi_l = 20^\circ$  and  $\varphi_r = 140^\circ$  following the closed loading path depicted in Fig. 7.18, which shows the Bauschinger effect, is shown in Fig. 7.23. To observe the size effect we plot the plastic distortions and normalized tensile stress versus tensile strain curves for different crystal heights,  $h$ , as can be seen in Fig. 7.24 and Fig. 7.25, respectively.

### 7.3 Plane-constrained combined loading of shear and uniaxial extension

For the case with combined loading of plane-constrained shear and uniaxial extension with two active slip systems, the same procedures as in uniaxial extension case will be implemented to energy functional (7.3) for the case with zero dissipation and effective energy functional (7.10) for the non-zero dissipation case.

#### 7.3.1 Dislocations nucleation at zero dissipation

For convenient, since one slip system is activated first before the second one, we employ again the condition (7.16) for the case where  $\beta_l$  becomes active first and the condition (7.17) for the case where  $\beta_r$  is activated first. Then we apply the dimensionless quantities (7.13) to energy functional (7.3). For short the bars over  $\bar{\beta}_e$ ,  $\bar{\beta}_f$ ,  $\langle \bar{\beta}_e \rangle$  and  $\langle \bar{\beta}_f \rangle$  are dropped.

When the total prescribed displacement,  $\delta$ , smaller than the first energetic threshold value,  $\delta_{en1}$ , the crystal deforms elastically. The onset of the nucleation of geometrically necessary dislocations is at  $\delta = \delta_{en1}$  where

$$\delta_{en1} = \frac{2k}{c} \frac{|\sin \varphi_e|}{|\cos(\theta - 2\varphi_e)|}, \quad (7.90)$$

with  $c = hb\rho_s$ . From this computation we found out that

$$\text{sign}\beta_e = \text{sign}(\cos(\theta - 2\varphi)), \quad (7.91)$$

so that

$$\text{sign}\beta'_e = \text{sign}(\beta_e), \quad (7.92)$$

for  $\eta \in (0, l)$  and changes into opposite sign for  $\eta \in (1 - l, 1)$ .

For the interval  $\delta_{en1} \leq \delta < \delta_{en2}$  (with  $\delta_{en2}$  being the second energetic threshold value where the second slip system becomes active), the crystal deforms in single slip system with the solutions of  $\beta_e$  and  $\alpha_e$  similar to (7.23) and (7.25), respectively, but now with

$$\beta_p = \frac{\delta \cos(\theta - 2\varphi_e) - (\cos^2 2\varphi_e + \kappa \sin^2 2\varphi_e) \langle \beta \rangle}{(1 - \kappa) \sin^2 2\varphi_e}, \quad \zeta = 2c \sqrt{\frac{1 - \kappa}{k}} |\cos \varphi_e|. \quad (7.93)$$

The average of plastic distortion reads

$$\langle \beta_e \rangle = B_e(l) \delta \cos(\theta - 2\varphi_e), \quad (7.94)$$

where  $B_e(l)$  from (7.27). The total prescribed displacement,  $\delta$ , in term of  $l$  is presented by

$$\delta(l) = \frac{2k |\sin \varphi_e| \text{sign}\beta_e \cosh \zeta l}{c(1 - 2l) \cos(\theta - 2\varphi_e) (1 - (\cos^2 2\varphi_e + \kappa \sin^2 2\varphi_e) B_e(l))}. \quad (7.95)$$

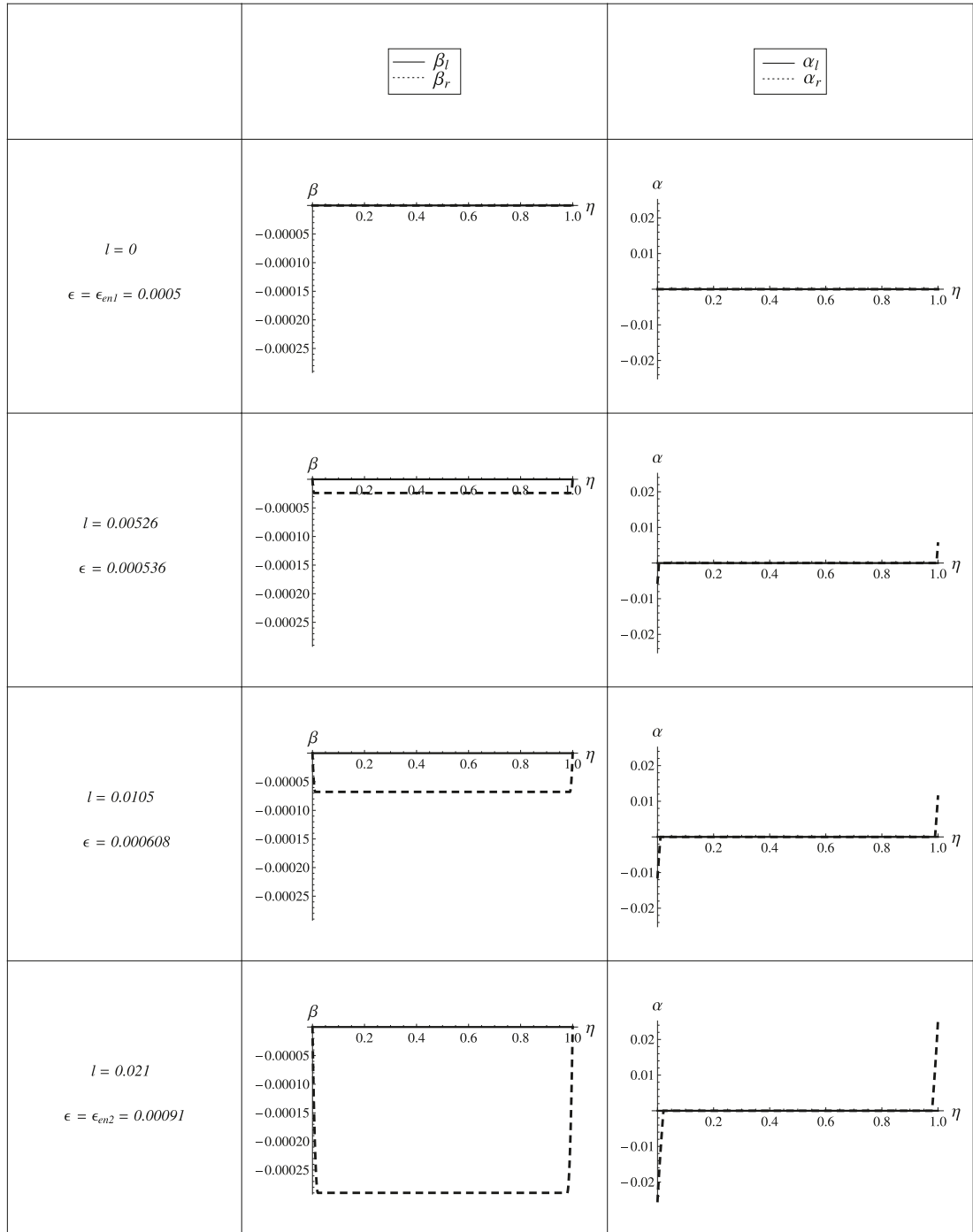


Figure 7.26: Evolution of plastic distortions ( $\beta_l$  and  $\beta_r$ ) and dislocation densities ( $\alpha_l$  and  $\alpha_r$ ) for general double slip combined loading case with zero dissipation at  $\varphi_l = 65^\circ$ ,  $\varphi_r = 120^\circ$  and  $\theta = 20^\circ$  in interval  $\delta_{en1} \leq \delta \leq \delta_{en2}$  where  $h = 1 \mu\text{m}$ .

We first need to solve the followings, that can give us the solution of  $l_{en2}$ , either

$$f(\text{sign}\beta_{fm} = 1, l_{en2}) = 0, \quad (7.96)$$

for  $\beta_f > 0$  or

$$f(\text{sign}\beta_{fm} = -1, l_{en2}) = 0, \quad (7.97)$$

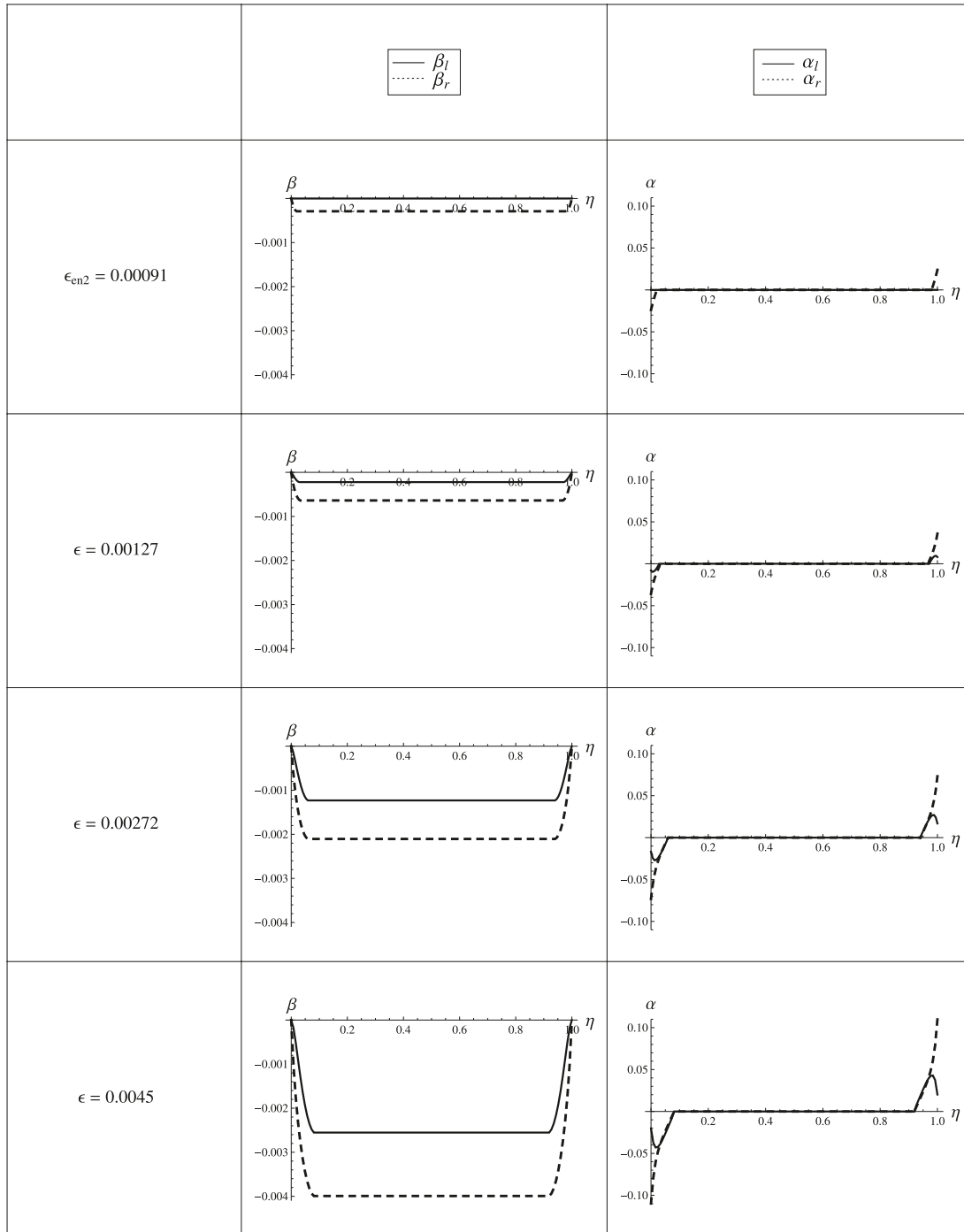


Figure 7.27: Evolution of  $\beta_l$  and  $\beta_r$  together with  $\alpha_l$  and  $\alpha_r$  for general double slip combined loading case with zero dissipation where  $h = 1 \mu\text{m}$ ,  $\varphi_l = 65^\circ$ ,  $\varphi_r = 120^\circ$  at  $\delta \geq \delta_{en2}$

for  $\beta_f < 0$  where

$$\begin{aligned}
 f(\text{sign}\beta_{fm}, l) = & -\frac{2k |\sin \varphi_f| \text{sign}\beta_{fm}}{c} - (1 - 2l)(1 - \kappa) \sin 2\varphi_e \sin 2\varphi_f \beta_{em}(l) \\
 & + \delta(l) \cos(\theta - 2\varphi_f) - (\cos 2\varphi_e \cos 2\varphi_f + \kappa \sin 2\varphi_e \sin 2\varphi_f) \langle \beta_e \rangle (l) \\
 & + \frac{2}{\zeta} (1 - \kappa) \sin 2\varphi_e \sin 2\varphi_f \beta_p(l) (\zeta l - \tanh \zeta l), \quad (7.98)
 \end{aligned}$$

then applying  $l_{en2}$  to (7.95) to obtain the second energetic threshold value,  $\delta_{en2}$ .

For plotting the results numerically, we adopt the same material parameters as before with addition of  $\theta = 20^\circ$ . The evolution of plastic distortions and dislocation densities as  $\delta$  grows for zero dissipation case at  $\varphi_l = 65^\circ$ ,  $\varphi_r = 120^\circ$  and  $\theta = 20^\circ$  in interval  $\delta_{en1} \leq \delta \leq \delta_{en2}$  can be seen in Fig. 7.26.

Analogous to plane-constrained shear and uniaxial extension cases, since the analytical solutions do not seem feasible for  $\delta \geq \delta_{en2}$ , we have to employ again the finite element procedure as before. Again, it is useful to employ the following dimensionless quantities to the energy functional (7.11).

$$\begin{aligned} E &= \frac{\Psi}{aLh\mu\epsilon^3}, \quad \eta = \frac{y}{h\delta}, \quad H = \frac{1}{\delta}, \\ m &= \frac{k}{\delta^2}, \quad \bar{\beta}_l(\eta) = \frac{\beta_l(y)}{\delta}, \quad \bar{\beta}_r(\eta) = \frac{\beta_r(y)}{\delta}, \end{aligned} \quad (7.99)$$

so that

$$\bar{\beta}'_l(\eta) = h\beta_{l,y}(y) \quad \text{and} \quad \bar{\beta}'_r(\eta) = h\beta_{r,y}(y),$$

and  $\eta \in (0, H)$ .

The discretized form of dimensionless energy (7.11) reduces to

$$\begin{aligned} E(c_j, d_j, l) &= \frac{1}{3n}l(1 - \kappa) \sum_{j=1}^n \left[ \sin 2\varphi_l \sin 2\varphi_r \left( c_{j-1}(2d_{j-1} + d_j) + c_j(d_{j-1} + 2d_j) \right) \right. \\ &\quad \left. + \sin^2 2\varphi_l (c_{j-1}^2 + c_{j-1}c_j + c_j^2) + \sin^2 2\varphi_r (d_{j-1}^2 + d_{j-1}d_j + d_j^2) \right] \\ &\quad + \frac{2m}{c} \sum_{j=1}^n \left[ |\sin \varphi_l (c_j - c_{j-1})| + |\sin \varphi_r (d_j - d_{j-1})| \right] \\ &\quad + \frac{mn}{lc^2} \sum_{j=1}^n \left[ \sin^2 \varphi_l (c_j - c_{j-1})^2 + \sin^2 \varphi_r (d_j - d_{j-1})^2 \right. \\ &\quad \left. + 2\chi |\sin \varphi_l (c_j - c_{j-1})| |\sin \varphi_r (d_j - d_{j-1})| \right] \\ &\quad + \frac{1}{2}(1 - \kappa)(H - 2l)(c_n \sin 2\varphi_l + d_n \sin 2\varphi_r)^2 \\ &\quad + \frac{H}{2\kappa} (\kappa (\langle \beta_l \rangle \sin 2\varphi_l + \langle \beta_r \rangle \sin 2\varphi_r) - \delta \cos \theta)^2 \\ &\quad + \frac{H}{2} (\langle \beta_l \rangle \cos 2\varphi_l + \langle \beta_r \rangle \cos 2\varphi_r - \delta \cos \theta)^2, \end{aligned} \quad (7.100)$$

where  $\langle \beta_l \rangle$  and  $\langle \beta_r \rangle$  similar to (7.78).

Minimizing (7.100) with respect to vectors  $(c_i, d_i, l)$  and with additional constraints  $0 \leq l \leq H/2$ , we obtain the numerical solution for  $\beta_l$  and  $\beta_r$ . The discretization of normalized dislocation densities are given in the same form as (7.79) and (7.79). The evolution of plastic distortions and dislocation densities for this case at  $\varphi_l = 65^\circ$ ,  $\varphi_r = 120^\circ$  as we increase  $\delta$  in interval  $\delta \geq \delta_{en2}$  can be seen in Fig. 7.27. Fig. 7.28 shows the evolution of plastic distortions and dislocation densities at  $\varphi_l = 65^\circ$  and  $\varphi_r = 120^\circ$  as  $\theta$  increasing.

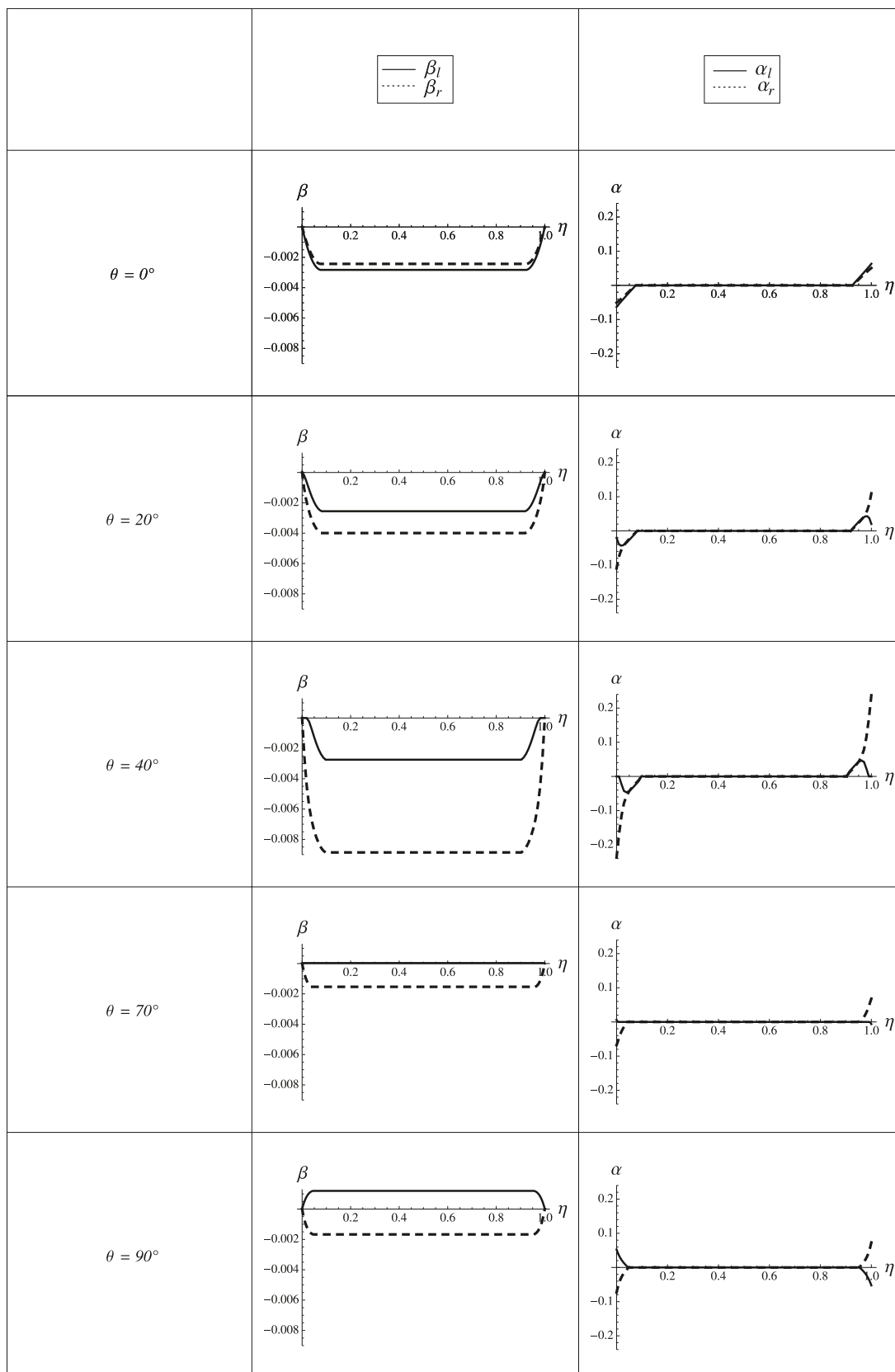


Figure 7.28: Evolution of  $\beta$  and  $\alpha$  for anti-plane zero dissipation case at increasing  $\theta$  where  $\varphi_l = 65^\circ$ ,  $\varphi_r = 120^\circ$  and  $\delta = 0.0045$

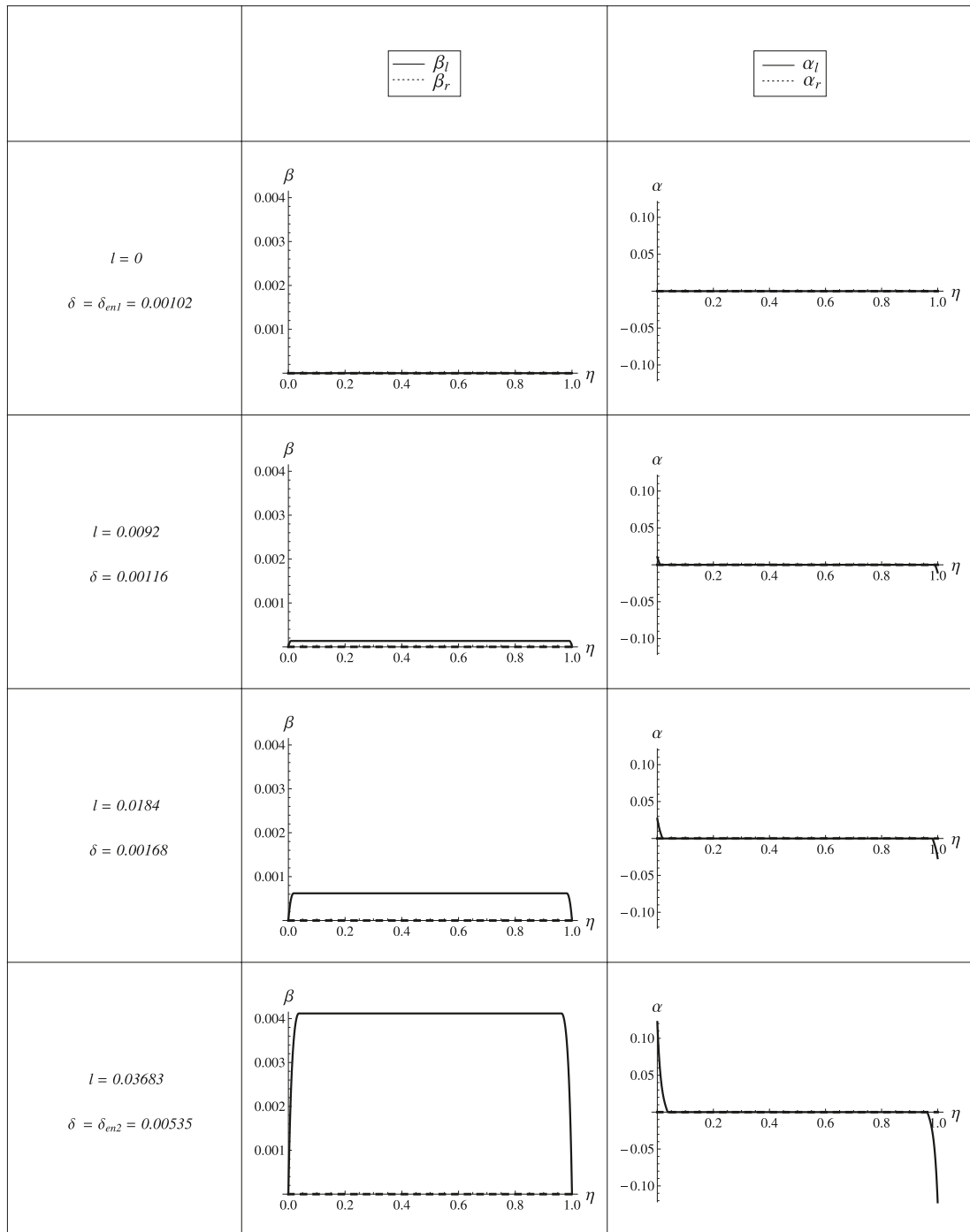


Figure 7.29: Evolution of  $\beta_l$  and  $\beta_r$  together with  $\alpha_l$  and  $\alpha_r$  for general double slip combined loading case with non-zero dissipation where  $h = 1 \mu\text{m}$ ,  $\varphi_l = 20^\circ$ ,  $\varphi_r = 140^\circ$  and  $\theta = 20^\circ$  as  $\delta$  increases at  $\delta_{en1} \leq \delta < \delta_{en2}$

### 7.3.2 Dislocations nucleation at non-zero dissipation

In the case of non-zero dissipation, rather than from minimizing the energy functional, the evolution of  $\beta_l$  and  $\beta_r$  must be obtained from solving the variational equation (6.114) with the dissipation potential from (6.115). In consideration of the assumption that  $\text{sign}\beta_l$  and  $\text{sign}\beta_r$  are constant as  $\delta$  being increased or decreased, the solutions can now be found by solving the minimization of the effective energy (7.10). In the following, we will discuss

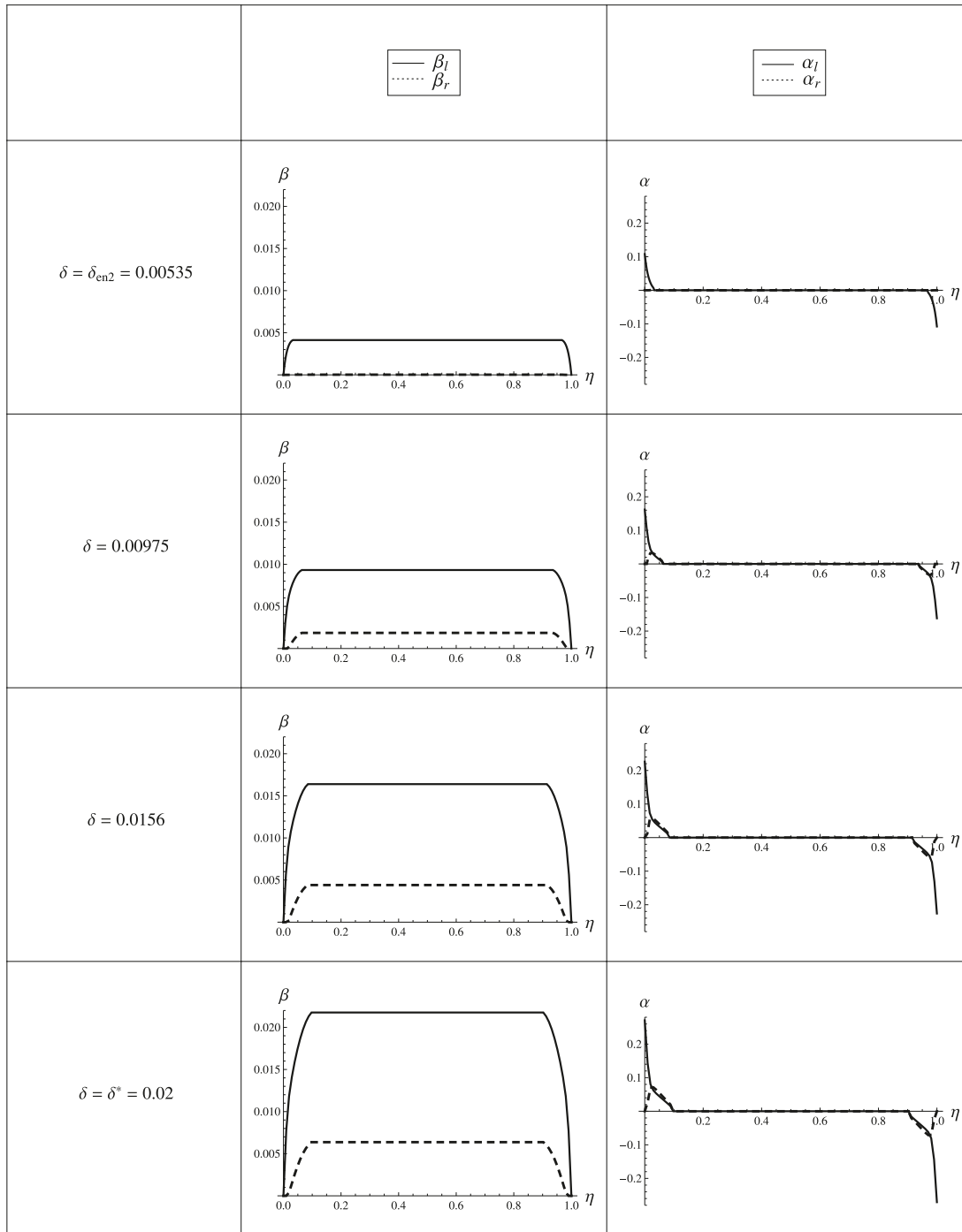


Figure 7.30: Evolution of  $\beta_l$  and  $\beta_r$  together with  $\alpha_l$  and  $\alpha_r$  for general double slip combined loading case with non-zero dissipation where  $h = 1 \mu\text{m}$ ,  $\varphi_l = 20^\circ$ ,  $\varphi_r = 140^\circ$  and  $\theta = 20^\circ$  as  $\delta$  increases at  $\delta \geq \delta_{en2}$

about five possible conditions throughout the loading processes.

The first condition is when  $\dot{\beta}_l = 0$  and  $\dot{\beta}_r = 0$  so that the minimization of the effective energy (7.10) needs not to be fulfilled and simply replaced by  $\beta_l = 0$  and  $\beta_r = 0$ . Which means that the plastic distortions,  $\beta_l$  and  $\beta_r$ , and dislocation densities,  $\alpha_l$  and  $\alpha_r$ , are frozen in the course of loading processes. As a consequence, the crystal is subjected to elastic deformation.

For the second condition, since both slip systems are activated at different time as  $\delta$  increases, the crystal deforms in single slip system at some interval of  $\delta$ . For convenient we first employ the relation (7.16) for the case when  $\beta_l$  appears first and the relation (7.17) for the case where  $\beta_r$  becomes active first then apply the dimensionless quantities (7.13) to effective energy (7.10). We have for this case the relation

$$\text{sign}\dot{\beta}_e = \text{sign}\beta_e. \quad (7.101)$$

The dislocations nucleation starts to appear on the first slip system at

$$\delta_{en1} = \frac{\delta_{cr}}{|\cos(\theta - 2\varphi_e)|} + \frac{2k}{c} \frac{|\sin\varphi_e|}{|\cos(\theta - 2\varphi_e)|}, \quad (7.102)$$

where  $c = hb\rho_s$ . Therefore, we will have the similar form of solutions as in non-zero dissipation case of combined loading but now with

$$\delta_l = \delta(l) - \frac{\delta_{cr}\text{sign}\beta_e}{\cos(\theta - 2\varphi_e)}, \quad (7.103)$$

where

$$\delta(l) = \frac{\text{sign}\beta_e}{\cos(\theta - 2\varphi_e)} \left( \delta_{cr} + \frac{2k |\sin\varphi_e| \cosh \zeta l}{c(1 - 2l) (1 - (\cos^2 2\varphi_e + \kappa \sin^2 2\varphi_e) B_e(l))} \right), \quad (7.104)$$

with  $\text{sign}\beta_e$  from (7.91). We first solve (7.96) for  $\beta_f > 0$  and (7.97) for  $\beta_f < 0$  but now with

$$\begin{aligned} f(\text{sign}\beta_{fm}, l) = & - \frac{2k |\sin\varphi_f| \text{sign}\beta_{fm}}{c} - (1 - 2l)(1 - \kappa) \sin 2\varphi_e \sin 2\varphi_f \beta_{em}(l) \\ & - (\cos 2\varphi_e \cos 2\varphi_f + \kappa \sin 2\varphi_e \sin 2\varphi_f) \delta(l) \cos(\theta - 2\varphi_e) B_e(l) \\ & + \frac{2}{\zeta} (1 - \kappa) \sin 2\varphi_e \sin 2\varphi_f \beta_p(l) (\zeta l - \tanh \zeta l) \\ & + \delta(l) \cos(\theta - 2\varphi_f) - \delta_{cr} \text{sign}\dot{\beta}_f, \end{aligned} \quad (7.105)$$

with  $\text{sign}\dot{\beta}_f = \text{sign}\beta_{fm}$ , then substituting the newly found  $l_{en2}$  to (7.103) in order to find the second energetic threshold value,  $\delta_{en2}$ . Fig. 7.29 illustrates the example of this case with the same material parameter as non-zero dissipation case with  $\delta_{cr} = 0.0008$  at  $\varphi_l = 20^\circ$ ,  $\varphi_r = 140^\circ$  and  $\theta = 20^\circ$ .

For the third condition is when  $\beta_l \neq 0$  and  $\beta_r \neq 0$  as we increase  $\delta$ . Therefore, it is useful to introduce the following dimensionless quantities

$$\begin{aligned} E &= \frac{\Psi}{aLh\mu\epsilon^3}, \quad \eta = \frac{y}{h|\delta|}, \quad H = \frac{1}{|\delta|}, \\ m &= \frac{k}{\delta^2}, \quad \bar{\beta}_l(\eta) = \frac{\beta_l(y)}{|\delta|}, \quad \bar{\beta}_r(\eta) = \frac{\beta_r(y)}{|\delta|}, \end{aligned} \quad (7.106)$$

where  $\eta \in (0, H)$  to effective energy (7.10) before applying the finite element procedure as in non-zero dissipation case. The discretized form of effective energy is presented by

$$\hat{E} = \frac{l}{3n} (1 - \kappa) \sum_{j=1}^n Q_1 + \frac{2m}{c} \sum_{j=1}^n Q_2 + \frac{mn}{lc^2} \sum_{j=1}^n Q_3 + \frac{l\delta_{cr}}{n|\delta|} \sum_{j=1}^n Q_4 + Q_5 + Q_6 + Q_7, \quad (7.107)$$

where

$$\begin{aligned}
Q_1 &= \sin 2\varphi_l \sin 2\varphi_r \left( c_{j-1}(2d_{j-1} + d_j) + c_j(d_{j-1} + 2d_j) \right) \\
&\quad + \sin^2 2\varphi_l (c_{j-1}^2 + c_{j-1}c_j + c_j^2) + \sin^2 2\varphi_r (d_{j-1}^2 + d_{j-1}d_j + d_j^2), \\
Q_2 &= |\sin 2\varphi_l| |a_i - a_{i-1}| + |\sin 2\varphi_r| |b_i - b_{i-1}| \\
Q_3 &= \sin^2 \varphi_l (c_j - c_{j-1})^2 + \sin^2 \varphi_r (d_j - d_{j-1})^2 \\
&\quad + 2\chi |\sin \varphi_l (c_j - c_{j-1})| |\sin \varphi_r (d_j - d_{j-1})|, \\
Q_4 &= (c_i + c_{i-1}) \text{sign} \beta_l + (d_i + d_{i-1}) \text{sign} \beta_r \tag{7.108} \\
Q_5 &= \frac{H}{2\kappa} (\kappa (\sin 2\varphi_l \langle \beta_l \rangle + \sin 2\varphi_r \langle \beta_r \rangle) - (\text{sign} \delta) \sin \theta)^2 \\
&\quad + \frac{H}{2} (\cos 2\varphi_l \langle \beta_l \rangle + \cos 2\varphi_r \langle \beta_r \rangle - (\text{sign} \delta) \cos \theta)^2, \\
Q_6 &= \frac{1 - \kappa}{2} (H - 2l) (c_n \sin 2\varphi_l + d_n \sin 2\varphi_r)^2, \\
Q_7 &= \frac{\delta_{cr}}{|\delta|} (H - 2l) (c_n \text{sign} \beta_l + d_n \text{sign} \beta_r),
\end{aligned}$$

with  $\langle \beta_l \rangle$  and  $\langle \beta_r \rangle$  analogous to (7.78). We find the solutions  $\beta_l$  and  $\beta_r$  by minimizing (7.107) with respect to  $c_i$ ,  $d_i$  and  $l$  under the additional constraints  $0 \leq l \leq H/2$ . The discretized dislocation densities for this case take the same form as in (7.79) and (7.79). The example of this case with the same material parameter and combination of angles as in previous example is shown in Fig. 7.30. The evolution of plastic distortions and dislocation densities as  $\theta$  increases for the same example can be seen in Fig. 7.31.

The fourth condition is the opposite of the previous condition where now we have  $\beta_l \neq 0$  and  $\beta_r \neq 0$  as we decrease  $\delta$ . Following the same procedure as before, the discretized form of the effective energy for this condition yields

$$\hat{E} = \frac{l}{3n} (1 - \kappa) \sum_{j=1}^n Q_1 + \frac{2m}{c} \sum_{j=1}^n Q_2 + \frac{mn}{lc^2} \sum_{j=1}^n Q_3 - \frac{l\delta_{cr}}{n|\delta|} \sum_{j=1}^n Q_4 + Q_5 + Q_6 - Q_7, \tag{7.109}$$

where  $Q_1$ - $Q_7$  from (7.108),  $\langle \beta_l \rangle$  and  $\langle \beta_r \rangle$  from (7.78). We obtain the solutions of  $\beta_l$  and  $\beta_r$  using the same procedure as the previous condition and the dislocation densities is similar to (7.79) and (7.79). Fig. 7.32 illustrates the example of this case with the same material parameters as previous examples.

The fifth condition is the opposite of the second condition where we have now either only  $\beta_l \neq 0$  and  $\beta_r = 0$  or  $\beta_l = 0$  and  $\beta_r \neq 0$  as we decrease  $\delta$ . Therefore, for this condition, we apply again the relation (7.16) if  $\beta_r = 0$  and (7.17) if  $\beta_l = 0$  throughout this inverse loading path. As a consequence, we have the similar form of solutions as in the second condition but now replacing  $\delta_l$  with

$$\delta_u = \delta(l) + \frac{\delta_{cr} \text{sign} \beta_e}{\cos(\theta - 2\varphi_e)}, \tag{7.110}$$

where

$$\delta(l) = \frac{\text{sign} \beta_e}{\cos(\theta - 2\varphi_e)} \left( -\delta_{cr} + \frac{2k |\sin \varphi_e| \cosh \zeta l}{c(1 - 2l) (1 - (\cos^2 2\varphi_e + \kappa \sin^2 2\varphi_e) B_e(l))} \right). \tag{7.111}$$

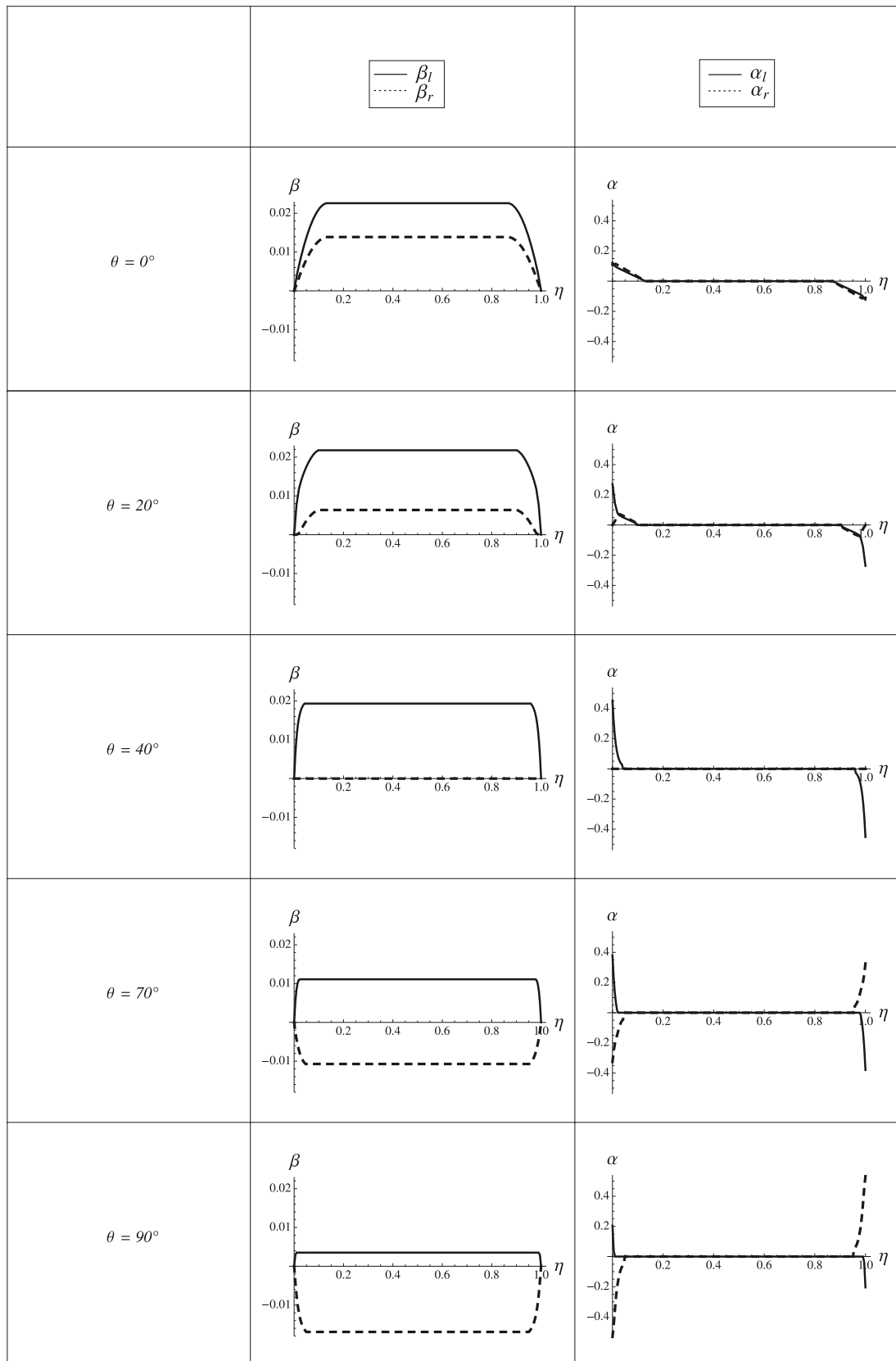


Figure 7.31: Evolution of  $\beta$  and  $\alpha$  for anti-plane non-zero dissipation case at increasing  $\theta$  where  $\varphi_l = 20^\circ$ ,  $\varphi_r = 140^\circ$  and  $\delta = 0.02$

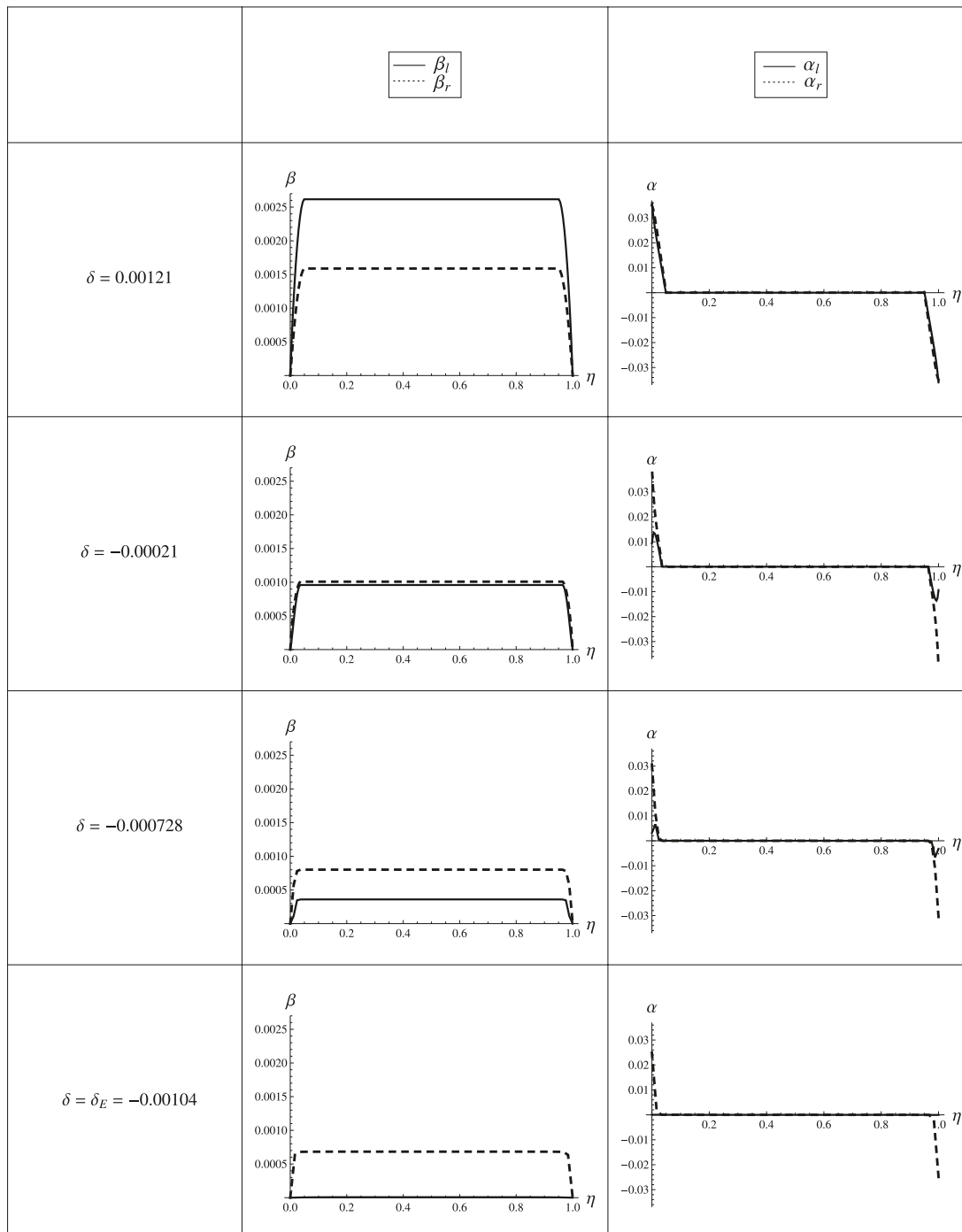


Figure 7.32: Evolution of  $\beta_l$  and  $\beta_r$  together with  $\alpha_l$  and  $\alpha_r$  for general double slip combined loading case with non-zero dissipation where  $h = 1 \mu\text{m}$ ,  $\varphi_l = 20^\circ$ ,  $\varphi_r = 140^\circ$  and  $\theta = 20^\circ$  as  $\delta$  decreases

## 8 Conclusion

It has been concluded in this thesis that the continuum dislocation theory can determine the plastic deformation of a strip made of single crystal undergoing several types of deformation such as: plane-strain constrained shear deformation or plane-strain uniaxial extension deformation or mixed deformation of shear and extension.

For each example of the application of one of these previous mentioned three deformation types to a single crystal strip with one active slip system, the solutions are obtained in a closed analytical form. If there is no resistance to the dislocation motion (no dissipation of energy), dislocations appear to minimize the energy of the deformed crystal. Due to the specific form of energy of the dislocation network which is proportional to the dislocation density for small densities, we show that there is an energetic threshold stress for the dislocation nucleation that depends on the slip direction. Due to the assumption of hard device (impenetrable grain boundary), the applied shear stress will cause the motion of dislocations towards the clamped boundaries resulting in dislocation pile-up leaving a dislocation-free zone in the center. It then leads to the material hardening. The work hardening caused by the dislocation pile-up and the energetic threshold stress are inversely proportional to the size of the crystal times the saturated dislocation density. This phenomena clearly explains the size effect. Since there exist no energy dissipation occurs, hence no residual strain, the stress-strain curve is completely reversible. If the resistance to dislocation motion (hence energy dissipation) is taken into account, the energy minimization is replaced by the minimization of the effective energy. Thus, there exist also the energetic threshold value for this case. Due to the dissipation of energy, the stress-strain curve becomes a hysteresis loop (Bauschinger effect). The energetic threshold stress and the kinematic hardening observed in Bauschinger effect are also inversely proportional to the size of the crystal which demonstrate the size effect. Therefore, it can be said that the smaller material is stronger and tougher than the bigger one.

For the case with symmetric double slip ( $\varphi_r = \pi - \varphi_l$ ) which undergoes plane-strain constrained shear deformation, we found out that the plastic distortions for both slip systems has the same value and sign. As a consequence, for this kind of problem, a closed analytical solution can be obtained not only for the case where the resistance to dislocation motion being negligible but also for the case where this resistant being considered. The closed analytical solution is also true for the case of plane-strain uniaxial extension problem with symmetric double slip since the plastic distortions for both slip systems have the opposite sign but equal in value. The analytical solution is not feasible for the case of symmetric double slip which is subjected to the mixed deformation of shear and extension. The analytical solutions for symmetric double slip mentioned above exhibit similar characteristics as for the single crystal.

For non-symmetric double slip case being subjected to any of three loading types mentioned above, we have the combination of analytical and numerical solutions. In double slip systems case, there exist the interaction among both of the slip systems. The shifting of dis-

locations on one slip system impede the dislocations motion on the other one near the grain boundary. Consequently, both slip systems are not activated at the same time. Therefore we have here two energetic threshold values, i.e. one for each slip system. Since only one slip system is active in the beginning the problem can be solved analytically as in single slip case. Above the second threshold value, hence the second slip system becomes active, the solutions have to be sought numerically. The numerical solutions are obtained by the finite element procedures. These numerical results can also describe the work hardening and the size effect.

The comparison of the results of the examples of plane constrained shear of single crystal slip deforming in single slip and symmetric double slip with the results of discrete dislocation simulations reported by Needleman and Van der Giessen [2001] and Shu et al. [2001] show good agreement between continuum and discrete approach.

## List of Figures

2.1	Tensile test. . . . .	5
2.2	Stress-strain diagram for a typical structural steel undergoing uniaxial extension test (not in scale). . . . .	6
2.3	The crystal structures of common metals: (a) face-centered cubic, (b) body-centered cubic, (c) hexagonal close-packed. . . . .	7
2.4	Macroscopic slip in a single crystal. . . . .	8
2.5	Slip in a zinc single crystal [Elam, 1935] (from Callister [2007]). . . . .	9
2.6	Geometry of slip in crystalline material. . . . .	10
2.7	Slip between two rows of atoms. . . . .	10
2.8	(a) Simple lattice cubic structure; (b) Positive edge dislocation DC formed by inserting an extra half-plane of atoms ABCD. . . . .	12
2.9	Left handed screw dislocation. . . . .	13
2.10	Dislocation motion mechanism of an edge dislocation in response to an applied shear stress. . . . .	14
2.11	(a) Burgers circuit around edge dislocation with positive sign of dislocation line into the paper; (b) the same circuit in a perfect crystal. . . . .	14
2.12	(a) Burgers circuit around screw dislocation; (b) the same circuit in a perfect crystal. . . . .	14
2.13	Mixed type of dislocation. . . . .	15
2.14	Decomposition of Burgers vector of mixed dislocation. . . . .	15
2.15	Dislocation loop. . . . .	16
2.16	Screw dislocation: (a) in a crystal; (b) in an elasticity model. . . . .	17
2.17	Edge dislocation: (a) in a crystal; (b) in an elasticity model. . . . .	17
2.18	Line tension of a dislocation. . . . .	19
2.19	Interaction of two edge dislocations lying on the same slip plane: (a) of the same sign; (b) of the opposite sign. . . . .	20
2.20	Interaction of two parallel: (a) edge dislocations; (b) screw dislocations. . . . .	21
2.21	Reaction of two dislocations to form a third. . . . .	22
2.22	Schematic representation of dislocation network in a well annealed crystal (From [Cottrell, 1957]). . . . .	22
2.23	Schematic representation of Frank-Read loop formation. . . . .	24
2.24	Dislocation pile-up against a grain boundary. . . . .	25
2.25	Additive decomposition of the total strain. . . . .	26
2.26	Examples of homogeneously elastic distorted states of Fig. 2.25(a): (a) $\varepsilon_{12}^e = \varepsilon_{21}^e$ ; (b) $\omega_{12}^e = -\omega_{21}^e$ ; (c) $\beta_{21}^e$ , (d) $\beta_{12}^e$ . . . . .	27
2.27	Examples of homogeneously plastic distorted states of Fig. 2.25(a): (a) $\varepsilon_{12}^p = \varepsilon_{21}^p$ ; (b) $\omega_{12}^p = -\omega_{21}^p$ ; (c) $\beta_{21}^p$ , (d) $\beta_{12}^p$ . . . . .	28
2.28	Dislocation flow leads to plastic rotation. . . . .	28
2.29	Energy density of dislocation network. . . . .	33
3.1	Anti-plane constrained shear . . . . .	39
3.2	Evolution of $\beta$ and $\alpha$ for zero dissipation anti-plane constrained shear of single crystal with $a = 1\mu\text{m}$ where $\eta = x/a$ for increasing $\gamma$ . . . . .	45

3.3	Normalized average shear stress versus shear strain curve for anti-plane constrained shear of single crystal at zero dissipation at $a = 1 \mu\text{m}$ . . . . .	47
3.4	Normalized shear stress versus shear strain curves for zero dissipation anti-plane constrained shear of single crystal with different crystal widths $a$ . . . . .	47
3.5	Plot of (a): $\beta$ within the interval $(0, 1)$ and (b): $\alpha$ within the interval $(0, 0.1)$ for zero dissipation anti-plane constrained shear of single crystal at $\gamma = 0.0025$ with different crystal widths $a$ . . . . .	48
3.6	A closed loading path for anti-plane constrained shear with non-zero dissipation problem . . . . .	49
3.7	Evolution of $\beta$ and $\alpha$ during loading process AB for anti-plane constrained shear of single crystal with dissipation where $a = 1 \mu\text{m}$ . . . . .	51
3.8	Evolution of $\beta$ and $\alpha$ during inverse loading DE for anti-plane constrained shear of single crystal with dissipation where $a = 1 \mu\text{m}$ . . . . .	52
3.9	Normalized shear stress versus shear strain curve of anti-plane constrained shear at non-zero dissipation of single crystal for $a = 1 \mu\text{m}$ . . . . .	53
3.10	Plot of (a): $\beta$ and (b): $\alpha$ within the interval $(0, 1)$ for non-zero dissipation anti-plane constrained shear of single crystal at $\gamma = 0.00625$ with different crystal widths $a$ . . . . .	53
3.11	Normalized shear stress versus shear strain curves for non-zero dissipation anti-plane constrained shear of single crystal with different crystal widths, $a$ , throughout the loading process OAB . . . . .	54
4.1	Plane-strain constrained shear of single crystal deforming in single-slip . . . . .	55
4.2	The form of minimizing sequence for finding the threshold value . . . . .	60
4.3	Evolution of $\beta$ and $\alpha$ for zero dissipation single-slip constrained shear of single crystal with $h = 1 \mu\text{m}$ and $\varphi = 30^\circ$ where $\eta = y/h$ for increasing $\gamma$ . . . . .	66
4.4	Evolution of $\beta$ and $\alpha$ for zero dissipation single-slip constrained shear of single crystal with $h = 1 \mu\text{m}$ and $\varphi = 60^\circ$ where $\eta = y/h$ for increasing $\gamma$ . . . . .	67
4.5	Normalized average shear stress versus shear strain curves for single-slip constrained shear of single crystal at zero dissipation with $h = 1 \mu\text{m}$ . . . . .	68
4.6	Plot of (a): $\beta$ within the interval $(0, 1)$ and (b): $\alpha$ within the interval $(0, 0.2)$ for zero dissipation single-slip constrained shear of single crystal at $\varphi = 30^\circ$ and $\gamma = 0.002$ with different crystal heights $h$ . . . . .	68
4.7	Normalized shear stress versus shear strain curves for zero dissipation single-slip constrained shear of single crystal at $\varphi = 30^\circ$ with different crystal heights $h$ . . . . .	69
4.8	A closed loading path for single slip plane-constrained shear problem . . . . .	70
4.9	Evolution of $\beta$ and $\alpha$ during loading process AB for single-slip constrained shear of single crystal with dissipation where $h = 1 \mu\text{m}$ and $\varphi = 30^\circ$ . . . . .	73
4.10	Evolution of $\beta$ and $\alpha$ during loading process AB for single-slip constrained shear of single crystal with dissipation where $h = 1 \mu\text{m}$ and $\varphi = 60^\circ$ . . . . .	74
4.11	Evolution of $\beta$ and $\alpha$ during inverse loading CD for single-slip constrained shear of single crystal with dissipation where $h = 1 \mu\text{m}$ and $\varphi = 30^\circ$ . . . . .	75
4.12	Evolution of $\beta$ and $\alpha$ during inverse loading CD for single-slip constrained shear of single crystal with dissipation where $h = 1 \mu\text{m}$ and $\varphi = 60^\circ$ . . . . .	76
4.13	Normalized shear stress versus shear strain curves of single-slip constrained shear at non-zero dissipation of single crystal by solving the effective energy minimization (4.72), for $\varphi = 30^\circ$ and $\varphi = 60^\circ$ . . . . .	77

4.14	Plot of (a): $\beta$ within the interval $(0, 1)$ and (b): $\alpha$ within the interval $(0, 0.2)$ for non-zero dissipation single-slip constrained shear of single crystal at $\varphi = 30^\circ$ and $\gamma = 0.005$ with different crystal heights $h$ . . . . .	78
4.15	Normalized shear stress versus shear strain curves for non-zero dissipation single-slip constrained shear of single crystal at $\varphi = 30^\circ$ with different crystal heights $h$ throughout the loading process OAB . . . . .	79
4.16	Comparison of the total shear strain profiles obtained from energy minimization, effective energy minimization and from the discrete dislocation simulations reported in [Needleman and Van der Giessen, 2001, Shu et al., 2001] . . . . .	80
4.17	Comparison stress strain behavior of results obtained from this approach and from the discrete dislocation simulations presented in [Needleman and Van der Giessen, 2001, Shu et al., 2001] . . . . .	80
5.1	Combined deformation of uniaxial extension $\epsilon$ and simple shear $\gamma$ of a single crystal with one active slip system . . . . .	83
5.2	Plane-strain constrained uniaxial extension of single crystal strip with one active slip system . . . . .	84
5.3	Evolution of $\beta$ and $\alpha$ for zero dissipation single-slip uniaxial extension of single crystal with $h = 1\mu\text{m}$ and $\varphi = 60^\circ$ where $\eta = y/h$ . . . . .	87
5.4	Evolution of $\beta$ and $\alpha$ for zero dissipation single-slip uniaxial extension of single crystal with $h = 1\mu\text{m}$ and $\varphi = 150^\circ$ where $\eta = y/h$ . . . . .	88
5.5	Normalized tensile stress versus strain curve for zero dissipation single-slip uni-axial extension of single crystal at $\varphi = 60^\circ$ and $\varphi = 150^\circ$ . . . . .	89
5.6	Normalized tensile stress versus strain curve for zero dissipation single-slip uni-axial extension of single crystal at $\varphi = 60^\circ$ with different crystal heights $h$ . . . . .	89
5.7	Plot of (a): $\beta$ within the interval $(0, 1)$ and (b): $\alpha$ within the interval $(0, 0.2)$ for zero dissipation single-slip uniaxial extension of single crystal at $\varphi = 60^\circ$ and $\gamma = 0.01$ with different crystal heights $h$ . . . . .	90
5.8	Plot $\text{sign}\beta$ at the range $0^\circ \leq \varphi \leq 180^\circ$ and $0^\circ \leq \theta \leq 90^\circ$ . . . . .	92
5.9	Evolution of $\beta$ and $\alpha$ for single slip combine loading of single crystal at zero dissipation where $h = 1\mu\text{m}$ , $\varphi = 60^\circ$ and $\theta = 20^\circ$ at increasing $\delta$ . . . . .	93
5.10	Evolution of $\beta$ and $\alpha$ for single slip minimization case at increasing $\theta$ where $\varphi = 60^\circ$ and $\delta = 0.01$ . . . . .	94
5.11	A closed loading path for plane constrained uniaxial extension of a single crystal strip with one active slip system . . . . .	95
5.12	Evolution of $\beta$ and $\alpha$ for zero dissipation single-slip uniaxial extension of single crystal with $h = 1\mu\text{m}$ and $\varphi = 60^\circ$ where $\eta = y/h$ throughout loading path AB . . . . .	96
5.13	Evolution of $\beta$ and $\alpha$ for zero dissipation single-slip uniaxial extension of single crystal with $h = 1\mu\text{m}$ and $\varphi = 150^\circ$ where $\eta = y/h$ throughout loading path AB . . . . .	97
5.14	Evolution of $\beta$ and $\alpha$ for zero dissipation single-slip uniaxial extension of single crystal with $h = 1\mu\text{m}$ and $\varphi = 60^\circ$ where $\eta = y/h$ throughout inverse loading path CD . . . . .	98
5.15	Evolution of $\beta$ and $\alpha$ for zero dissipation single-slip uniaxial extension of single crystal with $h = 1\mu\text{m}$ and $\varphi = 150^\circ$ where $\eta = y/h$ throughout inverse loading path CD . . . . .	99

5.16	Normalized uniaxial tension stress versus strain curves of single-slip constrained shear at non-zero dissipation of single crystal, for $\varphi = 60^\circ$ and $\varphi = 150^\circ$ . . . . .	100
5.17	Plot of (a): $\beta$ within the interval $(0, 1)$ and (b): $\alpha$ within the interval $(0, 0.2)$ for non-zero dissipation single-slip uniaxial extension of single crystal at $\varphi = 60^\circ$ and $\gamma = 0.01$ with different crystal heights $h$ . . . . .	101
5.18	Normalized shear stress versus shear strain curve for zero dissipation single-slip uniaxial extension of single crystal at $\varphi = 60^\circ$ and $\gamma = 0.01$ with different crystal heights $h$ . . . . .	102
5.19	Evolution of $\beta$ and $\alpha$ for single slip combine loading of single crystal at non-zero dissipation in the course of increasing $\delta$ where $h = 1\mu\text{m}$ , $\varphi = 30^\circ$ and $\theta = 20^\circ$ at increasing $\delta$ . . . . .	104
5.20	Evolution of $\beta$ and $\alpha$ of single crystal with one active slip system at non-zero dissipation in the course of loading at $\delta = 0.01$ for increasing $\theta$ . . . . .	105
6.1	Plane-strain constrained shear of single crystal deforming in double-slip . . . . .	107
6.2	Evolution of $\beta$ and $\alpha$ for symmetric double-slip constrained shear of single crystal at zero dissipation where $h = 1\mu\text{m}$ and $\varphi = 30^\circ$ where $\eta = y/h$ . . . . .	120
6.3	Evolution of $\beta$ and $\alpha$ for symmetric double-slip constrained shear of single crystal at zero dissipation where $h = 1\mu\text{m}$ and $\varphi = 60^\circ$ where $\eta = y/h$ . . . . .	121
6.4	Normalized shear stress versus shear strain curve for symmetric double-slip constrained shear of single crystal at zero dissipation with $h = 1\mu\text{m}$ when $l$ is increased from 0 to 0.1 . . . . .	122
6.5	Evolution of $\beta$ within the interval $\eta \in (0, 1)$ and $\alpha$ within the interval $\eta \in (0, 0.2)$ for zero dissipation symmetric double-slip constrained shear of single crystal at $\varphi = 30^\circ$ and $\gamma = 0.01$ with different crystal heights $h$ . . . . .	123
6.6	Normalized shear stress versus shear strain curves for zero dissipation symmetric double-slip constrained shear of single crystal at $\varphi = 30^\circ$ with different crystal heights $h$ . . . . .	124
6.7	Evolution of plastic distortions ( $\beta_l$ and $\beta_r$ ) and dislocation densities ( $\alpha_l$ and $\alpha_r$ ) at $\varphi_l = 35^\circ$ and $\varphi_r = 165^\circ$ for $\gamma_{en1} \leq \gamma \leq \gamma_{en2}$ where $h = 1\mu\text{m}$ . . . . .	125
6.8	Sketch illustrating the finite element model used to compute the numerical solution by energy minimization . . . . .	128
6.9	Physical coordinate $\eta$ and natural coordinate $\xi$ . . . . .	128
6.10	Evolution of $\beta_l$ and $\beta_r$ together with $\alpha_l$ and $\alpha_r$ for general case double-slip constrained shear of single crystal at zero dissipation where $h = 1\mu\text{m}$ , $\varphi_l = 35^\circ$ and $\varphi_r = 165^\circ$ at $\gamma \geq \gamma_{en2}$ . . . . .	131
6.11	Normalized shear stress versus shear strain curve for general case double-slip constrained shear of single crystal at zero dissipation at $\varphi_l = 35^\circ$ and $\varphi_r = 165^\circ$ with $h = 1\mu\text{m}$ . . . . .	132
6.12	Evolution of $\beta_l$ (continuous lines) and $\beta_r$ (dashed lines) within the interval $\eta \in (0, 1)$ for zero dissipation double-slip constrained shear of single crystal at $\varphi_l = 35^\circ$ , $\varphi_r = 165^\circ$ and $\gamma = 0.01$ with different crystal heights $h$ . . . . .	132
6.13	Normalized shear stress versus shear strain curves for zero dissipation double-slip constrained shear of single crystal at $\varphi_l = 35^\circ$ and $\varphi_r = 165^\circ$ with different crystal heights $h$ . . . . .	133
6.14	A closed loading path for plane-constrained shear problem with two active slip systems . . . . .	135
6.15	A closed loading path for plane-constrained shear problem with symmetric double slip systems . . . . .	138

6.16	Evolution of $\beta$ and $\alpha$ for the case of symmetric double slip systems with dissipation during the loading process as $\gamma$ increases at $\varphi = 30^\circ$ where $h = 1 \mu\text{m}$ . . . . .	140
6.17	Evolution of $\beta$ and $\alpha$ for the case of symmetric double slip systems with dissipation in the course of inverse loading process at $\varphi = 30^\circ$ where $h = 1 \mu\text{m}$ . . . . .	141
6.18	Normalized shear stress versus shear strain curve of single-slip constrained shear at non-zero dissipation of single crystal for $\varphi = 30^\circ$ and $h = 1 \mu\text{m}$ . . . . .	142
6.19	Plot of $\beta$ within the interval $\eta \in (0, 1)$ and $\alpha$ within the interval $\eta \in (0, 0.2)$ at $\varphi = 30^\circ$ and $\gamma = 0.012$ with different crystal heights $h$ for the symmetric double slip system case with non-zero dissipation . . . . .	142
6.20	Normalized shear stress versus shear strain curve at $\varphi = 30^\circ$ with different crystal heights $h$ during the loading for symmetric double slip systems case with dissipation . . . . .	143
6.21	Normalized shear stress versus shear strain curve for loading path OA at $\varphi_l = 35^\circ$ and $\varphi_r = 155^\circ$ where $h = 1 \mu\text{m}$ . . . . .	144
6.22	Evolution of plastic distortions and dislocation densities for loading path AB as $\gamma$ increased at $\varphi_l = 35^\circ$ and $\varphi_r = 155^\circ$ where $h = 1 \mu\text{m}$ . . . . .	145
6.23	Normalized shear stress versus shear strain curve for loading path AB at $\varphi_l = 35^\circ$ and $\varphi_r = 155^\circ$ where $h = 1 \mu\text{m}$ . . . . .	146
6.24	Evolution of plastic distortions and dislocation densities as $\gamma$ grows for loading path BC at $\varphi_l = 35^\circ$ and $\varphi_r = 155^\circ$ where $h = 1 \mu\text{m}$ . . . . .	149
6.25	Normalized shear stress versus shear strain curve for loading path BC at $\varphi_l = 35^\circ$ and $\varphi_r = 155^\circ$ where $h = 1 \mu\text{m}$ . . . . .	150
6.26	Normalized shear stress versus shear strain curve for loading path CD at $\varphi_l = 35^\circ$ and $\varphi_r = 155^\circ$ where $h = 1 \mu\text{m}$ . . . . .	150
6.27	Normalized shear stress versus shear strain curve for loading path DE at $\varphi_l = 35^\circ$ and $\varphi_r = 155^\circ$ where $h = 1 \mu\text{m}$ . . . . .	150
6.28	Evolution of plastic distortions and dislocation densities as $\gamma$ decreases for loading path DE at $\varphi_l = 35^\circ$ and $\varphi_r = 155^\circ$ where $h = 1 \mu\text{m}$ . . . . .	151
6.29	Evolution of plastic distortions and dislocation densities as $\gamma$ decreases for loading path EF at $\varphi_l = 35^\circ$ and $\varphi_r = 155^\circ$ where $h = 1 \mu\text{m}$ . . . . .	152
6.30	Normalized shear stress versus shear strain curve for loading path EF at $\varphi_l = 35^\circ$ and $\varphi_l = 150^\circ$ where $h = 1 \mu\text{m}$ . . . . .	153
6.31	Normalized shear stress versus shear strain curve for loading path FG at $\varphi_l = 35^\circ$ and $\varphi_l = 150^\circ$ where $h = 1 \mu\text{m}$ . . . . .	153
6.32	Normalized shear stress versus shear strain curve of general double slip constrained shear at non-zero dissipation of single crystal for $\varphi_l = 35^\circ$ and $\varphi_r = 155^\circ$ where $h = 1 \mu\text{m}$ . . . . .	153
6.33	Evolution of $\beta_l$ (continuous lines) and $\beta_r$ (dashed lines) within the interval $\eta \in (0, 1)$ during the loading process (increasing $\gamma$ ) for double-slip constrained shear with dissipation of single crystal at $\varphi_l = 35^\circ$ , $\varphi_r = 155^\circ$ and $\gamma = 0.015$ with different crystal heights $h$ . . . . .	154
6.34	Normalized shear stress versus shear strain curves for zero dissipation symmetric double-slip constrained shear of single crystal at $\varphi_l = 35^\circ$ and $\varphi_r = 155^\circ$ with different crystal heights $h$ . . . . .	154
6.35	Comparison of the total shear strain profiles obtained from zero and non-zero dissipation symmetric double slip systems cases and from the discrete dislocation simulations reported in [Needleman and Van der Giessen, 2001, Shu et al., 2001] . . . . .	156

6.36	Comparison stress strain behavior of results obtained from this approach and from the discrete dislocation simulations presented in [Needleman and Van der Giessen, 2001, Shu et al., 2001] . . . . .	157
7.1	Combined deformation of uniaxial extension $\epsilon$ and simple shear $\gamma$ of a single crystal with two active slip systems . . . . .	159
7.2	Plane-constrained uniaxial extension of single crystal strip with two active slip systems . . . . .	160
7.3	Evolution of $\beta$ and $\alpha$ for zero dissipation symmetric double-slip uniaxial extension of single crystal with $h = 1 \mu\text{m}$ and $\varphi = 60^\circ$ where $\eta = y/h$ . . .	168
7.4	Normalized tensile stress versus tensile strain curve for symmetric double-slip uni-axial extension of single crystal at zero dissipation with $\varphi = 60^\circ$ and $h = 1 \mu\text{m}$ . . . . .	169
7.5	Evolution of $\beta_l$ (continuous lines) and $\beta_r$ (dashed lines) within the interval $\eta \in (0, 1)$ together with $\alpha_l$ (continuous lines) and $\alpha_r$ (dashed lines) within the interval $\eta \in (0, 0.2)$ for zero dissipation symmetric double-slip plane-constrained uniaxial extension of single crystal at $\varphi = 60^\circ$ and $\epsilon = 0.003$ with different crystal heights $h$ . . . . .	170
7.6	Normalized tensile stress versus tensile strain curves for zero dissipation symmetric double-slip plane-constrained uniaxial extension of single crystal at $\varphi = 60^\circ$ with different crystal heights $h$ . . . . .	171
7.7	A closed loading path for plane constrained uniaxial extension of a single crystal strip with symmetric double slip systems . . . . .	171
7.8	Evolution of $\beta$ and $\alpha$ for the case of symmetric double slip systems for plane-constrained uniaxial extension of a single crystal strip with dissipation during the loading process as $\epsilon$ increases at $\varphi = 60^\circ$ where $h = 1 \mu\text{m}$ . . . .	172
7.9	Evolution of $\beta$ and $\alpha$ for the case of symmetric double slip systems for plane-constrained uniaxial extension of a single crystal strip with dissipation during the inverse loading process as $\epsilon$ decreases at $\varphi = 60^\circ$ where $h = 1 \mu\text{m}$ . . . .	173
7.10	Plot of $\beta$ within the interval $\eta \in (0, 1)$ and $\alpha$ within the interval $\eta \in (0, 0.2)$ at $\varphi = 60^\circ$ and $\epsilon = 0.005$ with different crystal heights $h$ for the symmetric double slip systems uniaxial extension case with non-zero dissipation . . .	174
7.11	EEvolution of $\beta_l$ (continuous lines) and $\beta_r$ (dashed lines) within the interval $\eta \in (0, 1)$ together with $\alpha_l$ (continuous lines) and $\alpha_r$ (dashed lines) within the interval $\eta \in (0, 0.2)$ for the case of symmetric double-slip plane-constrained uniaxial extension of single crystal with energy dissipation at $\varphi = 60^\circ$ and $\epsilon = 0.005$ for different crystal heights $h$ . . . . .	175
7.12	Normalized tensile stress versus tensile strain curve at $\varphi = 60^\circ$ with different crystal heights $h$ during the loading for symmetric double slip systems uniaxial extension case with dissipation . . . . .	176
7.13	Evolution of plastic distortions ( $\beta_l$ and $\beta_r$ ) and dislocation densities ( $\alpha_l$ and $\alpha_r$ ) for general double slip uniaxial extension case with zero dissipation at $\varphi_l = 65^\circ$ and $\varphi_r = 120^\circ$ in interval $\epsilon_{en1} \leq \epsilon < \epsilon_{en2}$ where $h = 1 \mu\text{m}$ . . . . .	178
7.14	Evolution of $\beta_l$ and $\beta_r$ together with $\alpha_l$ and $\alpha_r$ for general case double slip plane-constrained uniaxial extension of single crystal at zero dissipation where $h = 1 \mu\text{m}$ , $\varphi_l = 65^\circ$ and $\varphi_r = 120^\circ$ at $\epsilon \geq \epsilon_{en2}$ . . . . .	179
7.15	Normalized tensile stress versus tensile strain curve for general double-slip uni-axial extension of single crystal at zero dissipation at $\varphi_l = 65^\circ$ and $\varphi_r = 120^\circ$ with $h = 1 \mu\text{m}$ . . . . .	181

7.16	Evolution of $\beta_l$ (continuous lines) and $\beta_r$ (dashed lines) within the interval $\eta \in (0, 1)$ for zero dissipation double slip plane-constrained uniaxial extension of single crystal at $\varphi_l = 65^\circ$ , $\varphi_r = 120^\circ$ and $\gamma = 0.01$ with different crystal heights $h$ . . . . .	181
7.17	Normalized tensile stress versus tensile strain curves for zero dissipation double slip plane-constrained uniaxial extension of single crystal at $\varphi_l = 65^\circ$ and $\varphi_r = 120^\circ$ with different crystal heights $h$ . . . . .	182
7.18	A closed loading path for plane-constrained uniaxial extension problem with two active slip systems . . . . .	182
7.19	Evolution of plastic distortions and dislocation densities for loading path AB as $\epsilon$ increased at $\varphi_l = 20^\circ$ and $\varphi_r = 140^\circ$ where $h = 1 \mu\text{m}$ . . . . .	183
7.20	Evolution of plastic distortions and dislocation densities as $\epsilon$ grows for loading path BC at $\varphi_l = 20^\circ$ and $\varphi_r = 140^\circ$ where $h = 1 \mu\text{m}$ . . . . .	184
7.21	Evolution of plastic distortions and dislocation densities as $\epsilon$ decreases for loading path DE at $\varphi_l = 20^\circ$ and $\varphi_r = 140^\circ$ where $h = 1 \mu\text{m}$ . . . . .	185
7.22	Evolution of plastic distortions and dislocation densities as $\epsilon$ decreases for loading path EF at $\varphi_l = 20^\circ$ and $\varphi_r = 140^\circ$ where $h = 1 \mu\text{m}$ . . . . .	186
7.23	Normalized tensile stress versus tensile strain curve of general double slip plane-constrained uniaxial extension at non-zero dissipation of single crystal for $\varphi_l = 20^\circ$ and $\varphi_r = 140^\circ$ where $h = 1 \mu\text{m}$ . . . . .	187
7.24	Evolution of $\beta_l$ (continuous lines) and $\beta_r$ (dashed lines) within the interval $\eta \in (0, 1)$ during the loading process (increasing $\gamma$ ) for double slip plane-constrained uniaxial extension with dissipation of single crystal at $\varphi_l = 20^\circ$ , $\varphi_r = 140^\circ$ and $\epsilon = 0.006$ with different crystal heights $h$ . . . . .	188
7.25	Normalized tensile stress versus tensile strain curve of general double slip plane-constrained uniaxial extension at non-zero dissipation of single crystal for $\varphi_l = 20^\circ$ and $\varphi_r = 140^\circ$ with different crystal heights $h$ . . . . .	188
7.26	Evolution of plastic distortions ( $\beta_l$ and $\beta_r$ ) and dislocation densities ( $\alpha_l$ and $\alpha_r$ ) for general double slip combined loading case with zero dissipation at $\varphi_l = 65^\circ$ , $\varphi_r = 120^\circ$ and $\theta = 20^\circ$ in interval $\delta_{en1} \leq \delta \leq \delta_{en2}$ where $h = 1 \mu\text{m}$ . 191	
7.27	Evolution of $\beta_l$ and $\beta_r$ together with $\alpha_l$ and $\alpha_r$ for general double slip combined loading case with zero dissipation where $h = 1 \mu\text{m}$ , $\varphi_l = 65^\circ$ , $\varphi_r = 120^\circ$ at $\delta \geq \delta_{en2}$ . . . . .	192
7.28	Evolution of $\beta$ and $\alpha$ for anti-plane zero dissipation case at increasing $\theta$ where $\varphi_l = 65^\circ$ , $\varphi_r = 120^\circ$ and $\delta = 0.0045$ . . . . .	194
7.29	Evolution of $\beta_l$ and $\beta_r$ together with $\alpha_l$ and $\alpha_r$ for general double slip combined loading case with non-zero dissipation where $h = 1 \mu\text{m}$ , $\varphi_l = 20^\circ$ , $\varphi_r = 140^\circ$ and $\theta = 20^\circ$ as $\delta$ increases at $\delta_{en} \leq \delta < \delta_{en2}$ . . . . .	195
7.30	Evolution of $\beta_l$ and $\beta_r$ together with $\alpha_l$ and $\alpha_r$ for general double slip combined loading case with non-zero dissipation where $h = 1 \mu\text{m}$ , $\varphi_l = 20^\circ$ , $\varphi_r = 140^\circ$ and $\theta = 20^\circ$ as $\delta$ increases at $\delta \geq \delta_{en2}$ . . . . .	196
7.31	Evolution of $\beta$ and $\alpha$ for anti-plane non-zero dissipation case at increasing $\theta$ where $\varphi_l = 20^\circ$ , $\varphi_r = 140^\circ$ and $\delta = 0.02$ . . . . .	199
7.32	Evolution of $\beta_l$ and $\beta_r$ together with $\alpha_l$ and $\alpha_r$ for general double slip combined loading case with non-zero dissipation where $h = 1 \mu\text{m}$ , $\varphi_l = 20^\circ$ , $\varphi_r = 140^\circ$ and $\theta = 20^\circ$ as $\delta$ decreases . . . . .	200



## Bibliography

- Acharya, A. and Bassani, J. L. (2000). Lattice incompatibility and a gradient theory of crystal plasticity. *Journal of the Mechanics and Physics of Solids*, 48:1565–1595.
- Anand, L., Gurtin, M. E., Lele, S. P., and Gething, C. (2005). A one-dimensional theory of strain-gradient plasticity: formulation, analysis, numerical results. *Journal of the Mechanics and Physics of Solids*, 53:1789–1826.
- Berdichevsky, V. L. (2005). Homogenization in micro-plasticity. *Journal of the Mechanics and Physics of Solids*, 53:2457–2469.
- Berdichevsky, V. L. (2006a). Continuum theory of dislocations revisited. *Continuum Mechanics and Thermodynamics*, 18:195–222.
- Berdichevsky, V. L. (2006b). On thermodynamics of crystal plasticity. *Scripta materialia*, 54:711–716.
- Berdichevsky, V. L. and Le, K. C. (2007). Dislocation nucleation and work hardening in anti-plane constrained shear. *Continuum Mechanics and Thermodynamics*, 18:455–467.
- Berdichevsky, V. L. and Sedov, L. I. (1967). Dynamic theory of continuously distributed dislocations. its relation to plasticity theory. *Journal of Applied Mathematics and Mechanics*, 31:989–1006.
- Bilby, B. A. (1955). Types of dislocation source. In *Report of the Bristol Conference on Defects in Crystalline Solids*, pages 123–133. London: The Physical Society.
- Bilby, B. A., Bullough, R., and Smith, E. (1955). Continuous distributions of dislocations: a new application of the methods of non-riemannian geometry. *Proceedings of the Royal Society of London. Series A. Mathematical and Physical Sciences*, 231:263–273.
- Burgers, J. M. (1939). *Some considerations on the fields of stress connected with dislocations in a regular crystal lattice*. Koninklijke Nederlandse Akademie van Wetenschappen.
- Callister, W. D. (2007). *Materials science and engineering : An introduction*. New York: John Wiley & Sons, 7 edition.
- Cottrell, A. H. (1957). *Deformation of solids at high rates of strain*. Institution of Mechanical Engineers.
- Elam, C. F. (1935). *Distortion of Metal Crystals*. Clarendon Press.
- Ewing, J. A. and Rosenhain, W. (1899). Experiments in micro-metallurgy: Effects of strain. preliminary notice. *Proceedings of the Royal Society of London*, 65:85–90.
- Ewing, J. A. and Rosenhain, W. (1900). Bakerian lecture: The crystalline structure of metals. *Philosophical Transactions of the Royal Society of London. Series A, Containing Papers of a Mathematical or Physical Character*, pages 353–375.

- Fleck, N. A. and Hutchinson, J. W. (2001). A reformulation of strain gradient plasticity. *Journal of the Mechanics and Physics of Solids*, 49:2245–2271.
- Frank, F. C. (1950). In *Report of the Pittsburgh Conference on Plastic Deformation of Crystals*, page 100. Carnegie Institute of Technology and Office of Naval Research, Washington, DC.
- Frank, F. C. and Read, W. T. (1950). Multiplication processes for slow moving dislocations. *Physical Review*, 79:722.
- Frenkel, J. (1926). Zur Theorie der Elastizitätsgrenze und der Festigkeit kristallinischer Körper. *Zeitschrift für Physik*, 37:572–609.
- Friedel, J. (1964). *Dislocations*. Oxford: Pergamon.
- Friedman, L. H. and Chrzan, D. C. (1998). Continuum analysis of dislocation pile-ups: influence of sources. *Philosophical Magazine A*, 77:1185–1204.
- Gao, H., Huang, Y., Nix, W. D., and Hutchinson, J. W. (1999). Mechanism-based strain gradient plasticity—I. Theory. *Journal of the Mechanics and Physics of Solids*, 47:1239–1263.
- Groma, I., Csikor, F. F., and Zaiser, M. (2003). Spatial correlations and higher-order gradient terms in a continuum description of dislocation dynamics. *Acta Materialia*, 51:1271–1281.
- Groma, I., Györgyi, G., and Kocsis, B. (2007). Dynamics of coarse grained dislocation densities from an effective free energy. *Philosophical Magazine*, 87:1185–1199.
- Gurtin, M. E. (1973). The linear theory of elasticity. In *Linear Theories of Elasticity and Thermoelasticity*, pages 1–295. Springer.
- Gurtin, M. E. (2003). On a framework for small-deformation viscoplasticity: free energy, microforces, strain gradients. *International Journal of Plasticity*, 19:47–90.
- Gurtin, M. E. (2004). A gradient theory of small-deformation isotropic plasticity that accounts for the Burgers vector and for dissipation due to plastic spin. *Journal of the Mechanics and Physics of Solids*, 52:2545–2568.
- Gurtin, M. E. and Anand, L. (2005). A theory of strain-gradient plasticity for isotropic, plastically irrotational materials. part II: Finite deformations. *International journal of plasticity*, 21:2297–2318.
- Hall, E. O. (1951). The deformation and ageing of mild steel: III discussion of results. *Proceedings of the Physical Society. Section B*, 64:747.
- Han, C. S., Gao, H., Huang, Y., and Nix, W. D. (2005a). Mechanism-based strain gradient crystal plasticity—I. Theory. *Journal of the Mechanics and Physics of Solids*, 53:1188–1203.
- Han, C. S., Gao, H., Huang, Y., and Nix, W. D. (2005b). Mechanism-based strain gradient crystal plasticity—II. Analysis. *Journal of the Mechanics and Physics of Solids*, 53:1204–1222.
- Hill, R. (1998). *The mathematical theory of plasticity*. Clarendon Press Oxford University Press, Oxford and New York.

- Hirth, J. and Lothe, J. (1982). *Theory of Dislocations*. John Wiley, New York.
- Huang, Y., Gao, H., Nix, W. D., and Hutchinson, J. W. (2000). Mechanism-based strain gradient plasticity—II. Analysis. *Journal of the Mechanics and Physics of Solids*, 48:99–128.
- Huang, Y., Qu, S., Hwang, K. C., Li, M., and Gao, H. (2004). A conventional theory of mechanism-based strain gradient plasticity. *International Journal of Plasticity*, 20:753–782.
- Hull, D. (2001). *Introduction to Dislocations*. Butterworth-Heinemann, Oxford, 4 edition.
- Kaluza, M. and Le, K. (2011). On torsion of a single crystal rod. *International Journal of Plasticity*, 27:460–469.
- Khan, A. and Huang, S. (1995). *Continuum theory of plasticity*. John Wiley & Sons, Inc.
- Kochmann, D. M. (2009). *Mechanical modeling of microstructures in elasto-plastically deformed crystalline solids*. PhD thesis, Ruhr Universität Bochum.
- Kochmann, D. M. and Le, K. C. (2008). Dislocation pile-ups in bicrystals within continuum dislocation theory. *International Journal of Plasticity*, 24:2125–2147.
- Kochmann, D. M. and Le, K. C. (2009a). A continuum model for initiation and evolution of deformation twinning. *Journal of the Mechanics and Physics of Solids*, 57:987–1002.
- Kochmann, D. M. and Le, K. C. (2009b). Plastic deformation of bicrystals within continuum dislocation theory. *Mathematics and Mechanics of Solids*, 14:540–563.
- Kondo, K. (1952). On the geometrical and physical foundations of the theory of yielding. In *Proceedings of the 2nd Japan Congress on Applied Mechanics*, volume 2, pages 41–47.
- Kröner, E. (1955). Der fundamentale Zusammenhang zwischen Versetzungsdichte und Spannungsfunktionen. *Zeitschrift für Physik*, 142:463–475.
- Kröner, E. (1958). *Kontinuumstheorie der Versetzungen und Eigenspannungen*. Springer, Berlin.
- Kröner, E. (1992). Mikrostrukturmechanik. *GAMM-Mitteilungen*, 15:104–119.
- Le, K. C. (2010). *Introduction to Micromechanics*. Nova Science, New York.
- Le, K. C. and Berdichevsky, V. L. (2001). Energy distribution in a neutral gas of point vortices. *Journal of Statistical Physics*, 104:881–892.
- Le, K. C. and Günther, . (2014). Nonlinear continuum dislocation theory revisited. *International Journal of Plasticity*, 53:164–178.
- Le, K. C. and Nguyen, B. D. (2012). Polygonization: Theory and comparison with experiments. *International Journal of Engineering Science*, 59:211–218.
- Le, K. C. and Nguyen, B. D. (2013). On bending of single crystal beam with continuously distributed dislocations. *International Journal of Plasticity*, 48:152–167.
- Le, K. C. and Nguyen, Q. S. (2009). Plastic yielding and work hardening of single crystals in a soft device. *Comptes Rendus Mecanique*, 337:709–715.

- Le, K. C. and Nguyen, Q. S. (2010). Polygonization as low energy dislocation structure. *Continuum Mechanics and Thermodynamics*, 22:291–298.
- Le, K. C. and Sembiring, P. (2008a). Analytical solution of plane constrained shear problem for single crystals within continuum dislocation theory. *Archive of Applied Mechanics*, 78:587–597.
- Le, K. C. and Sembiring, P. (2008b). Plane constrained shear of single crystal strip with two active slip systems. *Journal of the Mechanics and Physics of Solids*, 56:2541–2554.
- Le, K. C. and Sembiring, P. (2009). Plane constrained uniaxial extension of a single crystal strip. *International Journal of Plasticity*, 25:1950–1969.
- Le, K. C. and Stumpf, H. (1996a). A model of elastoplastic bodies with continuously distributed dislocations. *International journal of plasticity*, 12:611–627.
- Le, K. C. and Stumpf, H. (1996b). Nonlinear continuum theory of dislocations. *International journal of engineering science*, 34:339–358.
- Le, K. C. and Stumpf, H. (1996c). On the determination of the crystal reference in nonlinear continuum theory of dislocations. *Proceedings of the Royal Society of London. Series A: Mathematical, Physical and Engineering Sciences*, 452:359–371.
- Leibfried, G. (1951). Verteilung von Versetzungen im statischen Gleichgewicht. *Zeitschrift für Physik*, 130:214–226.
- Lubliner, J. (1990). *Plasticity theory*. Macmillan Publishing, New York.
- Mott, N. F. and Nabarro, F. R. N. (1948). Report of a conference on the strength of solids. *The Physical Society, London*, 75.
- Needleman, A. and Van der Giessen, E. (2001). Discrete dislocation and continuum descriptions of plastic flow. *Materials Science and Engineering: A*, 309:1–13.
- Nye, J. F. (1953). Some geometrical relations in dislocated crystals. *Acta metallurgica*, 1:153–162.
- Orowan, W. (1934). Zur Kristallplastizität III. über den Mechanismus des Gleitvorganges. *Zeitschrift für Physik*, 89:634–659.
- Ortiz, M. and Repetto, E. A. (1999). Nonconvex energy minimization and dislocation structures in ductile single crystals. *Journal of the Mechanics and Physics of Solids*, 47:397–462.
- Ortiz, M., Repetto, E. A., and Stainier, L. (2000). A theory of subgrain dislocation structures. *Journal of the Mechanics and Physics of Solids*, 48:2077–2114.
- Petch, N. J. (1953). The cleavage strength of polycrystals. *Journal of the Iron and Steel Institute*, 174:25–28.
- Polanyi, M. (1934). Über eine Art Gitterstörung, die einen Kristall plastisch machen könnte. *Zeitschrift für Physik*, 89:660–664.
- Schmid, E. (1924). Neuere Untersuchungen an Metallkristallen. *Proceedings of the First International Congress for Applied Mechanics, Delft*, pages 342–353.

- Sedov, L. I. (1968). Variational methods of constructing models of continuous media. In *Irreversible aspects of continuum mechanics*. Springer Verlag, Wien and New York.
- Shu, J. Y. and Fleck, N. A. (1999). Strain gradient crystal plasticity: size-dependent deformation of bicrystals. *Journal of the Mechanics and Physics of Solids*, 47:297–324.
- Shu, J. Y., Fleck, N. A., Van der Giessen, E., and Needleman, A. (2001). Boundary layers in constrained plastic flow: comparison of nonlocal and discrete dislocation plasticity. *Journal of the Mechanics and Physics of Solids*, 49:1361–1395.
- Taylor, G. I. (1934). The mechanism of plastic deformation of crystals. part I. Theoretical. *Proceedings of the Royal Society of London. Series A, Containing Papers of a Mathematical and Physical Character*, pages 362–387.
- Volterra, V. (1905). Sull'equilibrio dei corpi elastici più volte connessi. *Il Nuovo Cimento (1901-1910)*, 10:361–385.
- Weertman, J. and Weertman, J. R. (1966). *Elementary dislocation theory*. Macmillan, New York.



# Pramio Garson Sembiring

## PERSONAL DATA

---

PLACE AND DATE OF BIRTH: Medan, Indonesia | 24 October 1976  
NATIONALITY: Indonesian  
MARITAL STATUS: Married

## EDUCATION

---

- JUNE 2014 Doktor-Ingenieur (Dr.-Ing). in CIVIL ENGINEERING  
**Ruhr-Universität Bochum**, Bochum, Germany  
*Lehrstuhl für Mechanik-Material Theorie, Institut für Mechanik*  
Dissertation: "ANALYTICAL AND NUMERICAL SOLUTIONS TO PLANE STRAIN  
PROBLEMS IN CONTINUUM DISLOCATION THEORY"  
Supervisor: Prof. Dr. Khanh Chau Le  
Examination date: 24.06.2014
- DECEMBER 2006 Master of Science (M.Sc.) in COMPUTATIONAL ENGINEERING  
**Ruhr-Universität Bochum**, Bochum, Germany  
Thesis: "ANALYTICAL AND NUMERICAL STUDY OF DISLOCATION NUCLEATION  
AND WORK HARDENING IN SINGLE CRYSTALS"  
Supervisor: Prof. Dr. Khanh Chau Le
- FEBRUARY 2000 Undergraduate Degree in MECHANICAL ENGINEERING  
**Bandung Institute of Technology**, Bandung, Indonesia

## WORK EXPERIENCE

---

- 2007-2012 | *Research Associate* at LEHRSTUHL FÜR MECHANIK-MATERIAL THEORIE  
**Ruhr-Universität Bochum**, Bochum, Germany
- 2006-2007 | *Research Assistance* at LEHRSTUHL FÜR MECHANIK-MATERIAL THEORIE  
**Ruhr-Universität Bochum**, Bochum, Germany

**Mitteilungen aus dem Institut für Mechanik  
RUHR-UNIVERSITÄT BOCHUM  
Nr. 162, Juni 2014**

**ISBN 978-3-935892-40-7**